SAND2008-4807P

The Pennsylvania State University

The Graduate School

College of Engineering

EFFECTS OF VAPOR-PHASE ENVIRONMENTAL CONSTITUENTS ON MACRO- TO NANO-TRIBOLOGICAL BEHAVIOR

A Dissertation in

Chemical Engineering

by

David Benjamin Asay

Submitted in Partial Fulfillment
of the Requirements
for the Degree of

Doctor of Philosophy

August 2008

The dissertation of David Benjamin Asay was reviewed and approved* by the following:

Seong H. Kim
Associate Professor of Chemical Engineering
Dissertation Advisor
Chair of Committee

Erwin A. Vogler
Professor of Materials Science & Engineering, Bioengineering, and Medical Materials

Joan M. Redwing
Professor of Materials Science and Engineering
Courtesy Appointment Professor of Chemical Engineering

Darrell Velegol
Associate Professor of Chemical Engineering

Andrew Zydney
Walter L. Robb Chair and Professor of Chemical Engineering
Head of the Department of Chemical Engineering

*Signatures are on file in the Graduate School

ABSTRACT

When surfaces come into contact, a number of fascinating phenomena occur; adhesion, friction, and wear, each a consequence of material properties, environment conditions and constituents, contacting geometry, applied loads and relative velocities. Changing any of these variables can drastically alter adhesion, friction, and/or wear. Approaches to prevent wear, reduce friction, and control adhesion are determined by the application in question. In many cases, devices requiring lubrication have predetermined geometries, loads, velocities, and are made of specific materials. Effective lubrication and wear prevention then depends on engineering constituents utilized as lubricants. Typically, bulk liquid hydrocarbons are used. As devices shrink in size, bulk lubricants are not practical due to the large capillary forces they create and extreme viscous dampening forces. Microscale devices (i.e. MicroElectroMechanical Systems MEMS) require new technologies for lubrication and wear prevention.

This thesis examines the capability of molecular thin films as lubricants and wear prevention films. These films are maintained by utilizing adsorption equilibrium of vapor-phase molecules. Water and various linear alcohol molecules are studied as potential vapor-phase lubricants. Because of the importance of silicon to microscale devices, tribological studies of wear, friction, and adhesion of silicon as a function of alcohol vapor pressure and chain length are studied. Additionally, the effectiveness of these molecular thin films as lubricants for single nano-asperity contact and macrosopic multi-asperity contacts is studied.

Adsorption of thin water or alcohol films drastically alters adhesion, friction, and wear. In the case of water adsorption on silicon oxide surface, at low relative humidity, water preferentially adsorbs into the silicon oxide surface in an ice-like structure. As the partial pressure of water increases, liquid water structure is observed to grow on top of the ice-like water structure. As a consequence of structured water at low relative humidities, adhesion between silicon oxide nano-asperity contacts is significantly larger than predicted from capillary forces alone. During sliding in humid environments, chemical wear of silicon oxide is accelerated. Altering the surface chemistry of the silicon oxide surface to prevent water adsorption via chemisorption of self-assembled monolayers is investigated. While these hydrophobic treatments lower the total average surface coverage of water at the interface, water adsorption is not completely prevented.

Adsorption of linear alcohols onto the silicon oxide surface is also investigated. In the case of alcohol vapors, monolayer coverage is observed to occur at ~10% of the saturation pressure of the alcohol. In contrast with water, alcohol is observed to drastically reduce adhesion between nano-scale contacts. The reduction in capillary adhesion is observed to decrease and is inversely proportional to the molar volume. In the case of contact asperities ranging from a single nano-scale asperity to multi-asperity macro-scale systems, alcohol vapor adsorption successfully lubricates (lowers friction) and prevents wear. Inside of the sliding contact region, high-molecular weight oligomeric species are formed via tribochemical reactions from alcohol precursor molecules forming wear protective coatings. Therefore, these oligomeric species/coatings form when and where lubrication is needed most; greatly aiding wear prevention. In the case of silicon based MEMS devices, these films completely prevent

wear and increase the lifetime of these devices over 4 to 5 orders of magnitude compared with current “state-of-the-art” self-assembled monolayer coatings.

TABLE OF CONTENTS

LIST OF FIGURES viii

LIST OF TABLES xvi

ACKNOWLEDGEMENTS xvii

Chapter 1 Introduction to Nanotibology and MicroElectroMechanical Systems (MEMS) 1

1.0.1 Summary 1
1.1 Introduction 2
1.2 MEMS History 5
1.3 Fabrication of MEMS 10
1.4 Nanotribology related to MEMS 12
1.5 Applications of Nanotribology to MEMS lubrication 19
1.5.1 Reducing Adhesion 19
1.5.2 Reducing friction and wear 20
1.6 The Road Ahead 25
1.7 References 28

Chapter 2 Evolution of the Adsorbed Water Layer Structure on Silicon Oxide at Room Temperature 36

2.1 Summary 36
2.2 Introduction to water adsorption on silicon oxide surfaces 37
2.3 Experimental Details 39
2.4 Results and Discussion 41
2.5 Conclusions 51
2.6 References 52

Chapter 3 Surface Chemistry Effects on the Adsorption of Water onto Chemically Modified Silicon Surfaces 56

3.1 Summary 56
3.2 Introduction 57
3.3 Experimental Details 58
3.4 Experimental Results and Discussion 61
3.5 Conclusions 74
3.6 References 75

Chapter 4 Effects of Adsorbed Water Layer Structure on Adhesion Force of Silicon Oxide Nanoasperity Contact in Humid Ambient 78

4.1 Summary....78
4.2 Introduction....79
4.3 Experimental Details....80
4.4 Results and Discussion....81
4.5 Conclusions....93
4.6 References....94

Chapter 5 Molar Volume and Adsorption Isotherm Dependence of Capillary Forces in Nano-asperity Contacts....97

5.1 Summary....97
5.2 Introduction....98
5.3 Experimental Setup....101
5.4 Modeling....103
5.5 Results and Discussion....105
5.6 Conclusions....119
5.7 References....120

Chapter 6 Direct Force Balance Method (DFBM) for AFM Lateral Force Calibration....123

6.1 Summary....123
6.2 Introduction....124
6.3 Force Balance for *f-d* Measurement on a Sloped Surface....129
6.4 Experimental Details....143
6.5 Results and Discussion....146
6.5.1 Macro-scale Cantilever Case....146
6.5.2 AFM Case....151
6.6 Conclusions....161
6.7 References....163

Chapter 7 Chain length Dependence and Capillary Effects in Nano-asperity Friction Forces of Vapor-phase Linear Alcohol Lubricants....165

7.1 Summary....165
7.2 Introduction....166
7.3 Fundamentals of Nano-asperity friction and contact mechanics....167
7.4 Effect of Capillary formation on Contact Mechanics and Friction of nano-asperity contacts....172
7.5 Experimental Setup....174
7.6 Results and Discussions....175
7.7 Conclusions....185
7.8 References....186

Chapter 8 Macro- to Nano-scale Wear Prevention via Molecular Adsorption....189

8.1 Summary....189
8.2 Introduction....190
8.3 Experimental Details....192
8.4 Results and Discussions....196
8.5 Conclusions....211
8.6 References....212

Chapter 9 In-situ Vapor-Phase Lubrication of MEMS....215

9.1 Summary....215
9.2 Introduction....216
9.3 Experimental Details....218
9.3.1 Specimen Preparation....219
9.4 MEMS Tribological Measurements....220
9.5 Pin-on-Flat (or Macroscopic) Friction Measurements....224
9.6 Results and Discussion....225
9.6.1 DRY Environment....225
9.6.2 Vapor-Phase Lubricating Environment....228
9.7 Conclusions....240
9.8 References....241

Chapter 10 Competitive Adsorption of Water and 1-Pentanol on Silicon under Tribological Conditions....243

10.1 Summary....243
10.2 Introduction....244
10.3 Experimental Setup....246
10.4 Results and Discussions....248
10.5 Conclusions....258
10.6 References....259
10.6 References....259

SYNOPSIS....264

FUTURE DIRECTIONS....267

Appendix Supporting Data....270

A.1 ATR-IR simulations were done with the following algorithm written in Mathcad....270
A.2 Capillary Force Calculations (MathCAD program)....277
A.3 Silicon Cleaved in Air or Liquid Alcohol. (ToF-SIMS Data) Evidence of alkoxide formation from base linear alcohols....285
A.4 Isotherm Data for Chapter 3....292

LIST OF FIGURES

Figure **1.1**: (a) Intermeshing gears and (b) mirror and drive systems produced by silicon surface micromachining in Sandia National Laboratories' SUMMiT^{TM} process. 7

Figure **1.2**: Variation of gravity and adhesion for a cube with a smooth surface as a function of size (L). Adhesion force falls linearly with surface or contact area while gravitational force falls with volume. 9

Figure **1.3**: Examples of surface morphology of MEMS fabricated by (a) silicon micromachining, (b) silicon-on-insulator, and (c) electroforming processes. 13

Figure **1.4**: Schematic view of atomic force microscopy (AFM) used in nanotribology studies. 14

Figure **1.5**: Maximum Contact Pressure for sphere-flat geometry when only adhesion forces ($F_{adh}=4\pi R\gamma$) are present. Both surfaces have a surface tension of γ. The material properties used for this figure are those of silicon. As the contact radius (R) decreases the contact pressure increases and is proportional to $R^{-1/3}$. 16

Figure **2.1**: Adsorption experiment setup illustrating the flow system and infrared evanescent wave used to detect the adsorbed species. 40

Figure **2.2**: ATR-IR spectra of water adsorbed on silicon oxide at different relative humidities. From lowest to highest log(1/R) signal intensity, relative humidity = 7.3, 9.7, 14.5, 19.4, 24.5, 29.4, 38.8, 49.4, 58.6, 64.3, 69.9, 74.5, 84.2, 92.2, 99.4 %. The O-H stretching vibration peak positions of "ice-like" water and liquid water are marked with dotted lines at ~3230 cm^{-1} and ~3400 cm^{-1}, respectively. The free-OH peak is marked at 3740 cm^{-1}. 42

Figure **2.3**: Adsorption isotherm of adsorbed water on silicon oxide surface. Square symbols are the total thickness of the adsorbed water layer calculated from the intensity of H-O-H bending vibration peak. The solid line is drawn to guide eyes. The dashed and dotted lines are the thickness of the ice-like water and liquid water layers, respectively. The thickness of each component is calculated by deconvoluting the observed O-H stretching peaks into two peaks at 3230 cm^{-1} and 3400 cm^{-1}. The sensitivity of the O-H stretching peak is assumed to be equal in both structures. Regions A, B, and C are shown, corresponding to ice-like water growth, transitional growth, and liquid water growth. 43

Figure **2.4**: Schematic illustrating the structural evolution of water molecules as the adsorbed layer thickness increases with RH. The ice-like structure grows

up to 3 molecular layers thick as relative humidity increases from 0 to 30%. In the relative humidity range from 30 to 60%, the ice-like structure continues to grow while liquid structure begins to form. In this transitional region, approximately one molecular layer grows. Further increase in the relative humidity above 60% causes water to adsorb in the liquid configuration. (--- Hydrogen bonds, ═ Covalent bonds) (note: 2-D illustration is not to scale) 48

Figure **3.1**: ATR-IR spectra of adsorbed water at 10°C on Silicon Oxide Surface. The "ice-like" structured water and liquid water structure peak positions are represented by the dash-dot and dashed lines respectively. Each condition's partial pressure is related to the saturation pressure of water (P^{sat}) at 10°C 63

Figure **3.2**: ATR-IR spectra of adsorbed water at 10°C on Silicon Oxide Surface treated with HMDS. The "ice-like" structured water and liquid water structure peak positions are represented by the dash-dot and dashed lines respectively while the "free-OH" structure is illustrated with a dotted line. Each condition's partial pressure is related to the saturation pressure of water (P^{sat}) at 10°C. 65

Figure **3.3**: ATR-IR spectra of adsorbed water at 10°C on Silicon Oxide Surface treated with OTS. The "ice-like" structured water and liquid water structure peak positions are represented by the dash-dot and dashed lines. Each condition's partial pressure is related to the saturation pressure of water (P^{sat}) at 10°C. 67

Figure **3.4**: Adsorption isotherms for clean hydroxylated silicon oxide surface, HMDS treated silicon oxide surface, and OTS treated silicon oxide surface. All data taken near 10 °C. Error bars are removed in order to simplify the figure. Typical x error bars are 3 to 4 (%) while the typical y-error bars are on the order of ~0.2 nm. 69

Figure **3.5**: Isosteric heat of adsorption of water on clean hydroxylated silicon oxide surface and HMDS treated silicon oxide surface..... 71

Figure **3.6**: Isosteric heat of adsorption of water on clean hydroxylated silicon oxide surface and HMDS treated silicon oxide surface..... 73

Figure **4.1**: Nanoasperity adhesion force as a function of relative humidity. Experimental data error bars represent 80% confidence interval. Inset shows the f-d curves at 10%, 70%, and 90%..... 82

Figure **4.2**: Thickness of the adsorbed water layer as a function of relative humidity. ATR-IR spectra of OH stretching vibration are shown for 15%, 50%, and 84% . The x-axis of the inset is wavenumber (cm^{-1}) and the y-axis is –log(reflectance). 84

Figure **4.3**: Schematics of the AFM tip position and ice-ice contact area as a function of relative humidity immediately prior to snap off. The inset illustrates the two curvatures (r and R_A) that contribute to the Laplace pressure. The tip is in contact in order to predict the maximum capillary force (y=1 case). 87

Figure **4.4**: Simulation of the contributions from capillary force term ($F_{capillary}$), van der Waals term (F_{VDW}), and the ice-ice bridge term (F_{ice}). The bottom dotted line represents the maximum $F_{capillary}$. The middle dashed line represents F_{VDW} + $F_{capillary}$. The solid lines represent the sum of three components, F_{ice} + F_{VDW} + $F_{capillary}$. The thin solid line is the simulation result with y = 1.0 fixed. The thick solid line is the result with the fitted y values to reproduce the experimental data. The fitted *y* values are marked in the graph. ... 90

Figure **5.2**: ATR-IR spectra of ethanol, 1-butanol, 1-pentanol on clean silicon ATR crystal each at 65% of P^{sat} 106

Figure **5.3**: Adsorption isotherm for ethanol, 1-butanol, 1-pentanol as measured by the ATR-IR experiment. The dotted line represents the representative fit for all three isotherms. 107

Figure **5.4**: Adhesion vs. P/P^{sat} for ethanol, 1-butanol, 1-pentanol. All data points were normalized to the saturated condition where $F_{adh} = 4\pi R\gamma$ 109

Figure **5.5**: Normalized capillary forces for various arbitrary isotherms. The solid (black), short dash (green), and long dash (red) isotherms in the insert correspond to their respective isotherm. Here the molar volume and surface tension used were those of 1-butanol. 111

Figure **5.6**: Molar volume dependence of the capillary force. The predicted normalized capillary adhesion for each alcohol is presented using the representative S-shape isotherm and each alcohol's surface tension; only the molar volume varies significantly. 113

Figure **5.7**: Normalized AFM adhesion force vs. Laplace pressure. 116

Figure **5.8**: Normalized AFM adhesion force to account for differences in meniscus area and molar volume (*V*) between alcohols vs. Laplace pressure. The relative partial pressure for each alcohol is included in the figure. 118

Figure **6.3**: Force balance between the forces the AFM tip applies on the surface (F_A and F_T) and the forces the surface applies against the tip (F_N). In this case there is no friction. The sum of the force vectors = 0. The insert illustrates the tip sliding down the surface causing it to twist and therefore generate torsional forces. 132

Figure **6.4**: Force balance between the forces the AFM tip applies on the surface (F_A and F_T) and the forces the surface applies against the tip (F_N and F_F). In this case, friction prevents the tip from twisting ($F_T = 0$). The sum of the force vectors = 0. 133

Figure **6.5**: Force balance between the forces the AFM tip applies on the surface (F_A and F_T) and the forces the surface applies against the tip (F_N and F_F) during the approach or retraction cycle of the *f-d* curve. Friction acts against the direction of motion. The dotted line represents the frictionless case. The sum of the force vectors = 0. 135

Figure **6.6**: The moment arms a_1, a_2, and a_3 are illustrated for the off-centered tip (long dashed lines). The amount a tip is off-centered is measured in angles as α. The point C indicates the shear center of the cantilever. All twisting of the cantilever is centered about this point. The position of a centered tip is illustrated in the insert. 137

Figure **6.7**: The percentage difference between the average lateral responses as given in Equations 18 and 19 when friction is present ($\mu \neq 0$) vs. the frictionless case ($\mu = 0$). 141

Figure **6.9**: Schematic representation of the homebuilt, macro-scale cantilever setup. 144

Figure **6.10**: Macro-scale *f-d* curves of the centered tip on a glass surface. The lines represent the frictionless response. 147

Figure **6.11**: Macro-scale *f-d* curves of the off-centered tip on a glass surface. The lines represent the frictionless response. 148

Figure **6.12**: Macro-scale *f-d* curves of the centered tip on a wood surface. The lines represent the frictionless response. 150

Figure **6.13**: Multiple AFM *f-d* curves on TFG-11 calibration grating. Each line represents approach and retraction. 152

Figure **6.14**: Single AFM *f-d* curves on TGF-11 calibration grating. Each line represents approach and retraction. The inset shows the snap-in and snap-off parts of one single *f-d* curve. In the inset, the approach and retraction lines are shifted vertically to show the lateral signals in the tensile region of the *f-d* curve. 154

Figure **6.15**: Percent error in Δz due to tip sliding during *f-d* curve collection. These data are calculated with equation **6-30**. 158

Figure **7.1**: Model tip (sphere) – substrate system with adsorbed film whose thickness is *h*. Here *R* is the tip radius, a_c the contact radius, α a trapped molecular layer, *d* the penetration depth of the undeformed sphere, and r_1 and r_2 the two principle radii of curvature..... 171

Figure **7.2**: AFM Friction-Load Curves of a silicon AFM tip as it slides against a silicon (100) substrate as a function of load at various relative partial pressures of ethanol. 176

Figure **7.3**: Log-log plot of the data presented in Figure **7.2**. When alcohol vapors are present and are well below the saturation pressure of alcohol, the data follows a more 1/3 slope dependence. In the dry and saturation conditions the data follows a 2/3 slope dependence suggesting classical DMT contact mechanic behavior. (The dashed lines represent 2/3 and dash-dot lines, 1/3 slope)..... 178

Figure **7.4**: Data fitting with a DMT contact mechanics vs. the 2/3 & 1/3 friction model described with equation **7-15.** The 2/3 component from equation **7-15** is also plotted. 180

Figure **7.5**: Friction vs. Total Load comparison of ethanol, 1-butanol, and 1-pentanol at P/P^{sat} of 10%, 30%, 60%, and 95%..... 181

Figure **7.6**: Coefficient of friction from the Friction-Load curves vs. P/P^{sat} of ethanol, 1-butanol, and 1-pentanol. 183

Figure **7.7**: Shear strength (top) and Meniscus friction contribution (bottom) of each alcohol for ethanol, 1-butanol, and 1-pentanol as a function of each alcohol's relative partial pressure. 184

Figure **8.1**: Adsorption isotherm for 1-pentanol on native silicon oxide surface. Insert: ATR-IR spectroscopy of 1-pentanol monolayer on native silicon oxide. 197

Figure **8.2**: (a) Frictional response of quartz sphere (dia. = 3 mm) sliding against silicon (100) wafer as a function of the relative vapor pressure (P/P^{sat}) of 1-pentanol. (b) Optical profilometry of wear tracks at increasing relative 1-pentanol vapor pressures (P/Psat)..... 198

Figure **8.3**: ToF-SIMS spectra inside the contact track (top) and outside of the contact region (bottom) for the condition 18% of P^{sat}. Inside the contact, a hydrocarbon product is made (denoted as C_1, C_2, …, C_{15}), providing a protective layer between the rubbing surfaces. The "C_x" labeling indicates the minimum number (x) of carbon atoms required to appear at the m/z (mass/charge). The distribution within each "C_x" labeling is due to differing amounts of hydrogenation of the fragments contained within the C_x manifold. .. 200

Figure **8.5**: (a) SEM image of the MEMS sidewall friction device. Both post and shuttle are driven by electrostatic comb drives. (b) MEMS sidewall friction device. Increased magnification of the contact region (circled). The post moves perpendicular to the contact and is used to apply the load while the shuttle moves laterally to the contact. 203

Figure **8.6**: Friction force vs. cycles in MEMS sidewall device under 500 nN load at 100 Hz oscillation. In dry nitrogen the device fails within a few minutes, when 1-pentanol vapors are present (15 and 95% of P^{sat}) no failure is observed. 205

Figure **8.7**: SEM image of the sidewall contact. On the top, following 10^8 cycles in a 15 ±5% P^{sat} environment a liquid-like buildup is observed. bottom, fresh unused sidewall surface is shown for comparison. 207

Figure **8.9**: Top: Reaction path of Si-O-Si bond rupture. Below: DFT cross section of β-cristobalite (111) surface of SiO_2 with chemisorbed water at the transition state prior to Si-O-Si bond rupture. (courtesy of Dr. Michael Janik) ... 210

Figure **9.1**: SEM image of MEMS sidewall diagnostic tribometer. Sidewall contact area encircled. Loading/Unloading actuators cause the post (Labeled "A") to move and come into and out of contact. Push/Pull actuators cause the shuttle (Labeled "B") to move laterally and shear the contact. 222

Figure **9.2**: Frictional response of three separate MEMS sidewall tribometer devices oscillating at 100 Hz under a 500 nN load, in dry N_2 at room temperature. Devices fail between 4000 and 8000 cycles. 226

Figure **9.3**: Adhesion force of two different MEMS sidewall devices as a function of the relative partial pressure of 1-pentanol (P/P^{sat} where P^{sat} is the saturation pressure of the alcohol). 230

Figure **9.4**: Static frictional force of the same two MEMS sidewall devices (Figure 3a) as a function of the relative partial pressure of 1-pentanol. 231

Figure **9.6**: SEM image of the MEMS sidewall surface following $1.02x10^8$ cycles at 100 Hz in a 15 ±5% P/P^{sat} 1-pentanol environment 234

Figure **9.7**: Friction coefficient of FOTAS coated silicon as measured by LWT. Initially the environment contains 95% P/P^{sat} 1-pentanol. The environment was cycled from this condition to a dry N2 condition then back to a 95% P/P^{sat} environment as indicated at 500 and 900 cycles. Two lines (red and black) represent two separate experiments. 235

Figure **9.8**: Friction coefficient of MEMS device vs. cumulative cycles. Initially the environment contains 95% P/P^{sat} 1-pentanol. After 6.65 million cycles

the environment was cycled from this condition to a dry N2 condition then back to a 95% P/P^{sat} environment labeled as "A" and "B" respectively. The insert is a magnification between points "A" and "B". 237

Figure **9.9**: Adhesion force of the MEMS sidewall device as a function of the number of cycles operating in a 1-pentanol P/P^{sat} environment of 15 ±5%. 239

Figure **10.1**: Coefficient of friction observed over time as a 3 mm diameter quartz ball slides against a silicon (100) surface under a 100 gram load. In this case, the environment gradually changes from a dry N_2 to an environment rich with 1-pentanol vapors (R-OH where R = C5H11). 249

Figure **10.2**: Coefficient of friction observed over time as a 3 mm diameter quartz ball slides against a silicon (100) surface under a 100 gram load. In this case, the N_2 environment maintains a environment with 1000 ppmv of water vapor and each trace represents a different amount of 1-pentanol vapors (R-OH where R = C5H11). 250

Figure **10.3**: Wear volume observed on the silicon (100) surface at different environmental conditions. 252

Figure **10.4**: Normalized wear volume of the quartz sphere at different loads, contact speeds, and environmental conditions. Data courtesy of Erik Hsiao. 254

Figure **10.5**: Diagnostic MEMS sidewall tribometer. 255

Figure **10.6**: MEMS Diagnostic device operating cycle lifetime vs. environmental conditions. Figure Courtesy of Mike Dugger. 257

Figure **A.1**: Time-of-flight SIMS images (total intensity) of various silicon surfaces cleaved in different environments (alcohol cleavage experiments were done in bulk liquid). Montage of images for processing 285

Figure **A.2**: M/Z 85 from the montage of images (primary alcohol fragment). 286

Figure **A.3**: M/Z 71 from the montage of images (primary alcohol fragment). 287

Figure **A.4**: M/Z 57 from the montage of images (primary alcohol fragment). 288

Figure **A.5**: M/Z 103 from the montage of images (primary alkoxide fragment). 289

Figure **A.6**: M/Z 117 from the montage of images (primary alkoxide fragment). 290

Figure **A.7**: M/Z 131 from the montage of images (primary alkoxide fragment). 291

Figure **A.8**: Adsorption Isotherm of water on clean silicon oxide surface at various temperatures. 292

Figure **A.9**: Adsorption Isotherm of water on the partially methylated silicon oxide surface at various temperatures.....293

LIST OF TABLES

Table **1.1**: Intertwined concepts dominating tribology, surface science and mechanical contacts. 3

Table **1.2**: Comparison of moduli and hardness of various materials used in MEMS fabrication and lubrication 23

Table **5.1**: Surface Tension (γ) and molar volume (V) of linear alcohols 112

Table **6.1**: Average lateral slope response 153

Table **6.2**: Lateral AFM DFBM calibration results 156

Table **8.1**: Table of different terminal groups studied and the relative activation energy required for Si-O-Si bond rupture (courtesy of Dr. Michael Janik) 209

Table **9.1**: Adhesion and static friction forces measured before operation and after failure in dry nitrogen. 228

Table **10.1**: Maximum recorded cycles in MEMS devices at different operating partial pressures of water and 1-pentanol vapors. 256

ACKNOWLEDGEMENTS

This work is dedicated to my loving family. Without the unconditional loving support of my wife Maria and my children, Johnathan, Kathleen, and Rachael, I would not have been able to accomplish this research. I am indebted to them for their patience with me and my "crazy" ways/ideas! Thank you and I love you. I have to also thank my parents, Elliott and Roxanne for their encouragement, love, and support. While young I recall seeing my father, a polymer chemist, work in fancy labs with cool tools/toys. Those experiences, along with others, guided me to the field of Chemical Engineering.

I must also acknowledge and thank all of my colleagues and friends that have helped me accomplish this work. First, I would like to thank my advisor, Seong H. Kim. I have been fortunate to work with an advisor that has treated me with respect and has genuine concern for me, my career, and my future. I will always remember my time with him in the lab, at conferences, and in the office discussing everything from research, to management, families, and goals. It has been a real pleasure to work with him.

I have also had the privilege to work with Maarten de Boer, Mike Dugger, and James (Tony) Ohlhausen; scientists at Sandia National Labs. I must thank Maarten for his critical thinking and the very constructive conversations we have had as well as the use of his exact capillary force program he wrote. Mike has also been a personal mentor and advisor to me and is someone that I look up to. I would like to thank him for his help, support, and genuine interest in me and this work. Mike and Tony have been instrumental in much of this research. All of the actual MEMS tests and SIMS work was accomplished under the guidance of Mike and Tony while visiting Sandia as a summer

intern. An expert in MEMS and tribology, I would like to thank Mike for his direct contributions to this work, specifically his direct involvement in publication and writing.

I am also grateful for the contributions Dr. Michael Janik has provided to this research. His *ab initio* calculations have provided unique insight into this project. I would also like to thank my lab mates and friends, Sudarshan Natarajan, Sujith Nair, Erik Hsiao, Anna Barnette, and MinYang. Each of these individuals has provided help for me in one way or another. I wish each success in their endeavors.

Lastly, I would like to acknowledge the various funding sources that provided the resources necessary for this research. This work was supported by the National Science Foundation (Grant No. CMS-0408369 and CMMI-0625493) and Sandia National Laboratories. Sandia is a multiprogram laboratory operated by Sandia Corporation, a Lockheed Martin Company,for the United States Department of Energy's National Nuclear Security Administration under contract DE-AC04-94AL85000.

Chapter 1

Introduction to Nanotibology and MicroElectroMechanical Systems (MEMS)

Portions Reprinted from Nano Today, Vol 2, S. H. Kim, D. B. Asay, and M. T. Dugger, Nanotribology and MEMS, 22-29, Copyright (2007), with permission from Elsevier.

1.0.1 Summary

The tribological phenomena of adhesion, friction, and wear arise when solid objects make contact. As the size of devices shrinks to micro- and nano-scales, the surface-to-volume ratio increases and the effects of body forces (gravity and inertia) become insignificant compared to those of surface forces (van der Waals, capillarity, electrostatic, chemical bonds). In microelectromechanical systems (MEMS), tribological and static interfacial forces are comparable with forces driving device motion. In this situation, macro-scale lubrication and wear mitigation methods, such as the use of bulk fluids and micrometer thick coatings, are ineffective; new nano-engineering approaches must be employed for MEMS devices with moving structures. This chapter reviews fundamental tribological problems related to micro- and nano-scale mechanical contacts and developments in MEMS lubrications.

1.1 Introduction

The word "Tribology" comes from the greek word "tribo", meaning rubbing. Tribology is therefore, the study of "rubbing things." General physics suggests that friction is simply the consequence of an applied load and the shear strength between two surfaces in "loose" contact. In the macrosopic world, frictional force is independent of the contact area and velocity, and is governed by Amontons' law. However, the fundamental physical and chemical relationships governing friction, adhesion, wear, and lubrication are not completely understood and have been elusive due to the multidisciplinary nature of the problem (chemistry, physics, and mechanical).

The forces acting on an asperity in contact with a moving surface are due to a complex set of variables, material properties, and conditions. Table **1.1** illustrates the complexity of this physical system. The left column lists the important subject matter within surface science and mechanical contacts that play a direct role in tribology. The opposite column lists the various challenging subject issues within tribology. Each of the arrows in the middle, connecting the left column with the right, ties the surface science or mechanical contact topic to a particular issue within tribology. Additionally, these arrows can represent a question. For example, "What role does the *multi-component isotherm* play in *adhesion*?" The outer arrows indicate connections between the different topics/ideas. For example, "How does the *surface chemistry* alter the *surface energy*?" and "How does the *adhesion* affect *friction*?" The table also illustrates the complexity of each concept within tribology.

Table **1.1**: Intertwined concepts dominating tribology, surface science and mechanical contacts.

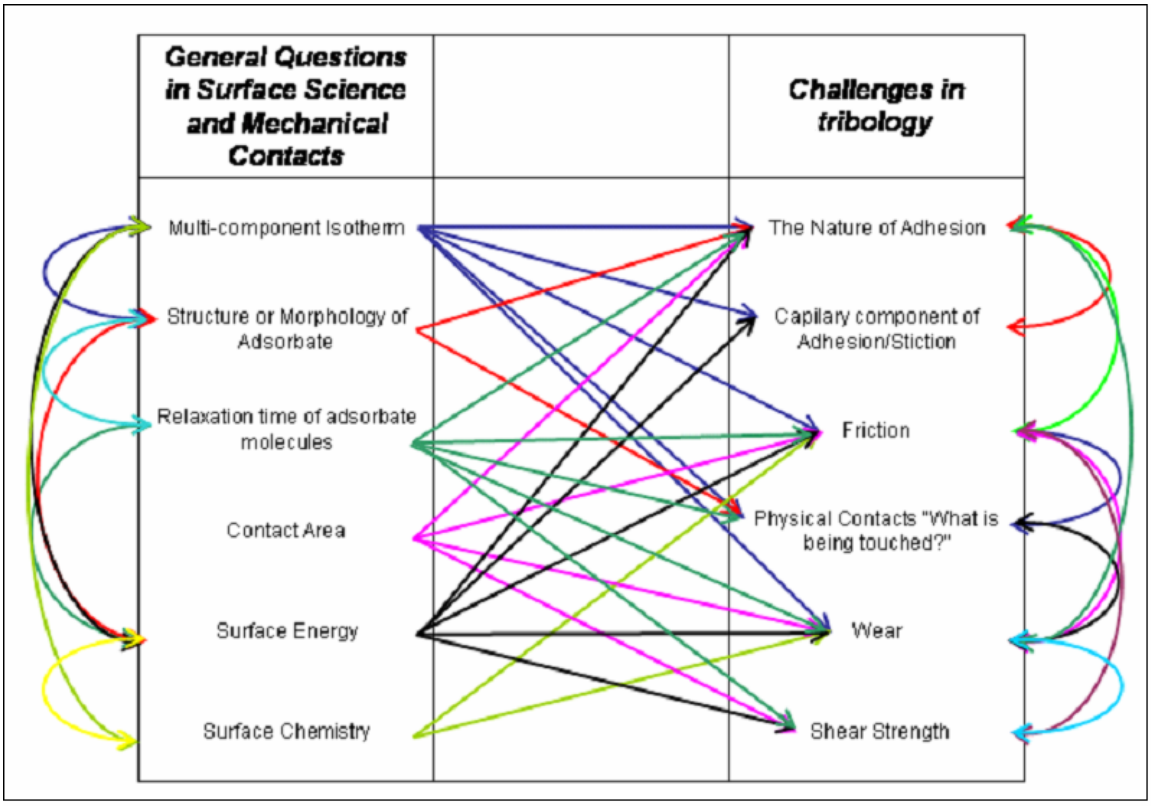

There exist numerous studies probing many of the questions suggested in the table. Most experimental research in nanoscale tribology is performed with the AFM or tiny machines. Micro-Electro-Mechanical Systems or MEMS are tiny devices with moving features whose length scale range from hundreds of nanometers to hundreds of micrometers. Due to the large surface-to-volume ratio of these devices, adhesion, friction, and wear are key challenges to MEMS technology, limiting device realization and reliability.[1] Surface forces such as adhesion and friction often exceed the forces driving the motion of the component.[2-4] The goal in MEMS Tribology is to minimize adhesion, friction, and wear between these moving surfaces while maintaining device performance and reliability. Current research involved with minimizing the adhesion, friction, and wear in MEMS are primarily based on surface coatings. A number of coating materials have been studied. These include diamond-like carbon[2], carbides[3], oxides[4], self-assembled monolayers (SAM)[5], polymers[6], and fluorinated organic molecules[7]. Inorganic hard coatings provide some improvement of anti-wear properties; however, these inorganic surfaces have a high surface energy that causes adhesion problems. Deposition of inorganic coatings typically relies on a line-of-sight process making uniform deposition on all sides of MEMS devices difficult. The advantages of organic coatings are their low surface energy and lowered friction force. However, the durability of monolayer coatings remains a question.[8] Regardless of surface treatment, all solid films and SAMs have shown to wear off during MEMS operation limiting the devices reliability. The self-healing or replenishment of lubricating film in MEMS devices is the key requirement for successful use over extended periods of time and is the missing property in current MEMS lubrication techniques today.

1.2 MEMS History

MEMS with movable structures were first demonstrated in the late 1980's when researchers at the University of California at Berkeley illustrated the use of standard integrated circuit fabrication technologies to produce pin joints, gears, and sliders.[9] These structural elements were subsequently used to produce an electrostatic micromotor based on previous design considerations from researchers at AT&T Bell Laboratories.[10, 11] This first device consisted of a rotor 60 μm in diameter and 1 μm thick, surrounded by stator elements separated from the rotor by 2 μm gaps. Application of voltage pulses to the stator elements in the proper sequence allowed the rotor to spin. Although these devices were built with a low friction design and materials, motion of these small devices was possible only with high drive voltages. Thus the development of the first mechanically complex micromachine was accompanied by the first manifestation of friction-related problems in micromachines.

The first efforts in MEMS fabrication were followed by a burgeoning of research activities in design, fabrication, control, and operation of micromachines in the early 1990's. In fact, there are some notable commercial successes in MEMS that impact the lives of millions of people every day. For example, every new automobile sold since the late 1990's uses one or more micromachined accelerometers to deploy airbags in the event of a crash. The accelerometer works by measuring the voltage required to keep a suspended mass at its rest position. In this device, there are no deliberately contacting surfaces once in service.[12] The low-cost color printer market has been dominated by MEMS since the late 1990's. Microfabricated channels deliver liquid ink near an exit

aperture, where an electrical pulse on a heater near the exit rapidly forms a bubble and ejects a droplet of ink, having well-controlled size, out of the exit aperture.[13] This device does not employ contacting surfaces, but fluid erosion due to the flow of ink containing pigment particles has been an issue. In the late 1990's, high-definition projectors and televisions came to market employing a light-modulating MEMS device.[14] This device consists of hundreds of thousands to millions of individual aluminum mirrors mounted on torsional hinges that can be tilted to reflect light towards a screen, or away from the screen for a dark pixel. Unlike the applications described above, this device does rely on contact between surfaces during normal operation. Each time a mirror changes its tilt angle, the mirror touches a landing tip to hold the mirror at a known stop position. The flexural motion of the support structure inevitably causes some minor rubbing action a few tens of nm wide. Even at this small rubbing amplitude, wear and excessive adhesion are observed unless careful surface treatments are employed. In this case, the mirrors are sealed inside a package with perfluorodecanoic acid.[14] A solid at room temperature, this material vaporizes at operating temperature due to the high intensity lamp shining on the mirrors, and is thereby able to redistribute within the package and passivate any aluminum surfaces that become exposed during operation.

Commercially successful MEMS devices to date have either nonmoving parts or contacts whose lateral motion is very restricted. Many more exciting applications can be attained with MEMS devices consisting of moving, touching, and rubbing structures. These include gears and motors that can enable much more complicated mechanical functions at the micro- and nano-scale. Examples shown in Figure **1.1** are parts of an electromechanical lock and a light-steering mirror. However, the effects of adhesion,

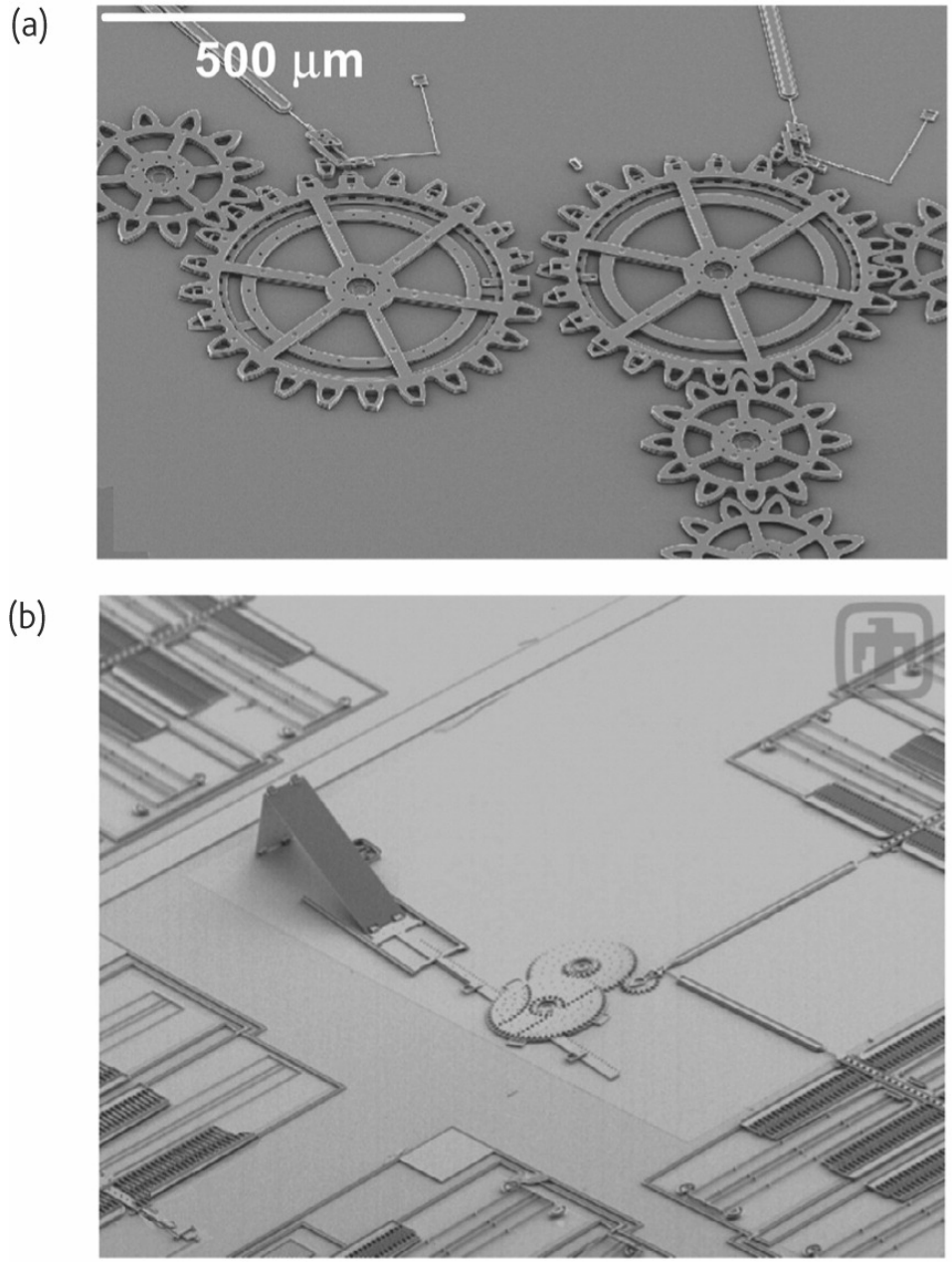

Figure **1.1**: (a) Intermeshing gears and (b) mirror and drive systems produced by silicon surface micromachining in Sandia National Laboratories' SUMMiT^{TM} process.

friction and wear of MEMS devices are challenging the development and commercialization of more sophisticated micromachines. Tribological problems associated with micromachines cannot be resolved by applying conventional lubrication methods utilized in the macro-scale, such as liquid lubricants. In micromachines, the viscosity of liquid lubricants causes severe power dissipation problems and causes devices to move slowly, negating one of the principal advantages of micromachines, i.e. low inertia that enables rapid mechanical switching.

The tribological behavior of contacts in MEMS technologies differs from those in macroscopic engineering structures. At the macroscopic scale, millions of asperities give rise to the parametric relationships that we are familiar with, such as Amonton's law which depicts the friction coefficient to be independent of contact area and applied load. In MEMS, real mechanical contacts typically consist of a few nanometer-scale asperities that touch. At these small scales, Amonton's law breaks down and individual asperity contact behavior must be considered. Additionally, forces that are negligible at the macro-scale become significant at the microscopic length scale and smaller. These include electrostatic or van der Waals forces between contacting and non-contacting surfaces, and capillary forces due to liquid menisci.[15] As an example, Figure **1.2** compares the magnitude of gravitation and adhesion forces as a function of size.[16] In the macroscopic scale, gravity dominates over adhesion. However, in the micro- and nano-scale, the gravitational body forces are negligible and adhesion becomes significant. It is important to point out that in some cases the magnitude of these forces is comparable to the actuation forces that can be provided with on-chip actuators.

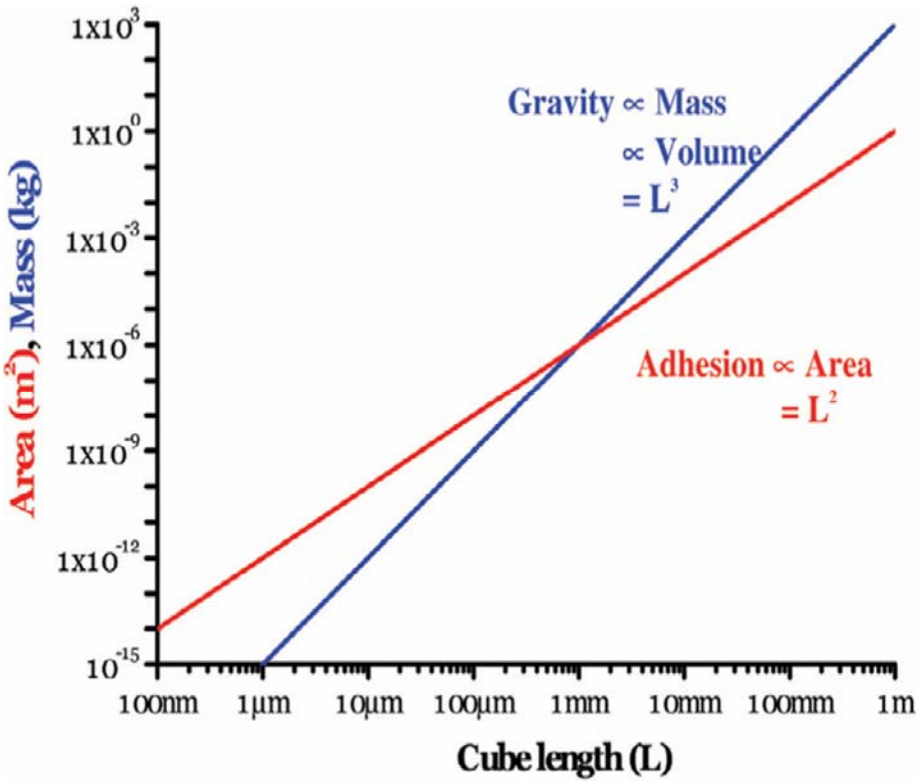

Figure **1.2**: Variation of gravity and adhesion for a cube with a smooth surface as a function of size (L). Adhesion force falls linearly with surface or contact area while gravitational force falls with volume.

The study of adhesion, friction, lubrication and wear in this small length scale is referred to as "nanotribology." The term was first used in the early 1990's by researchers examining friction between sharp atomic force microscope (AFM) tips and graphite surfaces,[17] and the slip of adsorbed Kr atoms on Ag and Au surfaces at liquid nitrogen temperature.[18] Since then, nanotribology has come to refer to the science and technology of friction, adhesion, lubrication and wear that involve phenomena at the nano-scale (a few 100 nm or less). Examples include MEMS, single asperity interactions, as well as other interfaces where the behavior of the system is governed by the response of limited numbers of atoms and molecules.

1.3 Fabrication of MEMS

MEMS devices are often fabricated using silicon-based processes. The prevalence of silicon as a structural material for MEMS is the result of a large amount of process knowledge developed for silicon in semiconductor industries. Three main MEMS fabrication processes are surface micromachining (SMM), silicon-on-insulator technology (SOI), and electroforming. A more in-depth review of many different microfabrication methods can be found elsewhere.[19]

In SMM, the MEMS structures are built on top of a substrate, layer by layer. These layers consist of structural materials that are patterned to form the movable elements, and sacrificial materials that are ultimately etched away to free the movable elements. In Sandia National Laboratories' SUMMiT^{TM} process,[20] four structural layers

of polycrystalline silicon plus a polycrystalline silicon ground plane can each be individually patterned to produce very complex mechanical structures. In this case, the sacrificial material is silicon dioxide. At the last stage of fabrication, the silicon dioxide is etched with hydrofluoric acid (HF) to free the silicon microstructure.

The SOI technology makes use of two silicon wafers bonded together with a layer of oxide between.[21] The "handle" wafer is the substrate and is typically polished on one side. A thermal or chemical vapor deposited oxide (1 to several microns thick) is grown on the polished surface, and ultimately acts as the sacrificial layer. Another single crystal silicon wafer is polished, anodically bonded to the oxide on the handle wafer, and then polished to the desired thickness (10 to hundreds of microns, depending on desired structure thickness) to form the structural layer. A pattern is created on the top of the stack using lithography, and then deep reactive ion etching (DRIE) is used to cut through the structural layer, stopping at the buried oxide. The oxide can be etched in HF vapor or in an aqueous HF solution to undercut the patterned structural layer and create free structures. These structures can be kept anchored to the substrate by using a timed etch that completely undercuts narrow patterns, but leaves residual oxide under larger patterns.

Electroforming relies on plating a metal into a mold created by lithographic techniques.[22] Metals that are easily plated such as nickel, copper, gold and alloys have been used to create metallic structures. Unlike the fabrication processes described above, this process is used to create individual parts, so that development of complex interacting structures requires assembly of these parts into components. This technique has been extensively used in Europe to make small gears for precision mechanical watches.

Each method employed for material deposition, patterning, and etching to create MEMS structures leaves behind unique surface morphologies. Examples of sidewall surfaces from each of the microfabrication methods discussed above are shown in Figure **1.3**. Because of this surface roughness (typically a few 10's to 100 nm), only a few asperities make actual physical contact when opposing surfaces with similar surface morphologies are brought together under a given load. As these surfaces slide past one another, some contacts are broken, while new ones are formed. However, the total number of contacting asperities is relatively constant during sliding assuming the total load and adhesive forces do not vary. Therefore, it is important to know tribological properties of single-asperity contacts at the nano-scale.

1.4 Nanotribology related to MEMS

The atomic force microscope (AFM) is an ideal tool for studying nano-scale single asperity contact behaviors.[23-25] A typical AFM set-up is shown in Figure **1.4**. Made up of a sharp tip fabricated at the end of a small cantilever, the AFM probes surface forces. The end of the tip is typically modeled as a sphere with a characteristic radius of curvature R (10 ~ 30 nm typical for unused tips). The sharpness of this asperity provides new insights into a single asperity contact not observable at the macroscopic scale. The force acting at the tip deforms the cantilever vertically and/or laterally. A laser beam is reflected at the back of the cantilever and detected with a position sensitive detector, which is then related to cantilever deformation. With various calibration methods, the

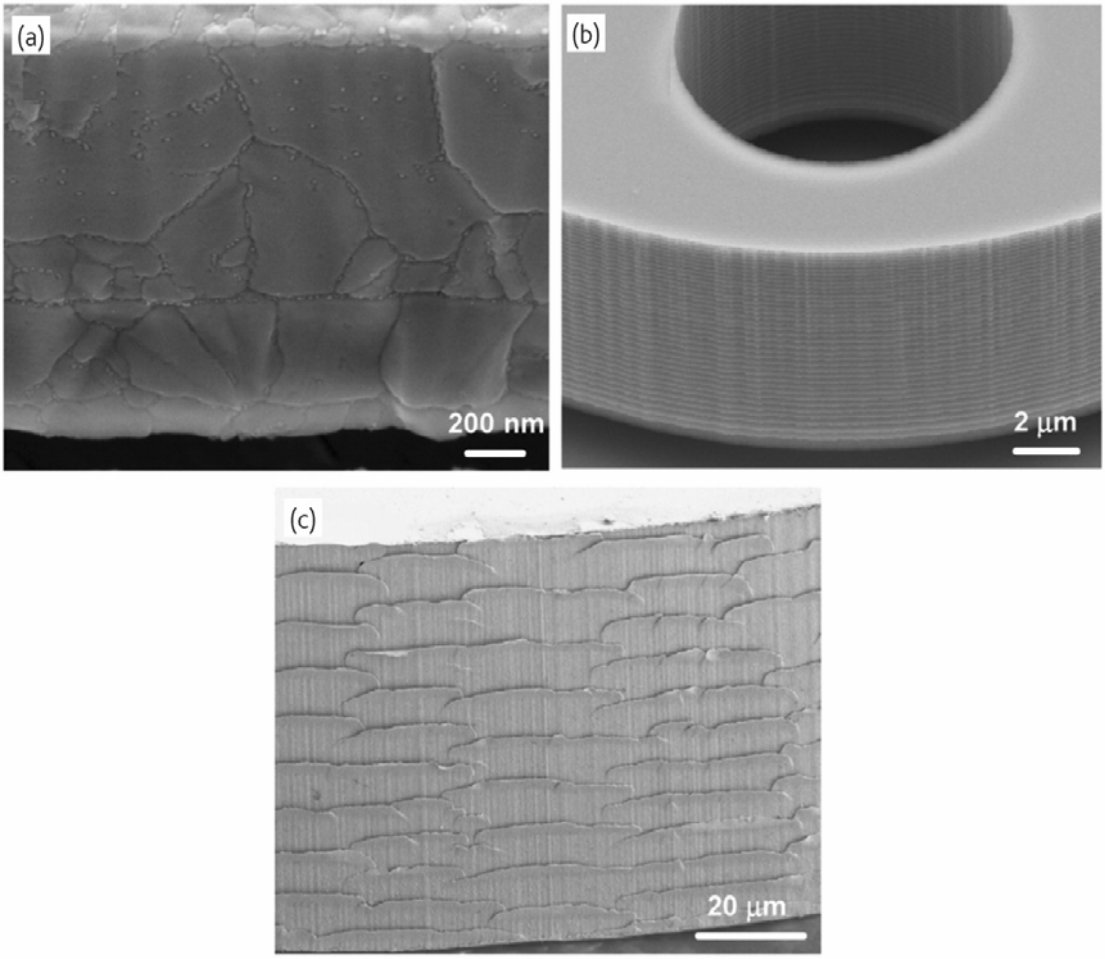

Figure **1.3**: Examples of surface morphology of MEMS fabricated by (a) silicon micromachining, (b) silicon-on-insulator, and (c) electroforming processes.

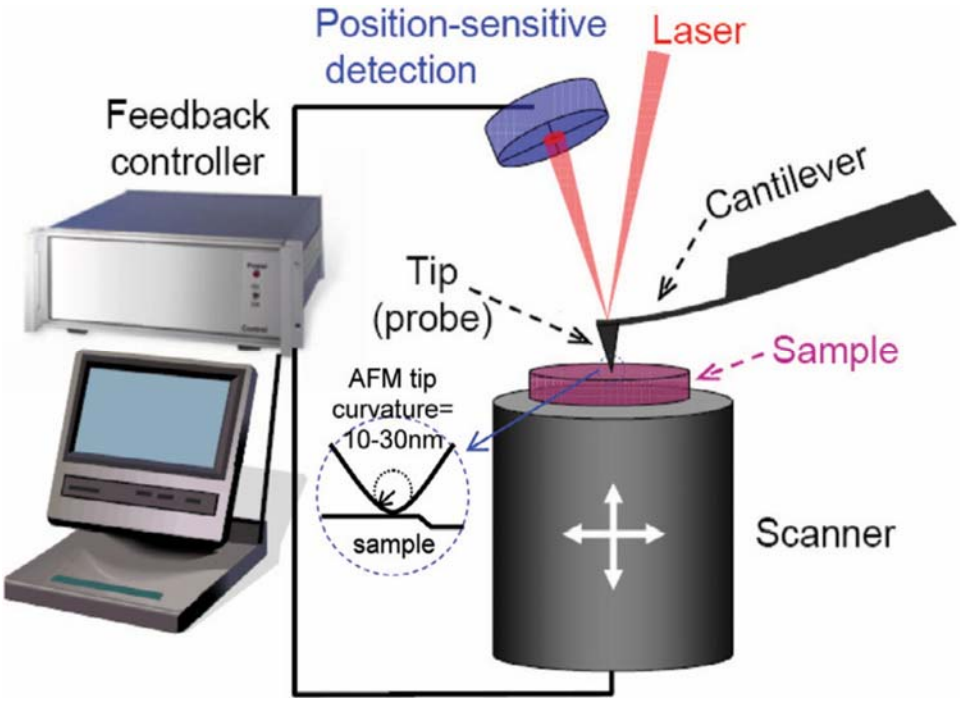

Figure **1.4**: Schematic view of atomic force microscopy (AFM) used in nanotribology studies.

normal (applied forces and adhesion) and lateral (frictional) forces acting on the cantilever can be determined with high resolution.[23-26]

Adhesion at the nano-scale is a consequence of van der Waals interactions, electrostatic interactions between surface dipoles and charges, as well as capillary phenomena. In AFM measurements, the adhesive force varies with the radius of the contacting asperity, R.[27] The Derjaguin-Mullter-Toporov (DMT) contact mechanics[28] states that in the absence of any external force, the adhesive contact pressure is proportional to $R^{-1/3}$. Figure **1.5** relates the maximum contact pressure to the size of a contacting asperity with a radius of curvature (R), based on the DMT contact mechanics. Extremely small contacts are unstable when the pressure exceeds the yield strength of the material. Therefore, as MEMS devices shrink, the adhesion force will increase the contact pressure. Unless reduced, adhesion will limit the size to which MEMS devices can be miniaturized.

Adhesion can be tailored by altering the outermost surface chemistry.[29-35] In the absence of capillary condensation, adhesion is modeled as $F_{adh} = 2\pi R W_{12}$ in the DMT model, where W_{12} is the Dupré energy of adhesion between two surfaces ($W_{12} = \gamma_1 + \gamma_2 - \gamma_{12}$, where γ = surface energy). The reduction in adhesion is therefore limited to the ability to keep the contact radius (R) small and manipulate the surface chemistry of the contacting surface (W_{12}). In humid air, capillary adhesion is particularly important for hydrophilic surfaces.[35-38] Effective solutions for mitigating these adhesion forces in MEMS applications are discussed in **1.5.1**.

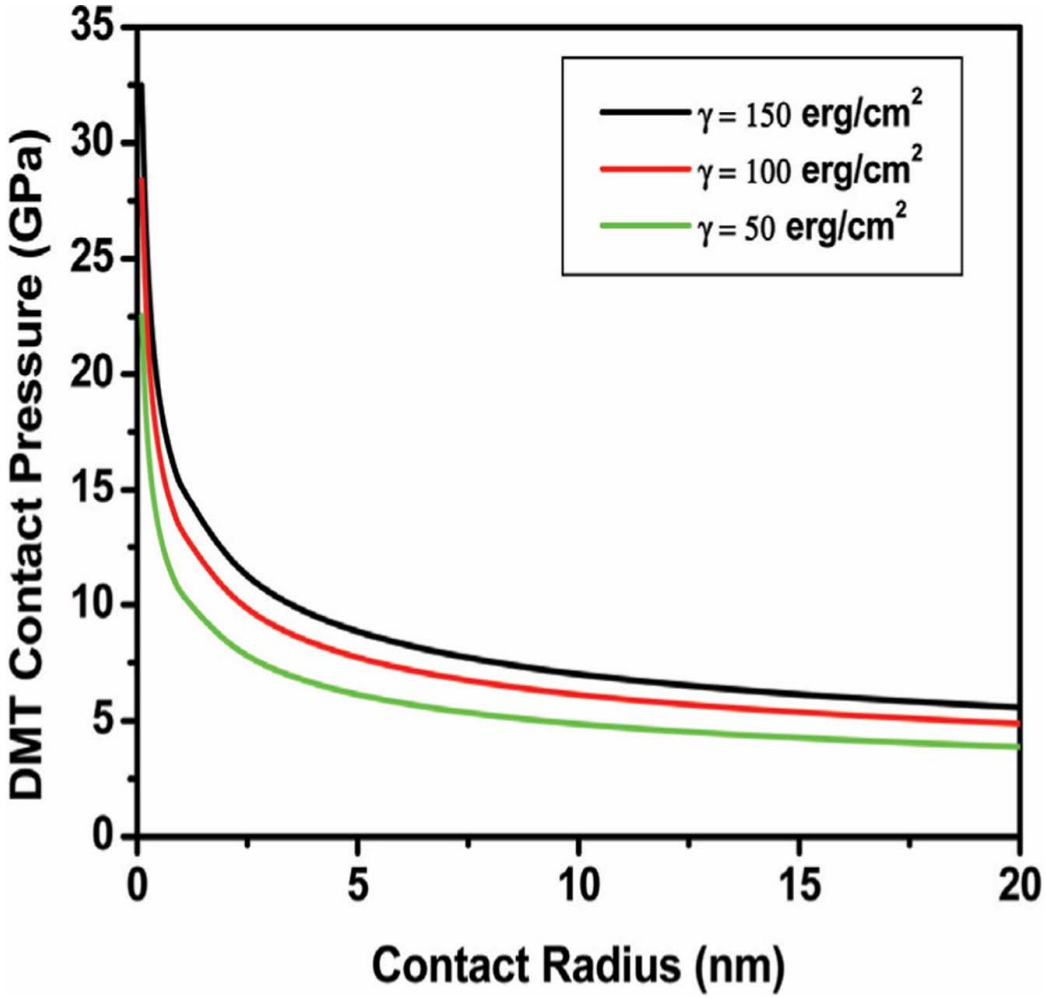

Figure **1.5**: Maximum Contact Pressure for sphere-flat geometry when only adhesion forces ($F_{adh}=4\pi R\gamma$) are present. Both surfaces have a surface tension of γ. The material properties used for this figure are those of silicon. As the contact radius (R) decreases the contact pressure increases and is proportional to $R^{-1/3}$.

There are many examples of friction and wear measured with AFM.[39-43] The frictional response of a nano-asperity contact is assumed to be proportional to the real contact area between the tip and the substrate.[44] For this reason, it is important to construct adequate models describing the contact area as a function of the total normal force (L_{total}). Typically the Johnson-Kendall-Roberts (JKR)[45] and DMT[28] contact mechanics are used to describe these phenomena, and transitions between these models have been investigated.[46, 47] Both JKR and DMT rely on Hertzian-like contact deformations. However, each model accounts for adhesion differently. Simply put, in the JKR model, adhesion forces only occur within the contact region, in contrast, DMT takes into account adhesion forces outside of the contact. In AFM measurements with sharp AFM tips and high modulus substrate materials, the DMT model is usually appropriate.[47] This model states that the contact area is proportional to the total load to the 2/3 power ($L_{total}^{2/3}$). Because of this proportionality, the observed frictional response vs. load is often nonlinear.

The AFM has been used to investigate self-assembled monolayers (SAMs) and other organic adsorbates as potential lubricants to reduce friction between nano-scale contacts. Carefully prepared SAMs can significantly lower frictional responses compared to bare surfaces.[41] The packing density of SAMs directly affects the efficiency of the SAM to lubricate.[48] In friction responses, hydrogenated SAMs seem to outperform fluorinated SAMs.[49] Stability of the SAM structure is dependent on the contact pressure. At low pressures, direct tip-substrate contact does not occur and wear is mitigated; however, when the contact pressure is increased higher than a critical pressure these

molecules are irreversibly worn.[50] Equilibrium adsorption of alcohol molecules from the vapor phase on silicon surfaces can also reduce friction at the interface up to a factor of ~4.[43]

Although AFM provides unique opportunities to study tribological properties of the nano-scale single asperity, there are several challenges in associating the frictional properties observed with AFM to tribological behaviors of MEMS. The sliding velocity of the contact in AFM is typically 2 to 4 orders of magnitude slower than that of real contacts in MEMS. Because of the sharpness of the AFM contact, the contact pressure is typically on the order of a few GPa (Figure **1.5**) which is several orders of magnitude higher than the contact pressures expected in real systems. Without an exact representation of the asperity shape, the pressure distribution within the contact can vary significantly.[51] The frictional response at the nano-scale contains an adhesive component. The adhesive friction components decrease as the size of contact increases from the nano-scale to the micro-scale, and eventually become negligible in the macro-scale. Wear of the AFM tip during contact scanning can occur due to insufficient mechanical strength or tribochemical reactions at the interface. This further complicates interpretation of the observed frictional response since the tip geometry is changing during the experiment.[52-54] Finally, relating the behavior of one single asperity to larger contact phenomena requires understanding how to model multiple contacts that are continually being broken, reformed, and sheared at different contact pressures at which elastic and plastic deformation may constantly occur. The integration of single asperity behaviors to capture the behavior of a real rough interface has not yet been achieved.[55, 56]

1.5 Applications of Nanotribology to MEMS lubrication

1.5.1 Reducing Adhesion

The last step of silicon-based MEMS fabrication is removal of the oxide sacrificial layer by HF. After the oxide etch is complete, the released MEMS structure is rinsed in water and dried. This step is often troubled by adhesion of microstructures to the substrate after drying. Either during the water rinse or upon subsequent exposure to air, a thin layer of native oxide (10 ~ 20 Å thick) is formed on the silicon surface, which has a high surface energy due to surface hydroxyl groups. Such hydrophilic surfaces exhibit strong capillary forces as the MEMS structure is pulled out of water or as they come in contact in humid air, leading to "release adhesion". The release adhesion problem has been circumvented by several approaches. Freeze-drying or supercritical CO_2 drying methods can be used in the last step.[57, 58] This avoids release adhesion by eliminating the liquid-vapor interface as the microstructure is dried. Another approach is to partially undercut the microstructure and deposit a polymer support layer. The polymer support prevents collapse of the microstructure during sacrificial layer etch and dry. The polymer support can be removed using an oxygen plasma without using liquid.[59]

Another adhesion related problem arises during MEMS operation. Movable MEMS structures are designed to make physical contacts during operation, which can lead to "in-use adhesion" problems. The initial attempts to alleviate in-use adhesion were to reduce the physical contact area by fabricating micro-dimples in the contact region or by roughening the silicon surface.[60,61] This approach can reduce the adhesion by a factor of up to 20.[62] Recently chemical passivation of the silicon surfaces using organic

coatings is employed more widely.[63] Organic molecules used for this purpose include long-chain alkyl trichloro- or dichlorosilanes and fluorinated trichlorosilanes which react with Si-OH groups on silicon oxide surfaces,[64-66] and primary alkenes which react with Si-H groups on hydrogenated silicon surfaces.[67, 68] When the silicon surface is chlorinated (Si-Cl), primary alcohols and amines can also be used.[69] All these organic layers render hydrophobicity to the device surface preventing water condensation and capillary-induced adhesion.

1.5.2 Reducing friction and wear

Strong interfacial adhesion between micro- and nano-scale structures induces high friction and wear leading to failure of MEMS devices. For example, a MEMS actuator (electrostatic lateral output motor) operated in vacuum fails very quickly due to catastrophic wear of device components (micro-dimples).[70] The initial asperity contact wears off silicon oxide layers on the device surface, exposing the bare silicon surface with dangling bonds. If these dangling bonds are not passivated fast enough, chemical junctions can be formed between two contacting silicon surfaces which are strong enough to pull polycrystalline silicon grains out of the surface. In dry air, the dangling bonds of the exposed silicon surface get oxidized fast enough that silicon junction formation is prevented.[71] Although catastrophic silicon wear is prevented, formation of silicon oxide and adhesive wear are still occurring constantly, which eventually leads to debris formation and device failure.[70]

In humid air, the adsorption of water on device surfaces also plays significant roles in friction and wear. In nano-asperity contact AFM experiments, it was shown that the water molecules in the sliding contact region can induce tribochemical reactions and accelerate wear of silicon oxide and silicon nitride surfaces.[54, 72, 73] In contrast, it is shown for MEMS actuator experiments that continuous replenishment of the adsorbed water layer (a few Å thick) at moderate relative humidity (RH) can improve the operation lifetime of the MEMS actuator.[74] However, excessive moisture (>70% RH) leads to capillary-induce adhesion that prevents the motor from running. Molecular origins of the adsorbed water effects on wear are currently an active research area.[75, 76]

The organic layers deposited to reduce in-use adhesion can also mitigate the friction of MEMS to a certain degree. Since the molecularly thin organic layers reduce the surface energy, they can significantly reduce friction and prevent capillary adhesion with water.[8, 77] However, practical application of this approach is quite limited due to degradation of organic layers even in normal storage conditions and their poor durability in operation conditions.[78] These organic layers can delay the beginning of wear; but, they do not have sufficient durability to prevent wear for the required duration of the MEMS operation lifetime.[79]

The lubrication effect of chemically-bonded organic films can be significantly extended by adding unbound mobile organic films.[80, 81] Fundamentally, as the bound lubricant layer is removed in the contact regions, the mobile species can diffuse along the surface to the freshly exposed regions, recoating the interface with the organic species. In fact, the use of mobile liquid lubricant film such as Fomblin Z-dol has been the key for the success of hard disk memory systems.[82] However, Z-dol is not very effective in

MEMS since the ether linkage in the Z-dol molecule is unstable on oxide surfaces. A simple process dip-coating has been shown to be effective to deposit hydrocarbon mobile layers on MEMS devices. In MEMS electrostatic motor tests, certain hydrocarbon coatings showed substantial improvement in performance over uncoated motors as well as Z-dol coated motors.[80] Recently, it has been shown that organic ionic liquids can also form bound and mobile lubricant layers.[83] In this case, inorganic anions are reacted and strongly bound to the substrate surface and bulky organic cations acts as a mobile phase. However, further improvements of these organic-based lubrication schemes are still needed for practical applications with high durability and fidelity.

For this reason, a number of hard coatings have been explored to reduce friction and wear of MEMS devices. The main idea is to coat the silicon device surfaces with high modulus / hardness and wear resistant materials. Table **1.2** summarizes some of these hard coating materials and their mechanical properties,[4, 84-89] and also includes

Table **1.2**: Comparison of moduli and hardness of various materials used in MEMS fabrication and lubrication

Material[#]	Elastic modulus (GPa)	Shear Modulus (GPa)	Hardness* (GPa)
Poly-Si	167		12 (V)
Si	112	44	11 (K)
SiO_2	75	31	8 (K), 11 (V)
SiC	420	165	30 (K)
Si_3N_4	300	119	16 (V)
TiC	450	150	20 (K), 32 (V)
TiN	600		20 (K)
Al_2O_3	370	150	21 (K), 14 (V)
W	400	156	32 (K), 31 (V)
diamond	900		100 (V)
a-C (DLC)	80~200		14 ~ 30 (V)

[#] bold typeface indicates those used as structural materials, regular typeface indicates coatings

* K = Knoop hardness, V = Vickers hardness

properties for some MEMS structural materials for reference. The intrinsic hardness of these materials typically gives lower friction (due to reduced contact area) and wear than silicon and silicon oxide as well as much higher durability than organic films. In this approach, one of the main challenges is conformal coating of complicated microstructures. The rubbing contact interfaces are often deeply-buried in complex structures; but typical physical vapor deposition methods are line-of-sight processes, i.e. only the top surfaces are coated well. This problem can be resolved if the hard coating is produced through chemical vapor deposition processes. For example, the wear-resistant W coating process is carried out through the selective deposition of tungsten through WF_6 reduction by silicon.[90] The tungsten film deposited in this way can significantly enhance the life-time of MEMS devices.

One of the most actively investigated hard coatings is amorphous carbon (often called diamond-like carbon, DLC) which is already successfully used in magnetic hard disk data storage systems.[91-94] These coatings are deposited through a plasma-enhanced chemical vapor deposition process. In MEMS electrostatic motor tests, the DLC-coated devices outperformed the uncoated devices by two or three orders of magnitude in operation time.[95] In order to produce even harder coatings, ultra-nanocrystalline diamond (UNCD) coatings have recently been produced on MEMS devices.[2]

In practice, the best choice of structural material or coating is a function of the application for the MEMS device, and is limited by the availability of mature deposition process control for the material and the degree to which it can be integrated with the device fabrication process. For example, resonators typically benefit from high modulus materials, while for springs a low modulus material is desired to reduce the required

actuation force. In most cases, coatings are applied at the end of fabrication, which requires a conformal process capable of penetrating high aspect ratio gaps in the released structures.

1.6 The Road Ahead

The self-sustaining continuous operation of a MEMS device with rubbing contacts requires the interface to have efficient and durable lubrication schemes. This necessitates self-healing or replenishing capability of lubricant films[14, 43, 80, 81] or low-friction and wear-free hard coatings.[2, 91-95] While each approach has shown some promise in laboratory tests, implementing these strategies in real MEMS devices with complicated structures and functions will require further research across various disciplines.

In the case of self-healing films, the surface diffusivity for the unbound mobile species is low. In practice, the mobility of these species will limit the time required for healing, ultimately constraining the operating speed of the device. In addition, because this technique requires a wetable surface, capillary formation either during dip-coating or during operation can occur, causing increased adhesive forces restraining device motion and/or potential collapse of the structure. Maintaining a constant film thickness in devices with various structures and shapes is a challenge not yet explored. Lastly, the mobile phase can run out during device operation, which will lead to device failure.

Vapor-phase lubrication is an in-situ technique where the lubricant molecule is delivered to the surface via gas diffusion and adsorption.[14, 43, 96] This technique has the

capability to conformally coat all surfaces, even deeply-buried ones, as long as the gap between the surfaces is longer than the mean free path of the lubricant molecule.[97] The thickness of the adsorbed film can be controlled from sub-nm to a few nm by controlling the partial pressure of the lubricant, because the isotherm is a function of the partial pressure. Adsorption occurs almost instantaneously as the gas-phase collision rate of the lubricant molecule to the surface is typically on the order of 10^6~10^8 collisions per sec. When lubricant molecules are desorbed from asperity contacts, the exposed surface is immediately passivated again with fresh lubricant. To minimize capillary adhesion of the condensed liquid between contacts, the ideal lubricant should have as low a surface tension as possible, a high liquid molar volume and vapor pressure, and a true Langmuir isotherm (adsorption saturated at 1 monolayer). Adsorbed lubricant molecules can undergo tribochemical reactions forming oligomeric species in the contact region.[98] Although the in-situ vapor phase lubrication is proved for sliding-contact devices in the laboratory, there are still engineering challenges remaining for practical applications. How can one control the vapor pressure of lubricant in a sealed MEMS device that works over a wide range of temperature? While MEMS packaging can be done in an inert environment, there is always some residual oxygen and water present inside the package. The effects of low-concentration oxygen and/or water trapped in the package must be understood and controlled for successful application of vapor phase lubrication in commercial MEMS.

Low-friction and wear-resistant hard coatings have been extensively investigated as a solid-phase lubrication coating for MEMS. The best coating material and method are still to be developed for real MEMS applications. These coatings must have good

adhesion to the surface of complicated MEMS structures with no or minimal residual stresses (both mechanical and thermal). In addition, these coatings must be formed uniformly on deeply-buried contact surfaces, without bonding those surfaces together during the coating process. In addition to conformality, another requirement of hard coatings or even new structural materials for microsystems is that the layers have low residual stress after deposition. Many deposition procedures result in a stress gradient through the film. Stressed films or differences in thermal expansion coefficient result in structures that curl after release of the sacrificial material. This can prevent proper alignment of mechanical structures in a complex device, such as gear teeth or electrostatic comb fingers, which render the device inoperative. Finally, the coating materials should be stable and function in various oxidizing or reducing environments.

1.7 References

1. S. M. Hsu; Z. C. Ying, *Nanotribology: Critical Assessment and Research Needs*. Kluwer Academic Publishers: Boston, Massachusetts, 2003.
2. A. R. Krauss; O. Auciello; D. M. Gruen; A. Jayatissa; A. Sumant; J. Tucek; D. C. Mancini; N. Moldovan; A. Erdemir; D. Ersoy; M. N. Gardos; H. G. Busmann; E. M. Meyer; M. Q. Ding, *Diamond and Related Materials* **2001,** 10, (11), 1952-1961.
3. S. Sundararajan; B. Bhushan, *Wear* **1998,** 217, (2), 251-261.
4. T. M. Mayer; J. W. Elam; S. M. George; P. G. Kotula; R. S. Goeke, *Applied Physics Letters* **2003,** 82, (17), 2883-2885.
5. W. R. Ashurst; C. Yau; C. Carraro; C. Lee; G. J. Kluth; R. T. Howe; R. Maboudian, *Sensors and Actuators a-Physical* **2001,** 91, (3), 239-248.
6. H. S. Ahn; D. Julthongpiput; D. I. Kim; V. V. Tsukruk, *Wear* **2003,** 255, 801-807.
7. K. C. Eapen; S. T. Patton; J. S. Zabinski, *Tribology Letters* **2002,** 12, (1), 35-41.
8. R. Maboudian; W. R. Ashurst; C. Carraro, *Tribology Letters* **2002,** 12, (2), 95-100.
9. L. S. Fan; Y. C. Tai; R. S. Muller, *Ieee Transactions on Electron Devices* **1988,** 35, (6), 724-730.
10. L. S. Fan; Y. C. Tai; R. S. Muller, *Sensors and Actuators* **1989,** 20, (1-2), 41-47.
11. W. S. N. Trimmer; K. J. Gabriel, *Sensors and Actuators* **1987,** 11, (2), 189-206.

12. K. H. L. Chau; S. R. Lewis; Y. Zhao; R. T. Howe; S. F. Bart; R. G. Marcheselli, *Sensors and Actuators a-Physical* **1996,** 54, (1-3), 472-476.

13. S. Verdonckt-Vandeboek in: *Proc. SPIE - The International Society for Optical Engineering*, SPIE-International Society for Optical Engineering, Bellingham, WA, 1997; K. Chau; F. P. J., (Eds.) SPIE-International Society for Optical Engineering: Bellingham, WA, 1997; p 180.

14. S. A. Henck, *Tribology Letters* **1997,** 3, (3), 239-247.

15. S. J. Timpe; K. Komvopoulos, *Journal of Microelectromechanical Systems* **2005,** 14, (6), 1356-1363.

16. K. Kendall, *Science* **1994,** 263, (5154), 1720-1725.

17. G. Neubauer; S. R. Cohen; G. M. McClelland; D. Horne; C. M. Mate, *Review of Scientific Instruments* **1990,** 61, (9), 2296-2308.

18. J. Krim; D. H. Solina; R. Chiarello, *Physical Review Letters* **1991,** 66, (2), 181-184.

19. M. J. Madou, *Fundamentals of Microfabrication 2nd Ed.* CRC Press: New York, 2002.

20. M. S. Roger; J. J. Sniegowski in: *In Technical Digest, Solid-State Sensors and Actuators Workshop, 8-11 June 1998, Hilton Head Island SC, USA, Transducer Research Foundation*, 5-Level Polysilicon Surface Micromachine Technology: Application to Complex Mechanical Systems, Cleveland, OH, 1998; Cleveland, OH, 1998.

21. D. C. Miller; B. L. Boyce; M. T. Dugger; T. E. Buchheit; K. Gall, *Sensors and Actuators a-Physical* **2007,** 138, (1), 130-144.

22. W. Bacher; W. Menz; J. Mohr, *Ieee Transactions on Industrial Electronics* **1995,** 42, (5), 431-441.

23. C. P. Green; H. Lioe; J. P. Cleveland; R. Proksch; P. Mulvaney; J. E. Sader, *Review of Scientific Instruments* **2004,** 75, (6), 1988-1996.

24. D. F. Ogletree; R. W. Carpick; M. Salmeron, *Review of Scientific Instruments* **1996,** 67, (9), 3298-3306.

25. J. E. Sader, *Journal of Applied Physics* **1998,** 84, (1), 64-76.

26. J. E. Sader; J. W. M. Chon; P. Mulvaney, *Review of Scientific Instruments* **1999,** 70, (10), 3967-3969.

27. Y. Ando; J. Ino, *Wear* **1998,** 216, (2), 115-122.

28. B. V. Derjaguin; V. M. Muller; Y. P. Toporov, *Journal of Colloid and Interface Science* **1975,** 53, (2), 314-326.

29. T. Han; J. M. Williams; T. P. Beebe, *Analytica Chimica Acta* **1995,** 307, (2-3), 365-376.

30. M. Y. He; A. S. Blum; D. E. Aston; C. Buenviaje; R. M. Overney; R. Luginbuhl, *Journal of Chemical Physics* **2001,** 114, (3), 1355-1360.

31. E. Hoque; J. A. DeRose; P. Hoffmann; B. Bhushan; H. J. Mathieu, *Journal of Physical Chemistry C* **2007,** 111, (10), 3956-3962.

32. R. Jones; H. M. Pollock; J. A. S. Cleaver; C. S. Hodges, *Langmuir* **2002,** 18, (21), 8045-8055.

33. H. Y. Nie; M. J. Walzak; B. Berno; N. S. McIntyre, *Applied Surface Science* **1999,** 145, 627-632.

34. G. W. Tormoen; J. Drelich; E. R. Beach, *Journal of Adhesion Science and Technology* **2004,** 18, (1), 1-17.

35. X. D. Xiao; L. M. Qian, *Langmuir* **2000,** 16, (21), 8153-8158.

36. D. B. Asay; S. H. Kim, *Journal of Physical Chemistry B* **2005,** 109, (35), 16760-16763.

37. D. B. Asay; S. H. Kim, *Journal of Chemical Physics* **2006,** 124, (17), 5.

38. D. B. Asay; S. H. Kim, *Langmuir* **2007,** 23, (24), 12174-12178.

39. E. Barrena; C. Ocal; M. Salmeron, *Surface Science* **2001,** 482, 1216-1221.

40. B. Bhushan; A. V. Kulkarni; V. N. Koinkar; M. Boehm; L. Odoni; C. Martelet; M. Belin, *Langmuir* **1995,** 11, (8), 3189-3198.

41. M. J. Brukman; G. O. Marco; T. D. Dunbar; L. D. Boardman; R. W. Carpick, *Langmuir* **2006,** 22, (9), 3988-3998.

42. J. Hu; X. D. Xiao; D. F. Ogletree; M. Salmeron, *Surface Science* **1995,** 327, (3), 358-370.

43. K. Strawhecker; D. B. Asay; J. McKinney; S. H. Kim, *Tribology Letters* **2005,** 19, (1), 17-21.

44. M. Enachescu; R. J. A. van den Oetelaar; R. W. Carpick; D. F. Ogletree; C. F. J. Flipse; M. Salmeron, *Tribology Letters* **1999,** 7, (2-3), 73-78.

45. K. L. Johnson; K. Kendall; A. D. Roberts, *Proceedings of the Royal Society of London Series a-Mathematical and Physical Sciences* **1971,** 324, (1558), 301-&.

46. D. S. Grierson; E. E. Flater; R. W. Carpick, *Journal of Adhesion Science and Technology* **2005,** 19, (3-5), 291-311.

47. D. Tabor, *Journal of Colloid and Interface Science* **1977,** 58, (1), 2-13.

48. S. Lee; Y. S. Shon; R. Colorado; R. L. Guenard; T. R. Lee; S. S. Perry, *Langmuir* **2000,** 16, (5), 2220-2224.

49. H. I. Kim; T. Koini; T. R. Lee; S. S. Perry, *Langmuir* **1997,** 13, (26), 7192-7196.

50. X. D. Xiao; J. Hu; D. H. Charych; M. Salmeron, *Langmuir* **1996,** 12, (2), 235-237.

51. B. Q. Luan; M. O. Robbins, *Nature* **2005,** 435, (7044), 929-932.

52. R. W. Carpick; N. Agrait; D. F. Ogletree; M. Salmeron, *Langmuir* **1996,** 12, (13), 3334-3340.

53. A. G. Khurshudov; K. Kato; H. Koide, *Wear* **1997,** 203, 22-27.

54. W. Maw; F. Stevens; S. C. Langford; J. T. Dickinson, *Journal of Applied Physics* **2002,** 92, (9), 5103-5109.

55. L. Kogut; I. Etsion, *Journal of Tribology-Transactions of the Asme* **2004,** 126, (1), 34-40.

56. A. Y. Suh; A. A. Polycarpou, *Journal of Tribology-Transactions of the Asme* **2003,** 125, (1), 193-199.

57. H. Guckel; J. J. Sniegowski; T. R. Christenson; F. Raissi, *Sensors and Actuators a-Physical* **1990,** 21, (1-3), 346-351.

58. G. T. Mulher; D. S. Soane; R. T. Howe in: *Proc. 7th Int. Conf. Solid-State Sensors and Actuators, Transducers '93*, Yokohama, Japan, 1993; Yokohama, Japan, 1993; p 296.

59. D. Kobayashi; C. J. Kim; H. Fujita, *Japanese Journal of Applied Physics Part 2-Letters* **1993,** 32, (11A), L1642-L1644.

60. L. S. Fan; Y. C. Tai; R. S. Muller in: *Proc. IEEE Int. Electron Devices Meeting*, San Francisco, CA, 1988, 1988; San Francisco, CA, 1988; p 666.

61. R. L. Alley; G. J. Cuan; R. T. Howe; K. Komvopoulos in: *The Effect of Release-Etch Processing on Surface Microstructure Stiction.*, Proc. of the 5th IEEE Solid-State Sensor and Actuator Workshop, New York, NY 1992; IEEE: New York, NY 1992; pp 22-25.

62. Y. Yee; K. Chun; J. D. Lee; C. J. Kim, *Sensors and Actuators a-Physical* **1996,** 52, (1-3), 145-150.

63. R. Maboudian, *Surface Science Reports* **1998,** 30, (6-8), 209-270.

64. W. R. Ashurst; C. Carraro; R. Maboudian, *Ieee Transactions on Device and Materials Reliability* **2003,** 3, (4), 173-178.

65. W. R. Ashurst; C. Yau; C. Carraro; R. Maboudian; M. T. Dugger, *Journal of Microelectromechanical Systems* **2001,** 10, (1), 41-49.

66. R. Banga; J. Yarwood; A. M. Morgan; B. Evans; J. Kells, *Langmuir* **1995,** 11, (11), 4393-4399.

67. M. R. Linford; P. Fenter; P. M. Eisenberger; C. E. D. Chidsey, *Journal of the American Chemical Society* **1995,** 117, (11), 3145-3155.

68. M. M. Sung; G. J. Kluth; O. W. Yauw; R. Maboudian, *Langmuir* **1997,** 13, (23), 6164-6168.

69. X. Y. Zhu; J. E. Houston, *Tribology Letters* **1999,** 7, (2-3), 87-90.

70. S. T. Patton; J. S. Zabinski, *Tribology International* **2002,** 35, (6), 373-379.

71. M. L. W. Vanderzwan; J. A. Bardwell; G. I. Sproule; M. J. Graham, *Applied Physics Letters* **1994,** 64, (4), 446-447.

72. B. Skarman; L. R. Wallenberg; S. N. Jacobsen; U. Helmersson; C. Thelander, *Langmuir* **2000,** 16, (15), 6267-6277.

73. Z. Tao; B. Bhushan, *Tribology Letters* **2006,** 21, (1), 1-16.

74. S. T. Patton; W. D. Cowan; K. C. Eapen; J. S. Zabinski, *Tribology Letters* **2000,** 9, (3-4), 199-209.

75. B. Bhushan; H. W. Liu; S. M. Hsu, *Journal of Tribology-Transactions of the Asme* **2004,** 126, (3), 583-590.

76. S. Kopta; M. Salmeron, *Journal of Chemical Physics* **2000,** 113, (18), 8249-8252.

77. R. Maboudian; C. Carraro, *Annual Review of Physical Chemistry* **2004,** 55, 35-54.

78. M. A. Baker; J. Li, *Surface and Interface Analysis* **2006,** 38, (4), 863-867.

79. R. Astrom; R. Mutikainen; H. Kuisma; A. H. Hakola, *Wear* **2002,** 253, (7-8), 739-745.

80. K. C. Eapen; S. T. Patton; S. A. Smallwood; B. S. Phillips; J. S. Zabinski, *Journal of Microelectromechanical Systems* **2005,** 14, (5), 954-960.

81. K. C. Eapen; S. A. Smallwood; J. S. Zabinski, *Surface & Coatings Technology* **2006,** 201, (6), 2960-2969.

82. C. M. Mate; M. F. Toney; K. A. Leach, *Ieee Transactions on Magnetics* **2001,** 37, (4), 1821-1823.

83. J. J. Nainaparampil; B. S. Phillips; K. C. Eapen; J. S. Zabinski, *Nanotechnology* **2005,** 16, (11), 2474-2481.

84. S. Achanta; D. Drees; J. P. Celis, *Wear* **2005,** 259, (1-6), 719-729.

85. W. R. Ashurst; M. B. J. Wijesundara; C. Carraro; R. Maboudian, *Tribology Letters* **2004,** 17, (2), 195-198.

86. X. K. Cao; T. M. Shao; S. Z. Wen; Y. Yao, *Tribology Transactions* **2004,** 47, (2), 227-232.

87. K. H. Chung; D. E. Kim, *Tribology Letters* **2003,** 15, (2), 135-144.

88. X. D. Li; B. Bhushan; K. Takashima; C. W. Baek; Y. K. Kim, *Ultramicroscopy* **2003,** 97, (1-4), 481-494.

89. G. Radhakrishnan; P. M. Adams; R. Robertson; R. Cole, *Tribology Letters* **2000,** 8, (2-3), 133-137.

90. S. S. Mani; J. G. Fleming; J. J. Sniegowski, in: *Proceedings of SPIE - The International Society for Optical Engineering* Society of Photo-Optical Instrumentation Engineers: 1999; pp 150-157.

91. R. Bandorf; H. Luthje; C. Henke; J. Wiebe; J. H. Sick; R. Kuster, *Surface & Coatings Technology* **2005,** 200, (5-6), 1777-1782.

92. D. M. Cao; T. Wang; B. Feng; W. J. Meng; K. W. Kelly, *Thin Solid Films* **2001,** 398, 553-559.

93. I. S. Forbes; J. I. B. Wilson, *Thin Solid Films* **2002,** 420, 508-514.

94. B. Zhou; L. Wang; N. Mehta; S. Morshed; A. Erdemir; O. Eryilmaz; B. C. Prorok, *Journal of Micromechanics and Microengineering* **2006,** 16, (7), 1374-1381.

95. S. A. Smallwood; K. C. Eapen; S. T. Patton; J. S. Zabinski, *Wear* **2006,** 260, (11-12), 1179-1189.

96. D. B. Asay; M. T. Dugger; S. H. Kim, *Tribology Letters* **2008,** 29, (1), 67-74.

97. A. J. Gellman, *Tribology Letters* **2004,** 17, (3), 455-461.

98. D. B. Asay; M. T. Dugger; J. A. Ohlhausen; S. H. Kim, *Langmuir* **2008,** 24, (1), 155-159.

Chapter 2

Evolution of the Adsorbed Water Layer Structure on Silicon Oxide at Room Temperature

2.1 Summary

The molecular configuration of water adsorbed on a hydrophilic silicon oxide surface at room temperature has been determined as a function of relative humidity using attenuated total reflection (ATR) infrared spectroscopy. A completely hydrogen bonded ice-like network of water grows up to 3 layers as the relative humidity increases from zero to 30%. In the relative humidity range of 30 ~ 60%, the liquid water structure starts appearing while the ice-like structure continues growing to the saturation. The total thickness of the adsorbed layer increases only 1 molecular layer in this humidity range. Above 60% relative humidity, the liquid water configuration grows on top of the ice-like layer. This structural evolution indicates that the outmost layer of the adsorbed water molecules undergo transitions in equilibrium behavior as humidity varies. These transitions determine the shape of the adsorption isotherm curve. The structural transitions of the outermost adsorbed layer are accompanied with interfacial energy changes and explain many phenomena observed only for water adsorption.

2.2 Introduction to water adsorption on silicon oxide surfaces

Water adsorbs onto virtually all surfaces. As a consequence, interfacial water plays important roles in biology,[1] meteorology,[2] geology,[3] and nanotechnology. Water structure at an interface is key to discerning wetting phenomena.[4] Surface chemistry and the structure of water molecules adsorbed at the surface determine biological phenomena like bioadhesion.[1, 5] In micro- and nano-material engineering the control of interfacial chemistry is critical because the surface-to-volume ratio is significantly large, surface properties dominate material performance.[6] For example, water adsorbed on hydrophilic silicon oxide surfaces cause large changes in adhesion and friction in nanoscale contacts.[7-9] Silicon oxide is abundant in nature and important in semiconductors, cements,[10] and geology.[3] This chapter shows how molecular configuration of water molecules at the interface of the clean silicon oxide surface evolves as a function of relative humidity at room temperature.

The configuration of adsorbed water molecules has been extensively studied in ultra-high vacuum conditions at cryogenic temperatures.[11, 12] The knowledge obtained from these studies is useful in understanding water chemistry in the upper atmosphere or in space. However, it cannot be extrapolated to elucidate surface chemistry occurring at ambient conditions. There have been many spectroscopic, microscopic, and theoretical studies of thin film interactions and molecular configurations at the bulk water/substrate interface[13-28] Sum frequency generation studies of water uptake on mica suggests a monolayer of ice-like water when the RH is near 90%,[21] however this data conflicts both ellipsometry and expected film thicknesses for type II adsorption isotherm on highly

hydrophilic surfaces.[14] These studies have not fully elucidated the structural evolution of the water molecule configuration as water molecules are adsorbed on the silicon oxide surface under ambient conditions directly relevant to atmospheric phenomena, material behavior, and device operations.

In this study, the structure of adsorbed water on a silicon oxide surface was investigated with an attenuated total reflection infrared (ATR-IR) spectroscopy.[29] A silicon ATR crystal covered with a native oxide was used. In this analysis, the probe IR beam travels inside the solid silicon substrate and is totally reflected at the substrate surface. A shallow evanescent wave penetrates into the adsorbed layer and the gas phase. However, the gas phase molecules are not detected due to the low molecular density. Even at the saturation vapor pressure of water at room temperature, the number of gas-phase molecules present in the probe volume above the 1 cm^2 ATR crystal surface is $\sim 3\times10^{13}$, or less than 4% of a single layer molecular density. Therefore, only the adsorbed molecules are detected, enabling a vibrational spectroscopic study for identification of the molecular configuration of water in the adsorbed layer without interference from the gas phase water molecules. The natural log of ATR-IR reflectance is proportional to distribution of different configurations as well as total thickness of the adsorbed water layers.[29]

The data presented in this chapter reveal the structural profile of the adsorbed water layers as they grow thicker with relative humidity. The first 3 layers adsorbed on the silicon oxide surface at low humidities conform to an "ice-like" configuration; the next layer formed in medium humidities is in a transition between the completely self-associated network and a liquid-like configuration; and finally the subsequently adsorbed

water layers at high humidities assume the bulk liquid configuration. The evolution of these structures indicates that transitions in equilibrium at the interface influence the shape of the adsorption isotherm curve. The structural changes of the outmost water layer of the interface due to these transitions illuminate lingering questions regarding adhesion, protein adsorption, water structure at interfaces, and wetting.

2.3 Experimental Details

ATR spectra were collected using a Thermo-Nicolet Nexus 670 spectrometer with a MCT detector and a multiple-bounce silicon ATR crystal. The crystal was prepared by washing with dichloromethane, rinsing with copious amounts of millipore water, drying with argon, and exposing it to UV/O_3 for 30 minutes. This procedure produced an organic-contaminant-free native oxide surface believed to be saturated with hydroxyl groups.[30] Following the cleaning, the silicon crystal was promptly mounted to the ATR assembly and purged with dry Ar until there was no change in background spectra. The adsorption of water onto this surface was accomplished by varying the ratio of dry argon flow to water-saturated argon stream. The experimental setup is illustrated in Figure **2.1**. The temperature of the system was maintained at 20.8 ± 0.5 °C while the partial pressure of water was varied from 0% to 100%. At an incident angle of 45°, the effective penetration depth of the evanescent wave was 482 nm at 1635 cm^{-1}. The molar

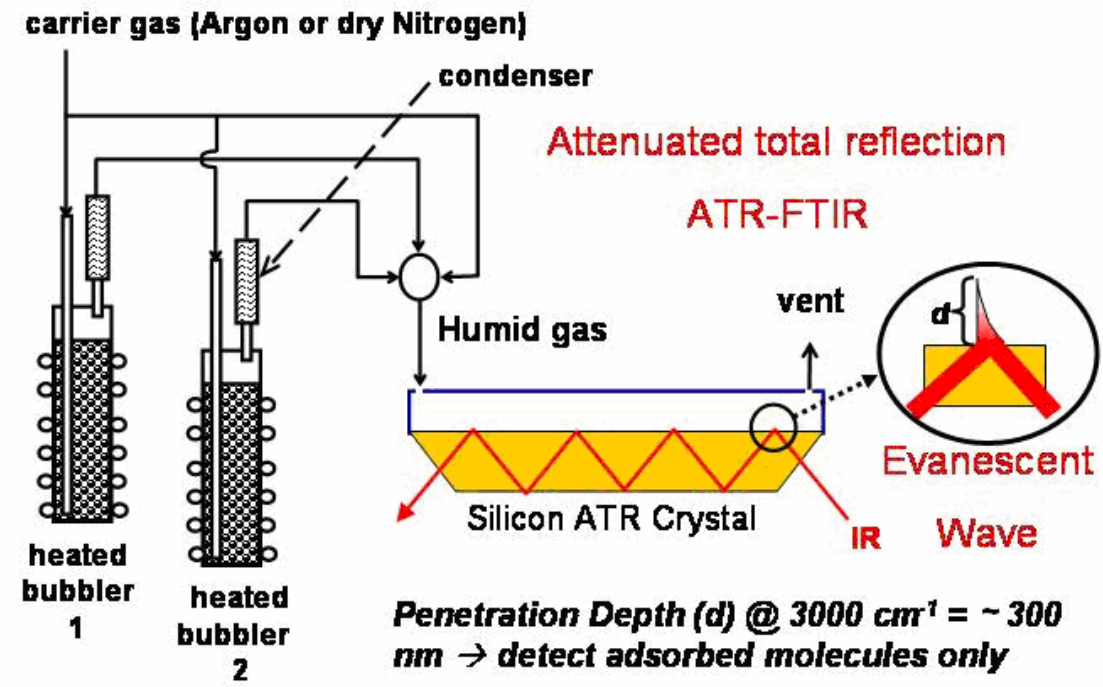

Figure **2.1**: Adsorption experiment setup illustrating the flow system and infrared evanescent wave used to detect the adsorbed species.

absorptivities of the H-O-H bending region of ice and liquid water estimated from refs.18, 31, 32 differ by less than 20%.

2.4 Results and Discussion

Figure **2.2** contains the ATR-IR spectra of the adsorbed water layers on the silicon oxide surface as a function of relative humidity. There are two absorption bands: a single peak at 1640 cm^{-1} due to the H-O-H bending vibration and a group of peaks in the 3000 ~ 3800 cm^{-1} region due to the O-H stretching vibrations.[33]

Because the bending vibration at 1640 cm^{-1} does not vary significantly with the configuration of water molecules in the adsorbed layer, its intensity is used to determine the average thickness of the adsorbed layer. The thickness is determined by comparing the IR absorption due to the adsorbed water molecules with the IR absorption of bulk water on the ATR crystal. The adsorption isotherm thickness determined from the intensity of the 1640 cm^{-1} peak is plotted in Figure **2.3**. The monolayer thickness is calculated by dividing the measured thickness by 2.82 Å, the mean van der Waals diameter of water. If the bilayer thickness (4 Å) is used, the number of water layers would be slightly larger. Details of the short-range ordering on native oxides are unknown at this time. The average thickness determined from the ATR intensity follows the typical type-II isotherm curve of water. The data are in good agreement with previously reported data for hydrophilic surfaces.[14, 23, 34]

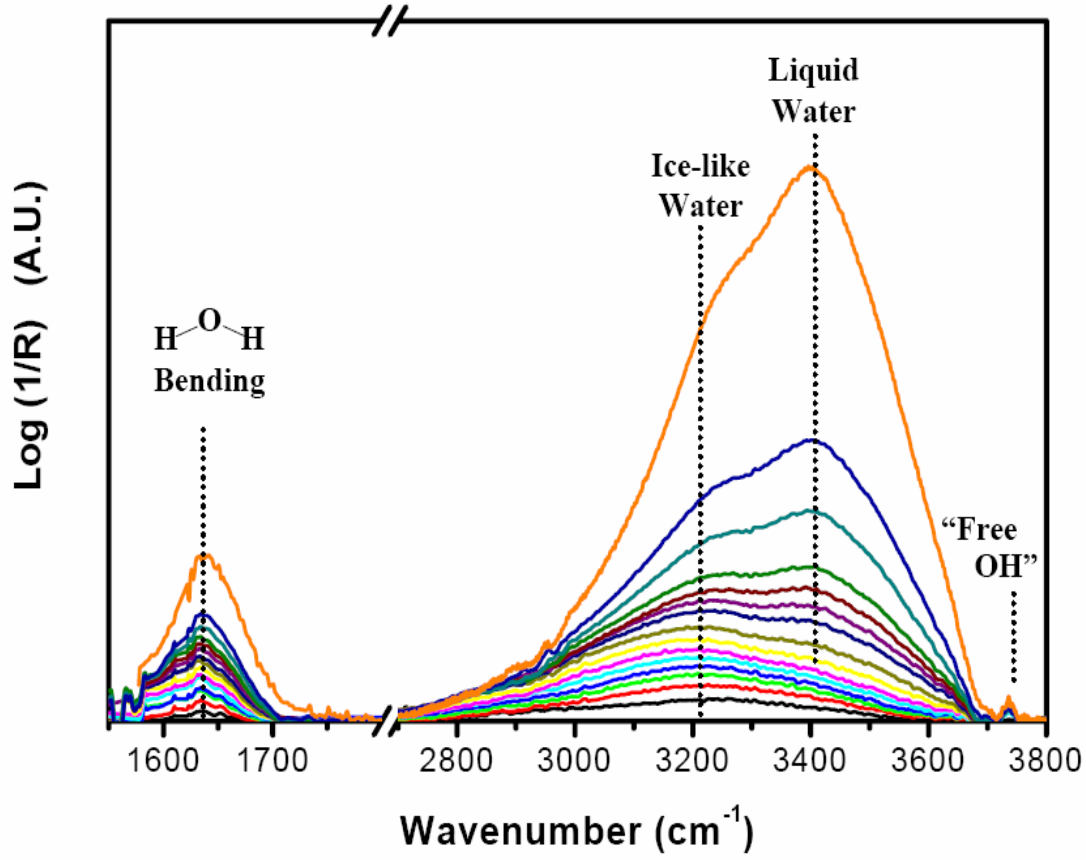

Figure **2.2**: ATR-IR spectra of water adsorbed on silicon oxide at different relative humidities. From lowest to highest log(1/R) signal intensity, relative humidity = 7.3, 9.7, 14.5, 19.4, 24.5, 29.4, 38.8, 49.4, 58.6, 64.3, 69.9, 74.5, 84.2, 92.2, 99.4 %. The O-H stretching vibration peak positions of "ice-like" water and liquid water are marked with dotted lines at ~3230 cm^{-1} and ~3400 cm^{-1}, respectively. The free-OH peak is marked at 3740 cm^{-1}.

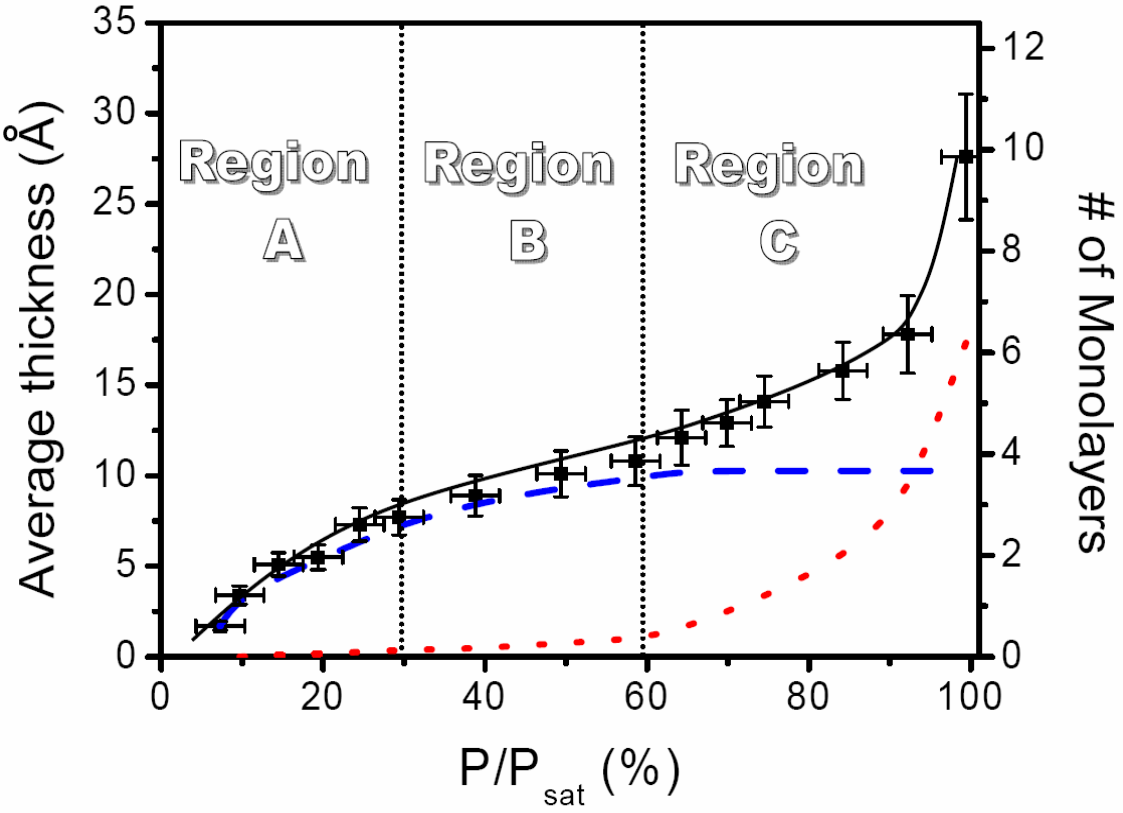

Figure **2.3**: Adsorption isotherm of adsorbed water on silicon oxide surface. Square symbols are the total thickness of the adsorbed water layer calculated from the intensity of H-O-H bending vibration peak. The solid line is drawn to guide eyes. The dashed and dotted lines are the thickness of the ice-like water and liquid water layers, respectively. The thickness of each component is calculated by deconvoluting the observed O-H stretching peaks into two peaks at 3230 cm^{-1} and 3400 cm^{-1}. The sensitivity of the O-H stretching peak is assumed to be equal in both structures. Regions A, B, and C are shown, corresponding to ice-like water growth, transitional growth, and liquid water growth.

In the O-H stretching vibration region there are three peaks of interest: a small sharp peak at 3740 cm^{-1} and two broad peaks at 3230 cm^{-1} and 3400 cm^{-1}. The peak at 3740 cm^{-1} corresponds to "free OH" or a hydroxyl group with no hydrogen bonds.[33,35] This peak appears because the outermost adsorbed water molecules do not have sufficient nearest neighbors to complete hydrogen bonding. The silicon oxide surface is initially covered with surface OH groups (those bonded to Si). The single beam spectrum of this surface was used as a background. As water adsorbs on this surface the surface-air interface eventually becomes saturated with water OH groups. The presence of the 3740 cm^{-1} peak in the background-subtracted spectra suggests a slight difference in free OH environments between the solid-dry air interface and the water-air interface.[36]

Detailed information regarding the molecular configuration of water in the adsorbed layer can be found from analysis of the two peaks at 3230 cm^{-1} and 3400 cm^{-1} corresponding to the stretching vibrations of completely self-associated "ice-like" water and "liquid" water, respectively.[16, 18, 33] As the degree of hydrogen bonding increases, the O-H stretching vibration shifts to lower wavenumbers. As water is initially introduced in the gas phase, the ice-like water peak at 3230 cm^{-1} grows exclusively up to a relative humidity (RH) of ~30%. The liquid water peak at 3400 cm^{-1} starts growing along with the ice-like water peak as the RH increases up to ~ 60%. At a RH of 65 ~ 70%, the apparent peak intensities of these two peaks appear the same. In further increase of RH the liquid water peak at 3400 cm^{-1} becomes dominant. It should be noted that the evolution of these two peaks does not originate from distortion of the ATR-IR band due to the nonlinear variation of the refractive index with wavelength near absorption bands and strong attenuation index of water.[37] In the case of ATR measurements of bulk water,

we observed a shift of the O-H stretching vibration peak position to a lower wavenumber (3370 cm^{-1}) due to the abnormal dispersion effects; but this kind of red shift is not observed at all for the adsorbed water molecules. These results clearly reveal that the molecular configuration of water changes as the adsorbed layer thickness increases.

The relative abundance of the ice-like and liquid water is determined by deconvolution of the IR spectra in the 2800 ~ 3700 cm^{-1} region into the 3230 cm^{-1} and 3400 cm^{-1} peaks. The result of this analysis is plotted in Figure **2.3**, along with the total thickness of the adsorbed water layer calculated from the H-O-H bending vibration peak. At RH below 30% (marked as region A), the ice-like structure grows up to ~3 molecular layers. The total thickness increases quickly at the beginning; then its growth rate slows down. In the RH range of 30 ~ 60% (marked as region B), the liquid structure starts growing slowly although the ice-like structure is still dominant. In this region, the total thickness increases linearly with RH from 3 to 4 monolayers. At RH above 60% (marked as region C), the ice-like structure growth ends and only the liquid structure grows rapidly with increase of RH. In the following paragraphs, we discuss the origin of different structure and growth pattern for each region.

In region A, the adsorption isotherm thickness increases rapidly and then retards giving a "knee-like" shape. In the case of many organic molecules, this shape is attributed to completion of the one monolayer adsorption. Once the monolayer is formed, the thickness does not grow until the relative partial pressure approaches saturation pressure.[38] In the case of water, the initial rise does not stop at the completion of a monolayer; instead it continues growing up to 3 layers. This is due to the hydrogen bonding capacity of the water molecule. Formation of hydrogen bonds with the

immobilized substrate hydroxyl groups forces water molecules in the first layer into an ordered structure. The induced structure of the first layer propagates through hydrogen bonds into upper layers. This is possible because water can form a tetrahedrally coordinated ice-like network. In this region, the interface can be considered in equilibrium between the surface-induced ice-like layer and water vapor, a pseudo-solid (ice) – vapor equilibrium.

In region B, the surface-induced structuring effect at the outermost adsorbed layer starts diminishing. We consider the growth in this region to be in transition between the two water structure growths. The structural rigidity of the hydrogen bonding network competes with thermal motions of the adsorbing water molecules at room temperature; the liquid water structure starts appearing at RH~30%. In other words, the growth of the liquid like layer begins before the growth of the ice-like water layer ends. However, the liquid water structure is not yet fully stable and does not form multi-layers because the relative humidity in the gas phase is not high enough. This is the reason that the growth rate of water in this region is small, accounting for only one molecular layer increase over RH increase from 30% to 60%. These transitions cause the change in curvature of the Type-II isotherm. The fact that growth of the ice-like structure is still dominating until it saturates at RH ~60% indicates that these molecules are still under a strong influence of the immobilized surface hydroxyl groups.

As the relative humidity increases above ~60%, the structure of the outmost layer is completely dominated by thermal motion so it assumes a liquid water configuration. The thickness of the adsorbed layer starts increasing exponentially with RH and bulk

condensation occurs at near saturation vapor pressure. In region C, the outermost adsorbed layer is in equilibrium between the liquid water layer and vapor.

Figure **2.4** summarizes the evolution of three distinct structures as water adsorbs on silicon oxide. The first 3 layers, those closest to the immobilized hydroxyl surface (Si-OH), form an ice-like network. Above the ice-like water, there exists a transitional region whose structure is more relaxed than the under-layers of the ice-like structure, but not completely disordered as is the liquid layers above it. Any additional water adsorbing on this surface behaves as a liquid. This structural evolution indicates changes in the nature of the interfacial equilibrium at different humidity regions and coincides with the smooth transitions of the adsorption isotherm curve.

The formation of ice-like structure at low humidities is consistent with what have been implicated from other spectroscopic observations. In nuclear magnetic resonance spectroscopy studies, the adsorbed water molecules exhibit two different relaxation times – one is close to that of bulk water and the other is much slower.[24] This slow relaxation time phase must be related to the "ice-like" water structure. As a matter of fact, the slow relaxation time phase is reported to be dominant at low humidity. Dielectric measurements of the adsorbed water on hydroxylated chromium oxide at room temperature also found that the relaxation time of the adsorbed water is several orders of magnitude lower than that of bulk water.[39]

The implications of structured water at the silicon oxide interface in nature are many. The structure of the adsorbed water layer at the interface of silicon oxide and humid gas (Figure **2.4**) provides insight into many phenomena observed for silicon oxide

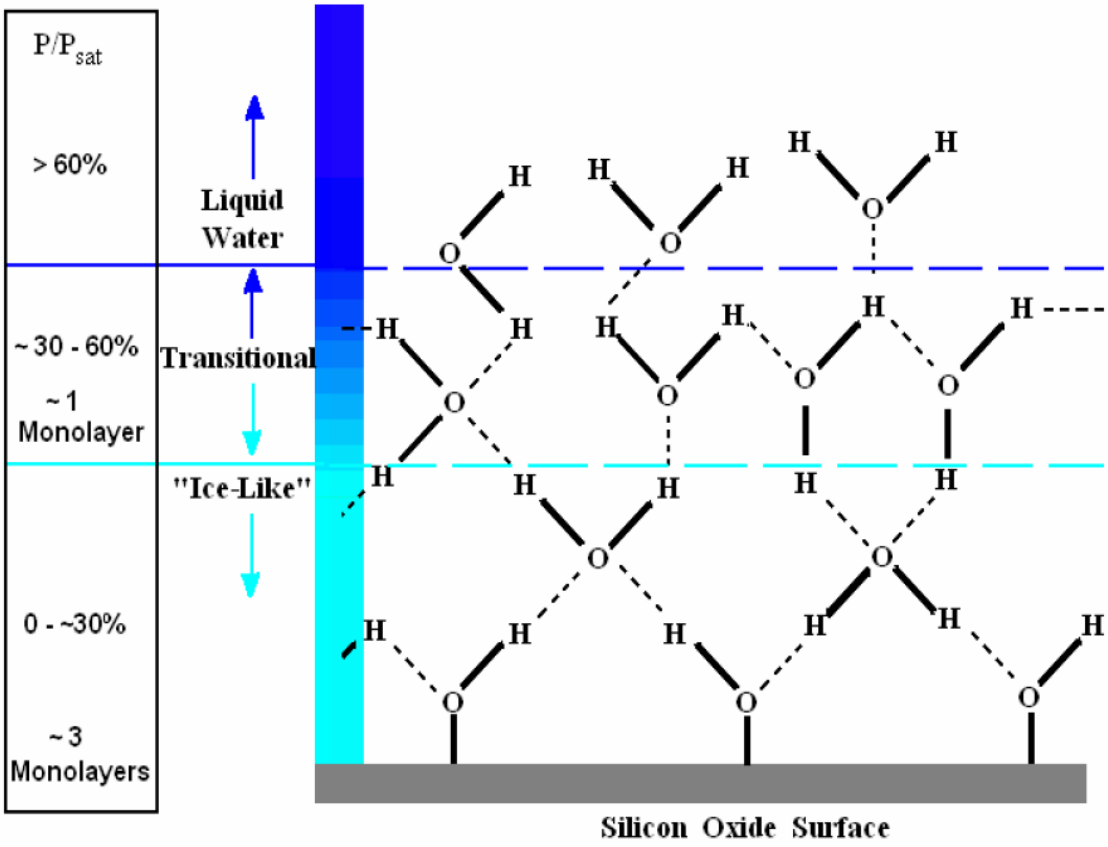

Figure **2.4**: Schematic illustrating the structural evolution of water molecules as the adsorbed layer thickness increases with RH. The ice-like structure grows up to 3 molecular layers thick as relative humidity increases from 0 to 30%. In the relative humidity range from 30 to 60%, the ice-like structure continues to grow while liquid structure begins to form. In this transitional region, approximately one molecular layer grows. Further increase in the relative humidity above 60% causes water to adsorb in the liquid configuration. (--- Hydrogen bonds, — Covalent bonds) (note: 2-D illustration is not to scale)

surfaces in humid environments. The hardening of cement upon drying would be an example that can be explained in part with our structural model.[10] As the cement dries, contacts between hydrophilic silica particles form ice-like bridges that are stronger than the liquid. Another example is the nanoscale contact mechanics of clean silicon oxide surfaces. The adhesion force of silicon oxide surfaces measured with atomic force microscopy increases as the humidity increases, reaches a maximum value at an intermediate humidity, and then finally decreases as the humidity approaches the saturation vapor pressure of water.[7, 9, 40] This kind of complicated adhesive behavior of nanoscale contacts is witnessed only with water. There have been many attempts to predict this complicated behavior with a simple capillary condensation theory using Kelvin equation and the surface tension of bulk water (72 erg/cm^2); but the estimated magnitude of the adhesion force change is much smaller than what is observed experimentally.[9] Our ATR-IR data and the model implicate that the surface tension value of bulk water cannot be used at RH < 60% because the adsorbed water molecules are in the ice-like configuration.

The surface tension of the ice-like layer may be estimated from the following calculation. The average hydrogen bond number of liquid water is about 2.5 per molecule, while that of ice is 4 per molecule.[41] The Fowkes theory predicts that the van der Waals contribution to the water surface tension is ~23 erg/cm^2.[42] The remaining ~50 erg/cm^2 can be attributed to 2.5 hydrogen bonds in liquid water. From this first-order approximation, the surface tension contribution for 4 hydrogen bonds is expected to be ~80 erg/cm^2. Therefore, the surface tension of the adsorbed water layer at RH below

60% will be ~103 erg/cm^2, which is close to the surface tension of ice.[43, 44] This is one reason that adhesion between silicon oxide surfaces at low RH is higher than that of high RH.[7, 9, 40] More details are the subject of a separate chapter.

Although the structure shown in Figure **2.4** is determined during the equilibrium adsorption from the gas phase, the entire structure can be applied to the silicon oxide and bulk water interface.[18, 19, 24] The structure and thickness of the bottom "ice-like" layer do not change with the thickness of the liquid-structure overlayer. The presence of these ice-like layers on hydrophilic silicon oxide surfaces can, in part, account for lower bio-fouling activity on these surfaces compared to hydrophobic surfaces. At hydrophobic surfaces water is not strongly bound with the surface so it is easy for biomolecules like proteins to displace the water and occupy space at the surface. At hydrophilic surfaces the cohesive hydrogen bonding within the ice-like network is so strong and thick that protein molecules cannot easily replace the water molecules in this ice-like network.[1, 5] Another interesting and important phenomenon is the nucleation kinetics of ice. It is recently found that nucleation of ice occurs much faster on quartz surfaces compared to alumina surfaces.[45] Since the preferential formation of ice-like structure on alumina is not observed,[13] these results may indicate that the ice-like layer on quartz acts as a seed for the nucleation of ice.

2.5 Conclusions

This chapter elucidates how hydrogen bonding with immobilized surface hydroxyl groups (Si-OH) effects the molecular configuration of the adsorbed water at ambient conditions. The equilibrium structure of the outmost layer varies in three different regions of the adsorption isotherm. In low humidity (RH below 30%), the adsorbed water forms an ice-like network on the silicon oxide surface that propagates up to ~3 layers from the surface at room temperature. The hydrogen bond network structure competes with the liquid water structure in the RH range of 30 ~ 60%, above which the liquid structure dominates. These structural transitions have profound effects on the adsorption isotherm of water and how the silicon oxide surface behaves in different environments.

2.6 References

1. E. A. Vogler, *Advances in Colloid and Interface Science* **1998,** 74, 69-117.
2. H. R. Pruppacher; J. D. Klett, *Microphysics of Clouds and Precipitation* Kluwer Academic Publishers: New York, 1997.
3. W. Stumm; L. Sigg; B. Sulzberger, *Chemistry of the Solid-Water interface: Processes at the Mineral-Water and Particle-Water Interface in Natural Systems* Wiley: New York, 1992.
4. P. G. Degennes, *Reviews of Modern Physics* **1985,** 57, (3), 827-863.
5. S. Margel; E. A. Vogler; L. Firment; T. Watt; S. Haynie; D. Y. Sogah, *Journal of Biomedical Materials Research* **1993,** 27, (12), 1463-1476.
6. R. Maboudian; R. T. Howe, *Journal of Vacuum Science & Technology B* **1997,** 15, (1), 1-20.
7. M. Binggeli; C. M. Mate, *Applied Physics Letters* **1994,** 65, (4), 415-417.
8. M. Urbakh; J. Klafter; D. Gourdon; J. Israelachvili, *Nature* **2004,** 430, (6999), 525-528.
9. X. D. Xiao; L. M. Qian, *Langmuir* **2000,** 16, (21), 8153-8158.
10. H. F. Taylor, *Cement Chemistry 2nd Edition*. Academic Press: London, 1997.
11. M. A. Henderson, *Surface Science Reports* **2002,** 46, (1-8), 5-308.
12. K. P. Stevenson; G. A. Kimmel; Z. Dohnalek; R. S. Smith; B. D. Kay, *Science* **1999,** 283, (5407), 1505-1507.
13. H. A. Al-Abadleh; V. H. Grassian, *Langmuir* **2003,** 19, (2), 341-347.

14. D. Beaglehole; H. K. Christenson, *Journal of Physical Chemistry* **1992,** 96, (8), 3395-3403.

15. F. Dorazio; S. Bhattacharja; W. P. Halperin; K. Eguchi; T. Mizusaki, *Physical Review B* **1990,** 42, (16), 9810-9818.

16. Q. Du; E. Freysz; Y. R. Shen, *Science* **1994,** 264, (5160), 826-828.

17. Q. Du; E. Freysz; Y. R. Shen, *Physical Review Letters* **1994,** 72, (2), 238-241.

18. G. E. Ewing, *Journal of Physical Chemistry B* **2004,** 108, (41), 15953-15961.

19. T. Hasegawa; J. Nishijo; T. Imae; Q. Huo; R. M. Leblanc, *Journal of Physical Chemistry B* **2001,** 105, (48), 12056-12060.

20. J. Hu; X. D. Xiao; D. F. Ogletree; M. Salmeron, *Science* **1995,** 268, (5208), 267-269.

21. P. B. Miranda; L. Xu; Y. R. Shen; M. Salmeron, *Physical Review Letters* **1998,** 81, (26), 5876-5879.

22. L. F. Scatena; M. G. Brown; G. L. Richmond, *Science* **2001,** 292, (5518), 908-912.

23. P. A. Thiel; T. E. Madey, *Surface Science Reports* **1987,** 7, (6-8), 211-385.

24. M. F. Toney; J. N. Howard; J. Richer; G. L. Borges; J. G. Gordon; O. R. Melroy; D. G. Wiesler; D. Yee; L. B. Sorensen, *Surface Science* **1995,** 335, (1-3), 326-332.

25. S. Trakhtenberg; R. Naaman; S. R. Cohen; I. Benjamin, *Journal of Physical Chemistry B* **1997,** 101, (26), 5172-5176.

26. M. R. Yalamanchili; A. A. Atia; J. D. Miller, *Langmuir* **1996,** 12, (17), 4176-4184.

27. J. J. Yang; S. Meng; L. F. Xu; E. G. Wang, *Physical Review B* **2005,** 71, (3).

28. J. R. Zimmerman; J. A. Lasater, *Journal of Physical Chemistry* **1958,** 62, (10), 1157-1163.

29. M. W. Urban, *Attenuated Total Reflectance Spectroscopy of Polymers Theory and Practice*. American Chemical Society: Washington, D. C., 1996.

30. V. M. Graubner; R. Jordan; O. Nuyken; B. Schnyder; T. Lippert; R. Kotz; A. Wokaun, *Macromolecules* **2004,** 37, (16), 5936-5943.

31. S. Y. Venyaminov; F. G. Prendergast, *Analytical Biochemistry* **1997,** 248, (2), 234-245.

32. S. G. Warren, *Applied Optics* **1984,** 23, (8), 1206-1225.

33. J. R. Scherer, *Advances in Infrafred and Raman Spectroscopy*. Heyden: London, 1978; Vol. 5.

34. A. Verdaguer; C. Weis; G. Oncins; G. Ketteler; H. Bluhm; M. Salmeron, *Langmuir* **2007,** 23, (19), 9699-9703.

35. C. I. Ratcliffe; D. E. Irish, *Journal of Physical Chemistry* **1982,** 86, (25), 4897-4905.

36. L. T. Zhuravlev, *Langmuir* **1987,** 3, (3), 316-318.

37. M. Hancer; R. P. Sperline; J. D. Miller, *Applied Spectroscopy* **2000,** 54, (1), 138-143.

38. A. W. Adamson; A. P. Gast, *Physical Chemistry of Surfaces, 6th Edition*. John Wiley & Sons: New York, 1997.

39. Y. Kuroda; S. Kittaka; S. Takahara; T. Yamaguchi; M. C. Bellissent-Funel, *Journal of Physical Chemistry B* **1999,** 103, (50), 11064-11073.

40. D. B. Asay; S. H. Kim, *Journal of Chemical Physics* **2006,** 124, (17), 5.

41. T. A. Weber; F. H. Stillinger, *Journal of Physical Chemistry* **1983,** 87, (21), 4277-4281.

42. F. M. Fowkes, *Journal of Physical Chemistry* **1963,** 67, (12), 2538-&.

43. J. M. Douillard; M. Henry, *Journal of Colloid and Interface Science* **2003,** 263, (2), 554-561.

44. J. Y. Jang; G. C. Schatz; M. A. Ratner, *Physical Review Letters* **2004,** 92, (8).

45. D. H. Dolan; Y. M. Gupta, *Journal of Chemical Physics* **2004,** 121, (18), 9050-9057.

Chapter 3

Surface Chemistry Effects on the Adsorption of Water onto Chemically Modified Silicon Surfaces

3.1 Summary

This chapter describes the effect of surface chemistry on the adsorption isotherm of water, isosteric heat of adsorption and entropy of adsorption, water contact angle, as well as the degree of hydrogen bonding within the adsorbed water layers. Three surface chemistries are investigated: hydroxylated silicon oxide, partially methylated silicon oxide via hexamethyldisilazane (HMDS) treatment and octadecyltricholosilane (OTS) self-assembled monolayer (SAM) coated silicon oxide. As the surface becomes more hydrophobic, the initial heat of adsorption (at low surface coverages) decreases. Additionally, the wettability of the surface is observed to dramatically affect both hydrogen bonding within adsorbed water molecules as well as the isotherm thickness.

3.2 Introduction

Water at interfaces has been the subject of intense research over many decades.[1-8] At the interface, the physical and structural properties of interfacial water vary from those in the bulk. For example, the viscosity of water under nano-confinement is observed to vary over many orders of magnitude depending on the surface chemistry.[9-13] Near the interface, the structure of water, as observed with various infrared (IR) spectroscopic techniques, is quite different than that of the bulk.[14-20] While these observations are perceived in films that are a few nanometers thick, the effect of the interface can be observed at the macroscale. For example, the ability of water to wet a flat surface (as measured by the water contact angle) depends greatly on the outermost surface chemistry.[8, 21-24] Understanding the structure of interfacial water and its impact is therefore of fundamental interest due to its significance in many systems i.e. geology, tribology, biology, and fuel cell research.

Water has the capacity to hydrogen bond with up to four nearest neighbors. This bonding depends on the local physical and chemical conditions or environments. When water is completely self-associated, each water molecule forms four hydrogen bonds with its nearest neighbors in a tetrahedral arrangement.[25] This structure is observed in crystalline ice structures. In IR spectroscopy, the OH infrared stretching vibration of this structured water is observed with a peak centered at ~3220 cm^{-1} with a full with at half max of ~190 cm^{-1}. At room temperature, liquid water has two to three hydrogen bonds

per water molecule on average.[26] This structure of water has a peak position centered at ~3400 cm^{-1} with a full with at half max of ~250 cm^{-1}.[18, 27] When the hydroxyl group in water has no hydrogen bonding (i.e. no self-association), this free-OH or dangling-OH vibration is observed at ~3640 cm^{-1} and has a much narrower full with at half maximum. Therefore, the peak position of the OH stretching vibration is very sensitive to the degree of hydrogen bonding and has been used as an indicative tool for investigating the structure of water.[14-19, 27]

In this chapter, the hydrogen bonding configuration in adsorbed water layers were investigated with attenuated total reflectance infrared (ATR-IR) spectroscopy for hydroxylated silicon oxide as well as partially methylated silicon oxide via chemisorption of hexamethyldisilazane (HMDS) and highly hydrophobic silicon oxide covered with octadecyltricholosilane (OTS) self-assembled monolayer. Silicon with a native oxide is was chosen for this study due to its relevance in micro- and nano-devices[28] as well as the large amount of research prevalent in the literature.[15, 17, 21-24, 27, 29-33] Due to changes in the outermost surface chemistry of the silicon oxide surface, the bulk water contact angles differ between these surfaces. These changes are also reflected in the isosteric heat of adsorption of water.

3.3 Experimental Details

Water adsorption experiments were performed with a Thermo Nicolet Nexus 640 infrared spectrometer with an ATR-IR setup using an MCTA detector. A silicon ATR crystal was used in all experiments. The crystal had a 45^{o} incidence angle providing a

total of 11 internal reflections at the probing surface. At these conditions, effective penetration depth of the evanescent IR field is ~240 nm at 3300 cm^{-1}.

The silicon ATR crystal was cleaned and oxidized in a UV ozone chamber for ~20 minutes and then placed in a 5:1:1 mixture of water: 30% ammonium hydroxide: 30% hydrogen peroxide at a temperature of 75 ±5°C (commonly known as RCA-1) for 15 minutes. This cleaning procedure produced a clean silicon oxide layer on the crystal removing organic contaminates.[34] Immediately following this cleaning step, the crystal was rinsed with copious amounts of milli-Q water (resistance = 18MΩ/cm) and dried with high purity argon. This procedure provided a clean silicon oxide surface for use in this study. In the case of the silicon oxide surface studies the sample was promptly mounted into the ATR holder and purged for ~1 hour with dry argon before beginning the experiment.

In the case of the partially methylated silicon oxide surface, the same cleaning procedure was used as described above; however, following these cleaning steps the crystal was placed inside of two Petri dishes forming a loose seal. Prior to sealing, 2-3 drops of HMDS were placed ~2 cm away from the crystal. The system was gently heated to ~65 °C for 45 min. This treatment allowed for HMDS to be deposited via vapor deposition onto the surface. At the surface the following reaction occurs:[31]

$$2 \cdot SiOH + (CH_3)_3 - Si - NH - Si - (CH_3)_3 \longrightarrow 2 \cdot Si - O - Si - (CH_3)_3 + NH_3 \qquad \textbf{3-1}$$

In the case of the OTS-SAM coated silicon oxide surface, the surface was further cleaned via a piranha solution (3:1 ratio of concentrated sulfuric acid to 30% hydrogen

peroxide) for 30 minutes and then rinsed with copious amounts of milli-Q water. Following this step, it was placed in a 30% hydrogen peroxide solution for 30 minutes and then dried with dry argon. After the drying process the crystal was placed in cleaned glassware and high purity toluene was added and kept under argon. This step is used to remove residual water on the crystal surface by dissolving it into toluene. Separately, a 1 μM solution of OTS in toluene was mixed and allowed to react with any residual water in the toluene solution over a 24 hour period. Next, the toluene was removed from the glassware and ATR crystal in an inert dry environment following which the OTS-toluene solution was added. During this addition, the OTS-toluene solution was filtered to remove any polymerized OTS contaminates. In an inert environment, the silicon ATR crystal and OTS-toluene solution was heated to 60 °C for 24 hours. The solution was removed from the system and a mixture of HMDS (~10μM) in toluene was used to rinse the system. The purpose of using HMDS-toluene solution was to remove water from the toluene before rinsing and to help react with any hydroxyl groups that had not reacted with OTS. After 10 minutes in this solution, the HMDS-toluene solution was removed from the container and replaced with pure toluene 3 times. Once the crystal was retrieved from the system after the toluene rinsing, it was placed in ethanol and in an ultrasonic bath for ~10 minutes. After this step the crystal was then dried with argon. Based upon ellipsometry, the thickness of the SAM layer was estimated to be between 3 to 5 nm.

Controlling the partial pressure of water to the crystal was performed using the techniques previously presented. The temperature of the crystal was maintained during each test to within ± 1 °C (typically). In the case of the silicon oxide surface, adsorption experiments were performed at 10°C, 22.4°C, and 35.5°C. In the case of HMDS treated

silicon oxide surface, adsorption experiments were performed at 9°C, 23.4°C, and 35.9°C. In the case of the OTS treated silicon oxide surface, adsorption at 11°C.

3.4 Experimental Results and Discussion

Water contact angles were measured on the clean silicon oxide surface, the partially methylated surface, and the OTS-SAM coated surface. The observed static contact angle of water on each was <5°, 45 ±5°, and 95 ±5° respectively. According to the literature, when quartz is dehydroxylated via intense heating, the measured water contact angle is ~42°.[24] When the quartz surface is saturated with hydroxyl groups, the contact angle is 0°. Using the Cassie equation[35] (which can relate the contact angle to surface coverage), based upon these previous literature[8, 24, 31] and in-house XPS measurements, in the case of the clean silicon oxide surface, it is estimated that the surface is ~98% saturated with silanol groups (Si-OH) on an amorphous SiO_2 surface. In the case of the HMDS treated silicon surface, the water contact angle suggests the surface coverage with methyl groups is ~50% of (assuming complete surface coverage with methyl groups provides a water contact angle of ~65°).[8] This is not unreasonable, since typical surface coverages of HMDS on silicate surfaces is typically less than 50%.[31] In the case of the OTS-SAM coated surface, the high water contact angle and ellipsometry thickness measurements suggest the surface is completely covered with octadecyl chains. While some un-reacted hydroxyl groups may remain under the surface, we are unable to estimate their concentration.

The structure of adsorbed water on each of these surfaces is measured via ATR-IR. In the case of the silicon oxide surface covered with silanol groups. The structure of adsorbed water at room temperature as a function of relative humidity (RH) or surface coverage was discussed previously. In Figure **3.1** the adsorption of water at 10 °C on the silicon oxide surface is presented. Each line represents a different partial pressure relative to the saturation pressure of water (P^{sat}) at 10 °C. Essentially P/P^{sat} is equivalent to RH. Like in the room temperature experiments, at the lowest RH, the IR spectra is dominated by an adsorbed ice-like water structure with the dominate peak centered around ~3220cm^{-1}. As the RH increases the ice-like structured water increases much faster than the liquid structure (~3400 cm^{-1}). However, between 25% and 55% RH, the growth rate of the ice-like structure decreases as more liquid like structure begins to grow on top of the under laying adsorbed ice-like water structure. Around 70% RH, the spectra shows equal intensities of both the liquid water structure as well as the ice-like structure.

While the surface chemistry of the silicon oxide surface is responsible for the observed structuring of water, it appears that the structure is not as sensitive to temperature. The change in chemical potential of the gas phase adsorbate species can be estimated using an ideal gas behavior. This change relative to the chemical potential of the gas at the saturation condition is simply, $RT \cdot \ln[P/P^{sat}(T)]$ (where R is the ideal gas constant and T is the absolute temperature). Since the change in the temperature was only modest (283K vs. 298K), there is no measurable increase in the thickness of the adsorbed ice-like structure as compared with the room temperature data as long as

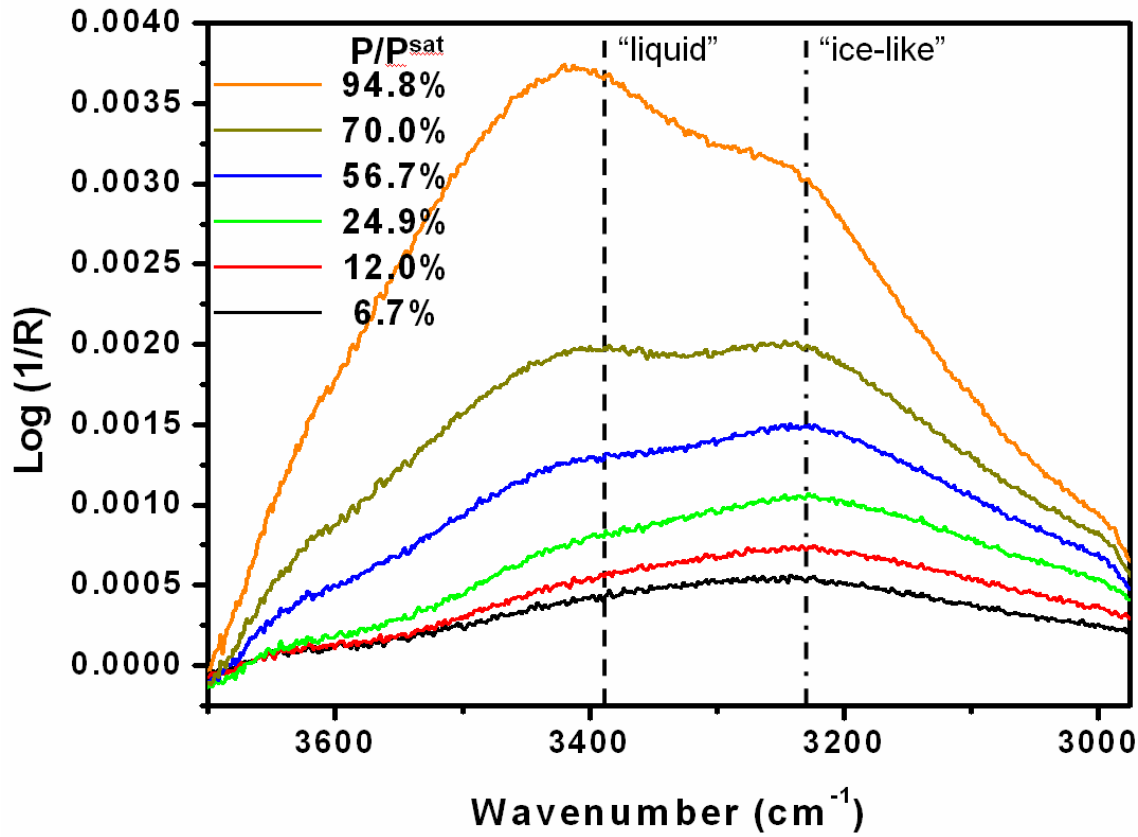

Figure **3.1**: ATR-IR spectra of adsorbed water at 10°C on Silicon Oxide Surface. The "ice-like" structured water and liquid water structure peak positions are represented by the dash-dot and dashed lines respectively. Each condition's partial pressure is related to the saturation pressure of water (P^{sat}) at 10°C .

$P/P^{sat}(T)$ is the same, since the difference in chemical potential at any given RH at either temperature is very small.

The ATR-IR adsorption spectra of water on the partially methylated surface is presented in Figure **3.2**. In this case, the only difference between Figure **3.1** and Figure **3.2** is the amount of hydroxyl and methyl groups at the outermost surface. The difference in total intensity between these two sets of data suggests that the amount of water adsorbed at P/P^{sat} near 95% on the partially methylated surface is approximately 1/2 to 1/3 that observed on the clean hydroxylated silicon oxide surface. This indicates that the average isotherm thickness is very sensitive with surface chemistry. Additionally, the structure of adsorbed water is very different on this surface. At the surface, there appear to be a larger percentage of adsorbed water molecules with dangling OH groups as evident in the relative magnitude of the free-OH region. Interestingly, at virtually all humidities, both the liquid structure and ice-like structure are observed to grow. Between the partial pressures of 0 and ~80% (P/P^{sat}), both liquid like water and ice-like water grow at the same rate, relative to one another. Only near saturation does the liquid structure start to grow more than the ice-like structure.

The observed growth of both ice-like and liquid water on the partially methylated surface over a much larger RH might be related to the inhomogeneity or incomplete methyl surface coverage. While the ice-like structure continues to grow at partial pressures much higher than those observed in the clean hydroxylated silicon oxide surface, its average thickness is much lower than the clean oxide surface case. In the HMDS-treated surface, not all surface hydroxyl groups react with HMDS yielding a surface with microscopic domains with varying hydrophilicity. Therefore, there may

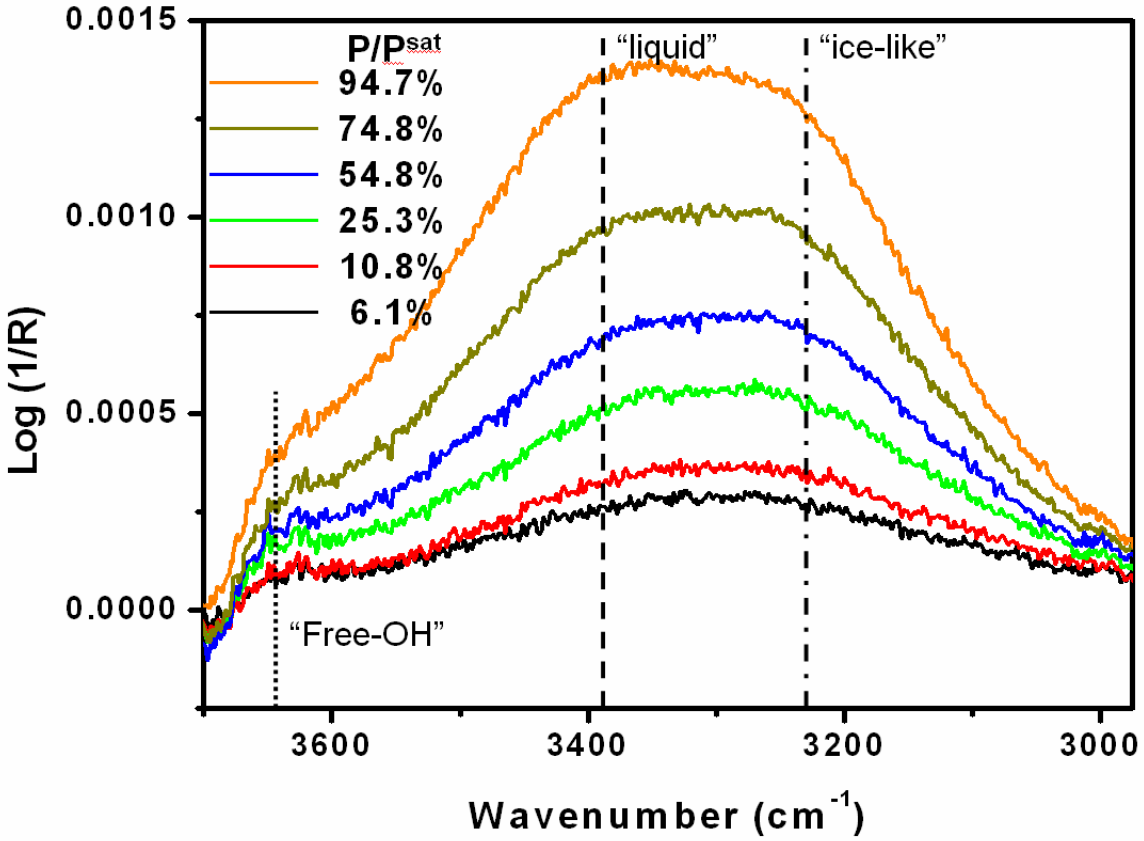

Figure **3.2**: ATR-IR spectra of adsorbed water at 10°C on Silicon Oxide Surface treated with HMDS. The "ice-like" structured water and liquid water structure peak positions are represented by the dash-dot and dashed lines respectively while the "free-OH" structure is illustrated with a dotted line. Each condition's partial pressure is related to the saturation pressure of water (P^{sat}) at 10°C.

exist regions with a varying film thickness. At this point, the thickness vs. surface chemistry of these domains is unknown. Due to this surface chemical morphology, some fraction of adsorbed water exist hydrogen bonded to un-reacted hydroxyl (Si-OH) groups while in close proximity to chemisorbed methyl groups where only weak dispersion forces are present.

Figure **3.3** shows the ATR-IR spectra for the OTS-SAM coated surface. On this surface, all the water detected in ATR-IR appears to have a high degree of hydrogen bonding and little to no liquid water structuring; nor are any dangling OH groups observed. Additionally, the amount of water that is adsorbed is very small. Considering the hydrophobicity of the highly-packed alkyl chain surface, it is speculated that the water peak observed for the OTS-SAM coated silicon oxide surface is not due to water adsorption on the OTS-SAM surface, but due to absorption into the SAM and direct interaction with the silicon oxide surface underneath the OTS layer. Recent molecular dynamic simulation studies have shown that water can absorb into the film at domain boundaries and/or defect sights and will damage (desorb) the OTS from the silicon surface, repopulating the surface with hydroxyl terminal chemistry.[36] Further spectroscopic evidence for water absorption into the oxide layer is observed by comparing water adsorption on gold thiol SAM surfaces. In these cases, water adsorption is not detected with methyl terminated long-chain thiols SAM surfaces as measured with x-ray photoelectron spectroscopy.

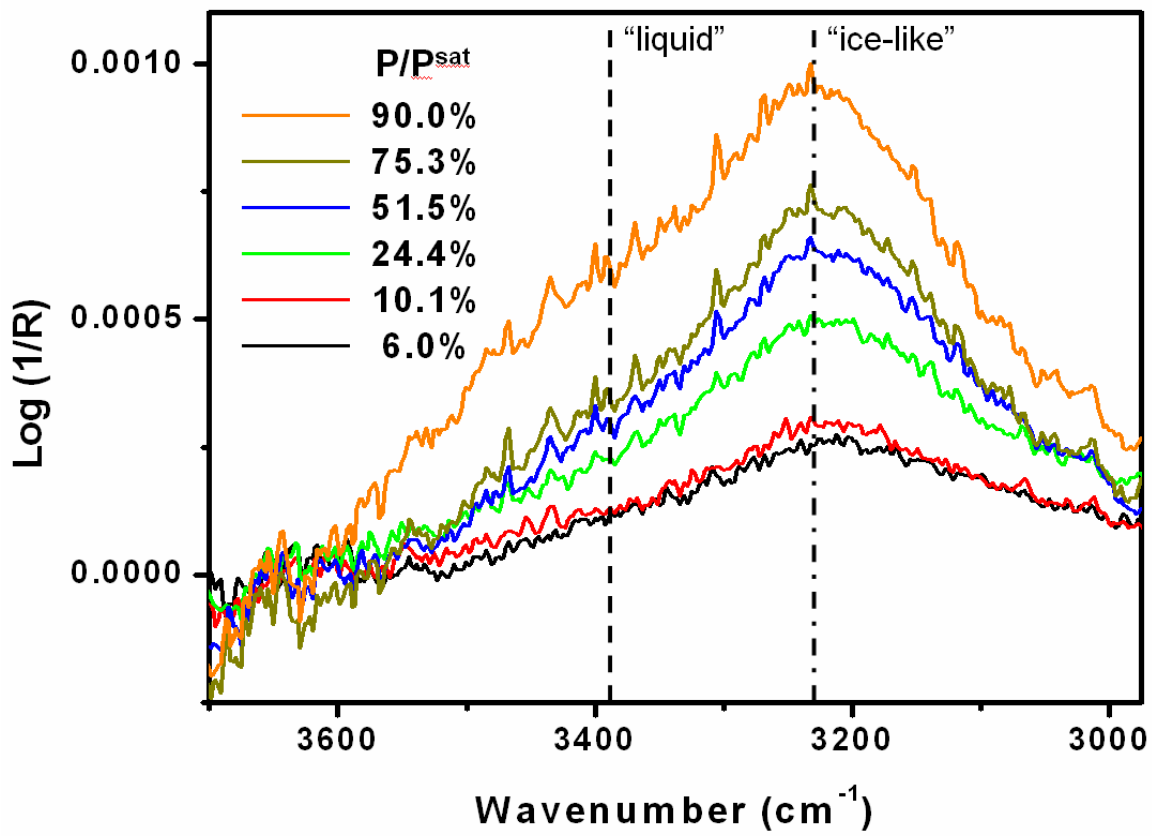

Figure **3.3**: ATR-IR spectra of adsorbed water at 10°C on Silicon Oxide Surface treated with OTS. The "ice-like" structured water and liquid water structure peak positions are represented by the dash-dot and dashed lines. Each condition's partial pressure is related to the saturation pressure of water (P^{sat}) at 10°C.

The adsorption isotherms for each of these systems are presented in Figure **3.4**. Each isotherm thickness is determined by integrating the area of the ATR-IR OH stretching vibration region at each condition. This area is then proportional to the amount of water molecules adsorbed in the system provided the adsorbate thickness is (1) much lower than the penetration depth of the IR evanescent field and (2) the IR absorption cross-section of both the liquid and ice-like structures are comparable to each other. Since the IR evanescent field penetration depth is a few hundred nm and the observed thicknesses are a few nm, the first assumption is valid. In order to check he validity of the second assumption, we have simulated the ATR-IR spetra of a 2 nm thick ice film and a 2 nm thick liquid film on a silicon surface using the optical constants of bulk ice and bulk liquid water. The difference between the integrated area under these simulated peaks is less than 10%. This suggests that the integrated area is not very sensitive to structural changes of water and can be used to determine the isotherm thickness. Based upon the total integrated intensity and the previous water adsorption at room temperature, a calibration factor relating the integrated intensity to the average thickness was determined. For a silicon ATR crystal having 11 reflections and an 45º incidence angle, the area of the log(1/R) from 3680 cm^{-1} to 2800 cm^{-1} was determined to be ~0.85 nm per unit area.

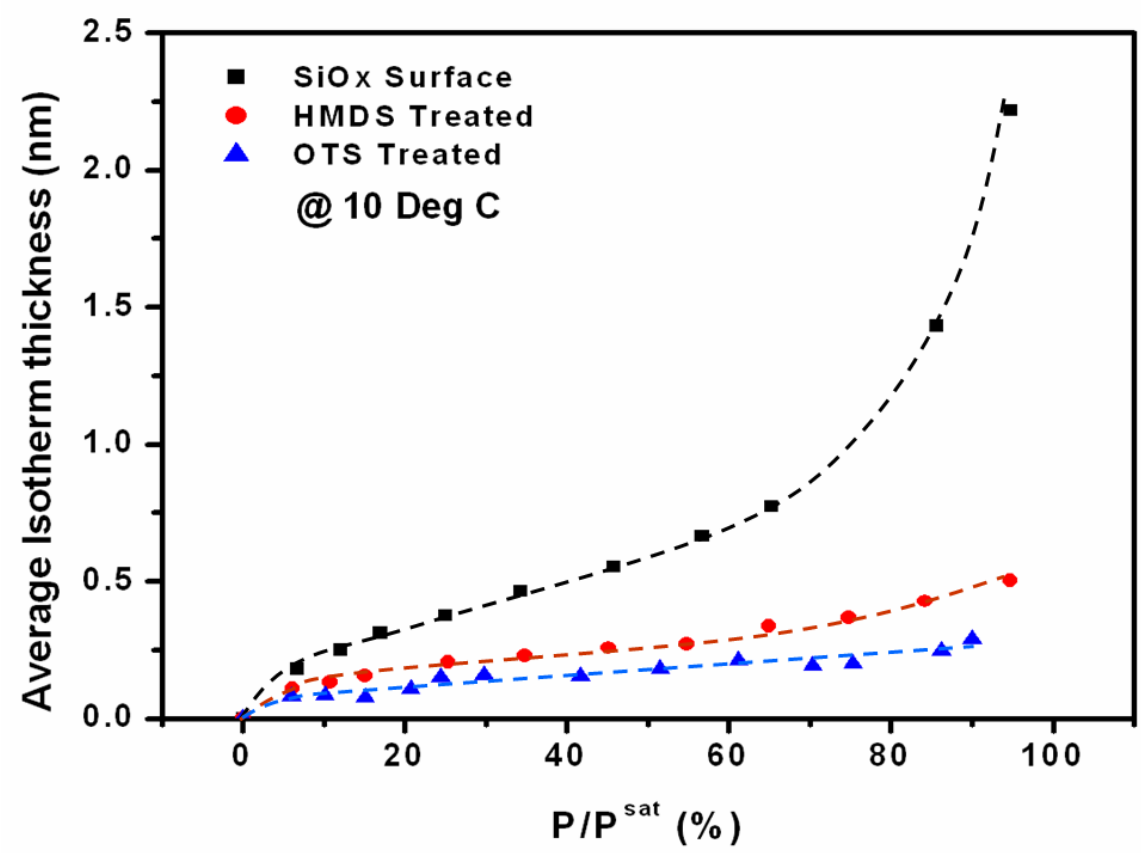

Figure **3.4**: Adsorption isotherms for clean hydroxylated silicon oxide surface, HMDS treated silicon oxide surface, and OTS treated silicon oxide surface. All data taken near 10 °C. Error bars are removed in order to simplify the figure. Typical x error bars are 3 to 4 (%) while the typical y-error bars are on the order of ~0.2 nm.

Immediately apparent in this figure is the large difference in isotherm thickness. As the surface becomes more hydrophobic, the propensity of water adsorption quickly decreases. Water uptake on each surface is significantly influenced by the surface chemistry of the interface. Water adsorption is greatly reduced when the surface is partially methylated, which also increases the water contact angle to ~45º from <5º for the clean hydroxylated surface.

Isotherms for both the clean silicon oxide surface as well the partially methylated surface were measured with this technique at three different temperatures. These temperatures were approximately 10, 22, and 35°C. From the temperature-dependence of the isotherms, the isosteric heat of adsorption and entropy of adsorption were determined using the Clausius-Clapeyron equation with ideal gas assumptions:

$$\ln(p) = -\frac{H^{ads}(X)}{R}\left(\frac{1}{T}\right) + const. \qquad \textbf{3-2}$$

where p is the pressure for a particular surface coverage X, and H^{ads} the isosteric heat of adsorption. By plotting ln(p) vs. 1/T for constant coverage, the isosteric heat of adsorption is determined. These results are presented in Figure **3.5**. The latent heat of evaporation or condensation of water is 44 kJ/mole. As the thickness increases, the RH increases. In each case, the measured isosteric heats of adsorption on each surface approach this value. What is interesting are the measured isosteric heats of adsorption at the low thicknesses (low RH). In both cases, the heat of adsorption is larger initially and then gradually decreases.

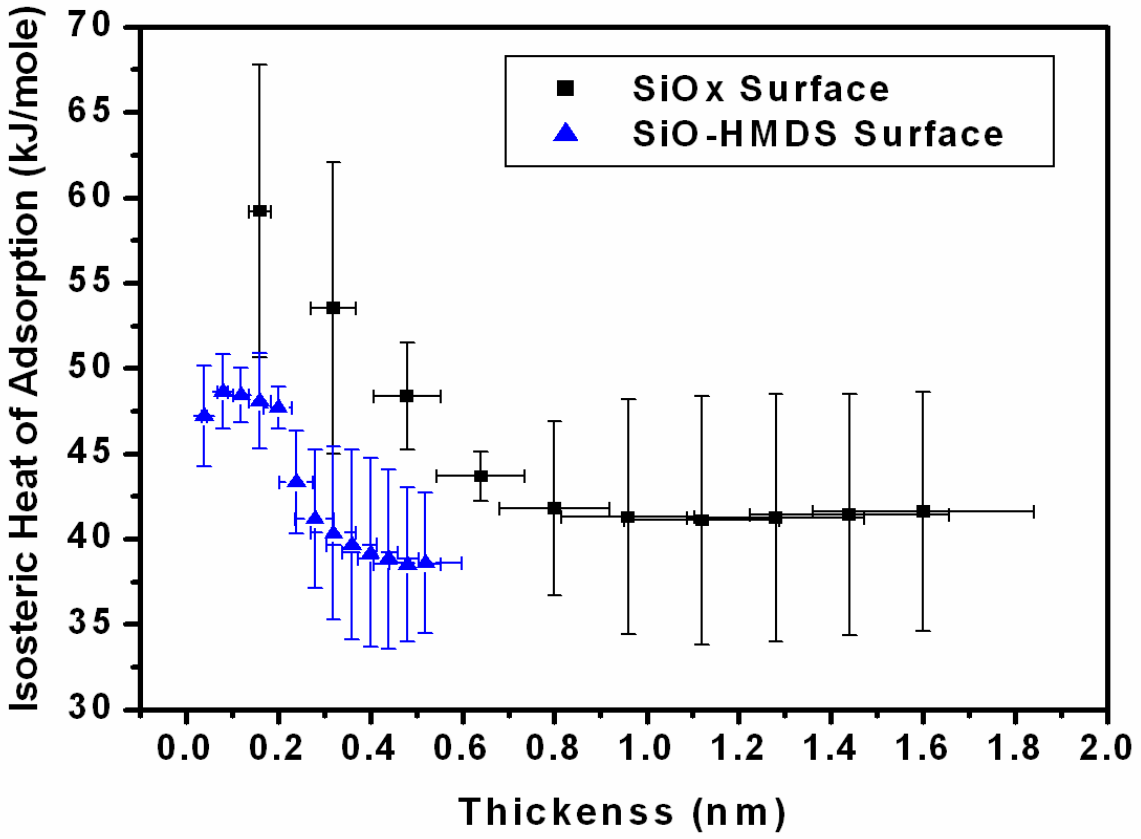

Figure **3.5**: Isosteric heat of adsorption of water on clean hydroxylated silicon oxide surface and HMDS treated silicon oxide surface.

Both surfaces uptake water as the RH increases. However, the amount of energy that is released upon adsorption is much larger for the more wettable surface. This is due to the high surface energy of dangling silanol groups as well as the observed increase in hydrogen bonding in these adsorbed layers. The energy of a hydrogen bond varies depending on temperature and its strength. In general, the energy of a hydrogen bond is approximately 4 – 12 kJ/mole. Since liquid water has 2 to 3 hydrogen bonds on average, the energy required to form 4 hydrogen bonds in ice-like layers is expected to be larger. The observed transition from a high isosteric heat of adsorption in the case of the clean silicon surface to a lower one corresponds well to the observed ice-like water structure growth and subsequent liquid water growth in the infrared spectra.

Based upon the isosteric heat of adsorption, the isosteric entropy of adsorption ,S^{ads} is also determined. In this case the thermodynamic expression for this is simply:

$$RT\ln\left(\frac{p}{P_{\inf}}\right) = H^{ads}(X) - H_{\inf} - \left[S^{ads}(X) - S_{\inf}\right]\cdot T \qquad \textbf{3-3}$$

where P_{inf} is the saturation pressure at T, H_{inf} the isosteric heat of adsorption measured at T and P^{sat}, and S_{inf} the entropy of vaporization of bulk water 69.9 J/mole K. The measured isosteric entropy of adsorption is presented in Figure **3.6**. Because of the close relationship as described in equation **3-3**, this figure almost mirrors the isosteric heat of adsorption. As the heat of adsorption increases, more order exists due to increased hydrogen bonding and hence the low entropy.

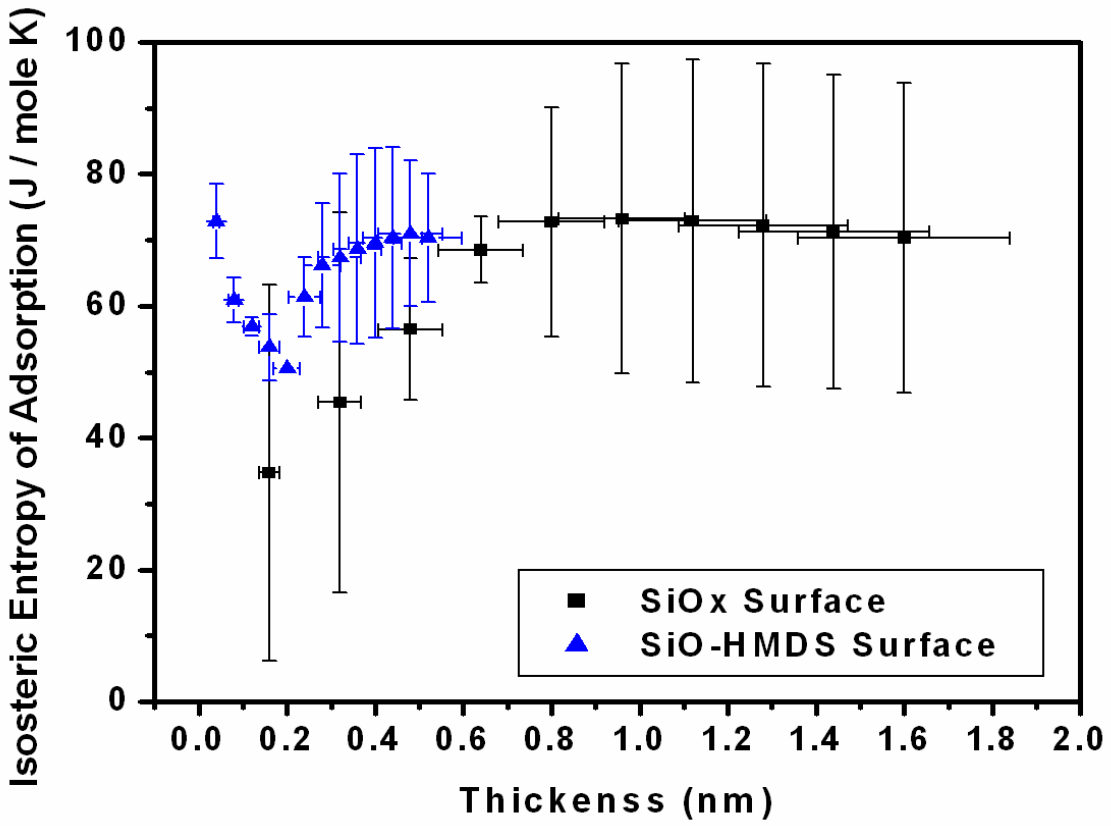

Figure **3.6**: Isosteric heat of adsorption of water on clean hydroxylated silicon oxide surface and HMDS treated silicon oxide surface.

3.5 Conclusions

Water adsorption on silicon oxide surfaces with differing surface chemistry and wettability was studied. These surfaces consisted of silicon oxide SiO_2 surface saturated with surface hydroxyl (silanol) groups, partially methylated surface, and OTS-SAM coated surface. These surfaces provided water contact angles of <5°, 45 ±5°, and 95 ±5° respectively. The amount of water molecules observed in an ice-like structure as observed in IR spectra was largest for the most hydrophilic surface and decreased with increasing hydrophobicity. The ability for multi-layer water adsorption at low and moderate partial pressures depends greatly on the concentration of available silanol groups at the surface. When the surface becomes partially hydrophobic via methylation treatment, multilayer adsorption is greatly hindered. Due to water structuring at the interface, the isosteric heat of adsorption of water is very large for the initial surface coverages. In the case of clean silicon oxide, the large heat of adsorption is observed in layers up to ~0.8 nm thick RH~60%. In the case of the OTS-SAM coated silicon oxide surface, a very small amount of solid-like water structure was observed. This water seemed to be due to absorption underneath the OTS SAM, rather than adsorption on top of the SAM surface.

3.6 References

1. A. W. Adamson; A. P. Gast, *Physical Chemistry of Surfaces, 6th Edition*. John Wiley & Sons: New York, 1997.
2. P. G. Degennes, *Reviews of Modern Physics* **1985,** 57, (3), 827-863.
3. M. A. Henderson, *Surface Science Reports* **2002,** 46, (1-8), 5-308.
4. J. Israelachvili, *Intermolecular & Surface Forces*. Academic Press: London, 1991.
5. W. Stumm; L. Sigg; B. Sulzberger, *Chemistry of the Solid-Water interface: Processes at the Mineral-Water and Particle-Water Interface in Natural Systems* Wiley: New York, 1992.
6. P. A. Thiel; T. E. Madey, *Surface Science Reports* **1987,** 7, (6-8), 211-385.
7. A. Verdaguer; G. M. Sacha; H. Bluhm; M. Salmeron, *Chemical Reviews* **2006,** 106, (4), 1478-1510.
8. E. A. Vogler, *Advances in Colloid and Interface Science* **1998,** 74, 69-117.
9. M. P. Goertz; J. E. Houston; X. Y. Zhu, *Langmuir* **2007,** 23, (10), 5491-5497.
10. R. C. Major; J. E. Houston; M. J. McGrath; J. I. Siepmann; X. Y. Zhu, *Physical Review Letters* **2006,** 96, (17), 4.
11. U. Raviv; J. Klein, *Science* **2002,** 297, (5586), 1540-1543.
12. U. Raviv; P. Laurat; J. Klein, *Nature* **2001,** 413, (6851), 51-54.
13. J. R. Zimmerman; J. A. Lasater, *Journal of Physical Chemistry* **1958,** 62, (10), 1157-1163.
14. H. A. Al-Abadleh; V. H. Grassian, *Langmuir* **2003,** 19, (2), 341-347.

15. D. B. Asay; S. H. Kim, *Journal of Physical Chemistry B* **2005,** 109, (35), 16760-16763.

16. W. Cantrell; G. E. Ewing, *Journal of Physical Chemistry B* **2001,** 105, (23), 5434-5439.

17. Q. Du; E. Freysz; Y. R. Shen, *Physical Review Letters* **1994,** 72, (2), 238-241.

18. G. E. Ewing, *Journal of Physical Chemistry B* **2004,** 108, (41), 15953-15961.

19. S. J. Peters; G. E. Ewing, *Journal of Physical Chemistry B* **1997,** 101, (50), 10880-10886.

20. R. Vlasak; I. Klueppel; G. Grundmeier, *Electrochimica Acta* **2007,** 52, (28), 8075-8080.

21. W. Chen; A. Y. Fadeev; M. C. Hsieh; D. Oner; J. Youngblood; T. J. McCarthy, *Langmuir* **1999,** 15, (10), 3395-3399.

22. A. Y. Fadeev; T. J. McCarthy, *Langmuir* **1999,** 15, (11), 3759-3766.

23. L. C. Gao; T. J. McCarthy, *Langmuir* **2006,** 22, (14), 6234-6237.

24. R. N. Lamb; D. N. Furlong, *Journal of the Chemical Society-Faraday Transactions I* **1982,** 78, 61-73.

25. J. J. Yang; S. Meng; L. F. Xu; E. G. Wang, *Physical Review B* **2005,** 71, (3).

26. T. A. Weber; F. H. Stillinger, *Journal of Physical Chemistry* **1983,** 87, (21), 4277-4281.

27. Q. Du; E. Freysz; Y. R. Shen, *Science* **1994,** 264, (5160), 826-828.

28. S. H. Kim; D. B. Asay; M. T. Dugger, *Nano Today* **2007,** 2, (5), 22-29.

29. D. B. Asay; M. T. Dugger; J. A. Ohlhausen; S. H. Kim, *Langmuir* **2008,** 24, (1), 155-159.

30. D. Beaglehole; H. K. Christenson, *Journal of Physical Chemistry* **1992,** 96, (8), 3395-3403.

31. V. M. Gun'ko; M. S. Vedamuthu; G. L. Henderson; J. P. Blitz, *Journal of Colloid and Interface Science* **2000,** 228, (1), 157-170.

32. M. R. Linford; P. Fenter; P. M. Eisenberger; C. E. D. Chidsey, *Journal of the American Chemical Society* **1995,** 117, (11), 3145-3155.

33. A. Y. Fadeev; T. J. McCarthy, *Langmuir* **2000,** 16, (18), 7268-7274.

34. V. M. Graubner; R. Jordan; O. Nuyken; B. Schnyder; T. Lippert; R. Kotz; A. Wokaun, *Macromolecules* **2004,** 37, (16), 5936-5943.

35. A. B. D. Cassie, *Discussions of the Faraday Society* **1948,** 3, 11-16.

36. J. M. D. Lane; M. Chandross; C. D. Lorenz; M. J. Stevens; G. S. Grest, *Langmuir* **2008,** 24, (11), 5734 - 5739.

Chapter 4

Effects of Adsorbed Water Layer Structure on Adhesion Force of Silicon Oxide Nanoasperity Contact in Humid Ambient

Reprinted with permission from D. B. Asay and S. H. Kim, J. Chem. Phys., ***124*** *(17) 174712, Copyright (2006), American Institute of Physics.*

4.1 Summary

The origin of the large relative-humidity (RH) dependence of the adhesion force in the single-asperity contact between silicon oxide surfaces is elucidated in this chapter. As relative humidity (RH) increases, the adhesion force measured with an atomic force microscopy (AFM) initially increases, reaches a maximum, and then decreases at high RH. The capillary force alone cannot explain the observed magnitude of the RH dependence. The origin of the large RH dependence is due to the presence of an ice-like structured water adsorbed at the silicon oxide surface at room temperature. A solid-adsorbate-solid model is developed calculating the contributions from capillary forces, van der Waals interactions, and the rupture of an ice-ice bridge at the center of the contact region. This model illustrates how the structure, thickness, and viscoelastic behavior of the adsorbed water layer influence the adhesion force of the silicon oxide nanoasperity contact.

4.2 Introduction

Water and other small volatile organic molecules have the propensity to adsorb onto solid substances with high surface energies and change interfacial properties.[1] The force of adhesion between nanoasperity contacts has been studied extensively with atomic force microscopy (AFM).[2] In the case of organic molecules, such as alcohols, the adhesive force of the silicon oxide nanoasperity contact decreases as alcohol adsorbs onto oxide surfaces.[3, 4] However, the effect of water adsorption on the singe-asperity adhesion force for hydrophilic surfaces such as silicon oxide or mica is quite different and complicated.[5-12] The observed trend shows the adhesion force as a function of humidity initially increases, reaches a maximum value, and then decreases.

This complicated humidity dependence has traditionally been attributed to changes in the capillary force due to condensation of water between two solid surfaces.[5-12] This explanation is valid for macroscopic contacts. However, theoretical capillary force calculations for the condensed liquid grossly underestimate the magnitude and shape of the humidity dependence observed experimentally for silicon oxide nanoasperity contacts.[11] In the nanoscopic phenomena, the molecular configuration of water in the adsorbed layer should be considered. The formation of "ice-like" structured water on solid surfaces has been observed experimentally and explained theoretically.[13-18] In addition, the molecular relaxation of the adsorbed water is much slower than that of bulk water.[19-21]

This chapter elucidates the effects of the molecular configuration and relaxation of the adsorbed water layer on the adhesive response of nanocontacts. AFM reveals the

non-linear behavior of the snap-off process. The structure and thickness of the adsorbed water layer were resolved from attenuated-total-reflection (ATR) infrared spectroscopy. A solid-adsorbate-solid model is developed to explain how these parameters influence the nanoasperity adhesion in humid environments.

4.3 Experimental Details

Adhesion forces were measured from force-distance (f-d) curves obtained with AFM. Silicon AFM tips were cleaned with UV/O_3 for 20 minutes immediately prior to use. The spring constant (k) of each cantilever, calibrated using the Sader method,[22] ranged from 0.605 to 1.09 N/m. The average tip curvature was ~15 ±5 nm. The tip curvature was estimated with a Nioprobe[23] substrate with one cantilever and, based on the adhesive force near 100% humidity, all the radius of curvature for all cantilevers were similar. Native oxides on silicon wafer substrates were cleaned by exposing to UV/O_3 followed by RCA-1 cleaning (Mixture of 5 parts water, 1 part 30% hydrogen peroxide, and 1 part 27% ammonium hydroxide maintained at 70 °C for 15 minutes), washing with Millipore water, and dried with argon. This process provided a water contact angle close to ~0^o. The AFM unit was placed in a home-built environmental chamber equipped with a hygrometer. The partial pressure of water vapor (relative humidity, RH) in the chamber was controlled by varying the ratio of water-saturated argon feed stream and dry argon stream. The calculated humidity from the flowrates and the measured humidity agreed within 3% of each other. For all experiments the temperature was maintained at 22 ± 0.5 °C. F-d curves were obtained after the chamber was fully equilibrated at a set humidity.

The adhesion force was determined from the f-d curve based upon the maximum deflection in the attractive region to the free standing position. The thickness and structure of the adsorbed water layer were determined with ATR-IR spectroscopy. Details of ATR-IR experiment are described in chapter **2.3**. A clean native oxide surface of a Si ATR crystal was as a model substrate. The same experimental flow system and humidity control used in the AFM experiments were also used in the ATR-IR experiments, minimizing uncertainties in RH between these two experiments.

4.4 Results and Discussion

The adhesion force as a function of RH is plotted in Figure **4.1**. Six separate experiments with at least 5 separate f-d curves were taken at each RH. The variation in adhesive force at 90% RH between different tips is within 20% suggesting that the variation in tip curvature between tips is minimal. On average, the adhesion force increases from 40 nN to 105 nN, becomes relatively constant, and then decreases from 100 nN to 20nN. The retraction f-d curves at different RH are also shown in the inset. At RH 10%, the slope of the f-d curve upon retraction does not change over the entire attractive region. At RH 70%, the f-d curve slope slightly deviates upward as the cantilever is pulled toward the snap-off position. At RH 90%, a sudden change in the f-d curve slope at ~20 nm indicates that the AFM tip is separated from the substrate surface when the force is -20 nN. It then pulls through the adsorbed water layer until it snaps off. Changes in the f-d curve slope before snap-off indicate transitions in the tip-surface snap-off dynamics as RH increases.

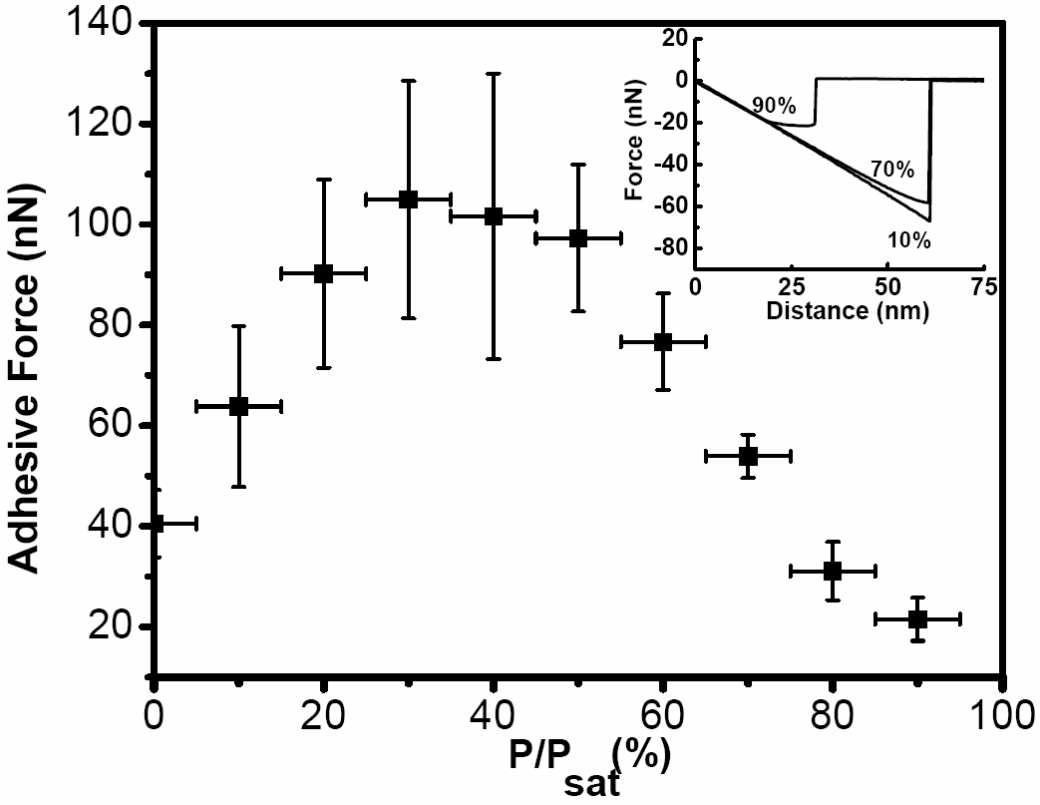

Figure **4.1**: Nanoasperity adhesion force as a function of relative humidity. Experimental data error bars represent 80% confidence interval. Inset shows the f-d curves at 10%, 70%, and 90%.

The thickness and structure of the adsorbed water layer is shown in Figure **4.2**. The thickness calculated from H-O-H bending vibration intensities reveals typical curvature of type II adsorption isotherm – initial convex growth between RH of 0 and 30%, linear growth between RH of 30 and 60%, and exponential growth above RH of ~60%.[13] The structure of the adsorbed water layers in these three different RH regions is determined from the O-H stretching vibration peak positions.[24] At RH < 30%, there is only one peak at 3230 cm^{-1} corresponding to a completely hydrogen bonded ice-like structure. In the RH 30 ~ 60% region, the 3400 cm^{-1} peak starts growing in addition to the 3230 cm^{-1} peak. This indicates the growth of liquid water structure on top of the ice-like structure. At RH > 60%, the liquid water peak at 3400 cm^{-1} dominates. These results clearly show that the thickness of the adsorbed water layer as well as the molecular configuration in the adsorbed layer change with RH. These parameters significantly influence interfacial properties in nanoasperity systems.

First, the surface energy of the adsorbed water layer will vary as a function of RH. The surface energy of pure liquid water at room temperature is ~72.8 erg/cm^2.[25] Based on Fowkes theory, the van der Waals component of the surface tension for water is estimated to be ~22 erg/cm^2.[26] The remaining ~50.8 erg/cm^2 is attributed to the hydrogen bonds in liquid water. In the case of liquid water, the average amount of hydrogen bonds per water molecule is estimated to be ~2.5.[27] By first-order approximation, the surface energy contribution per hydrogen bond is expected to be ~20.3 erg/cm^2. Since the number of hydrogen bonds per molecule in the ice-like structure is 4, the surface energy of ice-like water will be ~103.3 erg/cm^2.[18,28] This estimate is quite close to the value

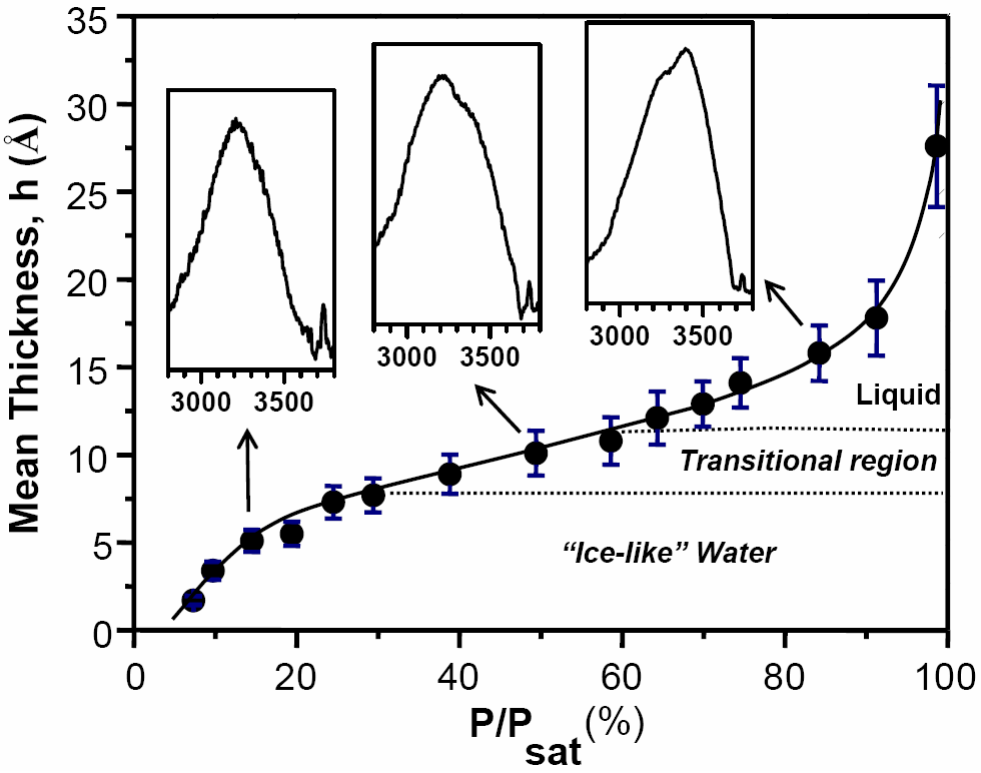

Figure **4.2**: Thickness of the adsorbed water layer as a function of relative humidity. ATR-IR spectra of OH stretching vibration are shown for 15%, 50%, and 84% . The x-axis of the inset is wavenumber (cm^{-1}) and the y-axis is –log(reflectance).

calculated from surface force apparatus measurements.[16] Therefore, the use of bulk water surface tension will underestimate the interfacial tension at low RH.

Secondly, the relaxation time of water molecules at an interface will deviate from that of bulk water and the extent of deviation will vary with RH.[19-21,29] The relaxation time of adsorbed water is important because the AFM tip is snapped off to the free standing position from the adsorbed water layer, not directly from the solid substrate surface. This view is supported from Monte Carlo simulations on meniscus stability at the nanoasperity contact.[30] On OH-terminated metal oxide surfaces, the relaxation time of the water in the first few monolayers is estimated to be on the order of 10^{-4} sec at room temperature, six to eight orders of magnitude slower than that of bulk water.[31, 32] A simple harmonic resonator model predicts that it takes ~1 μsec for the AFM tip to move 1 nm upon release from the surface. Therefore, the Deborah number (N_{DE} = relaxation time/probe time) in the low RH region is larger than 1, suggesting the adsorbed water behaves mostly elastically. As RH increases, the liquid structure grows thicker and the relaxation time of the water molecules in the outer layer approaches the bulk value. This will eventually make the snap-off process viscoelastic ($N_{DE} < 1$) at high RH.[33] This explains the changes of the f-d curve slope just prior to the snap-off as RH increases (Figure **4.1** inset).

From the experimental data, it is clear that (a) both tip and substrate surfaces are covered with an adsorbed water layer with the same thickness and structure and (b) the tip is released from the adsorbed water layer, not from the solid surface. Therefore, the conditions just before the snap-off process must be modeled with *a solid-adsorbate-solid contact system with the adsorbate layer being in equilibrium with the gas phase*. The

Johnson-Kendall-Roberts (JKR) and Derjaguin-Muller-Toporov (DMT) models are used to describe adhesion and elastic contact deformation.[34, 35] However, conventional JKR or DMT theories for solid-solid contacts do not consider the phase equilibrium. It should also be noted that the capillary force equation for sphere-plate geometry, $F_{capillary} \approx 4\pi R\gamma_{LV}\cos\theta$ (θ = the contact angle of *bulk* water on the substrate and γ_{LV} = the interfacial surface tension at the liquid vapor interface), cannot be used. This equation is an approximation with the assumption that the meniscus radius (r) is negligible compared to the contact area radius (R_A) which is in turn negligible compared to the tip radius (R).[1] However, these assumptions are not appropriate for small spheres such as AFM tips with R ~ 15 nm.[7, 11, 12] For clean silicon oxide surface, the contact angle is almost zero, giving rise to $\cos\theta \approx 1$ and $F_{capillary} \approx 4\pi R\gamma_{SL}$, which does not have give any RH dependence.

The details of the solid-adsorbate-solid contacts immediately before the snap-off for different RH regions are summarized in Figure **4.3** for three different RH regimes. At low RH, the tip is separated from the ice-like water. Between RH of 30 and 60%, both ice-like and liquid water structures coexist in the outmost layer. In this RH region only one layer of water grows. For simplicity we take the midpoint (9.4 Å at 45%) to be the maximum ice-like structure thickness. Above RH 45%, the contact just before snap-off is composed of two parts: ice-ice contact at the center and liquid-liquid annular contact. As the RH increases, the contact area of the central ice-ice bridge region at the snap-off moment decreases and eventually becomes zero near the saturation humidity. The ice contact area (A_{ice}) is a function of the ice thickness (h_{ice}), the total adsorbed water layer

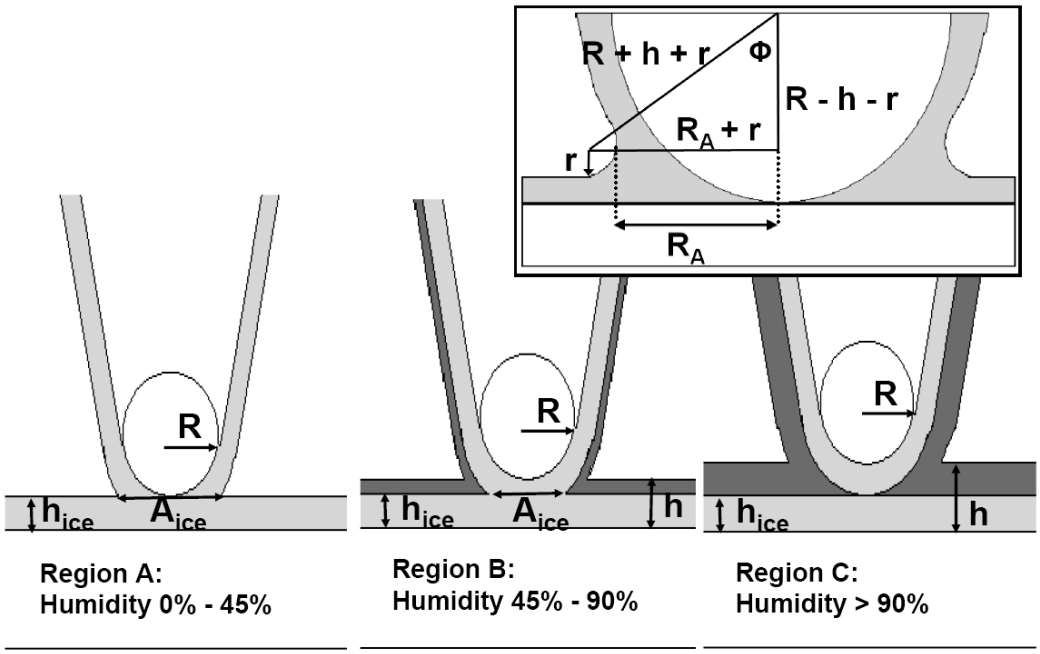

Figure **4.3**: Schematics of the AFM tip position and ice-ice contact area as a function of relative humidity immediately prior to snap off. The inset illustrates the two curvatures (r and R_A) that contribute to the Laplace pressure. The tip is in contact in order to predict the maximum capillary force (y=1 case).

thickness (h), and the relative position of the bottom of the tip with respect to the total layer thickness *y*h. Figure **4.3** shows the $y = 1$ case. If $y = 0$, the tip is snapped off directly from the substrate surface. If $y > 1$, the adsorbed layer is pulled up by the tip before the tip is snapped off. The $y > 1$ case is expected in the high RH region where the liquid water structure dominates the outer region of the adsorbed layer. In the following calculations, we estimate the surface tension of the outmost water layer ($\gamma_{surface}$) to 103.3 erg/cm^2 for RH < 30%, 72.8 erg/cm^2 for RH > 60%, and a linear transition from 103.3 to 72.8 erg/cm^2 for the RH 30 ~ 60 % region. This simple first-order approximation appears to be good enough to predict the measured adhesion force within experimental error ranges, as described below.

First, consider the van der Waals force term (F_{VDW}) assuming that the adsorbed layer behaves like a non-deformable boundary. This term can be expressed with the following approximation for a sphere of radius R on a flat surface in vapour:[1]

$$F_{VDW} = n\pi R\gamma_{surface} \qquad \textbf{4-1}$$

In the Derjaguin approximation, n = 4. The JKR model (n = 3) could also be used to estimate the van der Waals force term. However, the overall contribution of F_{VDW} to the total adhesion force is small; so the choice of model for the van der Waals force term does not have a significant effect.

Second, consider the capillary force due to the Laplace pressure that arises as water forms a meniscus between the AFM tip (sphere, radius = R) and the flat substrate (Figure 3 insert). The humidity dependence of the Laplace pressure due to the condensed molecules can be described with the Kelvin equation:[36]

$$P_{Laplace} = \gamma\left(\frac{1}{R_A} + \frac{1}{r}\right) = \frac{R_g T}{V}\ln\left(\frac{P}{P_{sat}}\right) \qquad \textbf{4-2}$$

where R_A is the inner radius of the capillary neck, r the meniscus radius, V the molar volume of water, R_g the ideal gas constant, T the temperature, P the partial pressure of water, and P_{sat} the saturated partial pressure of water. Based on the isotherm and the geometry of the sphere-plate system, the inner radius of the capillary neck is $R_A = 2\left(R \cdot r + R \cdot h\right)^{1/2} - r$. Using this expression, the isotherm, and Eq. **4-2**, r and R_A can be determined for different RH. The Laplace pressure acting over the capillary neck area ($A = \pi R_A^2$) is:

$$F_{capillary} = -P_{Laplace} \cdot A = -\frac{R_g T}{V}\ln\left(\frac{P}{P_{sat}}\right) \times \pi R_A^{\,2} \qquad \textbf{4-3}$$

The calculated capillary contribution as a function of RH is plotted in Figure **4.4** with a dotted line. In this calculation, the maximum possible R_A value (when $y = 0$) is used to estimate the upper limit of $F_{capillary}$. The general trend of the capillary force term calculated using Eq. **4-3** is similar to the one reported in ref. 11 for a spherical tip shape. The maximum $F_{capillary}$ for a tip with R = 15 nm is ~30 nN at RH ≈ 25%, which deviates significantly from the experimentally observed value, ~80 nN at RH = 30 ~ 40%.

The sum of F_{VDW} and $F_{capillary}$ is illustrated in Figure **4.4** with a dashed line. The exact value of the silicon oxide surface energy is not known; but it is expected to be higher than 103 erg/cm^2. For this reason, the model works for RH > 5%. At RH > 90%, the $F_{capillary}$ + F_{VWD} term agrees well with the experimental values. This indicates that liquid water properties dominate the adhesion behavior at very high RH. The predicted

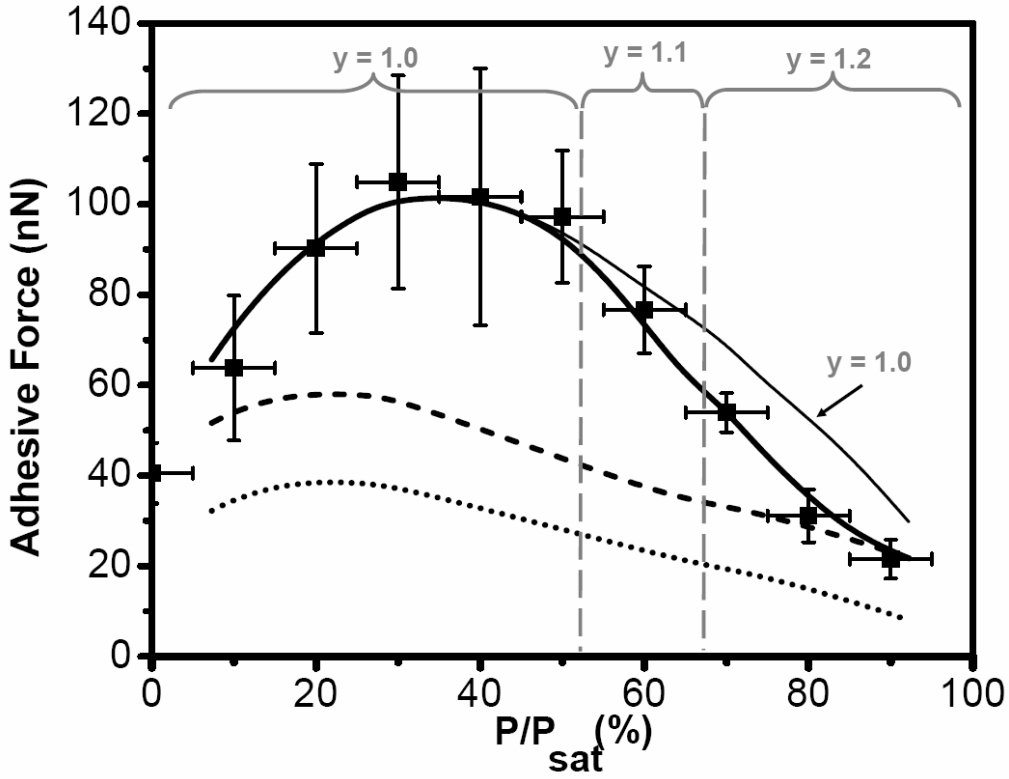

Figure **4.4**: Simulation of the contributions from capillary force term ($F_{capillary}$), van der Waals term (F_{VDW}), and the ice-ice bridge term (F_{ice}). The bottom dotted line represents the maximum $F_{capillary}$. The middle dashed line represents $F_{VDW} + F_{capillary}$. The solid lines represent the sum of three components, $F_{ice} + F_{VDW} + F_{capillary}$. The thin solid line is the simulation result with y = 1.0 fixed. The thick solid line is the result with the fitted y values to reproduce the experimental data. The fitted *y* values are marked in the graph.

magnitude of the RH dependence significantly underestimates the experimental results between RH 10% and 80%. This underestimation originates from ignoring the RH dependence of the ice-ice bridge at the center of the nanoasperity contact. The cross-section area of the ice-ice bridge, illustrated in Figure **4.3**, is not taken into account in Equations **4-2** and **4-3**. As RH increases from 0%, the ice-ice contact area increases. As the thickness of the liquid structure increases at higher RH, the ice-ice contact area decreases, giving rise to the observed RH dependence.

The force required for spontaneous rupture of the ice-ice area is approximated from the following analysis: $F_{ice} = dW/dz$ where $dW = 2\gamma_{ice} dA_{ice}$. Here A_{ice} is the ice-ice contact area when the bottom of the tip is at the position z (= *y*h) above the substrate. Since the AFM tip snaps off instantly at the critical force, dA_{ice} can be assumed to be A_{ice} at the snap-off position, z [$dA_{ice}(z) = A_{ice}(z) - 0$]. From a geometric analysis, A_{ice} at z = h (where $y = 1$) is expressed by:

$$A_{ice}(h) = \pi(h + 2R)(2h_{ice} - h) \qquad \textbf{4-4}$$

When RH < 45%, $h_{ice} = h$. For RH > 45%, h_{ice} is fixed at 9.4 Å. In this equation, y is set to unity for simplicity in mathematical expression. Based on theoretical simulations of spontaneous cleavages,[37] the critical distance over which the ice-ice contact ruptures (*dz*) is taken to be the equilibrium distance between water molecules: $dz \approx 2^{1/6}\sigma$ with σ = 3.15 Å, the Lennard-Jones parameter.[38] The final expression for F_{ice} as a function of h is written as:

$$F_{ice}(h) = \frac{2\pi\gamma_{ice}(h+2R)(2h_{ice}-h)}{2^{1/6}\sigma} \qquad \textbf{4-5}$$

The sum of $F_{capillary}$, F_{VDW}, and F_{ice} for $y = 1$ is plotted in Figure **4.4** as a thin solid line. The theoretical prediction based on our model accurately reproduces the shape and magnitude of the experimental RH dependence of adhesion. The simulation with $y = 1$ appears to predict slightly higher values at RH > 70%. This is due to the oversimplification of fixing h_{ice} to the h value at RH 45% and ignoring the RH dependence of *y*. As shown in the inset of Figure **4.1** , as RH increases, the tip is snapped to the free standing position farther away from the surface. When *y* is allowed to increase with RH, the model fits the experimental data within the experimental error range (the thick solid line in Figure **4.4**). This shows that our simple model captures the essence of the nano-asperity contact in humid ambient. The y value is related to the viscoelastic behavior of the adsorbed layer as RH increases. In order to estimate the *y* value accurately, mass transport terms such as viscosities of adsorbed layers should be considered. However, these values are not readily available.

The experimental data at low humidity (RH < 50%) scatters with large error bars, compared to the data at high humidity. This trend has also been observed by other groups.[7, 12] This can be attributed to inhomogeneity of the ice layer thickness. Scanning polarization force microscopy observed ice-like islands.[12] If there is any inhomogeneity in the ice-like island thickness, the adhesion force measurement is strongly dependent on where the tip makes contact with the substrate. As RH increases, liquid water dominates the adhesive behavior reducing any inhomogeneities in the ice-like layers.

4.5 Conclusions

In summary, the RH dependence of the nanoasperity adhesion force is explained with the presence of ice-like structure in the adsorbed water layer on clean silicon oxide surfaces at room temperature. The Laplace pressure alone originating from capillary necking between the tip and the substrate cannot explain the curvature and magnitude of the RH dependence. In the RH range between 10% and 90%, the adsorbed layer thickness dependence of the ice-ice bridge area must be taken into account. This ice-ice rupture term dominates the magnitude and shape dependence of the adhesion force of the nanoasperity contact in this intermediate RH region.

4.6 References

1. J. Israelachvili, *Intermolecular & Surface Forces*. Academic Press: London, 1991.
2. B. Cappella; G. Dietler, *Surface Science Reports* **1999,** 34, (1-3), 1-+.
3. D. B. Asay; S. H. Kim, *Langmuir* **2007,** 23, (24), 12174-12178.
4. K. Strawhecker; D. B. Asay; J. McKinney; S. H. Kim, *Tribology Letters* **2005,** 19, (1), 17-21.
5. B. Bhushan; C. Dandavate, *Journal of Applied Physics* **2000,** 87, (3), 1201-1210.
6. M. Binggeli; C. M. Mate, *Applied Physics Letters* **1994,** 65, (4), 415-417.
7. M. Y. He; A. S. Blum; D. E. Aston; C. Buenviaje; R. M. Overney; R. Luginbuhl, *Journal of Chemical Physics* **2001,** 114, (3), 1355-1360.
8. R. Jones; H. M. Pollock; J. A. S. Cleaver; C. S. Hodges, *Langmuir* **2002,** 18, (21), 8045-8055.
9. D. L. Sedin; K. L. Rowlen, *Analytical Chemistry* **2000,** 72, (10), 2183-2189.
10. G. Vigil; Z. H. Xu; S. Steinberg; J. Israelachvili, *Journal of Colloid and Interface Science* **1994,** 165, (2), 367-385.
11. X. D. Xiao; L. M. Qian, *Langmuir* **2000,** 16, (21), 8153-8158.
12. L. Xu; A. Lio; J. Hu; D. F. Ogletree; M. Salmeron, *Journal of Physical Chemistry B* **1998,** 102, (3), 540-548.
13. D. B. Asay; S. H. Kim, *Journal of Physical Chemistry B* **2005,** 109, (35), 16760-16763.
14. Q. Du; E. Freysz; Y. R. Shen, *Physical Review Letters* **1994,** 72, (2), 238-241.

15. J. Hu; X. D. Xiao; D. F. Ogletree; M. Salmeron, *Science* **1995,** 268, (5208), 267-269.

16. J. N. Israelachvili; P. M. McGuiggan, *Science* **1988,** 241, (4867), 795-800.

17. M. Odelius; M. Bernasconi; M. Parrinello, *Physical Review Letters* **1997,** 78, (14), 2855-2858.

18. J. J. Yang; S. Meng; L. F. Xu; E. G. Wang, *Physical Review B* **2005,** 71, (3).

19. M. C. Bellissent-Funel, *European Physical Journal E* **2003,** 12, (1), 83-92.

20. A. Dhinojwala; S. Granick, *Journal of the American Chemical Society* **1997,** 119, (1), 241-242.

21. C. F. Polnaszek; D. A. Hanggi; P. W. Carr; R. G. Bryant, *Analytica Chimica Acta* **1987,** 194, 311-315.

22. J. E. Sader; J. W. M. Chon; P. Mulvaney, *Review of Scientific Instruments* **1999,** 70, (10), 3967-3969.

23. www.aurorand.com

24. G. E. Ewing, *Journal of Physical Chemistry B* **2004,** 108, (41), 15953-15961.

25. A. W. Adamson; A. P. Gast, *Physical Chemistry of Surfaces, 6th Edition*. John Wiley & Sons: New York, 1997.

26. F. M. Fowkes, *Journal of Physical Chemistry* **1963,** 67, (12), 2538-&.

27. T. A. Weber; F. H. Stillinger, *Journal of Physical Chemistry* **1983,** 87, (21), 4277-4281.

28. J. M. Douillard; M. Henry, *Journal of Colloid and Interface Science* **2003,** 263, (2), 554-561.

29. A. J. Benesi; M. W. Grutzeck; B. O'Hare; J. W. Phair, *Journal of Physical Chemistry B* **2004,** 108, (46), 17783-17790.

30. J. Y. Jang; G. C. Schatz; M. A. Ratner, *Physical Review Letters* **2004,** 92, (8).

31. Y. Kuroda; S. Kittaka; S. Takahara; T. Yamaguchi; M. C. Bellissent-Funel, *Journal of Physical Chemistry B* **1999,** 103, (50), 11064-11073.

32. J. Teixeira; M. C. Bellissentfunel; S. H. Chen; A. J. Dianoux, *Physical Review A* **1985,** 31, (3), 1913-1917.

33. J. P. Rothstein; G. H. McKinley, *Journal of Rheology* **2002,** 46, (6), 1419-1443.

34. B. V. Derjaguin; V. M. Muller; Y. P. Toporov, *Journal of Colloid and Interface Science* **1975,** 53, (2), 314-326.

35. K. L. Johnson; K. Kendall; A. D. Roberts, *Proceedings of the Royal Society of London Series a-Mathematical and Physical Sciences* **1971,** 324, (1558), 301-&.

36. W. Thomson, *Philos. Mag.* **1871,** 42, 448-452.

37. J. B. Pethica; A. P. Sutton, *Journal of Vacuum Science & Technology a-Vacuum Surfaces and Films* **1988,** 6, (4), 2490-2494.

38. M. W. Mahoney; W. L. Jorgensen, *Journal of Chemical Physics* **2000,** 112, (20), 8910-8922.

Chapter 5

Molar Volume and Adsorption Isotherm Dependence of Capillary Forces in Nano-asperity Contacts

5.1 Summary

The magnitude of the capillary force at any given temperature and adsorbate partial pressure depends primarily on four factors: the surface tension of the adsorbate, its liquid molar volume, its isothermal behavior, and the contact geometry. At large contacting radii, the adsorbate surface tension and the contact geometry are dominating. This is the case of surface force apparatus measurements and atomic force microscopy (AFM) experiments with micron-size spheres. However, as the size of contacting asperities decreases to the nano-scale as in AFM experiments with sharp tips, the molar volume and isotherm of the adsorbate become very important to capillary formation as well as capillary adhesion. This effect is experimentally and theoretically explored with simple alcohol molecules (ethanol, 1-butanol, and 1-pentanol) which have comparable surface tensions but differing liquid molar volumes. Adsorption isotherms for these alcohols on silicon oxide are also reported in this chapter.

5.2 Introduction

Adhesion is a consequence of long range van der Waals attractive forces, dipole moments, electrostatic repulsion/attractions, and where condensed liquid films are present, capillary forces between surfaces. As the size of contacts shrink, i.e. microelectromechanical systems (MEMS) and colloids, surface forces like adhesion dominate their tribological behavior and operation or use.[1-3] In environments where adsorbed liquid films are on the surface, the capillary force between contacting asperities is often the dominant factor governing the adhesion behavior. The effect of these adsorbed liquid films on the adhesion becomes significant at the nano-scale since the thickness of these films is in the nano-scale. The AFM is an ideal tool for investigating single asperity contacts at the nanoscale; adhesion for a single asperity between surfaces of varying chemistry and environments can be probed.[4]

In previous literature, various approximations are utilized to predict the capillary force in AFM pull-off force (adhesion) measurements.[5-14] In some situations, the contact angle of the bulk liquid on solid surface (θ) and the surface tension of the liquid (γ) are the only variables other than the size of the contact (R). In this case, the capillary force is described as $F_{cap} = 4\pi R\gamma\cos(\theta)$.[15] The derivation of this expression is for systems where the radius of the meniscus (r_2 in Figure **5.1**) is insignificant compared to R. As R decreases as in AFM experiments with sharp tips, the assumptions used to yield this expression are no longer valid.[10, 16] Many AFM measurements showed that the capillary force for small contacts is a function of the relative partial pressure of the surrounding

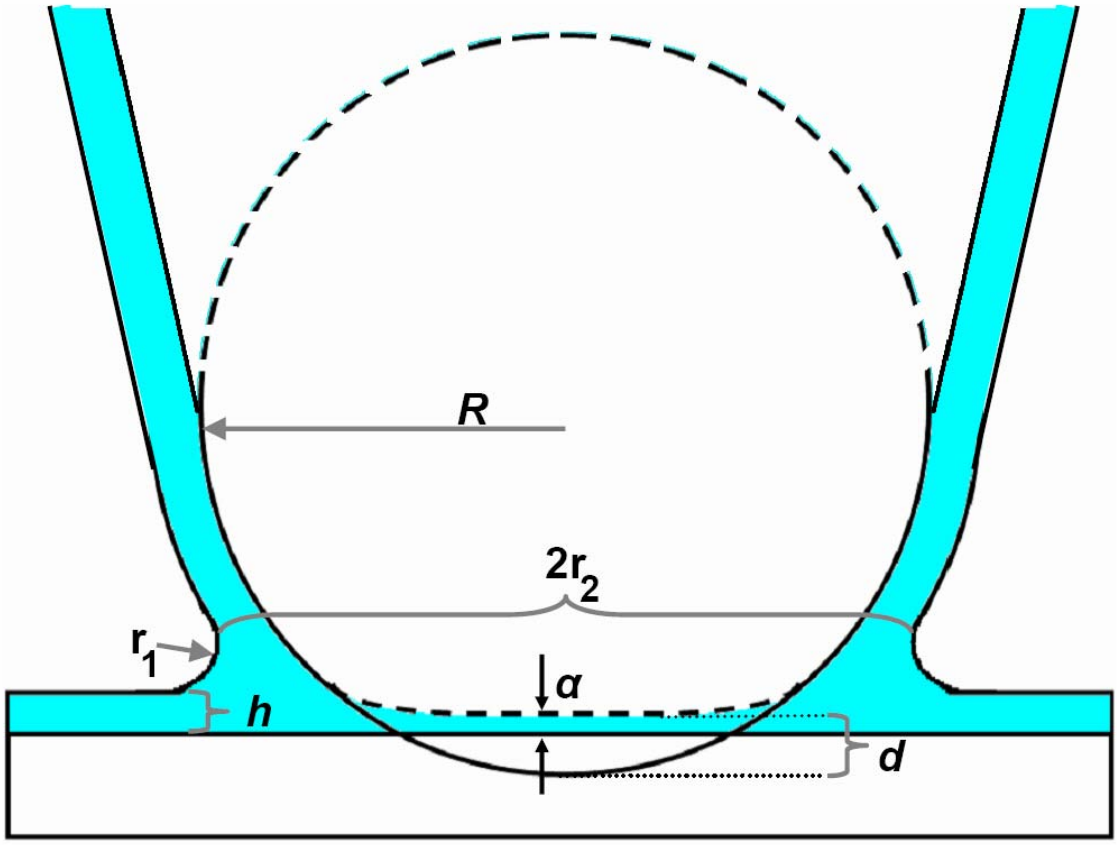

Figure **5.1**: Model tip (sphere) – substrate system with adsorbed film whose thickness is *h*. Here *R* is the tip radius, α a trapped molecular layer, *d* the penetration depth of the undeformed sphere, and r_1 and r_2 the two principle radii of curvature.

vapor (such as water in humid air), which is not captured in this approximation.[5-8, 10-14] These papers have shown that $F_{cap} = 4\pi R\gamma\cos(\theta)$ is a poor approximation of the capillary force for nano-asperity contacts. Additionally, θ is determined from a macroscopic measurement. The validity of using θ for estimating the wettability of contacting asperities that are several orders of magnitude smaller than the measurement of θ has yet to be verified.

In this chapter, the adsorption isotherm and single-asperity capillary force measurements are reported for ethanol, 1-butanol, and 1-pentanol on clean silicon oxide surfaces. These alcohols have comparable surface tensions (~15% difference between alcohols) but differing liquid molar volumes (up to a factor of 2 differences). Previously, the effect of the molar volume of adsorbates on the capillary force between small contacts has not been explored. The capillary force contribution in the AFM pull-off force measurements was modeled using the Kelvin and Young's equations and well-accepted geometric constraints for the liquid meniscus formed around a sharp tip (sphere) in contact with a flat surface. Both experimental and modeling results show that the capillary force is a strong function of both the adsorption isotherm (thickness) and liquid molar volume of the adsorbate molecule as well as the surface tension.

5.3 Experimental Setup

Adsorption isotherms at room temperature were measured using attenuated-total-reflection infrared (ATR-IR) spectroscopy. When the IR beam reflects inside of the ATR crystal, an evanescent wave penetrates into the space outside the ATR crystal surface. The penetration depth of this wave is determined from the difference in the refractive index of the crystal and the outside space as well as the angle of internal reflection.[17] Attenuation of the evanescent wave occurs when there are IR active molecules inside this penetration depth. The system is calibrated by measuring the reflectance of the bulk liquid on the crystal for which the penetration depth is known. By comparing the intensities of the natural log of reflectance between the adsorbed molecules with respect to bulk liquid on the ATR crystal, the thickness of the adsorbed film is determined.

IR-spectra were collected using a Thermo-Nicolet Nexus 670 spectrometer with a MCT detector and a multiple bounce ATR crystal. A silicon ATR crystal was used as the substrate for adsorption. Prior to its initial use, the silicon crystal was cleaned via an RCA-1 step (mixture of five parts of water, one part of 30% hydrogen peroxide, and one part of 27% ammonium hydroxide maintained at 70 °C for 15 min). Between each adsorption isotherm measurement, it was further cleaned by washing it with acetone, then ethanol, followed by copious amounts of Millipore water. After these washings, the silicon crystal was then placed in the UV/O_3 for 30-45 min immediately prior to use, providing a contact angle of 0° for all alcohols.

All AFM experiments were performed using a Molecular Imaging scanner and a RHK SPM-100 controller. Silicon (100) substrates were prepared by cleaning via 15 min

in an UV/O_3 followed by an RCA-1 step. This process provided a clean hydrophilic native silicon oxide surface. One silicon AFM cantilever, with an initial radius of curvature of ~15 ±5 nm was used for all force-distance (f-d) measurements in order to minimize differences in spring constants between cantilevers. The cantilever was calibrated using the Sader method,[18] providing a spring constant of 0.59 N/m. Prior to use in any of the alcohol vapor environments, the silicon AFM tip was placed in the UV/O_3 for approximately 15 min, then one high-load scan was performed on clean silicon substrate in dry argon. The high-load scan was used to remove any residual chemisorbed materials from the AFM tip. Adhesion measurements were obtained at room temperature at a constant loading/unloading rate of 20 nm/s.

The partial pressure for any given alcohol is maintained by mixing a dry argon stream with an alcohol-vapor-saturated argon stream, as has been illustrated previously (Figure **2.1**). The ratio of these streams determined the relative partial pressure P/P^{sat} (P^{sat} = saturation pressure for any given alcohol). Force-distance (f-d) curves were collected at approximately 0%, 5%, 10%, 15%, 30%, 60%, 85%, and 98% ±5% of P^{sat} for each alcohol. At each condition, the tip was scanned across the surface and various f-d curves were taken in different locations (before the scan and after). The load during each scan was kept low, so as to not dull the tip. This was verified by comparing the adhesion force in f-d curves taken before and after each condition. As the adhesion is proportional to the radius of tip curvature (R), the adhesion would increase after a scan if wear occurred. We observed little to no wear when alcohol vapors were present in these experiments (R increased less than 5% was the worse case observed).[19]

5.4 Modeling

In the case of the AFM single-asperity contact, the end of the tip is typically modeled as a sphere, while the substrate is illustrated as a flat plate. This approximation has provided great insights into contact mechanics across many length scales.[20] Figure **5.1**, is a simplistic yet valid view of the real contact. Here the tip, with a radius of curvature *R*, is in pseudo-contact with the substrate. As it is represented, a small molecular layer α, may become trapped between the tip and substrate. This is often observed where chemisorbed molecules are present between the tip and substrate.[21] Real tip-substrate contact occurs when $\alpha = 0$ and $d > 0$. The adsorbed layer is present with a thickness *h*. The penetration depth of the tip (without any elastic tip deformation) is *d*.

The capillary force is a consequence of the liquid meniscus around the tip-substrate contact and Laplace pressure (the pressure difference between inside and outside the meniscus). The Young's equation[22] defines the Laplace pressure ($P_{Laplace}$) exerted by this meniscus as a function of the surface tension of the liquid (γ_L) and two principal curvatures of the meniscus (r_1 and r_2):

$$P_{Laplace} \equiv \gamma_L \left(\frac{1}{r_1} + \frac{1}{r_2} \right) \qquad \textbf{5-1}$$

(Note: r_1 should be negative in sign in this expression because its center is outside of the meniscus as illustrated in Figure **5.1**.) Since the adsorbed liquid layer is in equilibrium with the gas phase, its chemical potential (μ_L) should be the same as the gas-phase chemical potential (μ_G). For an ideal system at a constant temperature, the change in the liquid chemical potential relative to a standard condition (say P^{sat} and T) is $\Delta\mu_L =$

$P_{Laplace} \times V$ and the change in the chemical potential of the gas relative to the same standard condition is $\Delta\mu_G = R_g T \times ln(P/P^{sat})$. Here R_g is the ideal gas constant, T is temperature, V is the molar volume of the condensing phase, and P the partial pressure of the vapor. These changes must be equal for chemical equilibrium. Therefore, one can get the relationship between the Laplace pressure of the liquid meniscus and the partial pressure of the adsorbate vapor at equilibrium ($\Delta\mu_L = \Delta\mu_G$ or $\mu_L = \mu_G$):

$$P_{Laplace} \equiv \frac{R_g T}{V} \ln\left(\frac{P}{P^{sat}}\right) \qquad \textbf{5-2}$$

This is also known as the Kelvin equation[22] that describes the relationship between the Laplace pressure of the adsorbed liquid and the vapor pressure of the molecule in the gas phase.

For simplicity, we can assume the meniscus-vapor interface to be circular in shape.[23-26] From a geometrical analysis of Figure 1, one can relate r_2 to r_1 as follows:

$$r_2 = \left((2R + \alpha - d)(d - \alpha + 2h + 2r_1)\right)^{0.5} - r_1 \qquad \textbf{5-3}$$

Note that h is also a function of P/P^{sat}. The circular meniscus or toroidal approximation holds well when $1/r_1 >> 1/r_2$.[27] As P/P^{sat} approaches 1, this approximation may not be valid. However, as P/P^{sat} approaches 1, the Laplace pressure goes to 0 and consequently so does the capillary force due to the Laplace pressure. Therefore, any error in r_2 at higher P/P^{sat} is mitigated making this first-order approximation valid for our purposes. Given any estimate of α, d, and the measured adsorption isotherm $h(P/P^{sat})$, Equations **5-1**, **5-2**, and **5-3** can be solved simultaneously to find values for both radii of the meniscus curvature (r_1 and r_2) at any given P/P^{sat}. The capillary force due to the pressure

inside of the meniscus (F_{Cap}) is the product of $P_{Laplace}$ and the cross-sectional area of the meniscus (πr_2^2):

$$F_{Cap} \equiv P_{Laplace} \times \pi r_2^2 = \frac{R_g T}{V} \ln\left(\frac{P}{P^{sat}}\right) \times \pi\left(\left((2R+\alpha-d)(d-\alpha+2h+2r_1)\right)^{0.5} - r_1\right)^2 \quad \textbf{5-4}$$

In general, this derivation holds when the toroidal approximation is valid and the surfaces completely wet (contact angle = 0) with a known thickness (h). The resulting force is negative in sign due to the fact that it is an attractive force pulling the two surfaces together. Note that F_{Cap} in Equation **5-4** is a function of the contact geometry (R and r_1), liquid molar volume (V), and adsorption isotherm (h), as well as relative vapor pressure (P/P^{sat}) at a constant temperature. It is also a function of the surface tension (γ) because the surface tension plays a role in determining r_1 and r_2.

5.5 Results and Discussion

The adsorption isotherm was determined from the IR spectra collected on a silicon ATR crystal. Figure **5.2** is an example of the IR spectra for ethanol, n-butanol, and n-pentanol at the same relative partial pressure ~65% of P^{sat}. The intensities of the CH_2 symmetric (~2860 cm^{-1}) and asymmetric (~2930 cm^{-1}) as well as the CH_3 (~2960 cm^{-1}) stretching modes are used to determine the isotherm thickness from the comparison with the intensities of these peaks for bulk liquid and the effective penetration depth at these wavenumbers.[28] The measured isotherm for each alcohol is given in Figure **5.3**.

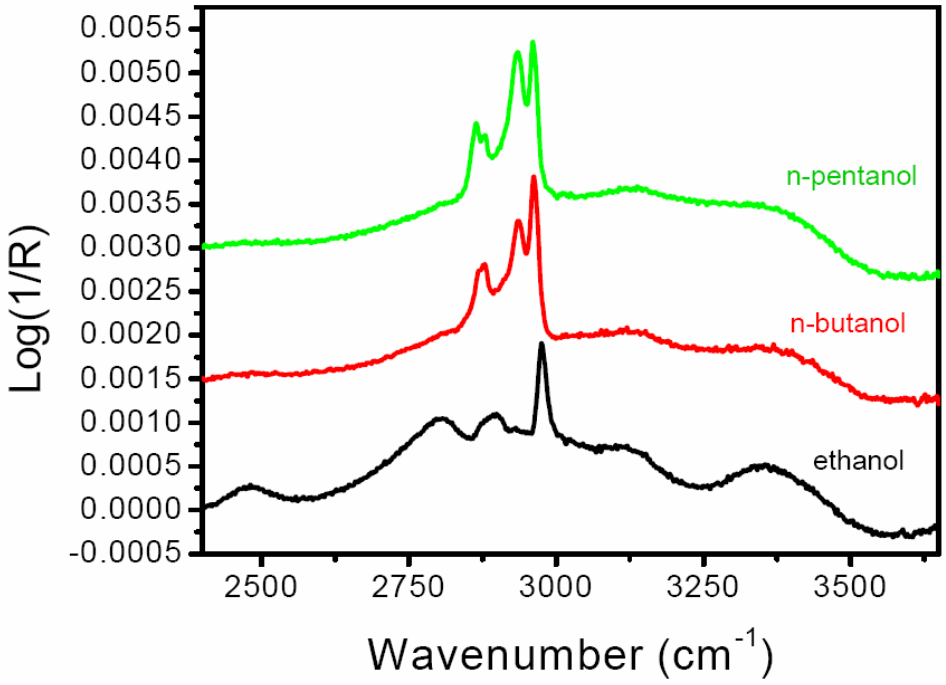

Figure **5.2**: ATR-IR spectra of ethanol, 1-butanol, 1-pentanol on clean silicon ATR crystal each at 65% of P^{sat}.

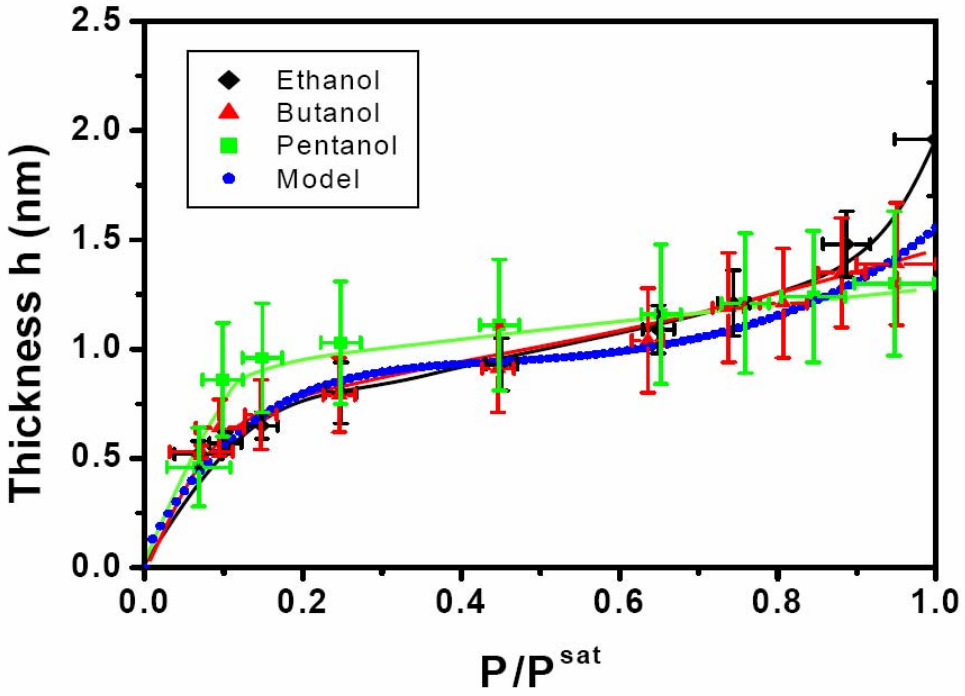

Figure **5.3**: Adsorption isotherm for ethanol, 1-butanol, 1-pentanol as measured by the ATR-IR experiment. The dotted line represents the representative fit for all three isotherms.

Error bars are included based on the deviation in thickness as calculated by the three peak intensities used. The overall shape of the isotherm appears to follow a type-II or S shape.

The adhesion (or AFM pull-off) forces measured as a function of relative partial pressure of ethanol, 1-butanol, and 1-pentanol are shown in Figure **5.4**. Lines are drawn to guide the eye. The data has been normalized to the adhesion force measured near P^{sat}. At this condition, F_{cap} is negligible because the Laplace pressure at this condition is zero ($\ln(P/P^{sat}) \approx 0$). Therefore, the measured adhesion at this vapor pressure should be ~$4\pi R\gamma$ with $\gamma = \gamma_{LV}$ of alcohol since the substrate and tip are covered with alcohol molecules. By normalizing the data in this way, we remove any differences in the shape of the tip (R) between the alcohol systems and can directly compare the capillary force contribution between each alcohol. This is because adhesion and capillary adhesion are proportional to R. Therefore, any deviation in adhesion at P/P^{sat} from 5% to ~100% for any given alcohol system is primarily due to capillary forces.

Two questions arise from the AFM pull-off force data. First, what determines the shape or curvature of the pull-off force vs. P/P^{sat} plot? Secondly, although all alcohols have similar adsorption isotherm behaviors and comparable surface tensions, why is there such a drastic difference in the capillary force for nano-asperity contact between these adsorbing molecules? Modeling the capillary force with Equations **5-1** through **5-4** for different adsorption isotherm shapes (P/P^{sat} dependence) and liquid molar volumes answers these observations. For simplicity, all cases are presented assuming both α and d are 0 nm. This represents the point of no elastic deformation of the tip just before the tip

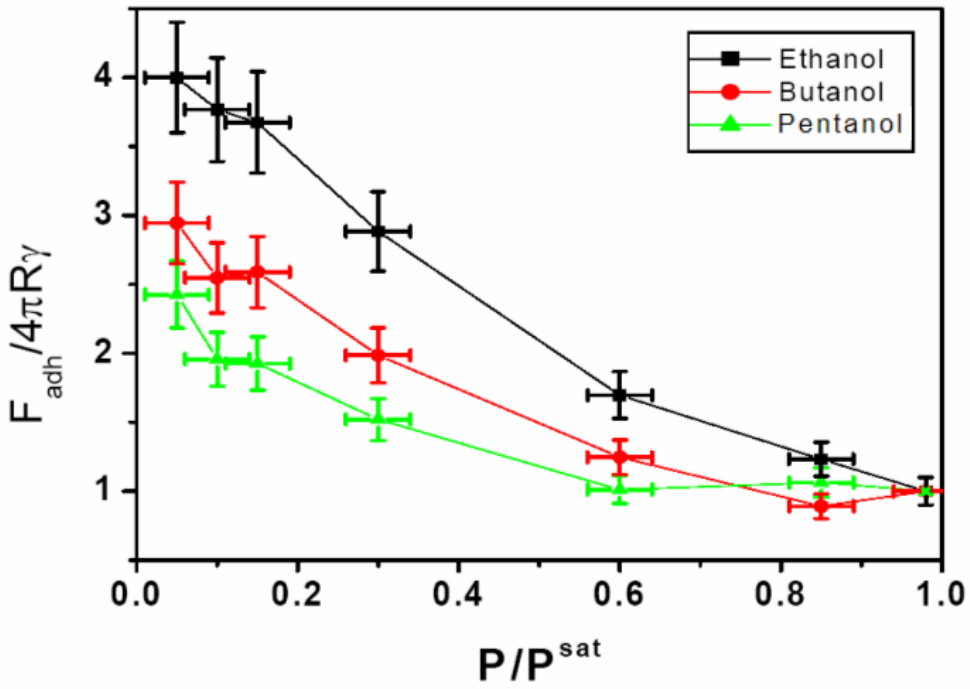

Figure **5.4**: Adhesion vs. P/P^{sat} for ethanol, 1-butanol, 1-pentanol. All data points were normalized to the saturated condition where $F_{adh} = 4\pi R\gamma$.

snap-off. Also, the thickness of the adsorbed film (h) on the silicon AFM tip (sphere) and substrate (flat) are the same.

When P/P^{sat} changes between 0 and 1, adsorption thickness (h) changes which in turn changes r_2 and ultimately F_{cap}. The isotherm shape dependence of the capillary force is illustrated in Figure **5.5**. Three different isotherm shapes are presented in the inset: a constant thickness, a linear increase with P/P^{sat}, lastly the realistic S-type isotherm curve. Since all three isotherms in Figure **5.3** are very close to each other, a best fit average of all three isotherms is constructed (dotted line in Figure **5.3**) and used in this model calculation for capillary force due to alcohol adsorption on the silicon oxide surface. The simulation results clearly show that the P/P^{sat} dependence of the capillary force varies greatly with the amount adsorbed. In this figure, only h and P/P^{sat} vary while V and γ are constant (butanol values were used for V and γ in Figure **5.5**). From this analysis, the shape of the isotherm greatly affects the change in the capillary force as a function of P/P^{sat}. When the isotherm is considered a flat line, the predicted capillary force is upward; however, the shape changes when using a linear or more realistic isotherm. This is due to the influence of h (isotherm thickness) on r_2 (meniscus radius). This effect can be neglected when the probing tip R is large; but it cannot be ignored when R approaches the isotherm thickness h.

Given the fact that each alcohol basically follows the same adsorption isotherm curve within experimental error range, the drastic difference in F_{cap} between alcohols observed in Figure 4 is in part due to the difference in liquid molar volume (V). Equation **5-4** predicts that F_{cap} is directly proportional to V^{-1} (ignoring effects of V on r_1 and r_2).

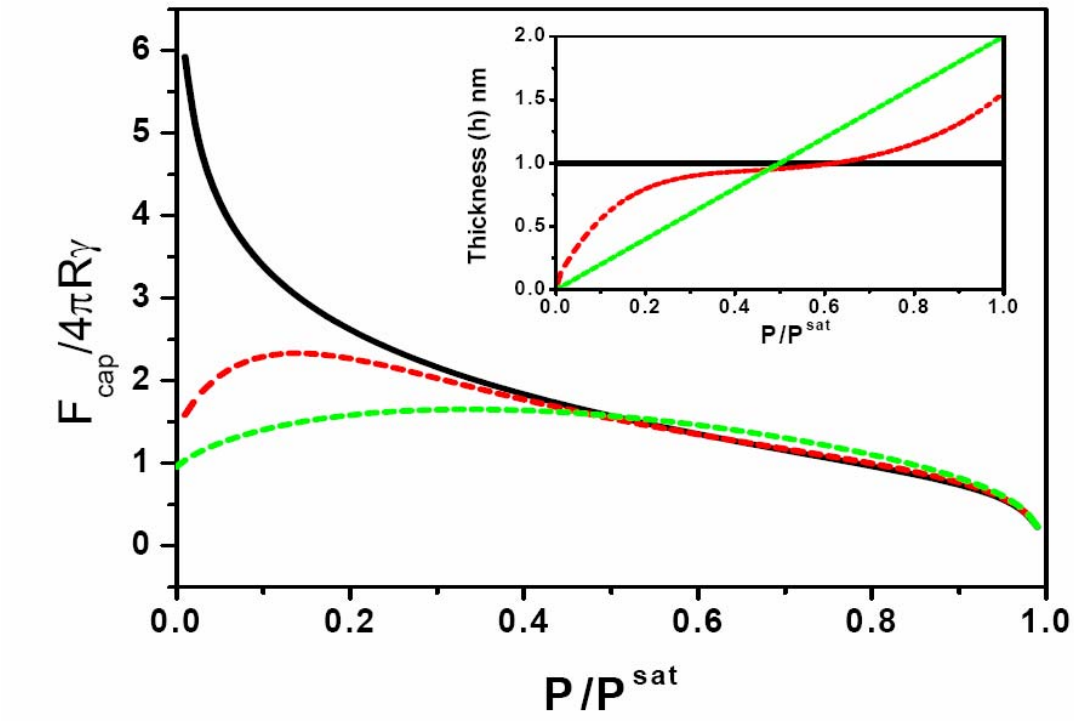

Figure **5.5**: Normalized capillary forces for various arbitrary isotherms. The solid (black), short dash (green), and long dash (red) isotherms in the insert correspond to their respective isotherm. Here the molar volume and surface tension used were those of 1-butanol.

Figure **5.6** illustrates how the capillary force decreases as V increases. Once again the representative model isotherm (dotted line in Figure **5.3**) was used to construct the capillary force while varying only V as a function of P/P^{sat}. Except at $P/P^{sat} < 10\%$, the general shape of the adhesion vs. P/P^{sat} plot reveals the experimentally observed behavior. As the molar volume increase as noted in Table **5.1**,[29] there appears to be a reduction in the capillary adhesion. This reduction is almost proportional to V^{-1}. Therefore, while the adsorption isotherm appears to determine the shape of the P/P^{sat} dependence of the single-asperity pull-off force for sphere-flat contact geometries (Figure **5.5**), the molar volume appears to constrain the magnitude of the capillary force (Figure **5.6**).

Table **5.1**: Surface Tension (γ) and molar volume (V) of linear alcohols

	Surface tension (erg/cm^2)	Molar volume (cm^3/mol)
Ethanol	21.8	58.7
1-Butanol	24.6	91.2
1-Pentanol	24.9	108.7

Comparison of Figure **5.4** and Figure **5.6** yields the following analysis. Above P/P^{sat} of ~10%, the data follows the same general trend as Equation **5-4** predicts. While

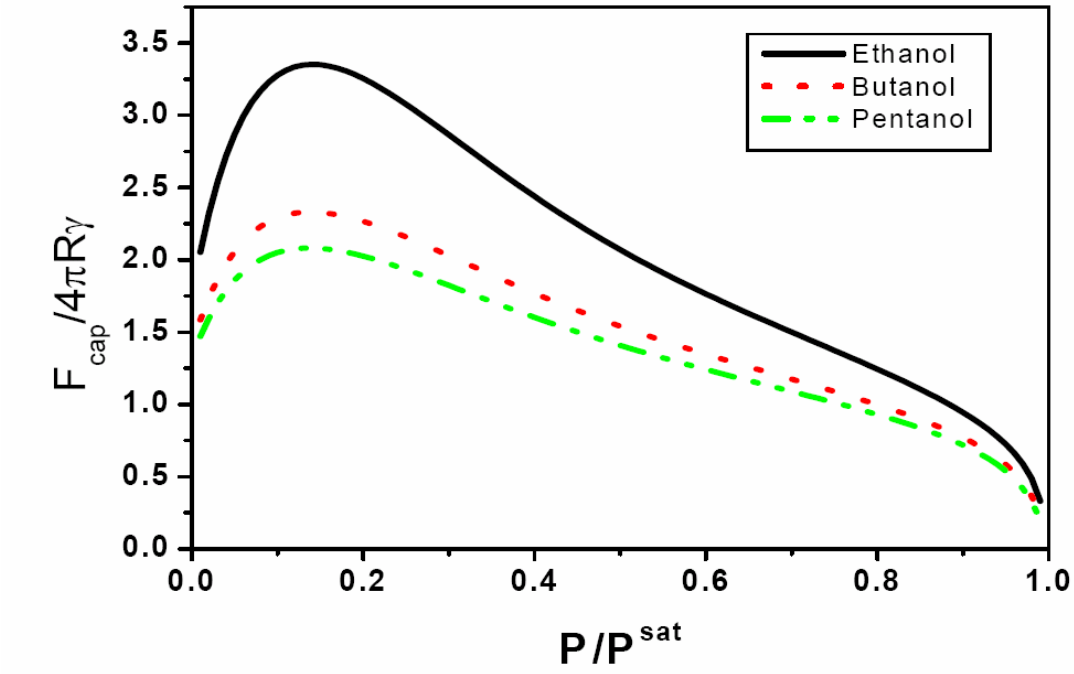

Figure **5.6**: Molar volume dependence of the capillary force. The predicted normalized capillary adhesion for each alcohol is presented using the representative S-shape isotherm and each alcohol's surface tension; only the molar volume varies significantly.

each alcohol has the same surface tension, its molar volume greatly determines the magnitude of the capillary pressure relative to each other. The capillary adhesion of ethanol is approximately 2.5 times larger than that of 1-pentanol. This is in good agreement with the theory which predicts a difference of ~1.6 for these two alcohols.

The experimental data at P/P^{sat} <10% shows excessively high adhesion and lacks the downward curvature of the predicted capillary force contribution. This is due to the fact that at these low partial pressures, the coverage of alcohols on the surface is not complete. Therefore the AFM tip may still be in direct interaction with the silicon oxide substrate surface which has much higher surface energy than the adsorbed alcohol layer. This is the P/P^{sat} region where the equilibrium thickness is lower than that of the plateau region of the isotherm curve (Figure **5.3**). Additionally, continuum models are probably not appropriate when incomplete coverage occurs and when the meniscus size becomes the size of molecular dimensions; other treatments should be used.[30] When P/P^{sat} is higher than the threshold value (monolayer coverage), the agreement between the simulated trend and the experimentally observed trend is remarkable.

While the model agrees qualitatively to the experiment, quantitatively there is some difference between the two results. This is most likely due to the fact that the tip geometry is not an exact sphere, α and d may not be 0 and the meniscus is not exactly circular in shape. At the same time, the adsorbed film thickness (h) on the AFM tip (sphere) may not follow the same isotherm trend as is observed on flat surfaces, especially at low partial pressures.

Combining Eqs. 1 and 2, one can write the relationship between the partial vapor pressure and two principal curvatures of the liquid meniscus:

$$\frac{R_g T}{V}\ln\left(\frac{P}{P^{sat}}\right) \equiv P_{Laplace} \equiv \gamma_L\left(\frac{1}{r_1}+\frac{1}{r_2}\right) \qquad \textbf{5-5}$$

Inspection of Equation **5-5** provides the following understanding. The left hand side represents chemical equilibrium while the right hand side represents a mechanical equilibrium. Chemical equilibrium states that the Laplace pressure is solely determined by the temperature, molar volume of the liquid, and the partial pressure of the vapor. In the case of ethanol, 1-butanol, and 1-pentanol, each alcohol has virtually the same surface tension γ, however their molar volumes (V) differ substantially. At the same relative partial pressure (P/P^{sat}) for any given alcohol the Laplace pressure differs by V^{-1} between each alcohol. The surface tension of the liquid plays a role by constraining the meniscus curvature radii for a given equilibrium vapor or Laplace pressure. Therefore, while the Laplace pressure is not dependent on the surface tension, the area over which that pressure acts (πr_2^2) does depend on γ.

In Figure **5.7**, the measured capillary force data are plotted with respect to Laplace pressure calculated from Equation **5-2** . In this plot, the molar volume effect is now normalized. Compared with Figure **5.4**, the data do appear more consistent with one another as would be expected. However, the capillary force for ethanol is still a bit higher than that of butanol which is again slightly higher than that of pentanol for the same given Laplace pressure.

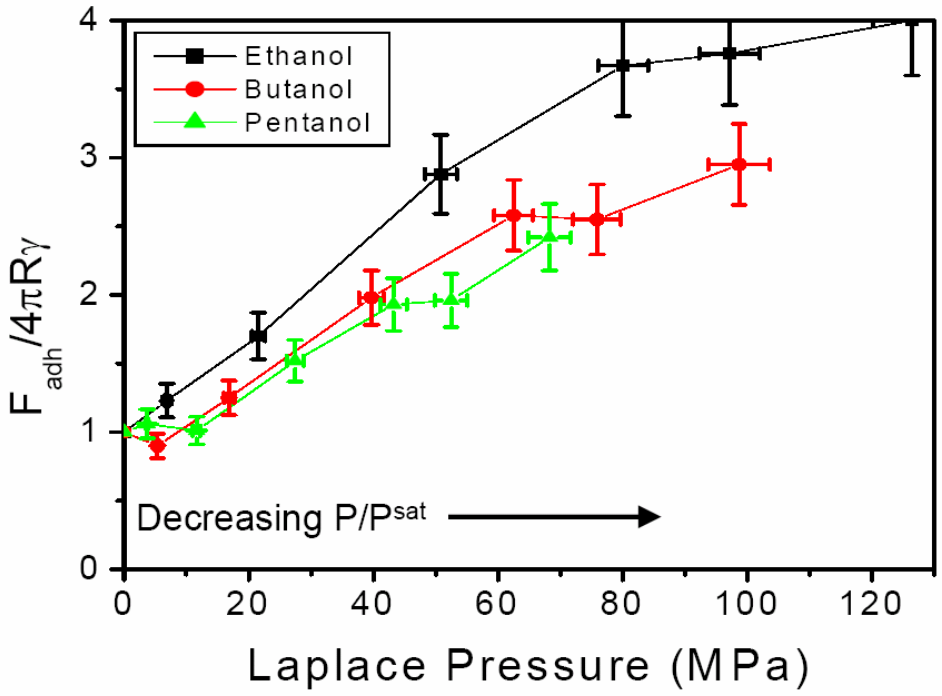

Figure **5.7**: Normalized AFM adhesion force vs. Laplace pressure.

The explanation for this difference is as follows. While Figure **5.7** plots the measured data points on the Laplace pressure scale, the area of the meniscus between each alcohol differs. At the same Laplace pressure, the isotherm thickness is highest for ethanol and lowest for pentanol. This difference in isotherm thickness changes the meniscus cross-section area (πr_2^2). A first order approximation shows that the difference in area is proportional to the difference in the adsorbed film thickness at the same Laplace pressure. Figure **5.8** accounts for this difference in area by normalizing the data with the film thickness (and hence meniscus area) of ethanol ($h_{ethanol}$) for each alcohol. With this taken into account, the data now fall on the same curve. The agreement of this fit proves that the molar volume and isotherm thickness are very important parameters in nano-asperity adhesion. The data taken at 5% P/P^{sat} are not included in this figure because at this partial pressure the uncertainty in alcohol coverage is significant and not well predicted.

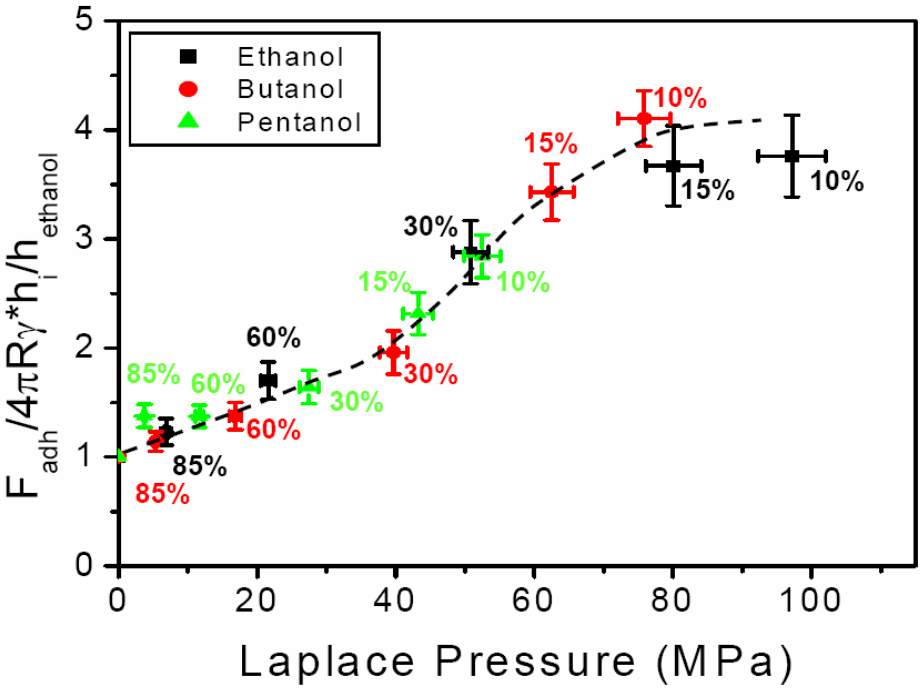

Figure **5.8**: Normalized AFM adhesion force to account for differences in meniscus area and molar volume (V) between alcohols vs. Laplace pressure. The relative partial pressure for each alcohol is included in the figure.

5.6 Conclusions

In considering the consequences of capillary adhesion for nanoscale contacts, the important constraints are the surface tension of the adsorbate, its liquid molar volume, the pressure dependence of the adsorbate thickness, and the contact geometry. Given the same contact geometry, the isotherm plays a dominate roll in the shape of the capillary force vs. P/P^{sat}, while the liquid molar volume of the adsorbate constrains the magnitude of the capillary force. The liquid surface tension determines the meniscus radii of curvature over which the Laplace pressure of the meniscus is exerted. In systems where control over surface forces are critical, i.e. microelectromechanical system (MEMS), nanoelectromechanical systems (NEMS), colloids, and nano-tribology, the effect of molar volume and adsorption isotherm of gas phase molecules cannot be neglected.

5.7 References

1. A. A. Feiler; P. Jenkins; M. W. Rutland, *Journal of Adhesion Science and Technology* **2005,** 19, (3-5), 165-179.
2. D. Maugis; B. Gauthiermanuel, *Journal of Adhesion Science and Technology* **1994,** 8, (11), 1311-1322.
3. A. D. Romig; M. T. Dugger; P. J. McWhorter, *Acta Materialia* **2003,** 51, (19), 5837-5866.
4. B. Cappella; G. Dietler, *Surface Science Reports* **1999,** 34, (1-3), 1-+.
5. D. B. Asay; S. H. Kim, *Journal of Chemical Physics* **2006,** 124, (17), 5.
6. B. Bhushan; C. Dandavate, *Journal of Applied Physics* **2000,** 87, (3), 1201-1210.
7. M. Binggeli; C. M. Mate, *Applied Physics Letters* **1994,** 65, (4), 415-417.
8. M. P. de Boer; P. C. T. de Boer, *Journal of Colloid and Interface Science* **2007,** 311, (1), 171-185.
9. P. C. T. de Boer; M. P. de Boer, *Langmuir* **2008,** 24, (1), 160-169.
10. M. Y. He; A. S. Blum; D. E. Aston; C. Buenviaje; R. M. Overney; R. Luginbuhl, *Journal of Chemical Physics* **2001,** 114, (3), 1355-1360.
11. R. Jones; H. M. Pollock; J. A. S. Cleaver; C. S. Hodges, *Langmuir* **2002,** 18, (21), 8045-8055.
12. D. L. Sedin; K. L. Rowlen, *Analytical Chemistry* **2000,** 72, (10), 2183-2189.
13. X. D. Xiao; L. M. Qian, *Langmuir* **2000,** 16, (21), 8153-8158.
14. L. Xu; A. Lio; J. Hu; D. F. Ogletree; M. Salmeron, *Journal of Physical Chemistry B* **1998,** 102, (3), 540-548.

15. J. Israelachvili, *Intermolecular & Surface Forces*. Academic Press: London, 1991.

16. B. L. Weeks; M. W. Vaughn; J. J. DeYoreo, *Langmuir* **2005,** 21, (18), 8096-8098.

17. M. W. Urban, *Attenuated Total Reflectance Spectroscopy of Polymers Theory and Practice*. American Chemical Society: Washington, D. C., 1996.

18. J. E. Sader; J. W. M. Chon; P. Mulvaney, *Review of Scientific Instruments* **1999,** 70, (10), 3967-3969.

19. K. Strawhecker; D. B. Asay; J. McKinney; S. H. Kim, *Tribology Letters* **2005,** 19, (1), 17-21.

20. K. L. Johnson, *Proceedings of the Royal Society of London Series a-Mathematical Physical and Engineering Sciences* **1997,** 453, (1956), 163-179.

21. E. Barrena; C. Ocal; M. Salmeron, *Surface Science* **2001,** 482, 1216-1221.

22. A. W. Adamson; A. P. Gast, *Physical Chemistry of Surfaces, 6th Edition*. John Wiley & Sons: New York, 1997.

23. W. C. Clark; J. M. Haynes; G. Mason, *Chemical Engineering Science* **1968,** 23, (7), 810-&.

24. A. de Lazzer; M. Dreyer; H. J. Rath, *Langmuir* **1999,** 15, (13), 4551-4559.

25. G. P. Lian; C. Thornton; M. J. Adams, *Journal of Colloid and Interface Science* **1993,** 161, (1), 138-147.

26. A. Marmur, *Langmuir* **1993,** 9, (7), 1922-1926.

27. H. J. Butt; M. Farshchi-Tabrizi; M. Kappl, *Journal of Applied Physics* **2006,** 100, (2).

28. D. B. Asay; S. H. Kim, *Journal of Physical Chemistry B* **2005,** 109, (35), 16760-16763.

29. L. Segade; J. J. de Llano; M. Dominguez-Perez; O. Cabeza; M. Cabanas; E. Jimenez, *Journal of Chemical and Engineering Data* **2003,** 48, (5), 1251-1255.

30. J. Y. Jang; G. C. Schatz; M. A. Ratner, *Physical Review Letters* **2004,** 92, (8).

Chapter 6

Direct Force Balance Method (DFBM) for AFM Lateral Force Calibration

6.1 Summary

A new and simple calibration method for atomic force microscopy (AFM) is developed. This non-scanning method is based on direct force balances on surfaces with known slopes. The lateral force calibration is performed during force-distance measurements for normal force calibration. This method requires a substrate with known slopes, the z-motion of the piezo calibrated, and the normal spring constant known. The direct force balance method employs the lateral force signal obtained during a force-distance measurement on a sloped surface and relates this signal to the applied load and the slope of the surface to determine the lateral calibration factor. Because it is non-scanning, the AFM cantilever can be calibrated without dulling the tip. This chapter develops the force balance equations for a tip sliding up and down a sloped surface during force-distance curve measurement. The agreement between the calculation from the force balance equations and the experimental data from a macro-scale model system is within 5% of each other. These results are extended to the AFM. Sources of error in DFBM of AFM cantilevers are also discussed.

6.2 Introduction

The atomic force microscope (AFM) has emerged as an important tool for studying mechanical properties as well as topography of surfaces at the nano-scale.[1, 2] Built of a cantilever with a probing tip or colloidal partial at the free end, the AFM is capable of measuring extremely small forces acting on the probe (tip or colloid). The ability to quantitatively and accurately determine the forces acting on the AFM tip with atomic-scale contrast depends greatly upon the accuracy and reliability of the calibration methods used to define the system.

Upon interaction with a substrate surface, the AFM cantilever deflects in two directions, normal to the plane of the cantilever (the z-direction) and torsional to the cantilever, illustrated in Figure **6.1**. During the operation of commercial AFMs, the degree of deflection is measured with a position sensitive detector that produces a voltage output in proportion to the location of the laser beam reflected from the back of the cantilever. This voltage output from the detector is then converted to units of force by multiplying the voltage output by a detector sensitivity factor. In contact mode scanning on a flat substrate, the normal deflection is a measure of force applied to the surface and the torsional deflection is a measure of force due to friction between the probe and the surface.

Converting normal deflection to the applied force requires detector calibration. This calibration factor is easily obtained from a force-distance (f-d) curve measurement.[2] During the f-d curve, the voltage output signal (V^{Normal}) from the detector is recorded as a function of the cantilever bending. The cantilever bending is equal to the z-piezo motion

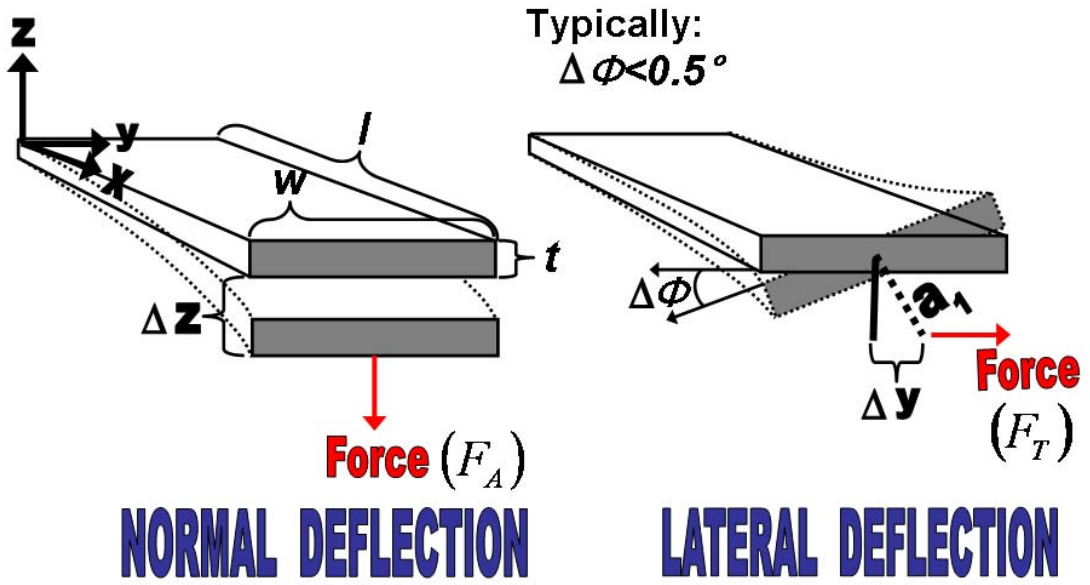

Figure **6.1**: Normal and lateral force deflections of AFM cantilevers. Here the cantilever's length, width, and thickness is labeled (*l*, *w*, and *t*). In the case of lateral deflection a lateral force is applied against the moment arm a_1. This force displaces the moment arm some distance Δy.

when the AFM tip-substrate contact is sufficiently ridged. The normal deflection sensitivity S_Z (V/m) is then defined as the slope of the f-d curve after the AFM tip makes contact with the substrate. The applied force at a position z, $F_A(z)$, is then calculated by this simple equation:

$$F_A(z) = \frac{k_N\left[V^{Normal}(z) - V_{FS}^{Normal}\right]}{S_Z} = k_N \Delta z \qquad \textbf{6-1}$$

where k_N is the normal force spring constant of the cantilever (N/m), $V^{Normal}(z)$ the voltage at the cantilever deflection z, and V_{FS}^{Normal} the voltage at the free standing position (zero deflection) and Δz is the degree of deflection from the free-standing position (m). The spring constant (k_N), is typically determined by one of three methods: the Sader method[3-5], the Cleveland method[6], or calculated when the cantilever dimensions and material properties are known.[7]

Unlike the normal force calibration, calibration of lateral forces twisting the AFM cantilever has, until now, been difficult and nontrivial. There are two methodologies employed for lateral force calibration: (1) calibration of the lateral force recorded during scanning and (2) calibration of the torsional properties of the cantilever without scanning. The scanning methods are more widely used than non-scanning methods because they are simpler to implement. The widely used scanning calibration methods are the wedge calibration methods[8, 9] and the vertical scan method.[7] In these methods, the measured lateral signal outputs ($V^{Lateral}$) under various load conditions are processed through a complicated mathematical algorithm based upon empirical relationships between friction force and normal load. These methods are indirect, as the actual lateral force causing the

cantilever to twist is determined empirically and not directly known or measured. The accuracy of these methods depend upon the following assumptions; (a) the tip does not wear significantly during contact mode scanning, (b) the detector cross-talk between the normal and lateral responses is negligible, and (c) the feedback error in normal force control is always constant regardless of the slope of the imaging surface. However, these assumptions are not applicable in many practical situations. This limits the validity of the scanning calibration methods and causes poor reproducibility of measurements between experimental groups.

The non-scanning method does not rely upon empirical friction relationships or make assumptions that limit the validity of the calibration result. This method requires two separate calibrations: calibrating the torsional sensitivity of the photodetector S_ϕ (V/rad) and determining the torsional spring constant k'_ϕ(N/rad) of the cantilever. The torsional sensitivity of the detector can be directly measured by monitoring the detector response as the laser beam is reflected from a mirror with a known tilt angle ϕ.[10] Once the detector torsional sensitivity is determined, the torsional spring constant of the cantilever can be determined by measuring the torsional response of the cantilever upon pushing the cantilever with a secondary sharp tip at different offsets from the cantilever centerline.[10] However, this method is not widely used because it requires fabrication of special tip substrates and fine alignment of this secondary tip and the cantilever. In principle, the torsional spring constant can also be calculated from the cantilever's geometry and characteristic mechanical properties. However, if the cantilever is made of crystalline materials such as silicon, the anisotropy of the Young's modulus and Poisson

ratio make it impractical to use simple geometric equations for calculation of k'_{ϕ}.[11, 12] Sadar and co-workers developed a resonance frequency measurement method for a free-standing cantilever. This method requires a high-frequency lock-in amplifier to measure the torsional resonance frequency because this frequency typically exceeds 250 kHz. The torsional Sader method was developed for free-standing cantilevers with no mass attached at the end. If the cantilever has a mass attached to the freestanding end (i.e. AFM tip or colloidal sphere), the torsional Sader method yields torsional spring constants that deviate from the true value up to a factor of ~3, making this method of determination invalid.[11] [Note: the Sader method is a valid calibration technique for the normal spring constant as the effect of mass on the calibration method is typically less than 10%.] Once k'_{ϕ} and S_{ϕ} are determined, the measured $V^{Lateral}$ can be converted to the lateral force by $(V^{Lateral} \cdot k'_{\phi})/(S_{\phi} \cdot a_1)$, where a_1 is the moment arm length which is the sum of the tip height and half of the cantilever thickness. Ultimately, this non-scanning method requires three separate measurements, the moment arm length (a_1), the torsional sensitivity of the detector (S_{ϕ}), and the torsional spring constant for the cantilever (k'_{ϕ}).

This chapter describes a simple and straightforward method for AFM lateral force calibration. This method is based on direct force balances. The lateral force signal is measured during the normal f-d curve measurements on a ridged substrate with known slopes. Since this calibration is performed without lateral scanning, AFM tip wear during calibration can be prevented. And, unlike other non-scanning methods, the direct force balance method does not require additional hardware, nor does it require any measurement of the moment arm length, the torsional spring constant (k'_{ϕ}) or pre-

calibration of S_ϕ. This method also takes into account the detector cross-talking and off-centered tip problems. Most of all, our direct force balance method determines the lateral force calibration factor from f-d curve measurements which are the first step in every AFM experiment before scanning.

6.3 Force Balance for *f-d* Measurement on a Sloped Surface

The basic technique behind the direct-force-balance-method (DFBM) requires the collection of force-distance (*f-d*) curves on surfaces with different slopes as illustrated in Figure **6.2**. By comparing the slopes of the lateral responses in the *f-d* curve on these facets, the lateral detector sensitivity (S_L) is easily determined. On each surface, the applied force (F_A) at any point in the *f-d* curve is known from the normal deflection of the cantilever. During the collection of *f-d* curves, all of the forces in the system are balanced ($\Sigma F_i=0$, no acceleration). Therefore, if the slope of the surface is known, then the lateral force measured at a given F_A can be calculated.

The implicit assumption behind this technique requires the forces applied by the AFM cantilever at the point of contact between the tip and the surface to be in equilibrium with the surface forces acting at the contact point. In this context, surface forces refer to the forces which the surface applies to the point of contact. In the case of surface forces, friction forces (F_F) act parallel to the surface and against the direction of sliding motion while surface normal forces (F_N) act perpendicular to the surface.

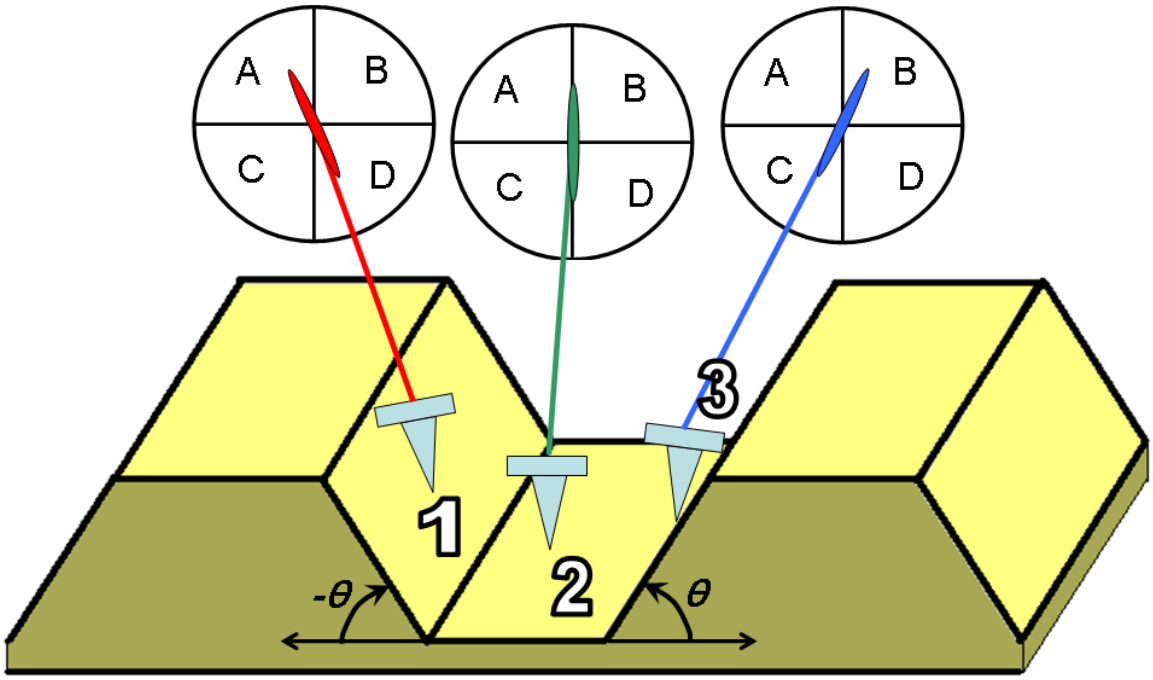

Figure **6.2**: Lateral calibration grating for AFM. Here is θ 54.7° (TGF-11 from macromasch). Force distance curves are taken on facets 1, 2, and 3. The response of the laser during the *f-d* curve is illustrated when the detector is orthogonal to the system. The lateral and normal responses are given by the individual voltages in each quadrant of the photo-detector as: $V^{Lateral} = \frac{(V_A + V_C) - (V_B + V_D)}{V_A + V_B + V_C + V_D}$ and $V^{Normal} = \frac{(V_A + V_B) - (V_C + V_D)}{V_A + V_B + V_C + V_D}$.

Therefore, F_F is perpendicular to F_N. Additionally, the frictional force (F_F) is a function of the normal load (F_N).

The AFM cantilever applies forces along the z direction (F_A) as well as perpendicular to the z direction (F_T). F_A is perpendicular to the xy shear plane of the cantilever as illustrated in Figure **6.1**. Depending on the position of the AFM tip relative to the shear plane on the cantilever (i.e., the degree of off-set of the tip from the center of the cantilever), both F_A and F_T can cause the cantilever to twist. During the collection of *f-d* curves on any surface slope, the vector sum of $\vec{F}_N$, $\vec{F}_F$, $\vec{F}_A$, and $\vec{F}_T$ equals zero. Provided that F_A and the surface angle θ are known, F_N , F_F and F_T can be determined from the slopes of the approach and retraction curves of the lateral signal in the *f-d* curve. It should be noted that F_F is not an independent variable and is a function of F_N therefore; we are left with two observed responses ($\vec{F}_A$ and $\vec{F}_T$) and two unknowns ($\vec{F}_N$ and $\vec{F}_F$).

If a surface with zero friction is tilted by an angle θ, the tip will slip downward along the slope during the approach cycle of a normal *f-d* curve measurement. The contact slides until the surface-parallel components of the torsional (F_T) and applied forces (F_A) are equal to each other, i.e, $F_T \cdot \sin(90-\theta) = F_A \cdot \sin(\theta)$. This is the "complete slip" case illustrated in Figure **6.3**. During the f-d curve measurement, the forces (F_A, F_N, and F_T) vary from positive to negative values as the measurement moves from a compressive to tensile load. Provided the AFM tip is centered on the cantilever, if the coefficient of friction (μ) is larger than tan(θ), friction prevents the tip from slipping. This "no slip" case is presented in Figure **6.4**. In this case, the vector sum of $\vec{F}_N$ and $\vec{F}_F$

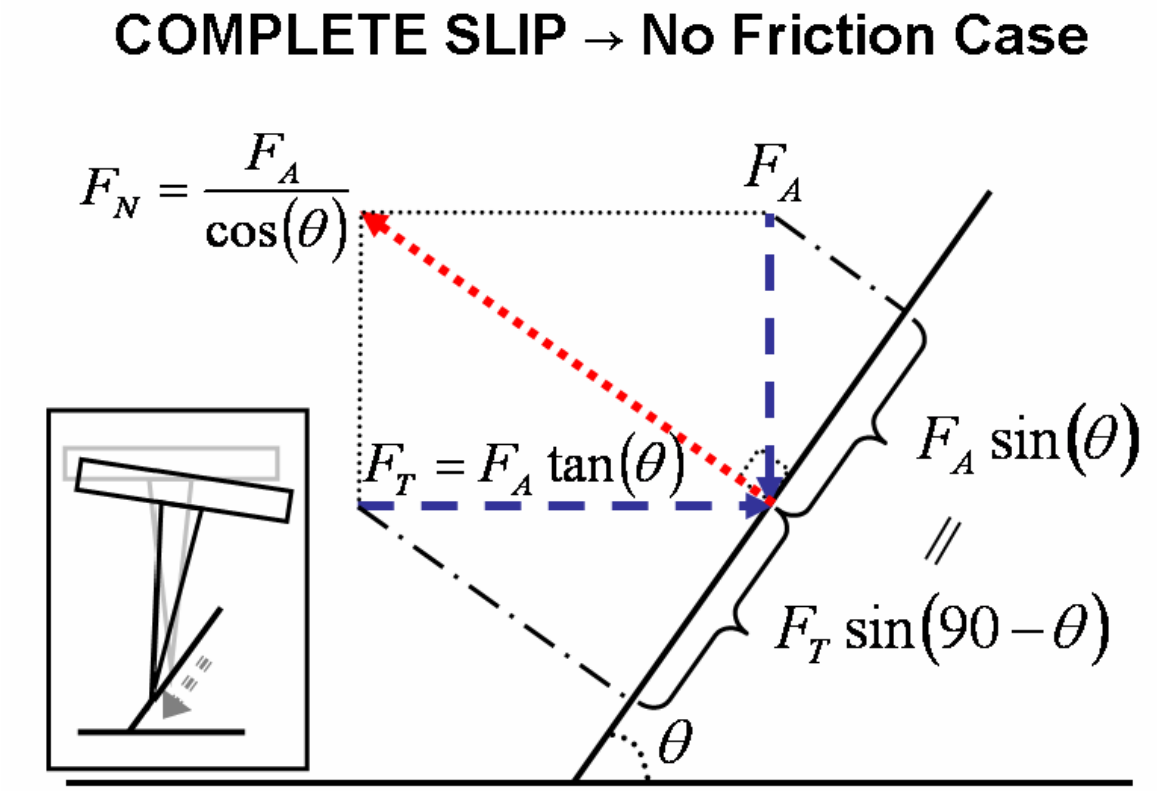

Figure **6.3**: Force balance between the forces the AFM tip applies on the surface (F_A and F_T) and the forces the surface applies against the tip (F_N). In this case there is no friction. The sum of the force vectors = 0. The insert illustrates the tip sliding down the surface causing it to twist and therefore generate torsional forces.

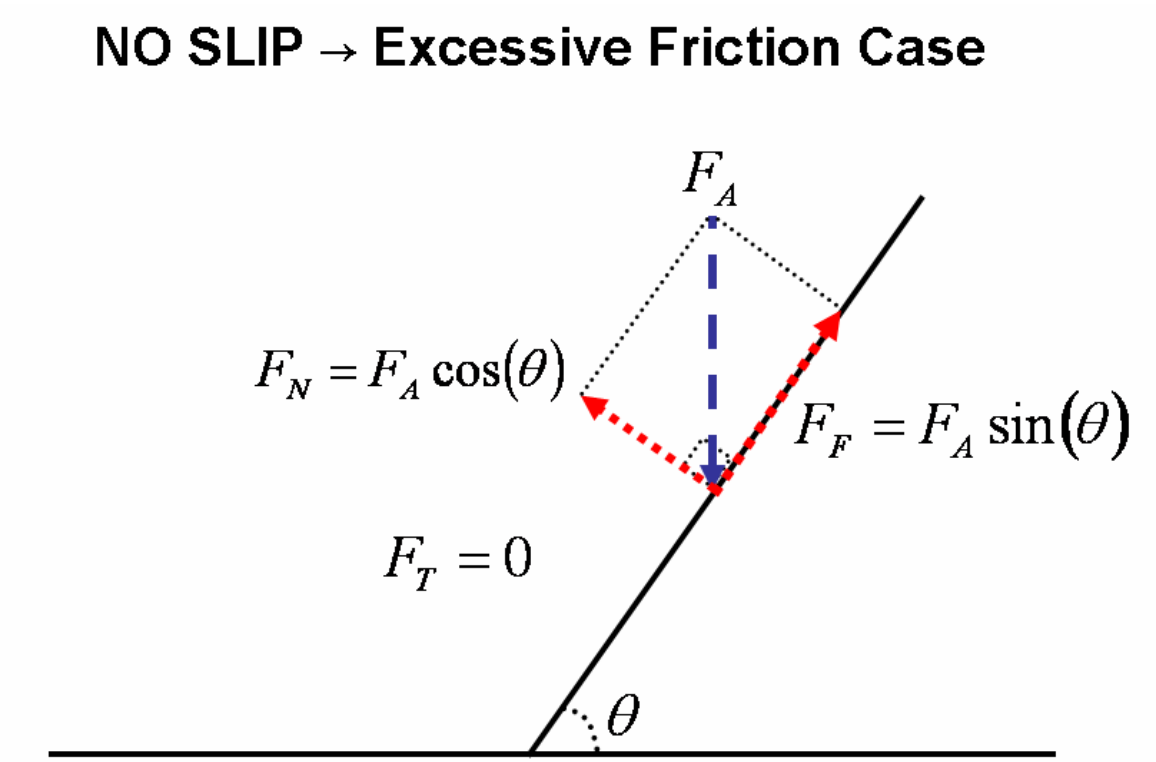

Figure **6.4**: Force balance between the forces the AFM tip applies on the surface (F_A and F_T) and the forces the surface applies against the tip (F_N and F_F). In this case, friction prevents the tip from twisting ($F_T = 0$). The sum of the force vectors = 0.

equals $-\vec{F}_A$ ($\Sigma F_i=0$) and no torsion forces will be observed ($F_T=0$). Typically, the "complete slip" or frictionless case does not exist in AFM calibrations. In order to calibrate the lateral signal with the direct force balance method, the substrate must have an appropriately large angle to guarantee some slip, and hence generate torsional forces (F_T). This case is termed the "limited slip" case and is illustrated in Figure **6.5**.

During the approach and retraction of *f-d* curve measurements, the tip also slips along the axial direction (the x-direction) of the cantilever.[13] Although this could reduce initial static friction against sliding along the surface, it is not directly involved in the lateral force balance since its slip direction and their forces are orthogonal to the lateral slip of the AFM tip along the surface slope. Therefore, slip along the cantilever axial direction is not included in the mathematical derivation of the force balance.

The frictional response observed with a sharp AFM tip under a positive applied load (in the "compressive region" of the applied force in the friction-load curve; $F_A > 0$) can be fitted empirically to a linear function:[7, 14, 15]

$$F_F = \mu \cdot F_N + offset \qquad \textbf{6-2}$$

Here μ is the coefficient of friction. Note that F_F is proportional to F_N, instead of F_A, on the sloped surface. Due to adhesive forces acting at the tip, the friction force at the zero applied load has a non-zero value. The solid contact mechanics explains that this value cannot be predicted simply by multiplying the coefficient of friction with the adhesion force.[16] For this reason, we have included an offset value to represent the frictional force at the zero applied load, instead of μ times the adhesive force.

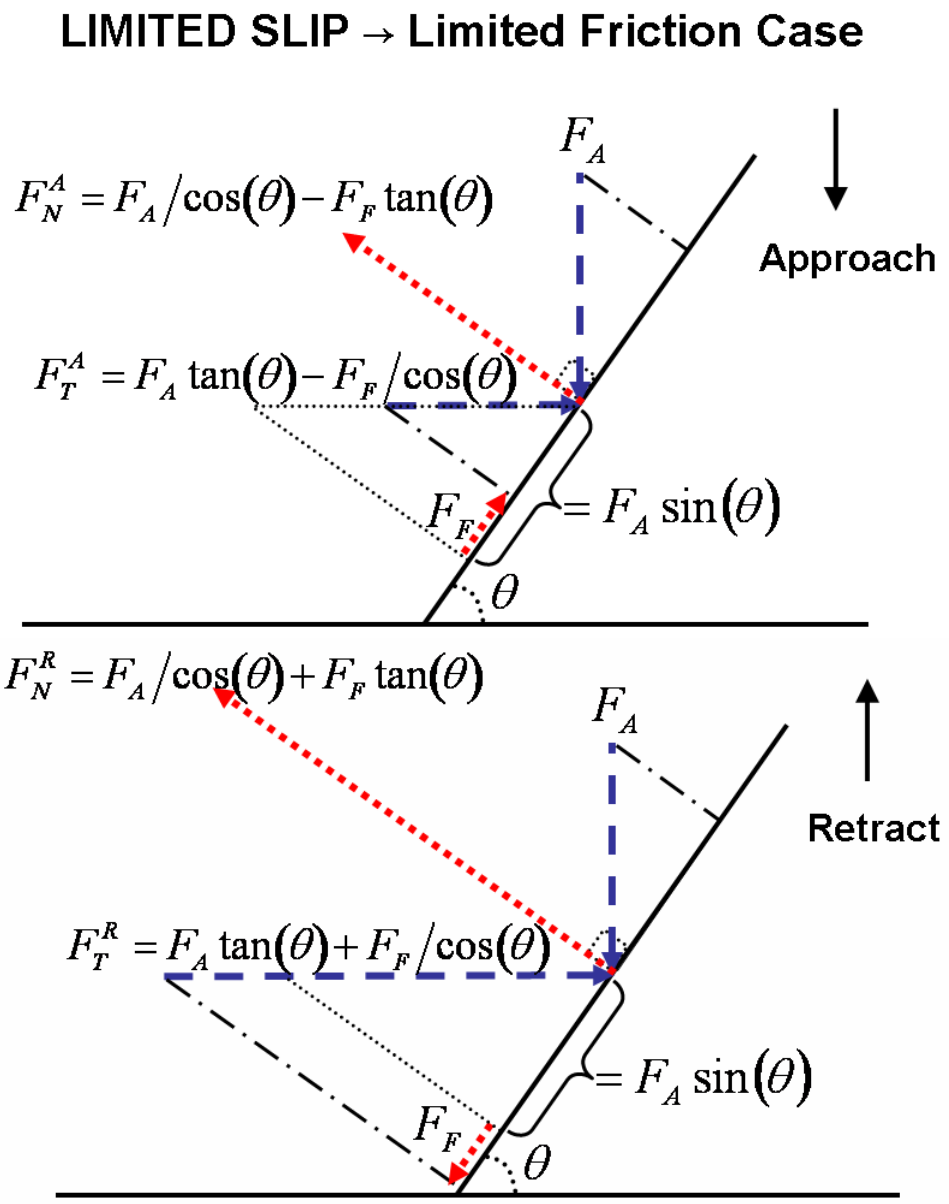

Figure **6.5**: Force balance between the forces the AFM tip applies on the surface (F_A and F_T) and the forces the surface applies against the tip (F_N and F_F) during the approach or retraction cycle of the *f-d* curve. Friction acts against the direction of motion. The dotted line represents the frictionless case. The sum of the force vectors = 0.

In the approach cycle of the *f-d* curve, the tip moves downward from the free standing position towards the surface. After contact, the AFM tip slides down the slope as the applied load increases. However, due to friction forces acting against the direction of motion, the degree of slip is smaller than that of the "complete slip" case (Figure **6.3**). The force balance in this case is illustrated in Figure **6.5** (top). From a simple force balance, F_N and F_T are expressed as functions of F_A and F_F:

$$F_N^A = \frac{F_A}{\cos(\theta)} - F_F \tan(\theta) \qquad \textbf{6-3}$$

$$F_T^A = F_A \tan(\theta) - \frac{F_F}{\cos(\theta)} \qquad \textbf{6-4}$$

Here the superscript *A* represents the direction of motion (approach).

In the retraction cycle of an *f-d* curve, the applied force on the cantilever decreases and the tip slides up the surface until snap-off. In this case, the friction force also acts against motion; however, compared with the approach, the direction of this vector is opposite. The force balance illustrated in Figure **6.5** (bottom) for F_N and F_T is then:

$$F_N^R = \frac{F_A}{\cos(\theta)} + F_F \tan(\theta) \qquad \textbf{6-5}$$

$$F_T^R = F_A \tan(\theta) + \frac{F_F}{\cos(\theta)} \qquad \textbf{6-6}$$

When the AFM tip is centered on the shear plane of the cantilever (labeled as point C) in Figure **6.6** insert, this is known as a "centered tip". In this case, the moment arm length (a_1 or L) corresponding to the torsion force (F_T) is given as:

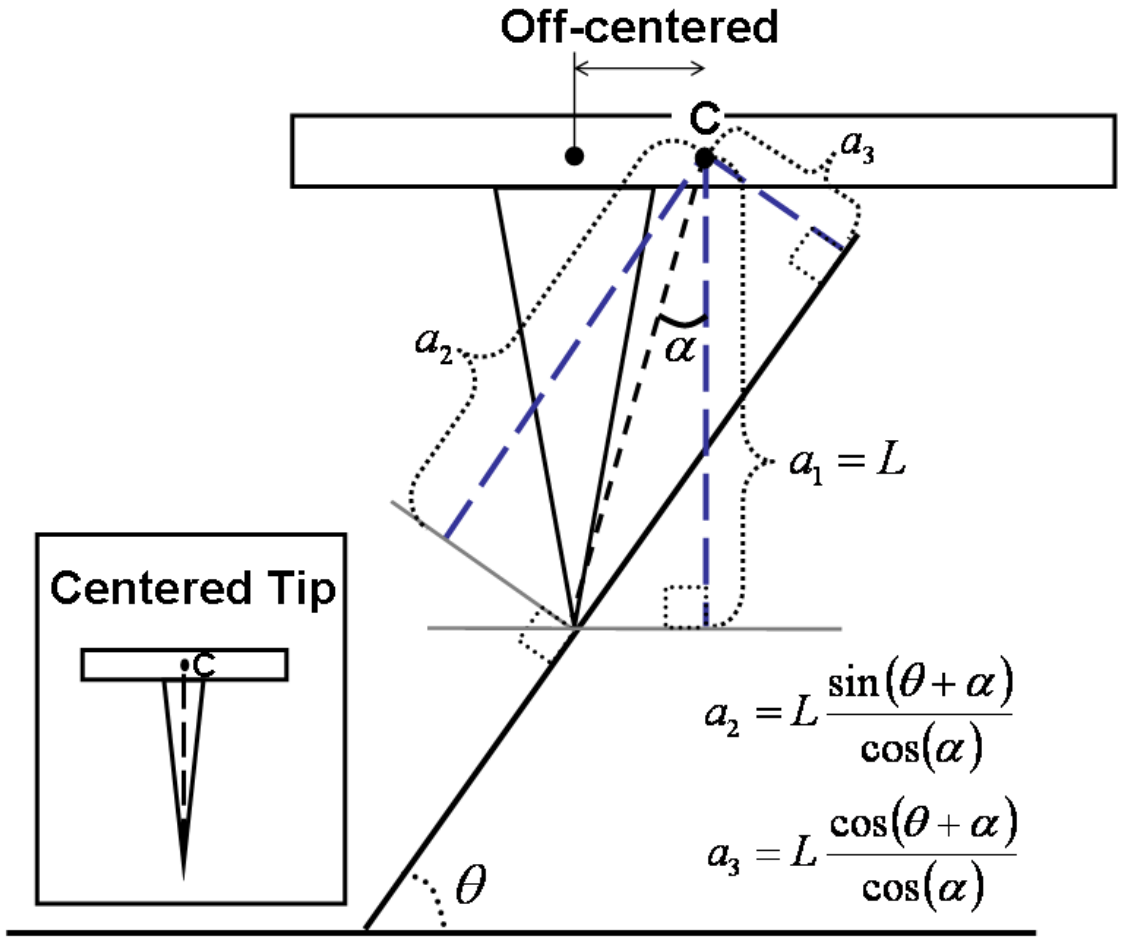

Figure **6.6**: The moment arms a_1, a_2, and a_3 are illustrated for the off-centered tip (long dashed lines). The amount a tip is off-centered is measured in angles as α. The point C indicates the shear center of the cantilever. All twisting of the cantilever is centered about this point. The position of a centered tip is illustrated in the insert.

$$a_1 = L = h_{tip} + t/2 \qquad \textbf{6-7}$$

where h_{tip} is the height of the AFM tip and t is the thickness of the cantilever. While this length is not explicitly necessary for DFBM calibration, a_1 will be utilized in the derivation to follow.

The torsional force applied to the moment arm (a_1) necessary to balance F_A, F_F and F_N is given in equations **6-4** and **6-6** and is the exact solution for the centered cantilever case. However, when the tip is off-centered as illustrated in Figure **6.6**, the cantilever will twist even on a horizontal surface ($\theta=0°$) provided friction is sufficiently small. In this case, two additional moment arms, a_2 and a_3, should be included in the force balance:

$$a_2 = \frac{a_1 \sin(\theta+\alpha)}{\cos(\alpha)} \qquad \textbf{6-8}$$

$$a_3 = \frac{a_1 \cos(\theta+\alpha)}{\cos(\alpha)} \qquad \textbf{6-9}$$

where α is the off-centering angle as illustrated in Figure **6.6**. For the off-centered tip, the equivalent F_T applied on the moment arm a_1 to balance the torsional components of F_F and F_N during the approach or retraction cycle of the *f-d* curve is expressed as:

$$a_1 F_T^A = a_2 F_N^A - a_3 F_F \qquad \textbf{6-10}$$

$$a_1 F_T^R = a_2 F_N^R + a_3 F_F \qquad \textbf{6-11}$$

Substituting equations 8 and 9 into equation 10 or 11 yields:

$$F_T^A = F_N^A \frac{\sin(\theta+\alpha)}{\cos(\alpha)} - F_F \frac{\cos(\theta+\alpha)}{\cos(\alpha)} \qquad \textbf{6-12}$$

$$F_T^R = F_N^R \frac{\sin(\theta+\alpha)}{\cos(\alpha)} + F_F \frac{\cos(\theta+\alpha)}{\cos(\alpha)} \qquad \textbf{6-13}$$

Substituting eq **6-3** into eq **6-12** or eq **6-5** into eq **6-13** yields eqs **6-4** and **6-6**, respectively, when α=0° (centered tip). However, when α≠0°, the result yields:

$$F_T^A = F_A[\tan(\theta)+\tan(\alpha)] - \frac{F_F}{\cos(\theta)} \qquad \textbf{6-14}$$

$$F_T^R = F_A[\tan(\theta)+\tan(\alpha)] + \frac{F_F}{\cos(\theta)} \qquad \textbf{6-15}$$

Substituting eqs **6-2** and **6-3** into eq **6-14** as well as eqs **6-2** and **6-5** into eq **6-15** yields F_T in terms of F_A, μ, and the *offset* (the friction force due to adhesion):

$$F_T^A = F_A[\tan(\theta)+\tan(\alpha)] - \frac{F_A\mu + offset\cdot\cos(\theta)}{\cos(\theta)^2 + \mu\sin(\theta)\cos(\theta)} \qquad \textbf{6-16}$$

$$F_T^R = F_A[\tan(\theta)+\tan(\alpha)] + \frac{F_A\mu + offset\cdot\cos(\theta)}{\cos(\theta)^2 - \mu\sin(\theta)\cos(\theta)} \qquad \textbf{6-17}$$

Assuming that the degree of sliding down and up the sloped surface is small such that the error in Δz is negligible (the validity of this assumption will be discussed later), the slope of the approach and retraction cycles (in units of N/m) of the lateral response of the *f-d* curve is then:

$$\Delta Lat^A = k_N[\tan(\theta)+\tan(\alpha)] - \frac{k_N\mu}{\cos(\theta)^2 + \mu\sin(\theta)\cos(\theta)} \qquad \textbf{6-18}$$

$$\Delta Lat^R = k_N[\tan(\theta)+\tan(\alpha)] + \frac{k_N\mu}{\cos(\theta)^2 - \mu\sin(\theta)\cos(\theta)} \qquad \textbf{6-19}$$

Mathematically, eqs **6-18** and **6-19** state that when friction is present, the slope of the retraction *f-d* curve ($\Delta Lat^R = dF_T^R/dz$) is larger than the slope of the approach *f-d* curve ($\Delta Lat^A = dF_T^A/dz$). Additionally, as μ increases, the response deviates non-

symmetrically from the frictionless response (μ≈0), i.e., the difference between ΔLat^A and ΔLat^R from the frictionless response becomes larger. The extent of this asymmetry can be calculated using Eqs **6-18** and **6-19** for a range of friction coefficients from 0.01 to 1. In Figure **6.7**, the percentage difference between the frictionless surface and the average lateral response $\left(\Delta Lat^A + \Delta Lat^R\right)/2$ is illustrated. This difference is predicted to be ~10% when μ ≈ 0.3. Therefore, if friction is small, the average slopes can be used as an approximation of the lateral force generated on the sloped surface.

Eqs **6-18** and **6-19** are not yet complete for AFM calibration. Typically, there is a detector crosstalk component due to the misalignment between the vertical and lateral laser reflection axes and the laboratory coordinates of the four-quadrant position-sensitive detector. Figure **6.8**A illustrates the case where the detector is perfectly aligned to the laser beam reflection axes for normal and lateral deflections. However, if the detector is not perfectly aligned with respect to the laser beam reflection, the detector crosstalk component alters the lateral response signal as shown in Figure **6.8**B. This misalignment essentially results in an additional slope (ΔD) in the lateral signal. With this addition, eqs **6-18** and **6-19** can be expressed with all the necessary variables for lateral AFM calibration. The corrected final result is:

$$\left(\Delta L^A + \Delta D\right)\cdot S_L = k_N\left[\tan(\theta) + \tan(\alpha)\right] - \frac{k_N \mu}{\cos(\theta)^2 + \mu\sin(\theta)\cos(\theta)} \qquad \textbf{6-20}$$

$$\left(\Delta L^R + \Delta D\right)\cdot S_L = k_N\left[\tan(\theta) + \tan(\alpha)\right] + \frac{k_N \mu}{\cos(\theta)^2 - \mu\sin(\theta)\cos(\theta)} \qquad \textbf{6-21}$$

Here, ΔL^i represents the slope of the lateral signal of the *f-d* curve in V/m and S_L the lateral calibration factor in (N/V). Again, the superscript *A* and *R* represent the direction

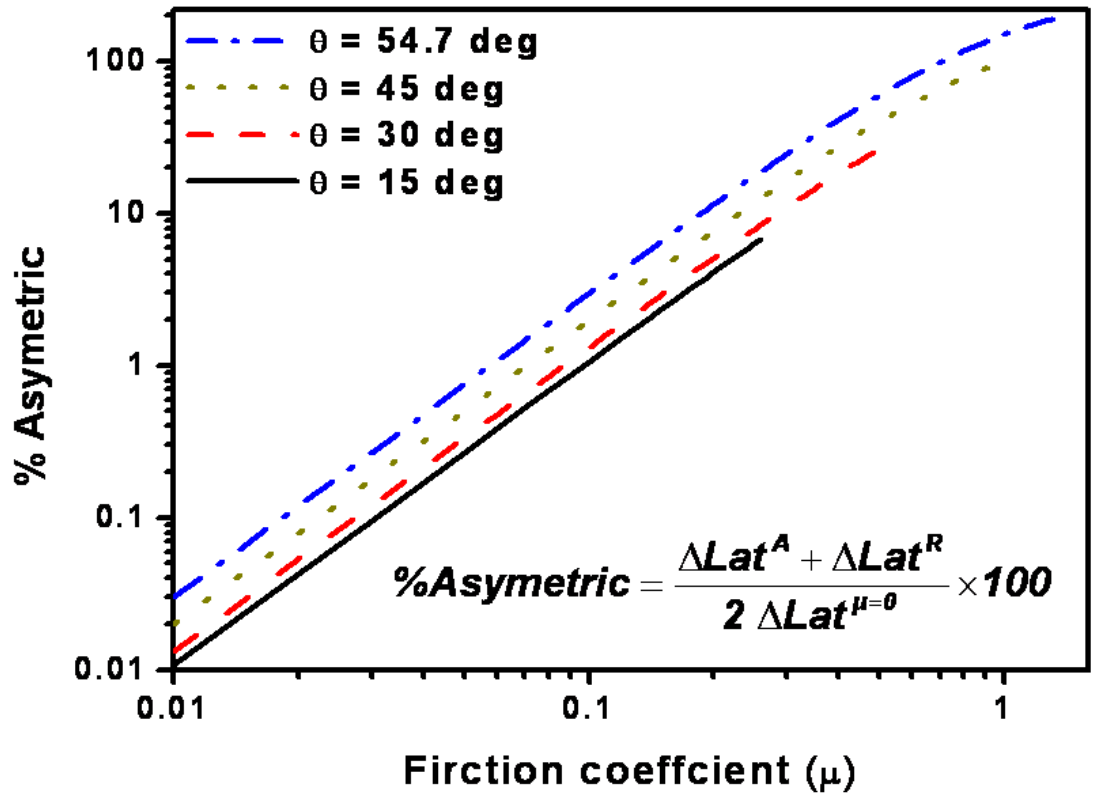

Figure **6.7**: The percentage difference between the average lateral responses as given in Equations 18 and 19 when friction is present ($\mu \neq 0$) vs. the frictionless case ($\mu = 0$).

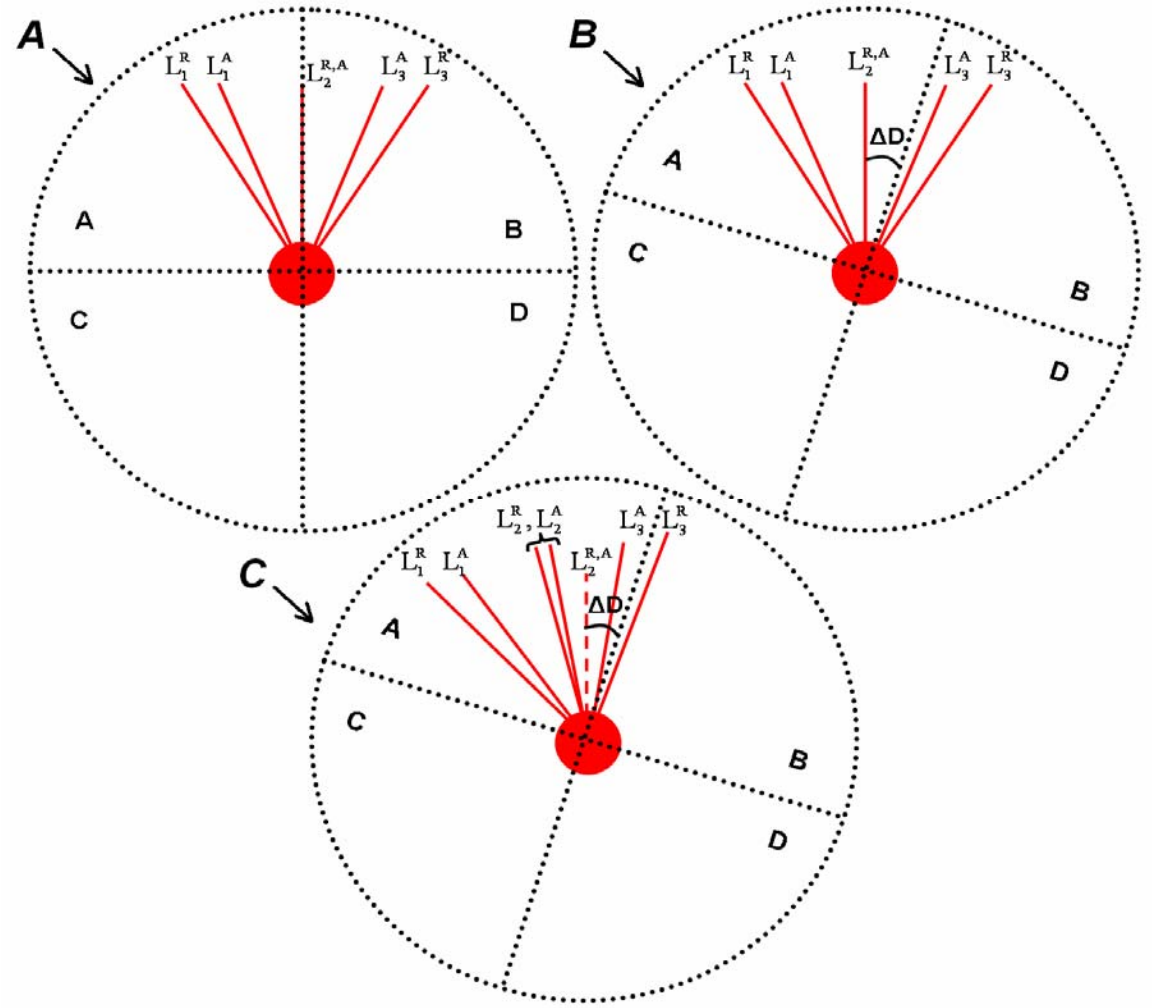

Figure **6.8**: Theoretical laser beam path on the four-quadrant photo detector on facets 1, 2, and 3 of TGF-11 during the approach and retraction curves in the repulsive region.

A) In this case no detector crosstalk is present (orthogonal).
B) In this case the detector is not orthogonal and detector crosstalk is present.
C) In this case the detector is not orthogonal and detector crosstalk is present. Additionally, the tip is off-centered. The solid lines for Facet 2 represents the laser beam path if the tip is allowed to slide laterally. The dashed line is when $\tan(\alpha) < \mu$.

of motion, approach and retraction, respectively. In the DFBM experiment, the detector crosstalk effect (ΔD) and the torsional motion due to the tip off-center ($\tan(\alpha)$) cannot be determined independently.

In this method, the detector crosstalk effect (ΔD) and the degree of tip off-center (α) cannot be determined simultaneously. If $\tan(\alpha) < \mu_{static}$, then the tip will not slide on the horizontal surface (facet 2). This is illustrated in Figure **6.8**C as the dashed line for L_2. The solid L_2 lines represent the case where the tip should slide laterally. When the tip does not slide, the lateral signals from facets 1 and 3 data look asymmetric with respect to facet 2. Additionally, asymmetric data occurs if the calibration grating is not mounted completely horizontal (θ on facet $2 \neq 0°$). Therefore, because of the difficulty in removing detector crosstalk and uncertainty in α, only the lateral data from facets 1 and 3 should be used in determining a calibration factor.

6.4 Experimental Details

Macro-scale model cantilever experiments were conducted with a home-built setup. The macro-cantilever was made up of a smooth Plexiglas (PMMA) plate [29.21 cm long (l), 3.8 cm wide (w), and 0.23 cm thick (t)] mounted on an aluminum holder with a position adjustable laser pointer mounted at the top (seen in Figure **6.9**). The position of the laser was adjusted such that the beam reflected off the cantilever approximately 3 cm from the end of the cantilever at an angle approximately 45° from the surface normal. Reflected beam displacements were measured with a graphical paper positioned

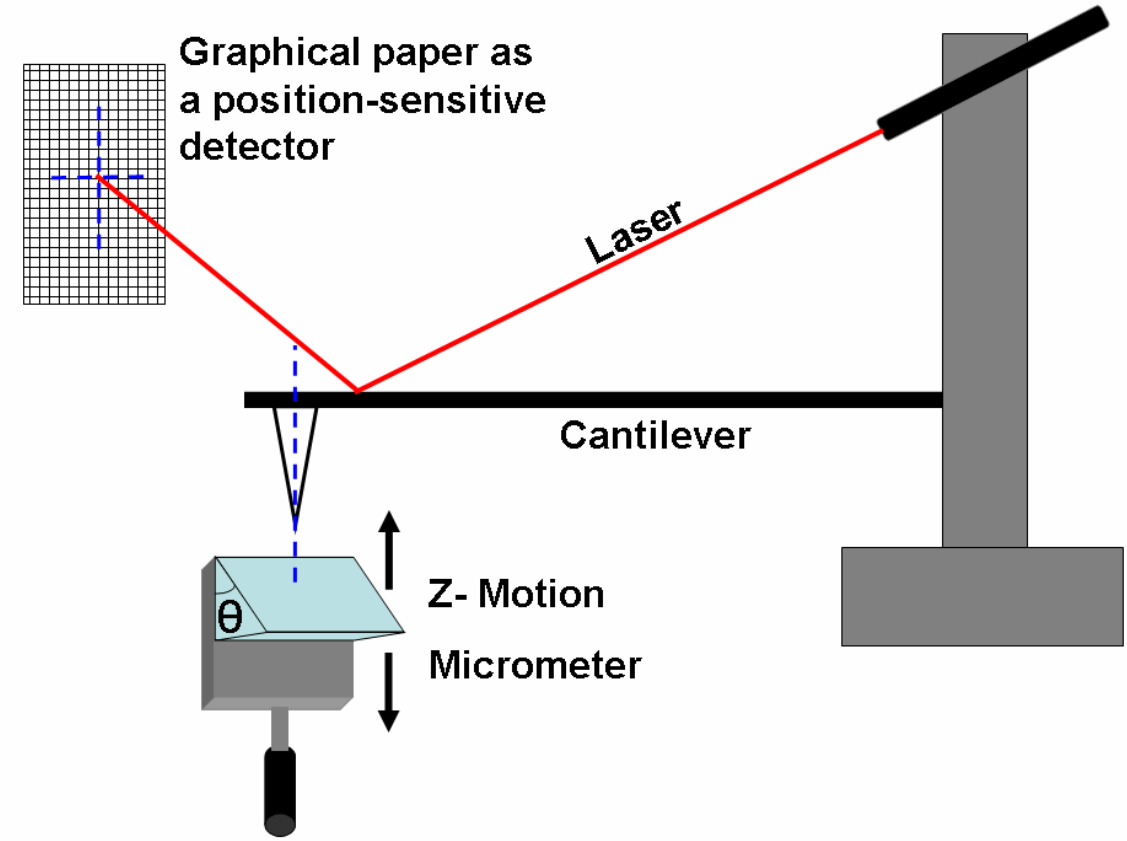

Figure **6.9**: Schematic representation of the homebuilt, macro-scale cantilever setup.

approximately 3.5 m from the cantilever. The paper was positioned such that the reflected beam of light from the laser hit the paper parallel to its surface normal. During each experiment, the displacement of the cantilever was controlled by using a micrometer. Various substrates mounted to the micrometer with differing frictional responses and angles deflected the cantilever. To model the sharp AFM tip, a sharp steel screw either ~2.6 cm long or ~1.3 cm long was positioned in the center of the cantilever or off-centered by ~1.3 cm. The distance from the tip mounting position to the cantilever end was 2.6 cm.

Prior to any experiments, the normal spring constant of the macro-scale cantilever was determined by placing weights of known mass (m) at the end of the tip with the xy plane of the cantilever perpendicular to the force of gravity, g = 9.81 m/s^2 (horizontal cantilever mounting). The applied force acting normal to the cantilever is then the product, $m \times g$. The displacement of the cantilever from its free standing position (m = 0 g) was measured simultaneously. These measurements yielded a normal spring constant k_N = 12.8 ±0.2 N/m. Based on cantilever beam theory, the value of k_N suggests a Young's modulus of ~2.8 GPa which is an acceptable value for PMMA.[17]

Calibration of the lateral signal was done directly on the graphical paper by performing all experiments with the cantilever xy plane parallel to the force of gravity (vertical cantilever mounting). Various weights of known mass were placed at the end of the tip and the change in the laser position on the graphical paper was recorded. The applied force acting perpendicular to the moment arm of the cantilever is then the product, $m \times g$. In this way, the lateral deflection sensitivity of the macro-scale cantilever was determined precisely.

AFM experiments were performed with a Molecular Imaging Pico scanning probe microscopy head with a 6 micron scanner and a RHK SPM 100 controller. Cantilevers from MikroMash (Ultrasharp series) were used as received. The normal spring constant for each cantilever was calibrated via the Sader Method.[5] All force distance curves were collected at a rate of 20 nm/s. Force-distance (*f-d*) measurements were performed on a commercially available calibration grating, an Ultrasharp TGF-11 procured from MikroMasch as illustrated in Figure **6.2**.

6.5 Results and Discussion

6.5.1 Macro-scale Cantilever Case

Figure **6.10** plots the results of various *f-d* curves on a glass surface with various slopes. The combination of a sharp stainless steel tip and a smooth glass surface provided macro-scale *f-d* measurements for the essentially frictionless surface case as the approach and retraction curves were identical. Data points were taken approximately every 0.13 cm of normal deflection. The lines in the figure represent the theoretical lateral response for a frictionless surface for a centered tip as expressed in equations **6-4** or **6-6** for a frictionless surface $F_F = 0$ N. The theoretical calculation reproduced the experimental data within the experimental error range.

When the tip is off-centered ($\alpha \neq 0°$), the lateral response differs. This is illustrated in Figure **6.11**. In this case, the ~2.6 cm long tip was off-centered by ~1.3 cm

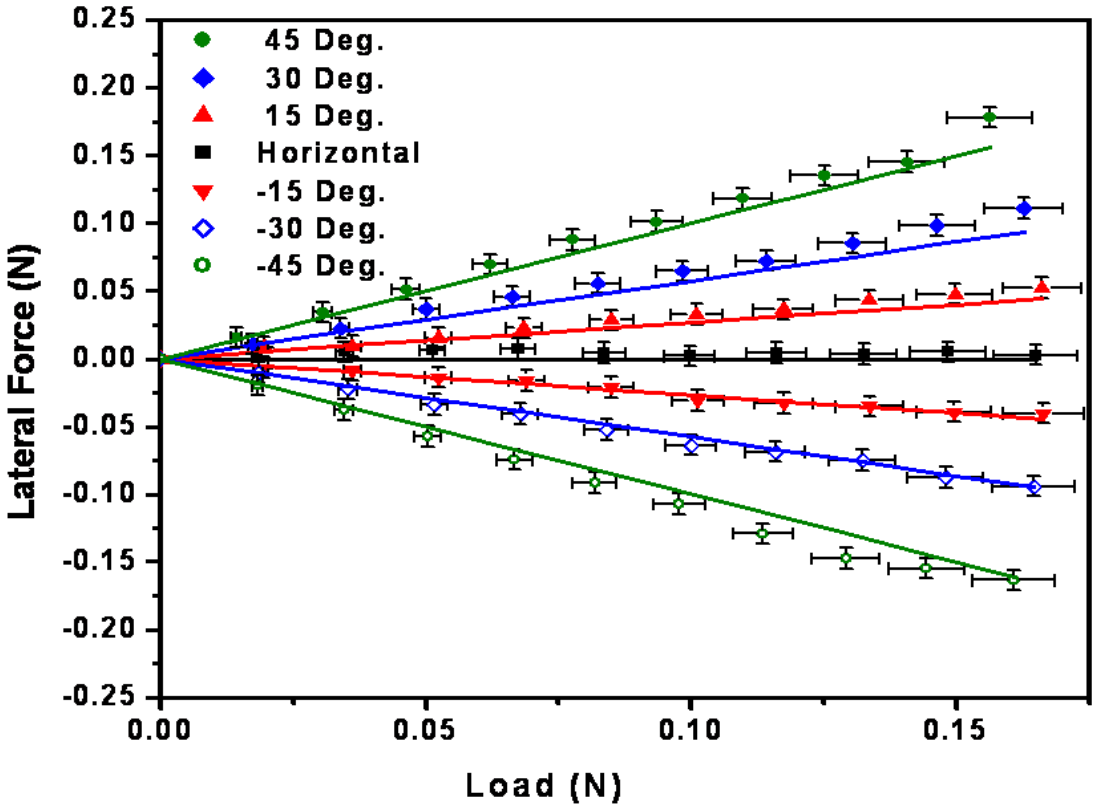

Figure **6.10**: Macro-scale *f-d* curves of the centered tip on a glass surface. The lines represent the frictionless response.

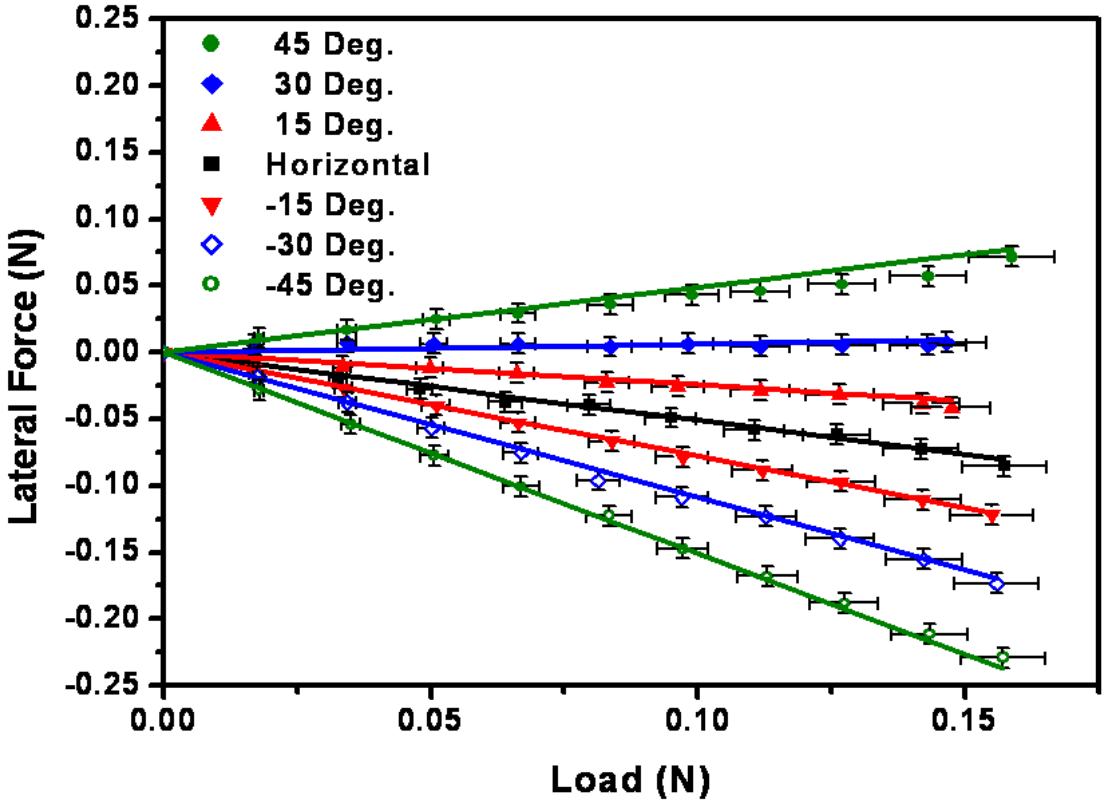

Figure **6.11**: Macro-scale *f-d* curves of the off-centered tip on a glass surface. The lines represent the frictionless response.

from the center of the cantilever, providing $\alpha = 27°$. Once again, the surface was glass and there was no noticeable difference in the approach and retraction. This indicated that the friction was negligible. The lines represent the theoretical prediction for the frictionless case ($F_F = 0$ N) for an off-centered tip as expressed in equations **6-14** or **6-15**. It is apparent that the deviation of the lateral response on the sloped surface from that of the horizontal case is opposite for the slopes θ and $-\theta$. Upon comparison of the centered and off-centered cases, it can be clearly seen that the result of the off-centered tip (Figure **6.11**) shifts the data from the centered tip case (Figure **6.10**) by $\tan(\alpha)$. These behaviors are well explained with the force balance relationship expressed in equations **6-14** and **6-15**.

It is also important to note that on the horizontal surface ($\theta = 0°$), the magnitude of the lateral deflection observed at the detector was the same with the shorter 1.3 cm long tip off-centered by 1.3 cm from the center of the cantilever (providing $\alpha = 45°$; data not shown). This is because the length of the moment arm a_2 is the same on the horizontal surface regardless of tip length. However, because this tip is shorter (by ½), the tangential forces (F_T) required to twist the cantilever the same degree must be twice as large. Therefore, the lateral calibration on the detector was 2 times that of the longer tip, as expected. While the deflection was the same on the horizontal surface, the actual lateral force applied at the end of the tip to the surface is larger.

In order to illustrate the contribution of friction to the lateral response, the 2.6 cm long tip was centered on the cantilever and *f-d* curves were acquired on a wood surface. There is a noticeable difference between the approach and retraction responses on the 45^o sloped wood surface as illustrated in Figure **6.12**. As predicted by eqs **6-18** and **6-19**,

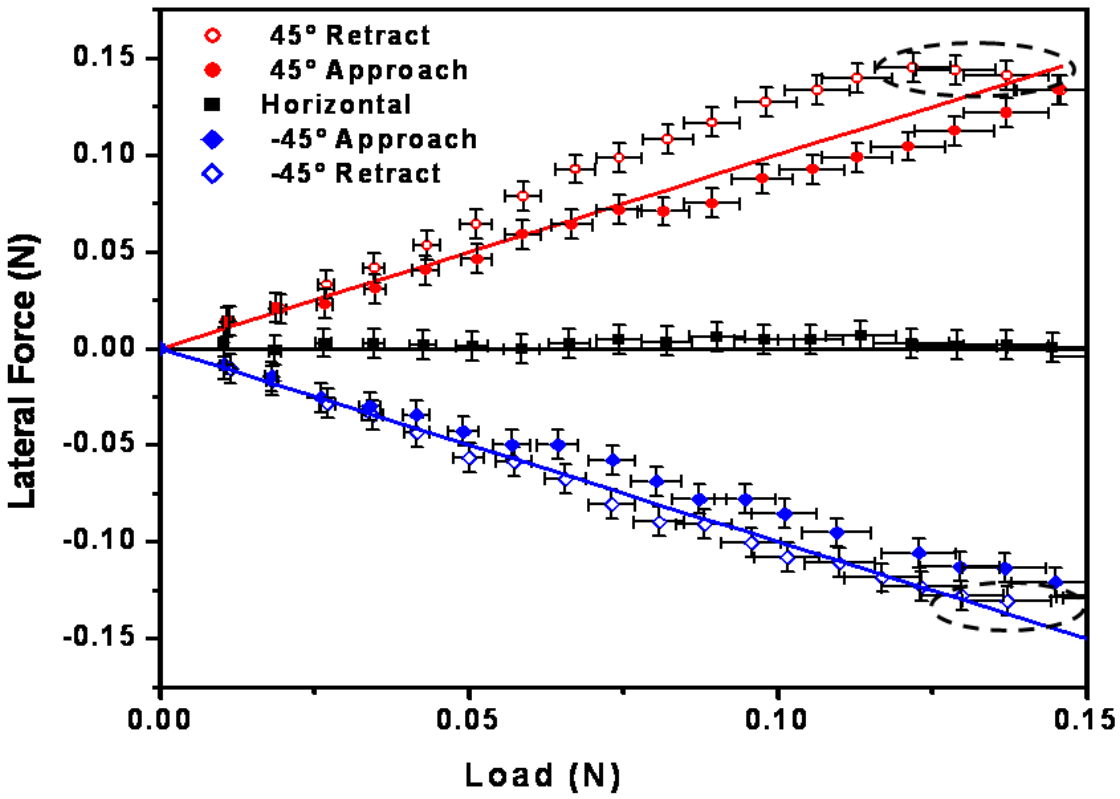

Figure **6.12**: Macro-scale *f-d* curves of the centered tip on a wood surface. The lines represent the frictionless response.

upon retraction there is more lateral twisting when compared with the approach cycle. This is due to the change of the frictional vector upon changing directions of motion. The lines in the figure represent the frictionless case. It is also apparent that different contact locations provide different frictional responses as observed in the difference in hysteresis between the 45° and -45° slopes. In the initial portions of the retraction curve (where the direction of motion turns 180^{o} from approach to retraction), the lateral response increases even though the applied normal load decreases (highlighted with dashed lines in Figure **6.12**). This is due to the change in frictional response at the turning point from approach (downward sliding) to retract (upward sliding). Taking the average slopes of the approach and retraction curves yielded an average error of <5% when compared with the theoretical lines for the frictionless case. In this case, only the linear portion of the retraction curve was used and the transitional lateral response at the turning point (circled region) was excluded.

6.5.2 AFM Case

Force-distance curves were collected on a three-facet calibration grating as illustrated in Figure **6.2**. Five sets of approach and retraction curves obtained on facets 1 and 3 as well as two approach/retraction curves from facet 2 are given in Figure **6.13**. The lateral signals in the *f-d* curves on facet 2 (horizontal surface) are very small. This implies that either the detector cross-talk and tip off-set effects are cancelling each other or they are very small. The data on facets 1 and 3 are symmetric with respect to those on facet 2 as should be expected.

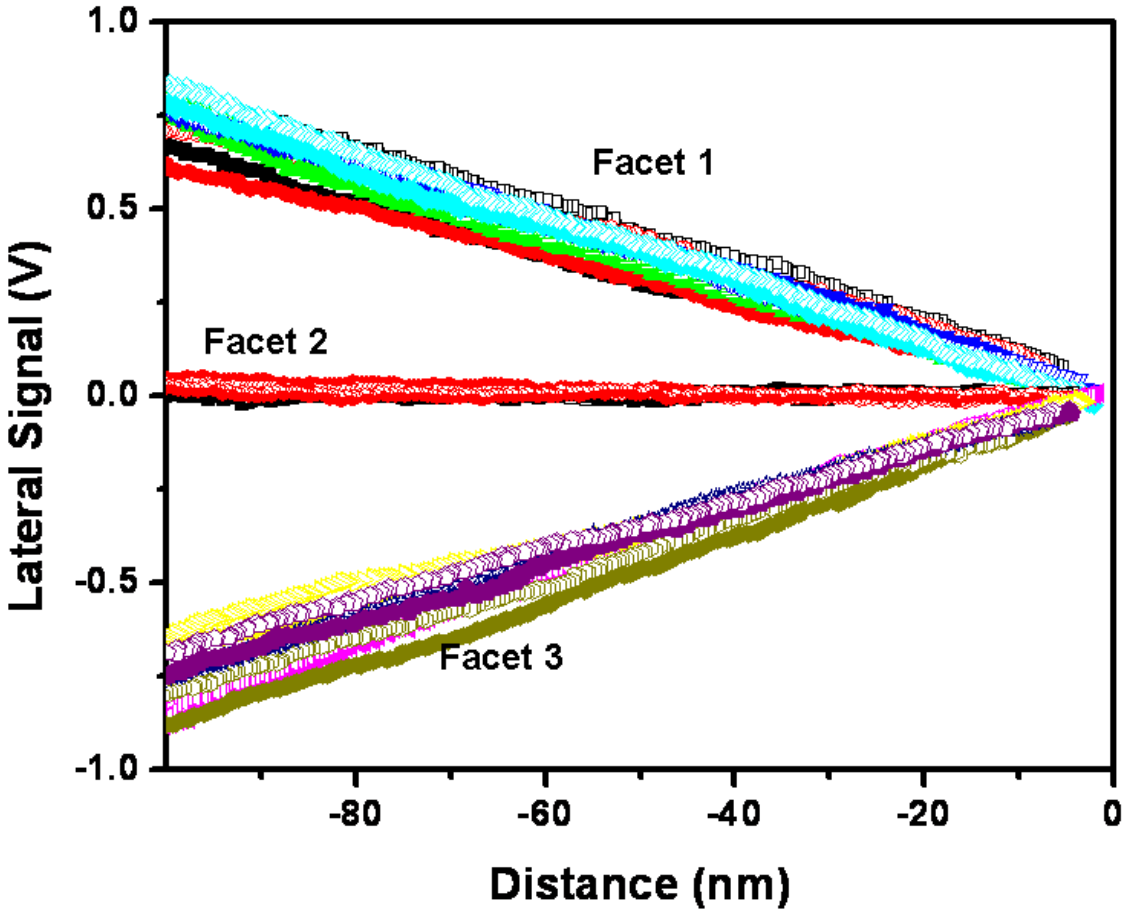

Figure **6.13**: Multiple AFM *f-d* curves on TFG-11 calibration grating. Each line represents approach and retraction.

A typical approach/retraction cycle on each facet is presented in Figure **6.14**. Like in the case of the macro-scale experiments, one facet appears to have a much larger frictional response than the other. This might be due to differences in the actual contacting area between the tip and these facets. Or this could be due to the piezo hysteresis, surface roughness, differences in localized surface chemistry, etc. However, these artifacts cannot be fully controlled in AFM experiments. Due to these uncertainties, the data is processed in two different approximation ways and compared to evaluate their practicality.

The first way to interpret the data is to take an average of all the approach curves and a separate average of all the retraction curves obtained for facets 1 and 3. Table **6.1** presents these average slopes from the data in Figure **6.13**.

Table **6.1**: Average lateral slope response

ΔL (MV/m)					
Facet 1		Facet 2		Facet 3	
Approach	Retract	Approach	Retract	Approach	Retract
8	8.09	-0.39	-0.32	-7.25	-7.7

These four slopes can be used to process the data to determine S_L, μ for each facet, and ΔD or α. Mathematically ΔD and α are indistinguishable and cannot be determined independently from the DFBM analysis. Importantly, S_L is not influenced by this uncertainty. Expressing equations **6-20** and **6-21** for facets 1 and 3 yields (where θ_1 = 54.7° and θ_3 = -54.7° for TGF-11):

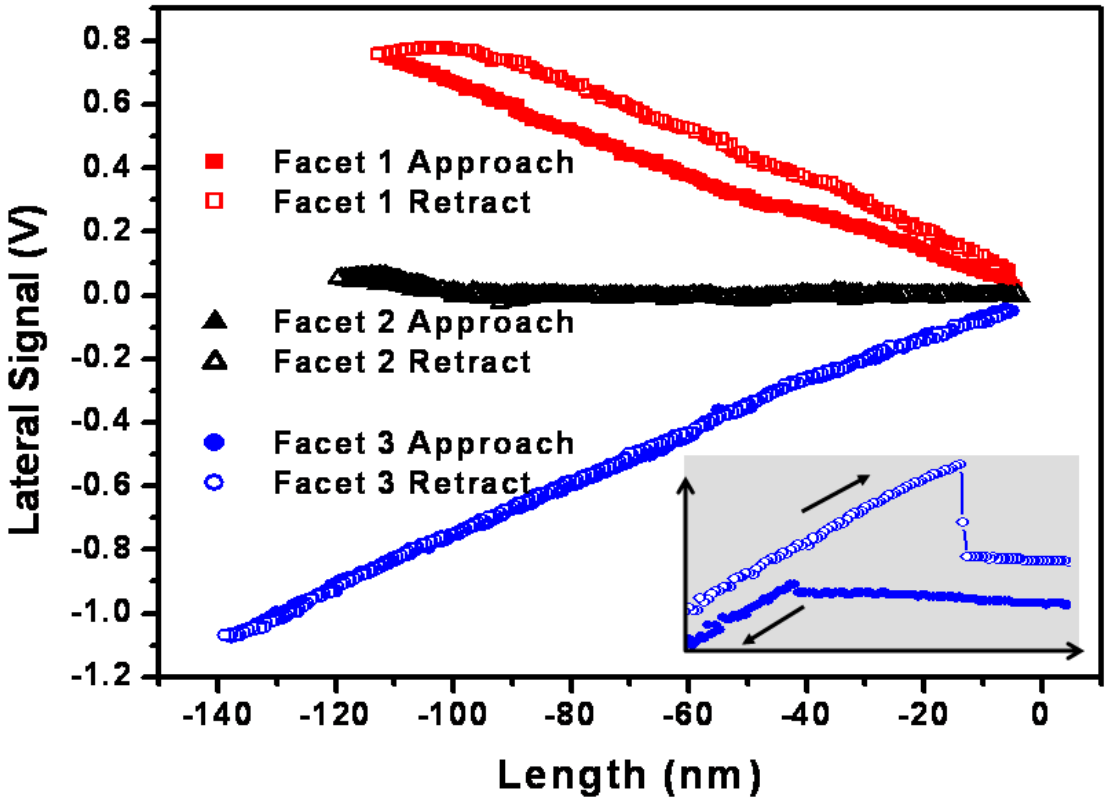

Figure **6.14**: Single AFM *f-d* curves on TGF-11 calibration grating. Each line represents approach and retraction. The inset shows the snap-in and snap-off parts of one single *f-d* curve. In the inset, the approach and retraction lines are shifted vertically to show the lateral signals in the tensile region of the *f-d* curve.

$$\left(\Delta L_1^A + \Delta D\right)\cdot S_L = k_N\left[\tan\left(\theta_1\right)+\tan\left(\alpha\right)\right]-\frac{k_N\mu_1}{\cos\left(\theta_1\right)^2+\mu_1\sin\left(\theta_1\right)\cos\left(\theta_1\right)} \qquad \textbf{6-22}$$

$$\left(\Delta L_1^R + \Delta D\right)\cdot S_L = k_N\left[\tan\left(\theta_1\right)+\tan\left(\alpha\right)\right]+\frac{k_N\mu_1}{\cos\left(\theta_1\right)^2-\mu_1\sin\left(\theta_1\right)\cos\left(\theta_1\right)} \qquad \textbf{6-23}$$

$$\left(\Delta L_3^A + \Delta D\right)\cdot S_L = k_N\left[\tan\left(\theta_3\right)+\tan\left(\alpha\right)\right]+\frac{k_N\mu_3}{\cos\left(\theta_3\right)^2-\mu_3\sin\left(\theta_3\right)\cos\left(\theta_3\right)} \qquad \textbf{6-24}$$

$$\left(\Delta L_3^R + \Delta D\right)\cdot S_L = k_N\left[\tan\left(\theta_3\right)+\tan\left(\alpha\right)\right]-\frac{k_N\mu_3}{\cos\left(\theta_3\right)^2+\mu_3\sin\left(\theta_3\right)\cos\left(\theta_3\right)} \qquad \textbf{6-25}$$

The subscript 1 and 3 represents the facet 1 (+54.7^o) and facet 3 (-54.7^o). The second way to interpret the data is to take an average of *all* the approach and retraction curves on facets 1 and 3. In this case, the data can be treated with the frictionless or "complete slip" model. The lateral calibration factor is then found by using the following equation:

$$S_L = \frac{k_N\left[\tan\left(\theta_1\right)-\tan\left(\theta_3\right)\right]}{\left(\Delta L_1^{Average}-\Delta L_3^{Average}\right)} \qquad \textbf{6-26}$$

These two methods of data interpretation are presented in Table **6.2**. The data shows that the frictionless approximation agrees very well with the more rigorous solution which includes friction. This is also explained with Figure **6.7**. When the coefficient of friction is less than 0.1, the average of the approach and retraction cycle is within 3% of the real value (when $\theta = 54.7°$). As the coefficient of friction increases, the error in eq **6-26** increases. Therefore, eq **6-26** can be used to estimate the lateral calibration factor for low friction cases. Once S_L is determined, the coefficient of friction should be checked to make sure the error is negligible. The coefficient of friction is easily estimated by taking the difference between eqs **6-22** and **6-23** or **6-24** and **6-25** and solving for μ_1 or μ_3 respectively. Once determined, Figure **6.7** can be used to validate the

use of the frictionless approximation. In the case of facet 3, where friction was the highest, the potential error in using the average frictional response is less than 0.1%. This is also consistent with the experimental data shown in Table **6.2**.

Table **6.2**: Lateral AFM DFBM calibration results

S_L (nN/V)		μ	
Frictionless approximation Eq. **6-26**	Taking into account friction Eq. **6-22** – Eq. **6-25**	Facet 1	Facet 3
85.5	85.6	0.003	0.014

The coefficient of friction on both facets is quite low in this case. This might be due to organic contaminates present on the calibration grating, since it was not cleaned. Recently, Salvadori and co-workers measured the coefficient of friction by performing f-d curves on sloped surfaces.[18] In their experiments, a silicon afm tip sliding against a silicon surface yielded a coefficient of friction of 0.047.

The validity of assuming that the error in Δz due to tip sliding is negligible depends on the cantilever properties, moment arm length a_1, and θ. The normal spring constant for a rectangular cantilever with isotropic material properties can be estimated from the material properties and its geometry:[7]

$$k_N = \frac{E \cdot w \cdot t^3}{4 \cdot l^3} \qquad \textbf{6-27}$$

Here, E is Young's modulus of the material and w, t, and l the width, thickness, and length of the cantilever, respectively. Similarly, the lateral twisting spring constant can be estimated as:

$$k_\phi = \frac{E \cdot w \cdot t^3}{6(1+\upsilon) \cdot l \cdot a_1^2} \qquad \textbf{6-28}$$

Here υ is Poisson's ratio. When the tip makes contact with the surface but the cantilever deflection is zero, the position of the cantilever in the z direction is set to be 0 nm. As the cantilever's tip is pressed against a slope surface, the contact will slide down the surface and so does the cantilever plane that reflects the laser beam. The actual degree of cantilever deflection (in the z-direction) from the point of contact (Δz^{actual}) is always smaller than the magnitude of motion in the z-direction recorded during the *f-d* curve on a sloped surface (in the limited or complete slip case). Equations **6-1**, **6-4**, **6-27**, and **6-28** can be used to determine the lateral slipping distance along the surface (Δy) for the frictionless surface. Additionally the geometry of the system requires $\Delta z^{error} = \Delta y \cdot \tan(\theta)$. The result yields the maximum possible error:

$$\frac{\Delta z^{error}}{\Delta z} = \frac{3a_1^2 \tan^2(\theta)(\upsilon+1)}{2l^2 + 3a_1^2 \tan^2(\theta)(\upsilon+1)} \qquad \textbf{6-29}$$

Here Δz is the magnitude of piezo motion in the z-direction after contact. When υ = 1/3, equation **6-29** yields:

$$\frac{\Delta z^{error}}{\Delta z} = \frac{2a_1^2}{l^2 \cot^2(\theta) + 2a_1^2} \approx \frac{2a_1^2}{l^2 \cot^2(\theta)} \qquad \textbf{6-30}$$

Typically, the cantilever length (l) is much longer than the moment arm (a_1) so the second term in the denominator can be dropped. Figure **6.15** illustrates the estimated error in z displacement of the cantilever. As the length of the moment arm increases, the lateral twisting of the cantilever increases, and hence the point of contact slips further down the slope, increasing the error in Δz. Therefore, in order to minimize this error, either

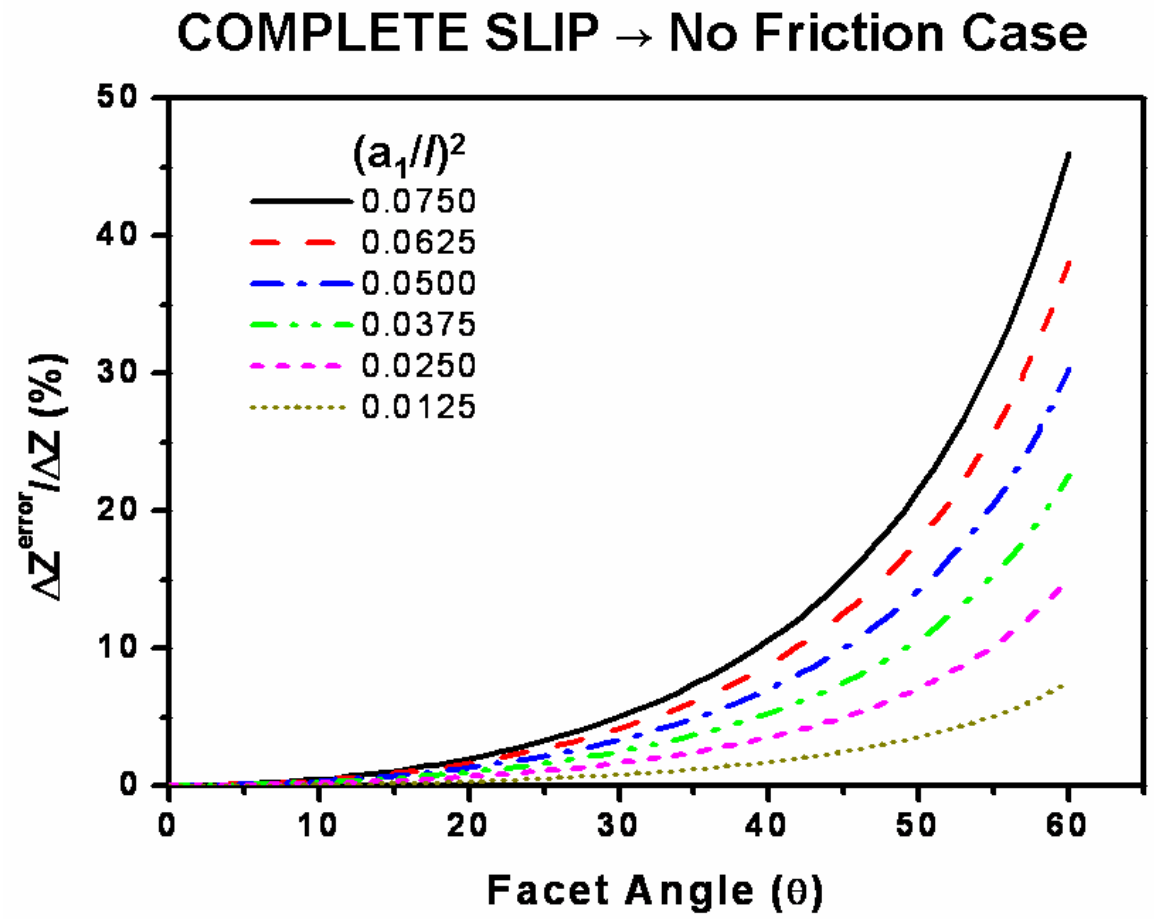

Figure **6.15**: Percent error in Δz due to tip sliding during *f-d* curve collection. These data are calculated with equation **6-30**.

cantilevers with very small a_1^2/l^2 ratios should be selected or substrates with only moderate tilt angles should be used; otherwise, this error should be incorporated into the calibration.

One additional requirement must be made in the selection of an appropriate cantilever for *any* lateral calibration technique and/or friction force measurements. Cantilevers should favor lateral twisting over lateral bending.[7, 12, 19] Forces generating a lateral response of the cantilever will cause lateral bending, lateral twisting, or a combination of these two modes, depending on the magnitudes of their spring constants. In the case of a four-quadrant position sensitive detector, only lateral twisting can be measured. Because of this, cantilevers favoring lateral twisting should be selected. The spring constant for lateral bending of the cantilever is simply:

$$k_{Lateral\_bend} = \frac{E \cdot t \cdot w^3}{4 \cdot l^3} \qquad \textbf{6-31}$$

The ratio of the lateral twisting to lateral bending for a cantilever with $\upsilon = 1/3$ is given as:

$$\frac{k_\phi}{k_{Lateral\_bend}} = \frac{1}{2}\left(\frac{l \cdot t}{a_1 \cdot w}\right)^2 \qquad \textbf{6-32}$$

Figure **6.16** plots the ratio of the lateral twisting to lateral bending spring constants for an isotropic material vs. various ratios of moment arm length vs. cantilever length $(a_1/l)^2$. In the case of our macro-scale cantilever experiments we estimate the ratio of the lateral twisting to lateral bending spring constant to be ~0.22. Since good

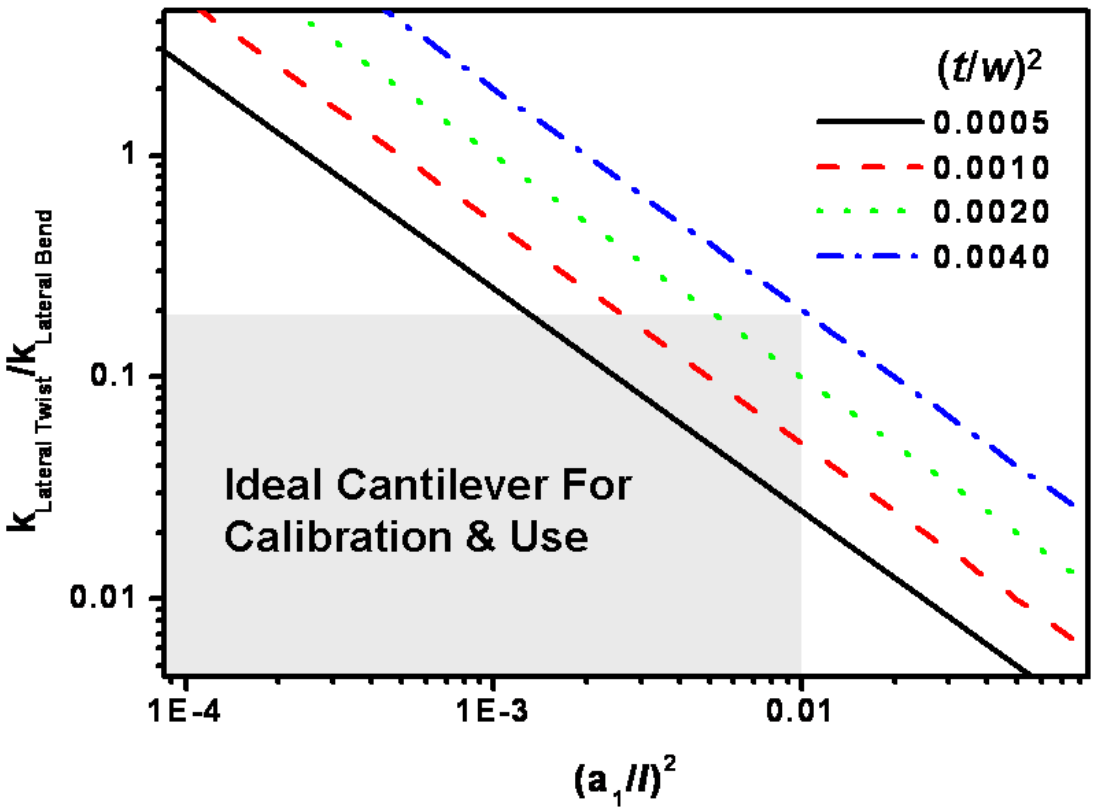

Figure **6.16**: Preference of lateral twisting over lateral bending vs. the cantilever geometry $(a_1/l)^2$.

agreement is observed between the data and the theory as presented in Figures **6.10** and **6.11**, it appears that this ratio is sufficient for lateral twisting to be observed over lateral bending of the cantilever.

When considering rectangular cantilevers for DFBM calibration with surfaces of high slopes, similar to that found in our system (54.7°), cantilevers that will provide little error in Δz as well as cantilevers that favor lateral twisting should be used. In Figure **6.16**, the x-axis is the same as that used in describing the error in Δz. Therefore, cantilevers with $(a_1/l)^2$ smaller than ~0.01 will have little error in Δz when θ = 54.7°. On the y-axis, the ratio of lateral twisting to lateral bending for various cantilevers of differing thickness to width ratios $(t/w)^2$ is presented. Based on the macro-scale cantilever experiments, the upper limit for the lateral twisting to lateral bending ratio ($k_\phi/k_{Lateral\_bend}$) can safely be set as ~0.2. These two requirements are boxed within Figure **6.16**, illustrating the window of rectangular cantilevers that are appropriate for lateral force imaging and calibration.

6.6 Conclusions

The force balance for AFM lateral force calibration from *f-d* curve measurements on sloped surfaces is described. During the *f-d* curve measurements on sloped surfaces, the AFM tip slide along the slope, which causes twisting of the cantilever. Since the degree of twisting is a function of the applied load (vertical deflection of the cantilever) and the slope of the surface, the AFM lateral signal can be calibrated with a correct force

balance. The force balance equations are derived and applied for calibration of a macro-scale cantilever system with both a frictionless surface as well as a surface with a moderate amount of friction. The experimental results were in good agreement with the values predicted from the force balance equations. By analogy, AFM cantilevers can be calibrated with this technique with much success. This method then provides a straightforward calibration of the lateral detector sensitivity without scanning. Additionally, this technique only requires the z-motion of the piezo and normal spring constant to be calibrated and is not sensitive to detector crosstalk or an off-centered AFM tip ($\alpha \neq 0°$). From simple *f-d* measurements on surfaces with known slopes, the lateral detector sensitivity is determined directly. Sources of error due to the tip sliding down the sloped surface can be minimized with the selection of appropriate cantilevers.

6.7 References

1. G. Binnig; C. F. Quate; C. Gerber, *Physical Review Letters* **1986,** 56, (9), 930-933.
2. B. Cappella; G. Dietler, *Surface Science Reports* **1999,** 34, (1-3), 1-+.
3. K. H. L. Chau; S. R. Lewis; Y. Zhao; R. T. Howe; S. F. Bart; R. G. Marcheselli, *Sensors and Actuators a-Physical* **1996,** 54, (1-3), 472-476.
4. J. E. Sader, *Journal of Applied Physics* **1998,** 84, (1), 64-76.
5. J. E. Sader; J. W. M. Chon; P. Mulvaney, *Review of Scientific Instruments* **1999,** 70, (10), 3967-3969.
6. J. P. Cleveland; S. Manne; D. Bocek; P. K. Hansma, *Review of Scientific Instruments* **1993,** 64, (2), 403-405.
7. B. Bhushan, *Handbook of Micro/Nanotribology*. CRC Press: Boca Raton, FL, 1995.
8. D. F. Ogletree; R. W. Carpick; M. Salmeron, *Review of Scientific Instruments* **1996,** 67, (9), 3298-3306.
9. M. Varenberg; I. Etsion; G. Halperin, *Review of Scientific Instruments* **2003,** 74, (7), 3362-3367.
10. G. Bogdanovic; A. Meurk; M. W. Rutland, *Colloids and Surfaces B-Biointerfaces* **2000,** 19, (4), 397-405.
11. C. P. Green; H. Lioe; J. P. Cleveland; R. Proksch; P. Mulvaney; J. E. Sader, *Review of Scientific Instruments* **2004,** 75, (6), 1988-1996.

12. W. C. Young, *Roark's Formulas for Stress and Strain, 6th Ed.* McGraw-Hill: New York, 1989.

13. R. J. Cannara; M. J. Brukman; R. W. Carpick, *Review of Scientific Instruments* **2005,** 76, (5).

14. R. W. Carpick; N. Agrait; D. F. Ogletree; M. Salmeron, *Journal of Vacuum Science & Technology B* **1996,** 14, (2), 1289-1295.

15. A. Podesta; G. Fantoni; P. Milani, *Review of Scientific Instruments* **2004,** 75, (5), 1228-1242.

16. D. S. Grierson; E. E. Flater; R. W. Carpick, *Journal of Adhesion Science and Technology* **2005,** 19, (3-5), 291-311.

17. R. Schirrer; C. Goett, *Journal of Materials Science Letters* **1982,** 1, (8), 355-357.

18. M. C. Salvadori; F. S. Lisboa; F. M. Fernandes; I. G. Brown, *Journal of Vacuum Science & Technology B* **2008,** 26, (2), 643-650.

19. J. E. Sader, *Review of Scientific Instruments* **2003,** 74, (4), 2438-2443.

Chapter 7

Chain length Dependence and Capillary Effects in Nano-asperity Friction Forces of Vapor-phase Linear Alcohol Lubricants

7.1 Summary

In this chapter, the influence of chain length on friction forces is investigated for ethanol, 1-butanol, and 1-pentanol vapor-phase lubricants on silicon oxide surfaces with an atomic force microscope. The friction force vs. load of a dull nano-asperity contact is reported. In dry conditions, the friction force scales with the applied load to the 2/3 power as expected from DMT contact mechanics. Due to the formation of a capillary at the point of contact when alcohol vapors are present, an additional frictional force is observed and appears to scale with the applied load to the 1/3 power. This chapter develops a model that describes the data well and suggests potential sources for the observed 1/3 dependence. Additionally, the shear strength of the vapor phase lubricants is observed to be inversely proportional to their chain length.

7.2 Introduction

The atomic force microscope (AFM) has been used to investigate single asperity friction and wear of various materials.[1-14] In many investigations, self-assembled monolayers (SAMs) have been deposited on oxide surfaces for use as potential molecular thin film lubricants. The AFM has been used to examine the monolayer's lubricity and wear resistance. While there have been many studies investigating the effect of SAMS on nano-asperity tribological phenomena,[13-19] what is missing were studies investigating the frictional properties of adsorbed hydrocarbon species in equilibrium with the vapor. Vapor phase lubrication using the adsorption of simple hydrocarbon species is being studied as a potential solution to the tribological challenges in MEMS.[20-23]

In this chapter, single-asperity friction force measurements are reported for ethanol, 1-butanol, and 1-pentanol on clean silicon oxide surfaces. These alcohols have comparable surface tensions (~15% difference between alcohols) but differing liquid molar volumes (up to a factor of 2 differences). Therefore, differences in the shear strength of these adsorbates are expected to be due to their differences in chain length. Both experimental and modeling results show that the effect of dragging a meniscus during sliding can be a strong contributor to the total friction force as well as the shape of the Friction-Load curve. Additionally, these molecules greatly lower the shear strength observed in friction measurements as compared with dry contact sliding.

7.3 Fundamentals of Nano-asperity friction and contact mechanics

The frictional forces exerted as an AFM tip slides against a surface depend on many variables. In the absence of capillary or meniscus formation, many studies have shown that the frictional force (F_F) to be proportional to the contact area and follow this relationship:[24-26]

$$F_F = \tau \cdot A \qquad \textbf{7-1}$$

where, A is the real contacting area between the AFM tip and the substrate and τ is the shear strength of the contact.

The contact area depends on the shape of the AFM tip, the elastic material properties, and the size of the system. In contact modeling, the end of an AFM tip is typically idealized as a sphere and the counter surface a flat plate. Depending on the size of the sphere, the adhesion forces, and deformation resistance of the materials, various different models can be used to describe the contact mechanics.

The Hertzian model is the most basic of the contact models.[27] In this model, adhesive forces are ignored. As a load is applied, the sphere deforms at the point of contact forming a contacting area between the sphere and the counter-surface. The radius of this contact area (a_{Hertz}) is simply,

$$a_{Hertz} = \left[\frac{R \cdot L}{K} \right]^{1/3} \qquad \textbf{7-2}$$

where L is the applied load, R the radius of curvature of the sphere (AFM tip), and K the effective modulus of elasticity expressed as:

$$K = \frac{4}{3}\left(\frac{1-\nu_{tip}^2}{E_{tip}} + \frac{1-\nu_{substrate}^2}{E_{substrate}} \right)^{-1} \qquad \textbf{7-3}$$

where E is the Young's modulus of elasticity and ν Poisson's ratio of the AFM tip and substrate materials.

Nano-asperity contacts often have significant adhesion force similar in magnitude with applied loads. In order to account for adhesive forces in contact mechanics, two models exist that incorporate adhesion in different ways. Each model describes the limiting conditions. One of these contact models is known as the JKR (Johnson, Kendall, Roberts) model[28] and describes the compliant limit. Due to attractive forces within the contact region, a finite contact radius, a_{JKR}, is in balance with the stored elastic energy of the tip and substrate and the loss in surface energy due to the contact area. Based on this premise, the contact radius is given as:

$$a_{JKR} = \left[\frac{R}{K}\left(L + 3\omega\pi R + \sqrt{6\omega\pi RL + (3\omega\pi R)^2} \right) \right]^{1/3} \qquad \textbf{7-4}$$

where ω is the Dupré work of adhesion and is defined as follows: $\omega = \gamma_1 + \gamma_2 - \gamma_{12}$ (where γ is the surface energy at the interface 1, 2 or 12).

As a consequence of equation **7-4,** at a critical negative load, the surfaces suddenly jump apart. This adhesion, or "pull-off" force is given as:

$$F_{JKR}^{Adh} = \frac{-3\omega\pi R}{2} \qquad \textbf{7-5}$$

At the point of pull-off, the contact radius is also non-zero. In fact, the contact radius at pull-off is:

$$a_{JKR}^{Critical} = \left(\frac{3\pi R^2 \omega}{2K} \right)^{1/3} \quad \textbf{7-6}$$

The second model that takes adhesion into account is known as the DMT (Derjaguin, Muller, Toporov) model[29] and is known as the noncompliant limit. In this model, the adhesive forces occur due to long range attractive forces between the two objects (outside of the point of contact). In this case, the contact radius (a_{DMT}) is given as:

$$a_{DMT} = \left[\frac{R}{K} (L + 2\pi R\omega) \right]^{1/3} \quad \textbf{7-7}$$

In this case, the critical negative load where the surfaces spontaneously separate is given as:

$$F_{DMT}^{Adh} = -2\omega\pi R \quad \textbf{7-8}$$

In contrast to the JKR model, at the pull-off point the contact radius is zero.

The assumptions behind the JKR and DMT contact mechanics result in differing contact mechanics behavior. Each model predicts a different dependence of the contact area with respect to the applied load. While these models may seem to contradict each other, each predicts the limits or boundaries between which real sphere-flat contacts are observed. When the materials are sufficiently compliant, have strong, short-range adhesion forces and large radii of curvature, JKR contact mechanics describe the physical phenomena quite well. If the materials are very stiff, the forces responsible for adhesion

occur over a large distance, and the contact radii are very small, the DMT model is more appropriate. Additionally, Maugis[30] and others[8] have developed models to describe systems that fall in between these limits. Tabor's parameter[31, 32] (μ_T) is often used to determine if the system falls into the JKR, DMT or transitional model and is given as:

$$\mu_T = \left(\frac{16R(\omega)^2}{9K^2 z_o^3} \right)^{1/3} \qquad \textbf{7-9}$$

where z_o is the equilibrium separation between the surfaces. This parameter is essentially a ratio between the elastic deformation due to adhesion and the length over which these adhesion forces act. In general, the DMT model applies when $\mu_T < \sim 0.1$ and the JKR model applies when $\mu_T > \sim 5$.[8] In the case of AFM tips, typically the DMT model is most appropriate. This is due to their small radius of curvature (10 to a few 100 nm's) and stiff material properties.

While these continuum models work well in many systems, they do not consider the effect of adsorbed films that may occur in ambient conditions, i.e. water on a humid day. The effect of an adsorbed film is expected to have a significant effect especially when the contacting asperity size approaches the thickness of the adsorbed film. Additionally, these films will form a meniscus at the point of contact. Capillary pressures inside the meniscus will then increase the total load applied at the tip. Such a system is described in Chapter **5.4**. Figure **7.1** illustrates this case.

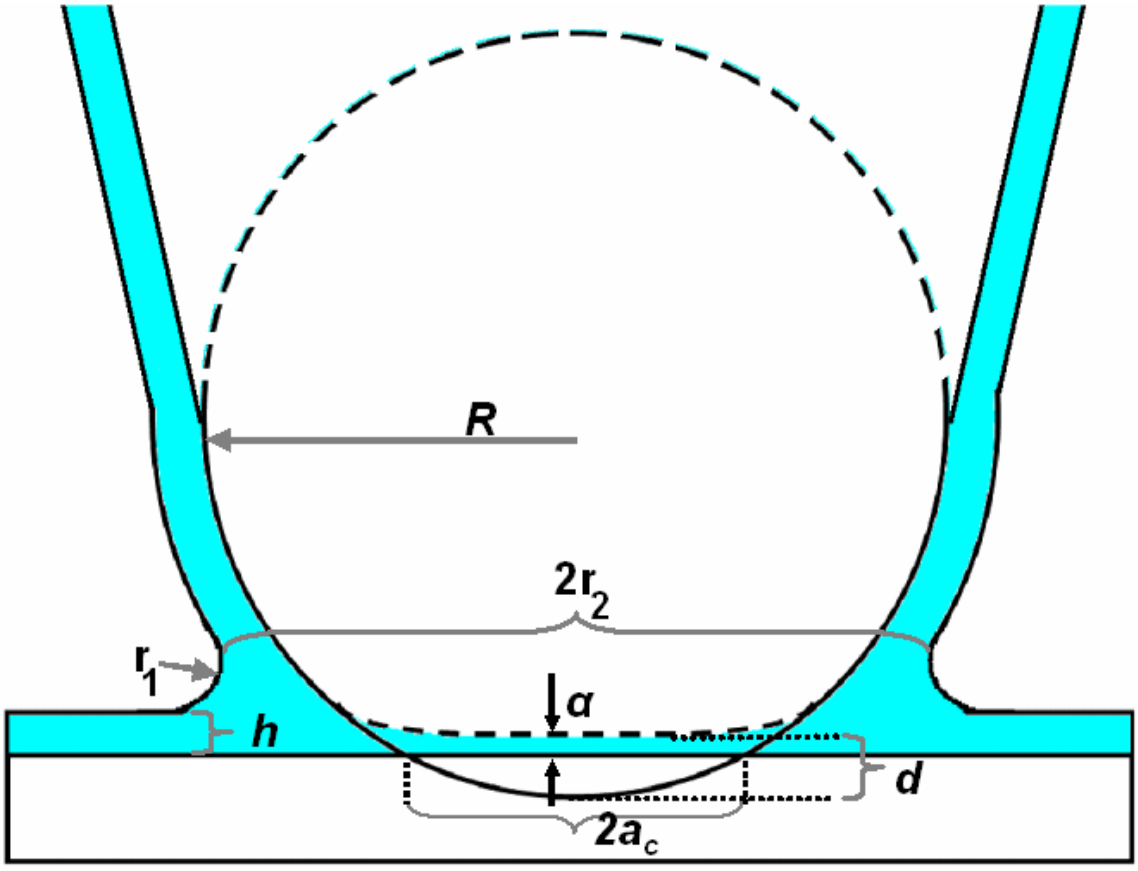

Figure 7.1: Model tip (sphere) – substrate system with adsorbed film whose thickness is *h*. Here *R* is the tip radius, a_c the contact radius, α a trapped molecular layer, *d* the penetration depth of the undeformed sphere, and r_1 and r_2 the two principle radii of curvature.

7.4 Effect of Capillary formation on Contact Mechanics and Friction of nano-asperity contacts

When a capillary meniscus exists, the capillary is expected to change the contact area, due to the increase in load from the meniscus forces. This force should be included into the contact mechanics describing the system. Fogden and White found that when a system follows DMT or Hertzian-like contact mechanics, the increase in adhesion due to a capillary forces is simply additive to the applied load.[33] In terms of DMT contact mechanics behavior should include this term as follows:

$$a_{DMT} = \left[\frac{R}{K}\left(L + F^{VDW} + F_{cap}\right)\right]^{1/3} \qquad \textbf{7-10}$$

where F_{cap} has been described in equation **5-4** from the previous chapter and F^{VDW} are the sum of the dispersion attractive forces (i.e. often described by equation **7-8)**.

In this case, friction occurring within the contact area is simply (assuming friction to be proportional to the contact area):

$$F_F = \tau \cdot \pi\left[\frac{R}{K}\left(L + F^{VDW} + F_{cap}\right)\right]^{2/3} \qquad \textbf{7-11}$$

In general however, this simple model does not seem to fully account for a more complex dependence of the friction force observed in many systems.[13, 34, 35] These systems investigated nano-asperity friction of different materials in various humid ambient conditions. One unpredictable complication in understanding the friction load curves in humid environments is due to the fact that water can cause wear of AFM tips during scanning complicating the data analysis (as R changes during the experiment.)[21]

Even with this problem, capillary forces are believed to influence friction. Sirghi suggests that friction is "enhanced" on account of energy loss due to dragging of the meniscus.[34] For example, differences in the advancing and receeding contact lines of the meniscus with the surface will cause this phenomena.[36] Additionally, surface roughness or chemical heterogeneity will cause "erratic" changes in the meniscus that can lead to these types of energy dissipations.

This additional friction force due to dragging of the meniscus ($F_F^{meniscus}$) should be proportional to the average contact line diameter and is expected to behave as follows:[34]

$$F_F^{meniscus} \propto \beta \cdot \langle CD \rangle \qquad \textbf{7-12}$$

where β depends on the sensitivity of the meniscus to energy dissipation during sliding and $\langle CD \rangle$ is the average contact line diameter of the meniscus during scanning at a given load. In the case of the torroidal approximation,[15, 37] at equilibrium the initial (undeformed) CD is estimated to be:

$$CD \propto 2\pi(r_2 + r_1) \qquad \textbf{7-13}$$

Additionally, CD is a function of the applied load. The load dependence on $\langle CD \rangle$ should follow the same proportionality as the contact radius. That is to say, as the load increases, so does the contact area/radius. This effectively displaces the meniscus contact line laterally. Therefore, the total frictional force as a function of the applied load is then:

$$F_F = \tau \cdot \pi \left[\frac{R}{K} \left(L + F^{VDW} + F_{cap} \right) \right]^{2/3} + \beta \cdot \langle CD \rangle (L) \qquad \textbf{7-14}$$

Since the real $\langle CD \rangle$ is not known during scanning, and can not be measured we can express equation **7-14** in terms of variables that can be used to describe nano-asperity friction forces measured with the AFM:

$$F_F = \tau \cdot \pi \left[\frac{R}{K} \left(L + F^{VDW} + F_{cap} \right) \right]^{2/3} + \beta' \cdot \pi \left[\frac{R}{K} \left(L + F^{VDW} + F_{cap} \right) \right]^{1/3} \qquad \textbf{7-15}$$

Where β' again depends on the sensitivity of the meniscus to energy dissipation during sliding and has units of surface energy. However, this parameter scales with the contact radius which is known, rather than an average meniscus contact line, $\langle CD \rangle$.

7.5 Experimental Setup

All AFM experiments were performed using a Molecular Imaging scanner and a RHK SPM-100 controller. Silicon (100) substrates with native oxides were prepared by cleaning via 15 min in an UV/O_3 followed by an RCA-1 step. This process provided a clean hydrophilic native silicon oxide surface. One silicon AFM cantilever, was dulled to a radius of curvature of ~125 ±25 nm and was used for all Friction-Load (*F-L*) measurements in order to minimize differences in spring constants between cantilevers and tip shapes. The cantilever was calibrated using the Sader method,[38] providing a spring constant of 0.59 N/m. Lateral calibration of the AFM was done with the DFBM method described in Section **6.5.2**. Prior to use in any of the alcohol vapor environments, the silicon AFM tip was placed in the UV/O_3 for approximately 15 min, then one short high-load scan was performed on clean silicon substrate in dry argon. The

high-load scan was used to help remove any residual chemisorbed materials from the AFM tip. *F-L* measurements were obtained at room temperature at a constant scan speed of 2 μm/s.

The partial pressure for any given alcohol is maintained by mixing a dry argon stream with an alcohol-vapor-saturated argon stream, as has been illustrated previously (Figure **2.1**). The ratio of these streams determined the relative partial pressure P/P^{sat} (P^{sat} = saturation pressure for any given alcohol). Friction-Load measurements were collected at approximately 0%, 5%, 10%, 15%, 30%, 60%, 85%, and 98% ±5% of P^{sat} for each alcohol. At each condition, the tip was scanned across the surface and various force-distance (f-d) curves were taken in different locations (before the scan and after). The load during each scan was kept low, so as to not dull the tip between the experiments. This was verified by comparing the adhesion force in f-d curves taken before and after each condition. As adhesion is proportional to the radius of tip curvature (R), the adhesion would increase after a scan if wear occurred. We observed little to no wear when alcohol vapors were present in these experiments (R increased less than 5% was the worse case observed).[21]

7.6 Results and Discussions

Friction-Load curves with varying amounts of ethanol vapor are presented in Figure **7.2**. The relative vapor pressure of ethanol in each condition is related to the saturation vapor pressure P^{sat}. In the dry case, when no alcohol vapors were present, the

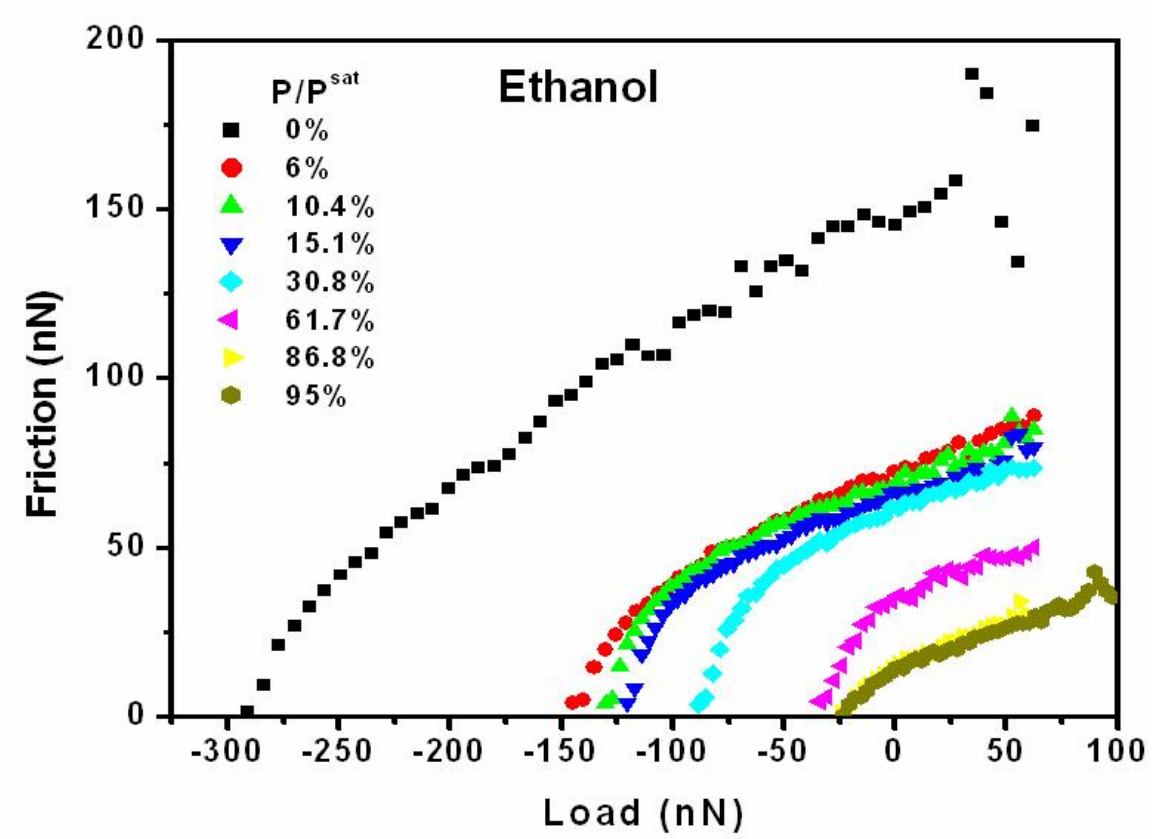

Figure **7.2**: AFM Friction-Load Curves of a silicon AFM tip as it slides against a silicon (100) substrate as a function of load at various relative partial pressures of ethanol.

pull-out force was observed near -300 nN. At the pull out condition, the friction force fell to ~0 nN, implying that snap-off occurred when the contact area fell to 0 nm^2 as DMT contact mechanics suggests. Additionally, snap-off occurs when the friction force falls to ~0 nN suggesting DMT like mechanics for each condition. Also significant is the reduction in friction observed when the environment chemistry is changed from dry to alcohol rich. These types of behaviors were observed for all the alcohol vapors (ethanol to 1-pentanol).

In order to determine if DMT contact mechanics describe the contact area as a function of load, the ethanol data is plotted in a log-log format (Figure **7.3**). In this case, the total load is the sum of the applied load as and adhesion force (–snap-off force). If the data follows a 2/3 slope, then DMT contact mechanics appear to be valid. If the data does not follow this slope, then either DMT contact mechanics does not describe the contact area, the shear strength of the contact is not constant, or there are other components contributing to friction. As the plot shows, at the dry and near saturation conditions, the slope of the data follows a 2/3 dependence (dry slope = 0.68 ±0.01 and 95% slope = 0.63 ±0.01). However, in between these conditions, the slope is not 2/3 nor is it completely 1/3 (although it is closer to 1/3). Since the dry and near saturation conditions appear to obey DMT contact mechanics, other forces must also be responsible for friction in the intermediate conditions. This is precisely what equation **7-15** would suggest. Additionally, comparison of the dry and 95% P/P^{sat} data also show a shift downward in the frictional force due to the adsorbed alcohol film.

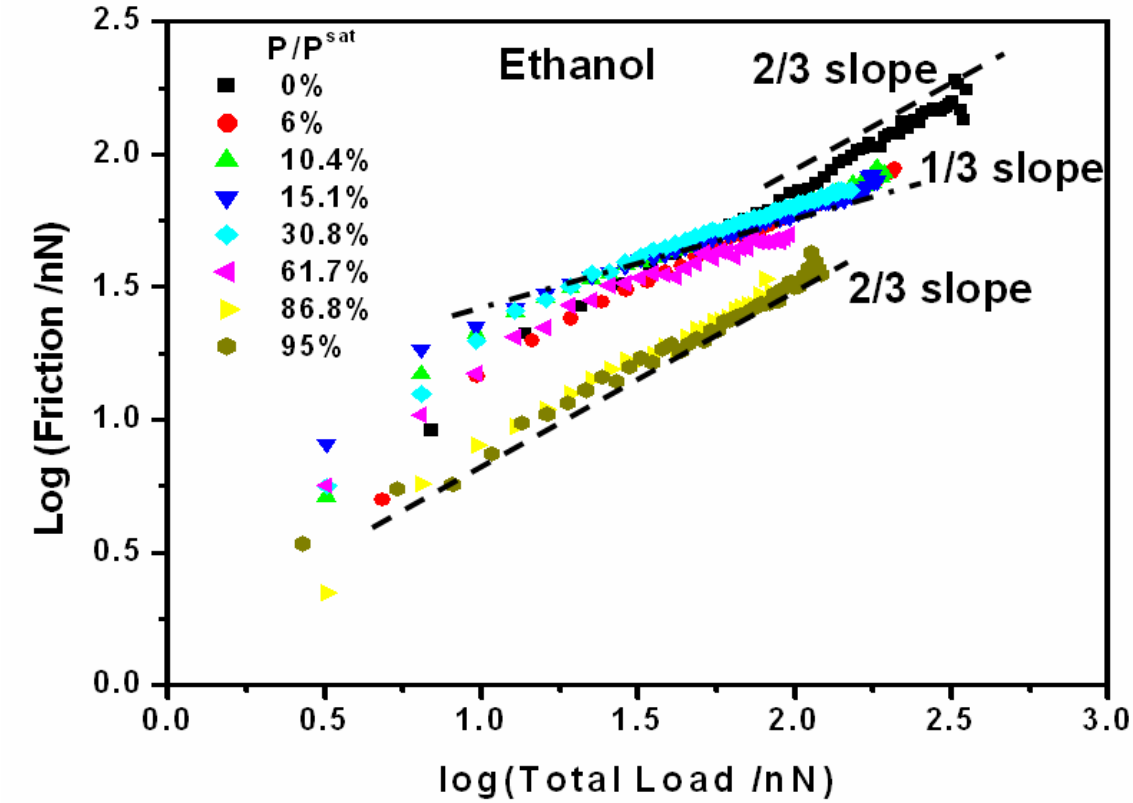

Figure **7.3**: Log-log plot of the data presented in Figure **7.2**. When alcohol vapors are present and are well below the saturation pressure of alcohol, the data follows a more 1/3 slope dependence. In the dry and saturation conditions the data follows a 2/3 slope dependence suggesting classical DMT contact mechanic behavior. (The dashed lines represent 2/3 and dash-dot lines, 1/3 slope)

An example of fitting the data with equation **7-15** or **7-11** at the intermediate condition of P/P^{sat} ~ 15% is presented in Figure **7.4**. Both the DMT and our model fits were optimized by a least squares method. What is apparent is the difficulty of the DMT model to represent the data. However, the data fits quite well with the model we present here. The "direct contact contribution" represents the component of friction due to the 2/3 dependent term in equation **7-15** which is effectively the contact area contribution of friction and follows a 2/3 dependence with respect to the load. Therefore, what dominates the frictional response is due to energy dissipations of the meniscus as it is "dragged" along the surface. Also, the magnitude of the "direct contact contribution" is remarkably similar to that of the 95% P/P^{sat} data, suggesting similar contact shear strengths.

The frictional response between each alcohol as a function of total load is presented in Figure **7.5**. In each plot, the relative partial pressure was represented for the alcohol studied relative to its saturation pressure. Based upon the isotherm presented in Figure **5.3** at the same P/P^{sat}, the average thickness of adsorbed alcohol molecules is comparable. In each condition, at the same P/P^{sat}, the friction is highest for the shortest chain length and smallest for the longest chain as should be expected. Additionally, the frictional response, as plotted in terms of total load, does not vary much between P/P^{sat} values of 10% to 30% regardless of the alcohol. A small decrease is observed as P/P^{sat} approaches 60%, while the most significant change occurs once P/P^{sat} approaches saturation conditions. This is most probably due to improved surface coverage as the partial pressure increases.

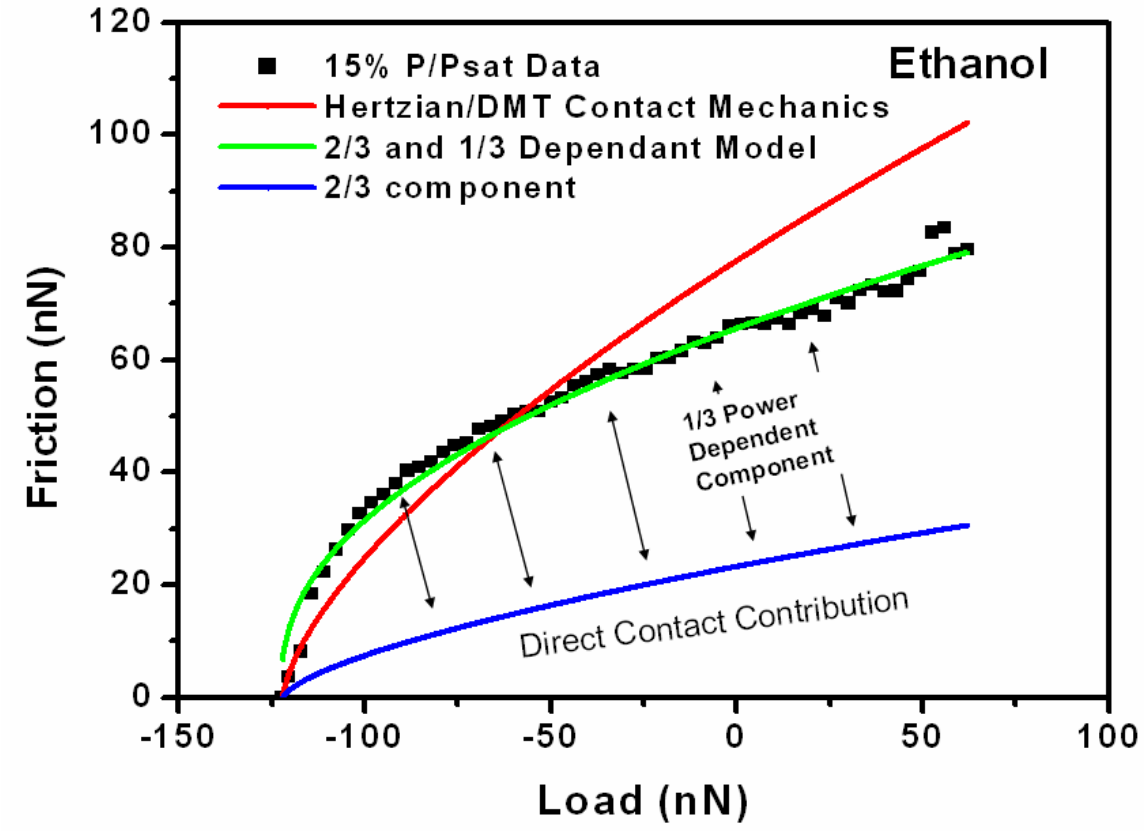

Figure **7.4**: Data fitting with a DMT contact mechanics vs. the 2/3 & 1/3 friction model described with equation **7-15.** The 2/3 component from equation **7-15** is also plotted.

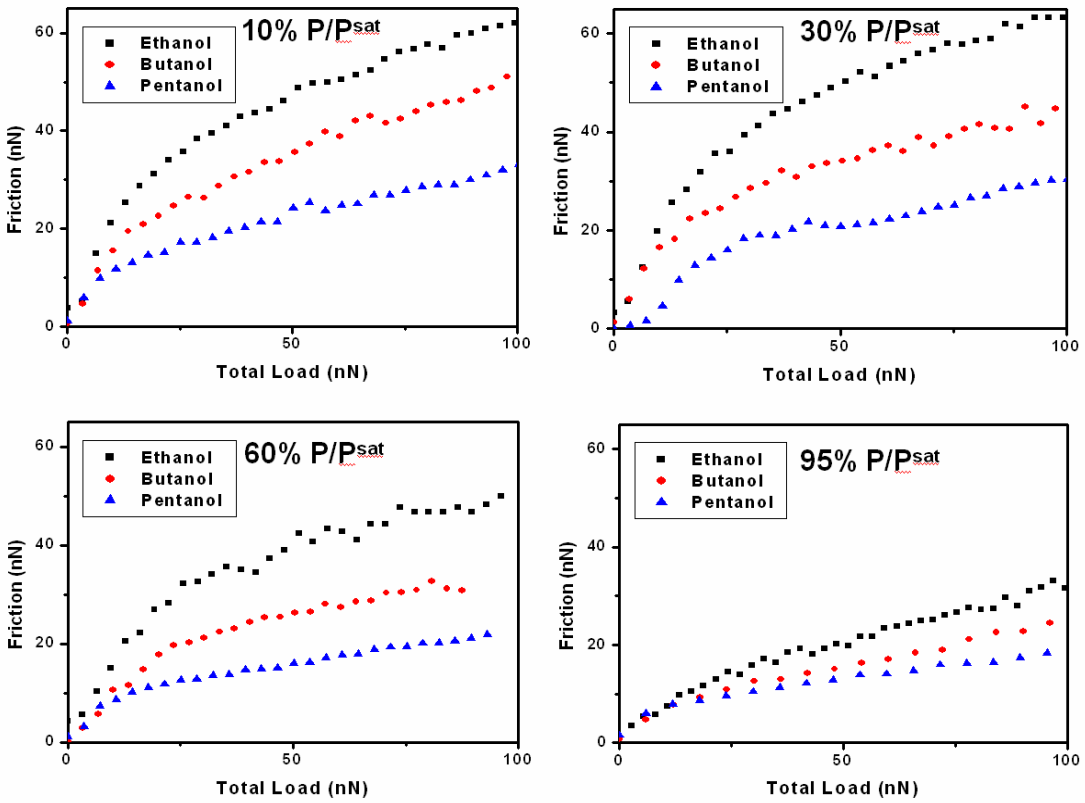

Figure **7.5**: Friction vs. Total Load comparison of ethanol, 1-butanol, and 1-pentanol at P/P^{sat} of 10%, 30%, 60%, and 95%.

Another comparison between each alcohol's influence on friction is done by plotting a pseudo-coefficient of friction (μ) for each condition. In this case we define the pseudo-coefficient of friction as the observed coefficient of friction which is the slope in the linear region of the F-L curve. The observed coefficient of friction, μ, is presented in Figure **7.6**. As expected, upon the introduction of alcohol vapors to the surface, these vapors adsorb onto the silicon AFM tip and substrate and help lubricate the surfaces. The initial reduction is quite large. As P/Psat increases, from 10% to 60% P/P^{sat}, there is a gradual decrease in the coefficient of friction. Near saturation, where the surface is expected to be well covered, the coefficient of friction is, generally speaking, the lowest.

In order to see the influence of chain-length on the shear strength of the contact as a function of each alcohol and P/P^{sat}, each experimental condition was fitted with equation **7-15**. The model parameters τ (shear strength), and β' (meniscus friction dissipation) are plotted in Figure **7.7** (top and bottom respectively). Upon the introduction of alcohol vapors, the shear strength of the contact initially drops by a factor of about 2 to 3. As the partial pressure increases, the shear strength gradually decreases. Near saturation, like the coefficient of friction, the shear strength of the longest alcohol molecule is the smallest.

The trend of β' however, seems to follow the capillary pressure dependence observed and predicted in section **5.4**. Since β' is scaled with the contact radius, the absolute magnitude of the y-scale has no real meaning. However, since these experiments were done with the same tip, the relative trend between each alcohol should be significant. It appears that the smaller the molar volume or shorter the vapor lubricant is, the more susceptible or more significant meniscus dissipation is.

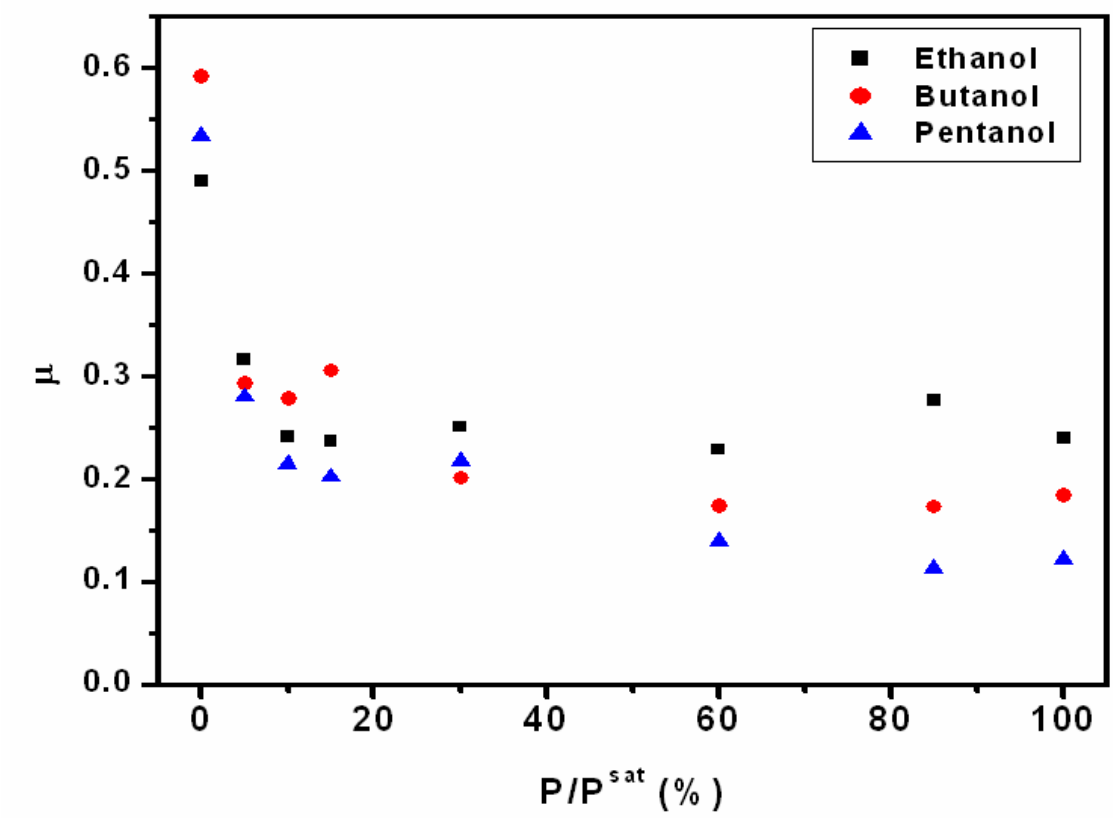

Figure **7.6**: Coefficient of friction from the Friction-Load curves vs. P/P^{sat} of ethanol, 1-butanol, and 1-pentanol.

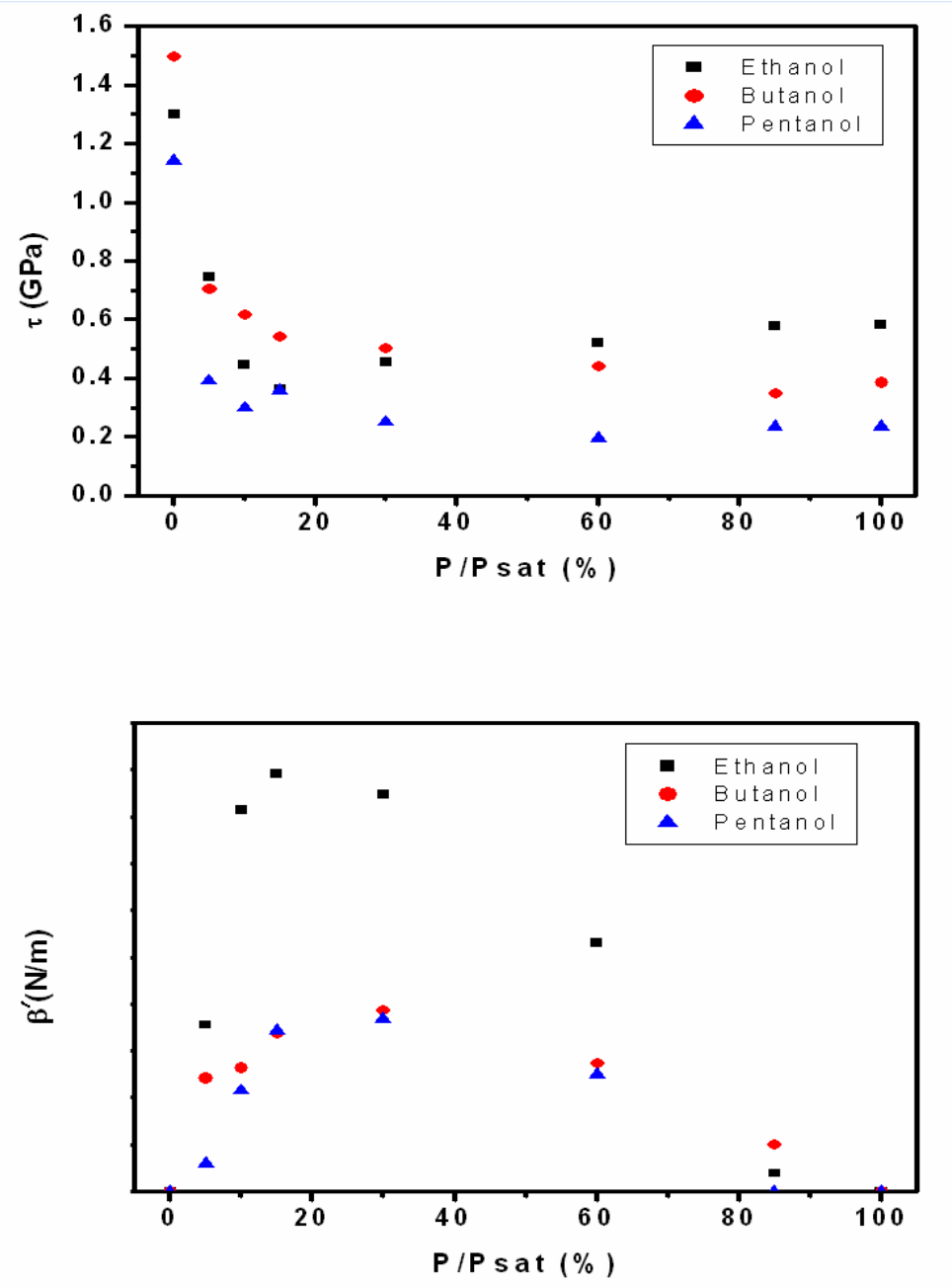

Figure **7.7**: Shear strength (top) and Meniscus friction contribution (bottom) of each alcohol for ethanol, 1-butanol, and 1-pentanol as a function of each alcohol's relative partial pressure.

7.7 Conclusions

In considering the consequences of capillary formation for nanoscale contacts, and their influence on friction, depending on the size of the meniscus and surface conditions, contact line hysteresis can increase the frictional response. However, as the chain length increases or the molar volume of the adsorbate increases the magnitude of this dependence seems to decrease. Also, as the chain length increases, the shear strength decreases, leading to a reduction in friction. In systems where control over surface forces are critical, i.e. microelectromechanical system (MEMS), nanoelectromechanical systems (NEMS), colloids, and nano-tribology, these effects should not be neglected.

7.8 References

1. Y. Ando; J. Ino, *Wear* **1998,** 216, (2), 115-122.
2. B. Bhushan, *Handbook of Micro/Nanotribology*. CRC Press: Boca Raton, FL, 1995.
3. H. J. Butt; B. Cappella; M. Kappl, *Surface Science Reports* **2005,** 59, (1-6), 1-152.
4. R. W. Carpick; N. Agrait; D. F. Ogletree; M. Salmeron, *Langmuir* **1996,** 12, (13), 3334-3340.
5. R. W. Carpick; N. Agrait; D. F. Ogletree; M. Salmeron, *Journal of Vacuum Science & Technology B* **1996,** 14, (2), 1289-1295.
6. R. W. Carpick; M. Salmeron, *Chemical Reviews* **1997,** 97, (4), 1163-1194.
7. K. H. Chung; D. E. Kim, *Tribology Letters* **2003,** 15, (2), 135-144.
8. D. S. Grierson; E. E. Flater; R. W. Carpick, *Journal of Adhesion Science and Technology* **2005,** 19, (3-5), 291-311.
9. J. Hu; X. D. Xiao; D. F. Ogletree; M. Salmeron, *Surface Science* **1995,** 327, (3), 358-370.
10. F. Katsuki; K. Kamei; A. Saguchi; W. Takahashi; J. Watanabe, *Journal of the Electrochemical Society* **2000,** 147, (6), 2328-2331.
11. A. G. Khurshudov; K. Kato; H. Koide, *Wear* **1997,** 203, 22-27.
12. S. Kopta; M. Salmeron, *Journal of Chemical Physics* **2000,** 113, (18), 8249-8252.
13. L. M. Qian; F. Tian; X. D. Xiao, *Tribology Letters* **2003,** 15, (3), 169-176.
14. X. D. Xiao; J. Hu; D. H. Charych; M. Salmeron, *Langmuir* **1996,** 12, (2), 235-237.

15. D. B. Asay; S. H. Kim, *Journal of Chemical Physics* **2006,** 124, (17), 5.

16. W. R. Ashurst; C. Carraro; R. Maboudian, *Ieee Transactions on Device and Materials Reliability* **2003,** 3, (4), 173-178.

17. W. R. Ashurst; C. Yau; C. Carraro; R. Maboudian; M. T. Dugger, *Journal of Microelectromechanical Systems* **2001,** 10, (1), 41-49.

18. B. Bhushan; A. V. Kulkarni; V. N. Koinkar; M. Boehm; L. Odoni; C. Martelet; M. Belin, *Langmuir* **1995,** 11, (8), 3189-3198.

19. H. I. Kim; T. Koini; T. R. Lee; S. S. Perry, *Langmuir* **1997,** 13, (26), 7192-7196.

20. D. B. Asay; M. T. Dugger; S. H. Kim, *Tribology Letters* **2008,** 29, (1), 67-74.

21. D. B. Asay; M. T. Dugger; J. A. Ohlhausen; S. H. Kim, *Langmuir* **2008,** 24, (1), 155-159.

22. A. J. Gellman, *Tribology Letters* **2004,** 17, (3), 455-461.

23. S. H. Kim; D. B. Asay; M. T. Dugger, *Nano Today* **2007,** 2, (5), 22-29.

24. M. Enachescu; R. J. A. van den Oetelaar; R. W. Carpick; D. F. Ogletree; C. F. J. Flipse; M. Salmeron, *Tribology Letters* **1999,** 7, (2-3), 73-78.

25. M. A. Lantz; S. J. O'Shea; M. E. Welland, *Physical Review B* **1997,** 56, (23), 15345-15352.

26. M. A. Lantz; S. J. Oshea; M. E. Welland; K. L. Johnson, *Physical Review B* **1997,** 55, (16), 10776-10785.

27. H. Hertz, *Miscellaneous papers*. Macmillan: London, 1896; p 146.

28. K. L. Johnson; K. Kendall; A. D. Roberts, *Proceedings of the Royal Society of London Series a-Mathematical and Physical Sciences* **1971,** 324, (1558), 301-313.

29. B. V. Derjaguin; V. M. Muller; Y. P. Toporov, *Journal of Colloid and Interface Science* **1975,** 53, (2), 314-326.

30. D. Maugis, *Journal of Colloid and Interface Science* **1992,** 150, (1), 243-269.

31. J. A. Greenwood, *Proceedings of the Royal Society of London Series a-Mathematical Physical and Engineering Sciences* **1997,** 453, (1961), 1277-1297.

32. D. Tabor, *Journal of Colloid and Interface Science* **1977,** 58, (1), 2-13.

33. A. Fogden; L. R. White, *Journal of Colloid and Interface Science* **1990,** 138, (2), 414-430.

34. L. Sirghi, *Applied Physics Letters* **2003,** 82, (21), 3755-3757.

35. R. R. M. Zamora; C. M. Sanchez; F. L. Freire; R. Prioli, *Physica Status Solidi a-Applications and Materials Science* **2004,** 201, (5), 850-856.

36. M. Nosonovsky, *Journal of Chemical Physics* **2007,** 126, (22).

37. D. B. Asay; S. H. Kim, *Langmuir* **2007,** 23, (24), 12174-12178.

38. J. E. Sader; J. W. M. Chon; P. Mulvaney, *Review of Scientific Instruments* **1999,** 70, (10), 3967-3969.

Chapter 8

Macro- to Nano-scale Wear Prevention via Molecular Adsorption

8.1 Summary

As the size of mechanical systems shrink from macro to nano scales, surface phenomena such as adhesion, friction and wear become increasingly significant. This chapter demonstrates the use of alcohol adsorption as a means of continuously replenishing the lubricating layer on working device surfaces and elucidates the tribochemical reaction products formed in the sliding contact region. Friction and wear of native silicon oxide were studied over a wide range of length scales covering from macro- to nano-scales using ball-on-flat tribometer (millimeter scale), side-wall microelectromechanical-system (MEMS) tribometer (micrometer scale), and atomic force microscopy (nanometer scale). In all cases, the alcohol vapor adsorption successfully lubricates and prevents wear. Imaging time-of-flight secondary ion mass spectrometry (imaging ToF-SIMS) analysis of the sliding contact region revealed that high-molecular weight oligomeric species were formed via tribochemical reactions of the adsorbed linear alcohol molecules. These tribochemical products seem to enhance the lubrication and wear prevention. In the case of sidewall MEMS tests, the lifetime of the MEMS device is radically increased via vapor phase lubrication with alcohol.

8.2 Introduction

Lubrication is required to minimize friction and wear between repetitive sliding contacts; and is especially critical when mechanical movements require longevity. Efficient protective lubricant layers are often produced *in situ*. In the human body, synovial fluid needed for joint (cartilage) lubrication is produced by chondrocyte cells in the articular cartilage only when they are properly supplied with reactive ingredients and stimulated by cycles of mechanical stress (body weight).[1, 2] An engineering example is anti-wear additives such as zinc dialkyldithiophosphates used in automobile engines. These additives are incorporated in current lubricant formulas to form surface films that protect the underlying material from the destructive forces produced under sliding conditions. This anti-wear film forms only when additives are readily supplied and proper loads are applied between sliding interfaces.[3] These examples emphasize the importance of reactions within the tribological system to generate protective self-replenishing films under the action of mechanical stresses. This paper demonstrates that continuous tribochemical reactions of adsorbed alcohol molecules can reduce friction and prevent wear of silicon surfaces over a wide range of size scales, from macro-scale to nano-scale. This finding is especially important for lubrication of ceramic components and micro- and nano-scale mechanical devices made of silicon, since a robust lubrication approach for micromachine devices has eluded development until now, and new applications of micromachines requiring long duration operation should now be possible.

As the size of mechanical systems shrinks from macro to nano scales, the surface-to-volume ratio increases and surface phenomena such as adhesion, friction, and wear

become increasingly significant to device feasibility and reliability. Although the first demonstration of a microelectromechanical system (MEMS) was reported in the literature more than two decades ago[4], no commercial MEMS devices with repetitive sliding contacts exist today. MEMS devices are typically fabricated with silicon-based materials because mature lithographic fabrication techniques are available from the semiconductor industry;[5] however, silicon and its native oxide exhibit high friction and poor wear resistance in sliding contacts.[6]

To overcome these problems, various coatings are being developed and extensively studied,[7, 8] yet their reliability and feasibility remain in question. Thin protective coatings are subject to wear during operation, limiting device lifetime.[9] A means of continuously replenishing the protective layer on these surfaces is required to overcome this limitation. An additional requirement is that the lubricant must be deposited conformal to the surfaces, not possible with typical physical vapor deposition (PVD) techniques which deposit via line-of-site or chemical vapor deposition (CVD) techniques which deposit non-uniformly and do not easily coat buried surfaces. In vapor-phase lubrication (VPL), the adsorption of gas-phase molecules on device surfaces can produce a conformal lubricant layer. During sliding contact, adsorbed molecules may be desorbed from the surface; however, as long as the vapor pressure of lubricating molecules is maintained, these molecules immediately re-adsorb and replenish the surface. Adsorbed films have been used to repassivate dynamic digital mirror arrays;[10] but this device does not have deliberate sliding contacts. Previous VPL required elevated temperatures and/or lubricant molecule activation via precursor catalytic metal

coatings.[11-13] Missing were vapor-phase lubrication strategies that worked in ambient conditions without special coatings.

This paper presents tribochemical reactions and tribological responses of native silicon oxide contacts in an alcohol vapor environment. Alcohol molecules exhibit appreciable vapor pressure at room temperature, and have a strong interaction with oxide-terminated silicon surfaces through hydrogen bonding. Additionally, VPL molecules adsorb conformally to all the surfaces. The equilibrium adsorption of simple alcohol molecules prevented silicon oxide wear over a large range of length scales (macroscopic to nanoscopic). Additionally, tribochemical reactions occurring within the contact produced high molecular weight oligomers which help prevent wear. This discovery provided efficient ways to greatly improve operation lifetimes of MEMS devices and mitigate wear of atomic force microscopy (AFM) tips during contact scanning.

8.3 Experimental Details

Environmental conditions were controlled by passing either dry argon or nitrogen through columns of liquid alcohol. The exiting gas from these bubblers was saturated with alcohol vapor molecules. The relative partial pressure of these molecules was maintained by mixing the saturated vapor stream with either dry nitrogen or argon at a constant ratio. Details of the vapor feed system were published elsewhere and described earlier.[14] This vapor feed stream was used for various size-scale experiments. In the case

of the linear wear tests (LWT), the vapor stream (0.5 L/min) was directed towards the ball-on-flat approximately 2 cm away. The LWT was kept in a large glove box (490 L volume), which was constantly purged with dry nitrogen at a rate of ~9.5 L/min. Because of the close proximity, the partial pressure of the lubricant molecules immediately surrounding the contact is assumed to be equivalent to the relative partial pressure of the feed vapor stream. AFM experiments were conducted in an environmental chamber (~30 L volume) where the lubricant vapor was purged and allowed to come to equilibrium. Equilibrium adsorption experiments with attenuated total reflection infrared (ATR-IR) spectroscopy were carried out by passing the vapor gas over a clean silicon ATR crystal. MEMS testing was performed in a stainless steel environmental chamber (~0.5 L volume) where the vapor stream enters and then exits, vented to the laboratory exhaust. In this study, all measurements were at room temperature.

Adsorption isotherm was measured using ATR-IR spectroscopy. IR spectra were collected using a Thermo-Nicolet Nexus 670 spectrometer with a MCT detector and a multiple bounce silicon ATR crystal. The penetration depth of the evanescent wave above the crystal was calculated based upon the difference in the refractive index of the silicon and the outside space (air) as well as the angle of internal reflection.[15] Attenuation of the signal occurs when there are IR active molecules inside this penetration depth. By comparing the intensities of the natural log of reflectance between the adsorbed molecules with respect to bulk liquid on the ATR crystal, the thickness of the adsorbed film was determined.

LWT testing was performed with a home built ball-on-flat tribometer with a 3.125 mm diameter quartz (SiO_2) ball sliding on a Si(100) wafer at a speed of ~1.5 mm/sec with an applied load of 98 mN for 500 reciprocating cycles. Each test was performed with fresh surfaces. Silicon wafers with native oxide layers were cleaved to create samples ~ 1cm square for testing. The quartz balls were cleaned via 15 min in a UV/Ozone chamber.

The sidewall MEMS devices were made up of polycrystalline silicon layers ~ 2 μm thick that were initially separated by silicon dioxide layers of similar thickness. The silicon and oxide layers were patterned to create complex structures and electrostatic actuators.[16] After etching away the oxide layers in HF, the surfaces were oxidized by exposure to peroxide, and then rinsed in methanol. The methanol was extracted in supercritical CO_2 to avoid capillary formation. These devices were treated with a chemisorbed organic monolayer to make surfaces hydrophobic. A fluorinated monolayer [tridecafluorotris(dimethylamino)silane, $CF_3(CF_2)_5(CH_2)_2Si(N(CH_3)_2)_3$] was applied by exposing cleaned surfaces to the molecule in a vacuum chamber at a total pressure of 2 mTorr for 12 minutes.

Lifetime for the MEMS devices was defined as the length of time (or number of cycles) the device continued to oscillate using the on-chip electrostatic actuator under a given load. Friction in these devices was determined by monitoring the difference between the ranges of shuttle motion with and without load. This difference in range of motion (a length) was multiplied by the spring constant of the shuttle to yield the frictional force. Adhesion was measured by applying a voltage to the unloading actuators on the post. At the point of separation this voltage was recorded. The adhesive force is

the sum of the force applied at the unload actuators (proportional to the applied voltage squared) and the initial loading force required to make the contact..[17]

AFM testing was performed with a Molecular Imaging Pico-SPM head and a RHK SPM 100 controller and AIM-MI interface. Silicon AFM tips with ~ 20 nm radius of curvature were cleaned via 15 min in a UV/Ozone chamber. The silicon (100) substrate was cleaned with UV/Ozone (15 min) followed by an RCA-1 procedure (mixture of five parts of water, one part of 30% hydrogen peroxide, and one part of 27% ammonium hydroxide maintained at 70 °C for 15 min).

Time-of-flight secondary ion mass spectrometry (ToF-SIMS) spectral imaging was performed on a Physical Electronics TRIFT I Time-of-Flight Secondary Ion Mass Spectrometer. A pulsed and bunched 15kV, 600pA $^{69}Ga+$ beam was rastered over a 140x140 μm^2 area for 5 minutes while acquiring positive secondary ions. Bunched mode was used for high mass resolution to aid in peak identification. For high-resolution imaging, a pulsed 25kV, 600pA $^{69}Ga^+$ beam was used. A 5 minute acquisition in a 140x140 μm^2 region was also employed in this mode. Multivariate analysis was performed using AXSIA (Automated eXpert Spectral Image Analysis) developed at Sandia National Laboratories.[18] The multivariate curve resolution method was used to separate the spectral image into its unique components.

8.4 Results and Discussions

In order to understand the influence of adsorbed 1-pentanol layers on tribological phenomena, the isotherm thickness should be determined. This was accomplished via ATR-IR spectroscopy. Figure **8.1** insert shows typical vibration peaks of the pentyl (2860 cm^{-1} CH_2 symmetric stretch, ~2930 cm^{-1} CH_2 asymmetric stretch, and 2960 cm^{-1} CH_3 asymmetric stretch) and OH (broad peak centered at ~3400 cm^{-1}) groups adsorbed on silicon oxide. The OH vibration peak shows a reduction at ~3600-3700 cm^{-1} and ~3220 cm^{-1}. These negative peaks correspond to free and ice-like water layers, respectively.[19] The reduction in these peak intensities indicates some removal of strongly bound water on the oxide surface upon 1-pentanol adsorption. Chemical equilibrium of the initially strongly adsorbed water changes with the addition of alcohol, driving the removal of some water species from the surface. The adsorption isotherm behavior of 1-pentanol on native silicon oxide is presented in Figure **8.1**. The adsorption follows a Langmuir-type adsorption isotherm. Monolayer coverage occurs around P/P^{sat} ~10%, and above this vapor pressure alcohol adsorption increases only slightly.

At the millimeter scale, a linear wear test was used to investigate the efficacy of alcohol adsorption in wear prevention. The LWT data for silicon (with ~20Å native oxide) sliding against silicon oxide (quartz) spheres in varying amounts of 1-pentanol vapor confirm the isotherm behavior. A ~0.1 N load applied to the sphere provides a Hertzian contact pressure of ~115 MPa. Figure **8.2**a illustrates the change in frictional behavior as a function of the relative partial pressure of 1-pentanol. As the concentration of 1-pentanol vapor increases towards the saturation pressure (P^{sat}), the observed

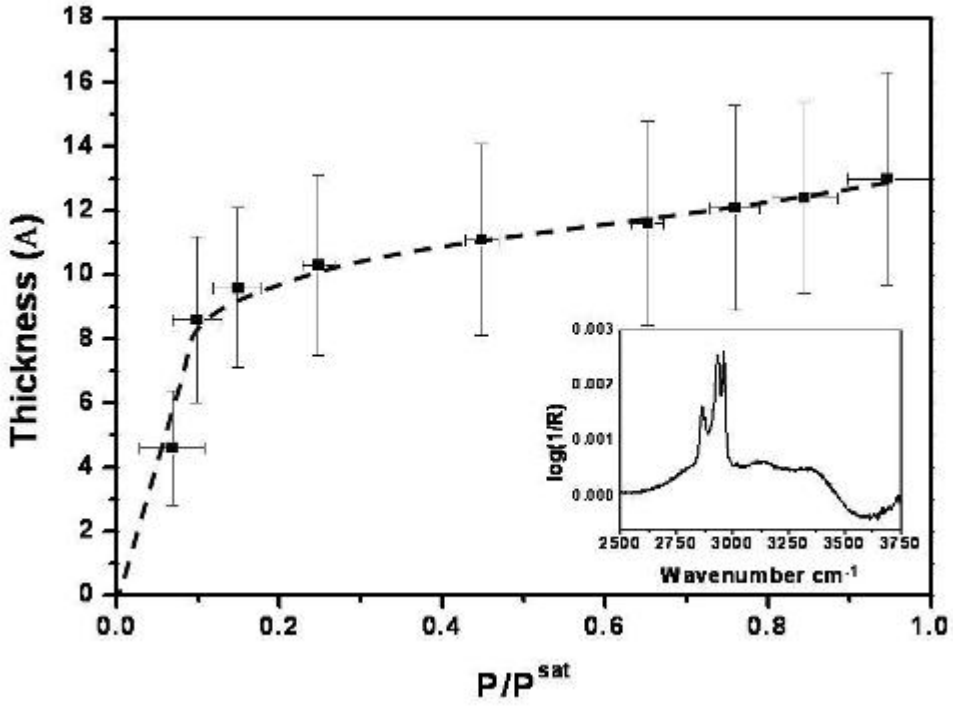

Figure **8.1**: Adsorption isotherm for 1-pentanol on native silicon oxide surface. Insert: ATR-IR spectroscopy of 1-pentanol monolayer on native silicon oxide.

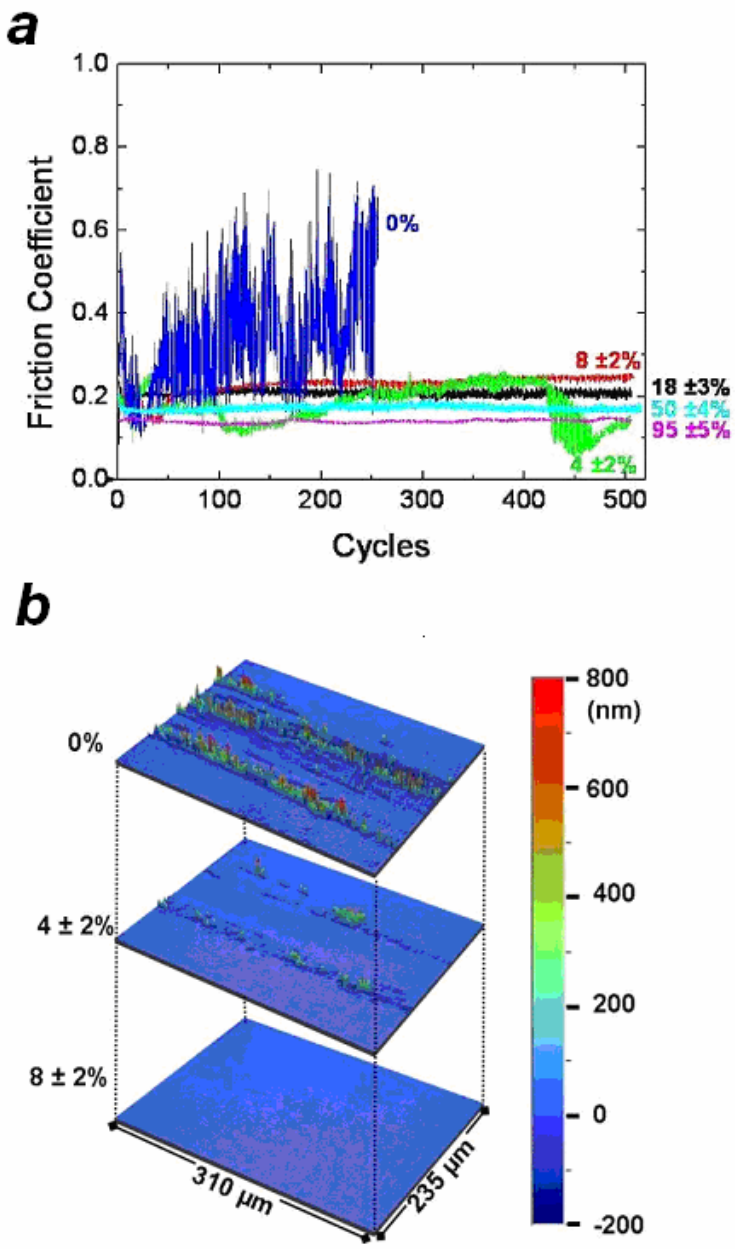

Figure **8.2**: (a) Frictional response of quartz sphere (dia. = 3 mm) sliding against silicon (100) wafer as a function of the relative vapor pressure (P/P^{sat}) of 1-pentanol. (b) Optical profilometry of wear tracks at increasing relative 1-pentanol vapor pressures (P/Psat).

frictional response decreases. When no alcohol vapors are present, erratic behavior is observed and wear debris are generated causing sporadic 3rd body contact effects, manifested as large fluctuations in friction. With a small amount of alcohol vapors present, this behavior quickly changes. At ~4% of P^{sat}, some erratic behavior is observed; however when ~8% of P^{sat} is achieved this behavior disappears. The lower regions of frictional response at 4% could be attributed to 3rd body lubrication. As the surface wears, some smaller particles become trapped in between the sphere and substrate. These smaller particles have some adsorbed alcohol molecules and this combination of loose debris with partial alcohol coverage provides lower frictional response. However, wear is not completely prevented at this condition. Any additional alcohol above 8% reduces the friction coefficient only modestly. These conditions correspond well with the isotherm thickness behavior, i.e. effective lubrication is demonstrated once the surface is covered with a monolayer of adsorbed alcohol. Optical profilometry images of the sliding contact region (Figure **8.2**b) illustrate that small amounts of alcohol vapors drastically reduce the wear debris production on silicon. No wear debris is observed for any conditions when the relative partial pressure of alcohol is $\geq$8 % of P^{sat}. If alcohol vapors are removed, the wear process eventually resumes, suggesting that alcohol lubrication requires continual replenishment.

ToF-SIMS spectral imaging of an area containing both the contact region and the virgin silicon surface provides valuable insight into the cause of this wear reduction. Typical ToF-SIMS spectra of VPL with 1-pentanol are shown in Figure **8.3**. Inside the contact region, the spectra show features characteristic of polymeric species fragmentation. Masses higher than the molecular weight of 1-pentanol (m/z = 88)

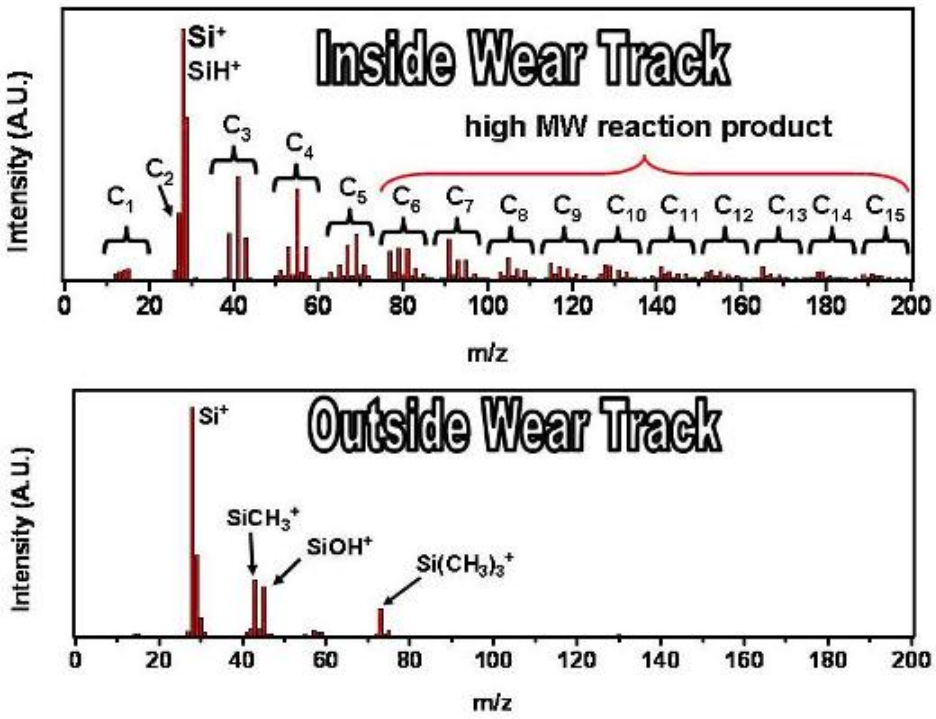

Figure **8.3**: ToF-SIMS spectra inside the contact track (top) and outside of the contact region (bottom) for the condition 18% of P^{sat}. Inside the contact, a hydrocarbon product is made (denoted as C_1, C_2, …, C_{15}), providing a protective layer between the rubbing surfaces. The "C_x" labeling indicates the minimum number (x) of carbon atoms required to appear at the m/z (mass/charge). The distribution within each "C_x" labeling is due to differing amounts of hydrogenation of the fragments contained within the C_x manifold.

suggest complex oligomer formation. When alcohol vapors are present during sliding, dynamically-grown oligomeric products are generated inside the contact track and are not present outside the contact region. Additionally, many of the peaks present only in the contact region are consistent with fragmentation of unsaturated hydrocarbons (m/z 67 [$C_5H_7^+$], 77 [$C_6H_5^+$], 79 [$C_6H_7^+$], 91 [$C_7H_7^+$], 103 [$C_8H_7^+$], 105 [$C_8H_9^+$], 115 [$C_9H_7^+$], 117 [$C_9H_9^+$], 128 [$C_{10}H_8^+$]).[20] These features are not present outside the contact region. The growth of these oligomeric species during sliding is observed by compiling a montage of spectral images acquired from surfaces with increasing numbers of reciprocating cycles. The resulting spectral image montage is processed with multivariate algorithms described elsewhere.[18] The multivariate component corresponding to the oligomeric product is then used to plot the total number of counts of oligomeric species verses the number of cycles (Figure **8.4**). These results indicate that the oligomeric species are produced during sliding contact. Although the origin of oligomerization reaction in the sliding contact region is not known, it appears that simply exposing silicon dangling bonds is not sufficient to cause the observed oligomerization process. When a Si(100) wafer was cleaved in the presence of liquid alcohol and imaged with ToF-SIMS, only chemisorbed 1-pentanol was observed on the cleaved surface and no evidence was present suggesting oligomer formation.

MEMS sidewall friction devices were employed to investigate tribology at the micro-scale.[21] These devices are initially covered with (FOTAS) the tridecafluorotris(dimethylamino)silane monolayer. In a regulated environment, a movable shuttle was driven back and forth (~3 mm/sec) against a stationary post while a 500 nN load was applied (Figure **8.5**a & b). Contact pressure in the MEMS device was estimated

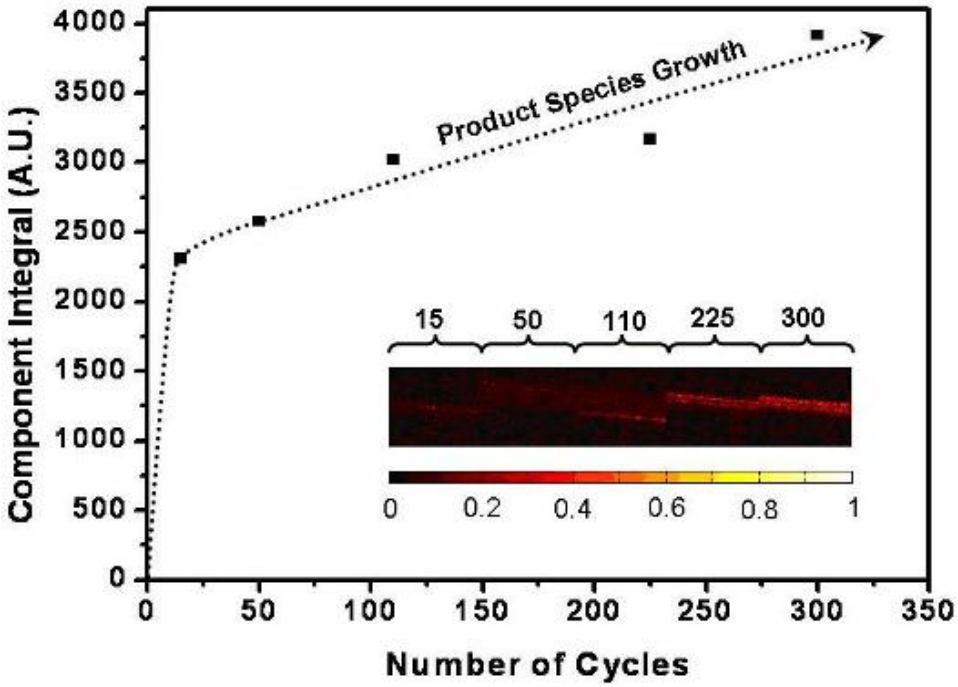

Figure **8.4**: Growth of product found inside the contact region as a function of contact cycles. Insert: Product component (intensity) from the multivariate analysis of the ToF-SIMS montage of images (700 μm x 140 μm) of the various contact tracks as a function of cycles. (P/P^{sat} =18%)

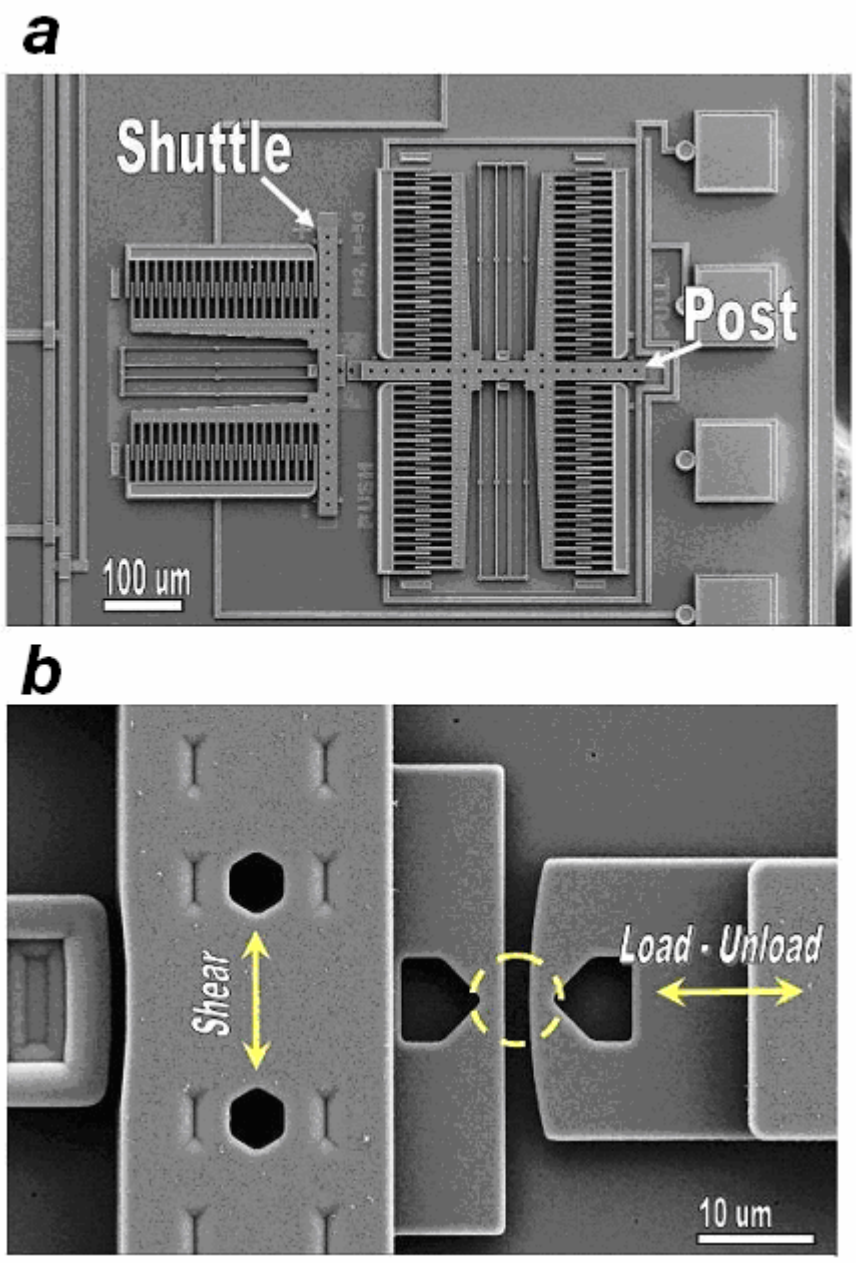

Figure **8.5**: (a) SEM image of the MEMS sidewall friction device. Both post and shuttle are driven by electrostatic comb drives. (b) MEMS sidewall friction device. Increased magnification of the contact region (circled). The post moves perpendicular to the contact and is used to apply the load while the shuttle moves laterally to the contact.

to be ~ 20 MPa assuming smooth surfaces and Hertzian deformations. However, in a real contact, only a handful of contacting asperities are present due to the surface roughness. Therefore, the actual contact stresses inside the real asperity contacts probably lie somewhere between this value and a few GPa (the typical contact stress of a single nano-asperity).

Figure **8.6** illustrates the vast improvement in friction and lifetime of the MEMS device in the presence of 1-pentanol vapor. In dry N_2 conditions, with the tridecafluorotris(dimethylamino)silane monolayer alone, friction quickly and sporadically increases and the device fails in less than 10^4 cycles (<2 minutes at a 100 Hz operation). This failure is due to wear.[22] Although no significant debris is observed upon examination in scanning electron microscopy (SEM) due to device failure before accumulation of wear debris, a change in friction is an indication of removal of the surface passivation. Additionally, the initial tridecafluorotris(dimethylamino)silane coated surfaces provided an average adhesion of ~100 nN. At failure, the measured adhesion increased 2 to 4 times the initial value, indicating a change in surface chemistry. In dry nitrogen, wear of the fluorinated layer exposes bare silicon on both the shuttle and post; their interactions eventually cause the surfaces to stick together.

The lifetime of MEMS devices in the presence of 1-pentanol vapors is greatly increased. When the 1-pentanol vapor pressure is maintained above the partial pressure needed for monolayer coverage, friction remains low and the device does not fail. After more than 3 hours of operation at 95% of P^{sat}, the device was stopped by the user and adhesion was measured. There was no discernable change in adhesion compared to the adhesion prior to lateral motion, indicating no wear of the contact surfaces. Even after

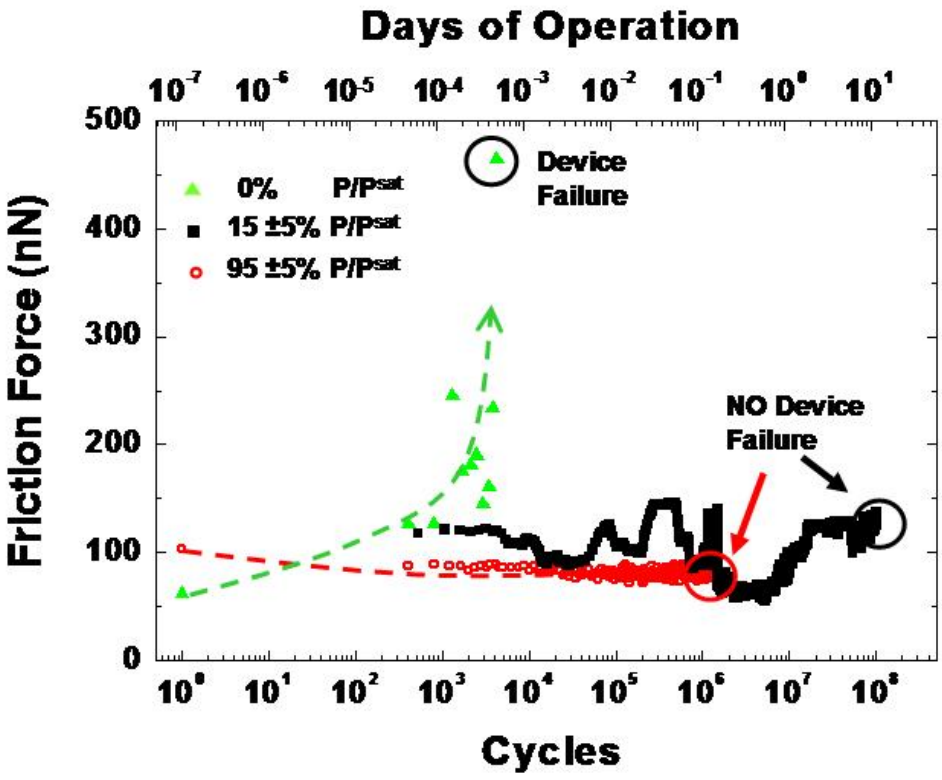

Figure **8.6**: Friction force vs. cycles in MEMS sidewall device under 500 nN load at 100 Hz oscillation. In dry nitrogen the device fails within a few minutes, when 1-pentanol vapors are present (15 and 95% of P^{sat}) no failure is observed.

more than 10^8 cycles of operation (11 days at a reciprocating rate of 100 Hz) at ~15% of P^{sat}, the device does not fail or show any sign of wear under SEM examination (Figure **8.7**). In this case, small liquid-like deposits are observed adjacent to tall asperities. Additionally, there is a small increase in the observed adhesion following 10^8 cycles. However, the change in adhesion was not sufficient to interrupt the device performance. This material does not dissolve in pentanol even with gentle heating. It is believed that this product is the same that is observed in the LWT by ToF-SIMS, although at less than 200 nm in size, they are too small to probe directly.

At the nano-scale, the AFM was utilized to study the effect of adsorbed alcohol molecules on silicon single asperity sliding. Sliding experiments were conducted by reciprocating an AFM silicon tip on a clean Si(100) substrate at a speed of 2 μm/sec over a ~1 μm long line for 512 times with a 75 nN applied load, providing a Hertzian contact pressure of ~3 GPa. Then, the scratched region was imaged using a 3 nN load. As shown in Figure **8.8**, the test in 1-propanol vapor at 75% of P^{sat} makes no discernable wear trench while the test in 75% humid vapor leaves a 1 nm deep wear trench. On high surface energy silicon oxide surfaces exposed to humid air, there are always thin water layers adsorbed on the surface which are in equilibrium with water in the gas phase. Although strongly bound hydrating layers formed on certain mineral surfaces (such as mica) show remarkable lubrication ability for atomically smooth surfaces,[22-24] water is not a good lubricant for silicon oxide asperity contacts.[25] The adsorbed water forms hydrated silicon oxide, which is susceptible to wear.[26-28] By replacing water (H–OH) with alcohol (R–OH), chemical wear of silicon is prevented. Nano-scale wear prevention was also

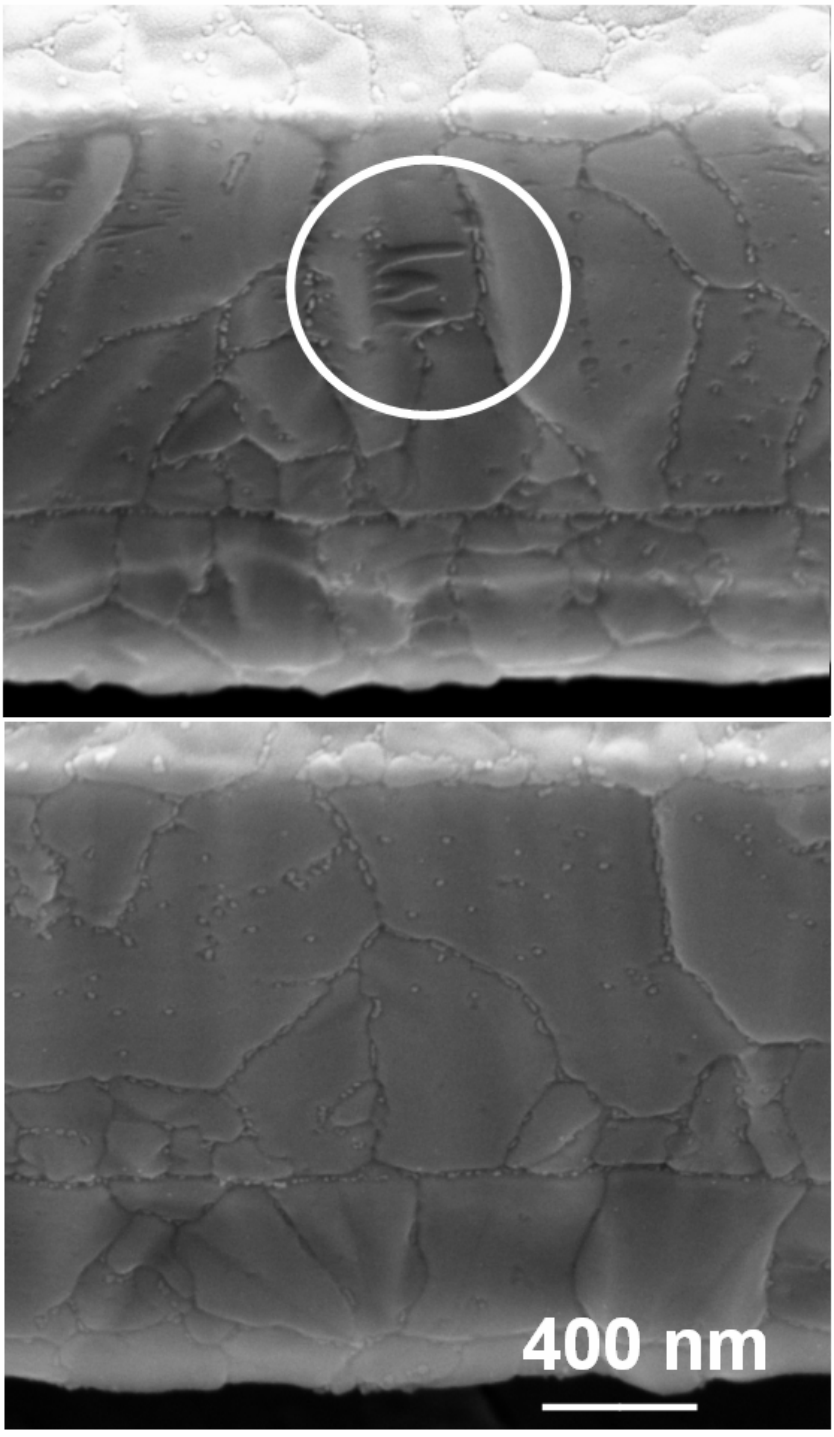

Figure **8.7**: SEM image of the sidewall contact. On the top, following 10^8 cycles in a 15 ±5% P^{sat} environment a liquid-like buildup is observed. bottom, fresh unused sidewall surface is shown for comparison.

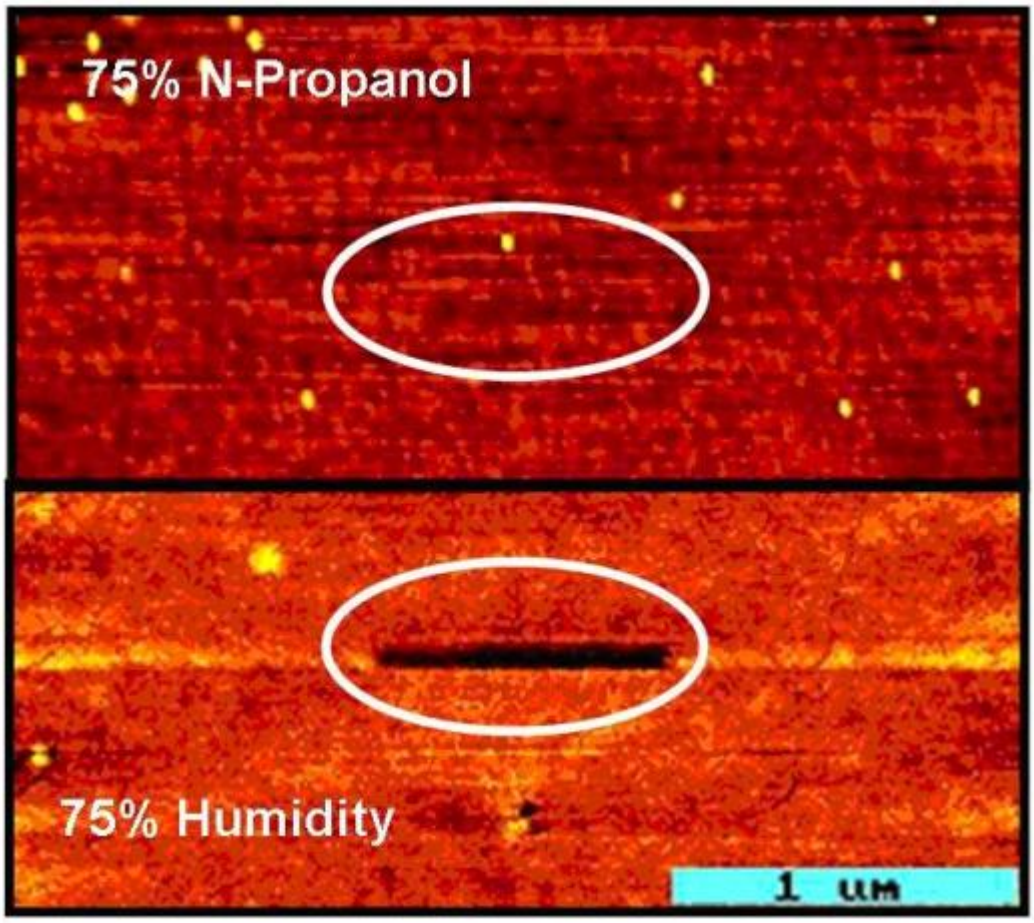

Figure **8.8**: AFM topography images. The 75 nN load line scan region is encircled. In an alcohol environment (top), no wear trench is observed.

observed for other alcohols tested in this experiment (ethanol (C_2) through 1-pentanol (C_5)).

Density functional theory (DFT) has been used to illuminate part of the reasons for alcohol's success in wear prevention vs. water. In this study, the system modeled was the open β-cristobalite (111) surface of SiO_2. This is a very low density or open form of the SiO_2 surface, and hence should be more susceptible to Si-O-Si bond rupture. In this study with Michael Janik at Penn State, effective activation energies for Si-O-Si bond rupture was studied as a function of various terminal groups. Figure **8.9** illustrates the structure and location of chemisorbed terminal groups. Depending on the species chemisorbed onto the silicon surface and the gas phase lubricant, the activation energy required to break Si-O-Si was observed to change as illustrated in Table **8.1**.

Table **8.1**: Table of different terminal groups studied and the relative activation energy required for Si-O-Si bond rupture (courtesy of Dr. Michael Janik)

R_1	R_2	E_{act} (eV)
H	H	1.18
CH_3	H	1.56
H	CH_3	1.16
CH_3	CH_3	1.60
propyl	propyl	2.32

What was observed is the terminal group R_1 (the group already chemisorbed onto the silicon surface) greatly increases the activation energy barrier for further Si-O-Si bond cleavage.

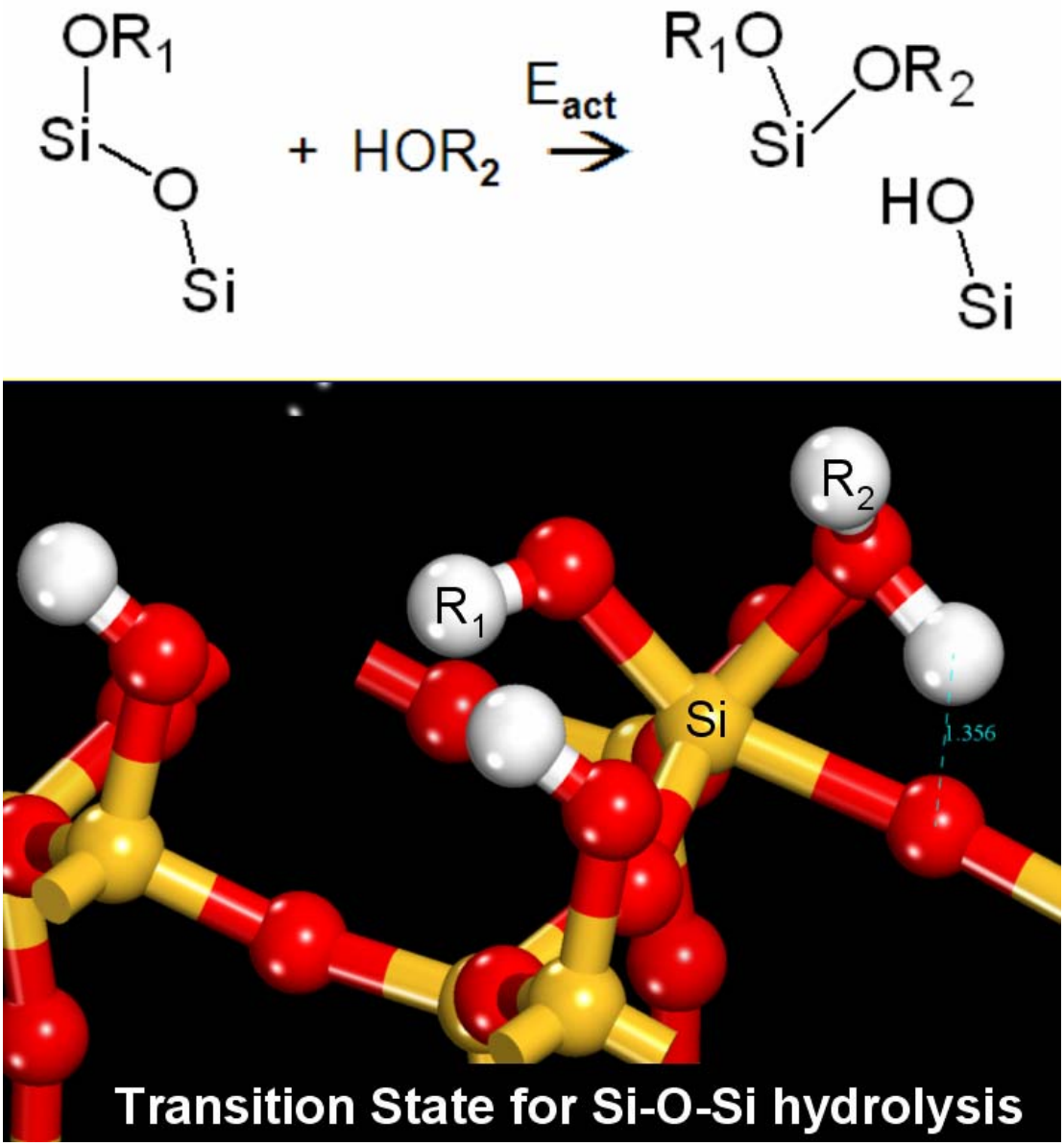

Figure **8.9**: Top: Reaction path of Si-O-Si bond rupture. Below: DFT cross section of β-cristobalite (111) surface of SiO_2 with chemisorbed water at the transition state prior to Si-O-Si bond rupture. (courtesy of Dr. Michael Janik)

These remarkable effects on wear resistance of molecularly thin alcohol layers formed by gas-phase adsorption, over a wide range of length scales (covering the contact pressure from ~20 MPa to 3 GPa), is in part attributed to the reduction in shear strength that occurs upon adsorption,[14] and to tribochemical reactions[29] creating a dynamically-grown oligomeric species under high stresses between asperities in sliding contact. The key to the effectiveness of the vapor phase lubrication is its continual replenishment. During sliding contact, adsorbed molecules may undergo tribochemical reactions in the contact region or desorb from the surface. If the desorption dominates over the tribochemical reactions, or the reaction products are not sustained to some minimum level, friction increases and wear begins. As devices such as MEMS continually shrink in size, vapor phase lubrication can maintain protective films at the sliding contact region without affecting device functionality unlike typical solid coating deposition techniques.

8.5 Conclusions

At all length scales studied in these experiments, it was found that maintaining a certain vapor pressure of lubricant provides a replenishing environment that maintains its tribological response and limits wear. In the contact region, tribochemical reactions produce high molecular weight oligomers that prevent wear. This phenomenon provides successful lubrication of a MEMS test diagnostic structure, improving the lifetime of the device by over four orders of magnitude, prevents AFM tip wear at substantial contact pressures, and prevents wear between macroscopic silicon contacts.

8.6 References

1. A. J. Grodzinsky; M. E. Levenston; M. Jin; E. H. Frank, *Annual Review of Biomedical Engineering* **2000,** 2, 691-+.
2. W. A. Hodge; R. S. Fijan; K. L. Carlson; R. G. Burgess; W. H. Harris; R. W. Mann, *Proceedings of the National Academy of Sciences of the United States of America* **1986,** 83, (9), 2879-2883.
3. N. J. Mosey; M. H. Muser; T. K. Woo, *Science* **2005,** 307, (5715), 1612-1615.
4. L. S. Fan; Y. C. Tai; R. S. Muller, *Ieee Transactions on Electron Devices* **1988,** 35, (6), 724-730.
5. S. M. Spearing, *Acta Materialia* **2000,** 48, (1), 179-196.
6. K. Komvopoulos, *Wear* **1996,** 200, (1-2), 305-327.
7. R. Maboudian; W. R. Ashurst; C. Carraro, *Tribology Letters* **2002,** 12, (2), 95-100.
8. J. A. Williams; H. R. Le, *Journal of Physics D-Applied Physics* **2006,** 39, (12), R201-R214.
9. R. Maboudian; C. Carraro, *Annual Review of Physical Chemistry* **2004,** 55, 35-54.
10. S. A. Henck, *Tribology Letters* **1997,** 3, (3), 239-247.
11. E. E. Graham; E. E. Klaus, *Asle Transactions* **1986,** 29, (2), 229-234.
12. A. Rossi; F. M. Piras; D. Kim; A. J. Gellman; N. D. Spencer, *Tribology Letters* **2006,** 23, (3), 197-208.
13. J. C. Smith; M. J. Furey; C. Kajdas, *Wear* **1995,** 181, 581-593.

14. K. Strawhecker; D. B. Asay; J. McKinney; S. H. Kim, *Tribology Letters* **2005,** 19, (1), 17-21.

15. M. W. Urban, *Attenuated Total Reflectance Spectroscopy of Polymers Theory and Practice*. American Chemical Society: Washington, D. C., 1996.

16. M. S. Rogers; J. J. Sniegowski in: *In Technical Digest, Solid-State Sensors and Actuators Workshop, 8-11 June 1998, Hilton Head Island SC, USA, Transducer Research Foundation*, 5-Level Polysilicon Surface Micromachine Technology: Application to Complex Mechanical Systems, Cleveland, OH, 1998; Cleveland, OH, 1998.

17. S. J. Timpe; K. Komvopoulos, *Journal of Microelectromechanical Systems* **2005,** 14, (6), 1356-1363.

18. V. S. Smentkowski; J. A. Ohlhausen; P. G. Kotula; M. R. Keenan, *Applied Surface Science* **2004,** 231-2, 245-249.

19. D. B. Asay; S. H. Kim, *Journal of Physical Chemistry B* **2005,** 109, (35), 16760-16763.

20. J. G. Newman; B. A. Carlson; R. S. Michael; J. F. Moulder; T. A. Hohlt, *Static SIMS Handbook of Polymer Analysis*. Perkin-Elmer Corporation: Eden Prairie, MN, 1991.

21. A. D. Romig; M. T. Dugger; P. J. McWhorter, *Acta Materialia* **2003,** 51, (19), 5837-5866.

22. S. T. Patton; J. S. Zabinski, *Tribology International* **2002,** 35, (6), 373-379.

23. U. Raviv; J. Klein, *Science* **2002,** 297, (5586), 1540-1543.

24. U. Raviv; P. Laurat; J. Klein, *Nature* **2001,** 413, (6851), 51-54.

25. J. M. Helt; J. D. Batteas, *Langmuir* **2005,** 21, (2), 633-639.

26. F. Katsuki; K. Kamei; A. Saguchi; W. Takahashi; J. Watanabe, *Journal of the Electrochemical Society* **2000,** 147, (6), 2328-2331.

27. W. Maw; F. Stevens; S. C. Langford; J. T. Dickinson, *Journal of Applied Physics* **2002,** 92, (9), 5103-5109.

28. M. L. W. Vanderzwan; J. A. Bardwell; G. I. Sproule; M. J. Graham, *Applied Physics Letters* **1994,** 64, (4), 446-447.

29. T. E. Fischer; W. M. Mullins, *Journal of Physical Chemistry* **1992,** 96, (14), 5690-5701.

Chapter 9

In-situ Vapor-Phase Lubrication of MEMS

With kind permission from Springer Science + Business Media: Tribology Letters, In-situ Vapor-Phase lubrication of MEMS, ***29*** *(1), 2008, 67-74, D. B. Asay, M. T. Dugger, and S. H. Kim.*

9.1 Summary

In-situ vapor phase lubrication of sidewall MicroElectroMechanical System (MEMS) devices is investigated with 1-pentanol vapor. The 1-pentanol vapor successfully maintains lubricating properties between silicon contacts of MEMS devices. This is attributed to the ability of alcohol to adsorb on the silicon surface and sustain a lubricating layer, which prevents wear of the MEMS surfaces and minimizes friction. In the presence of these vapors, MEMS devices with sliding contacts operated *without failure* for up to a factor of 1.7 x 10^4 longer than in dry N_2 gas alone, representing a dramatic improvement in operating life. Adhesion and friction were also investigated as a function of alcohol vapor pressure. The adhesive force between microfabricated MEMS sidewall surfaces increases from ~30 to ~60 nN as the alcohol vapor pressure is increased from 0 to 20% of saturation, and then only slightly increases to ~75 nN at 95% of saturation vapor pressure. This increase in force is well within the capabilities of even the lowest force on-chip actuators, such as electrostatic comb drives which can typically

generate a few μN of force. The static friction force was found to be independent of alcohol vapor pressure within the uncertainties in the measurement.

9.2 Introduction

Despite over a decade of process development, design demonstration, and materials investigations encompassing the full spectrum from basic research to product manufacturing, the only microelectromechanical system (MEMS) devices that have met with large-scale commercial success are those that do not rely on sliding surfaces. Examples include accelerometers,[1] pressure sensors,[2] and print heads.[3] In fact, since the very first demonstration of devices with moving mechanical assemblies and functions that relied upon surface contact, problems associated with friction and wear were manifested.[4]

The most successful device containing contacting surfaces is the digital micromirror device from Texas Instruments, which contains aluminum spring tips that touch an aluminum landing pad and experience a maximum of about 50 nm in translational sliding motion. This small degree of sliding is due to flexural motion of the support structure upon mirror landing; it is an inevitable consequence of the MEMS structural design, rather than a critical motion designed for device function. Even though the contact sliding is small, this contact region requires lubrication; otherwise, the entire device fails. This is accomplished by encapsulating the micromirrors with perfluorodecanoic acid in a hermetically sealed package.[5] At an operating temperature of about 80ºC, the acid which is solid at room temperature exists as a vapor, and is therefore

able to adsorb on damaged aluminum surfaces to repassivate them. In this device, the acid vapors are used to prevent excessive adhesion between the landing pads and the micromirrors such that the mirrors can easily be detached from the pad, rather than to control frictional response between the landing pads and micromirrors.

Although untested, this approach may also be viable for silicon, a far more common material for microsystems due to the process knowledge gained from integrated circuit fabrication. However, the potential difficulty with perfluorodecanoic acid is that it exists as a solid at room temperature. In the absence of device heating, the material may not have sufficient vapor pressure to replenish the surface passivation. A more generally-applicable lubricating strategy for MEMS would involve species that have significant vapor pressure at or below room temperature, adsorb readily on silicon and silicon oxides, and do not present potential corrosion issues in long term storage.

Chemisorbed monolayers, commonly known as self-assembled monolayers (SAMs), have been successfully applied to silicon-based MEMS to make surfaces hydrophobic and prevent initial capillary adhesion.[6, 7] However, they wear off during initial mechanical contact, resulting in surfaces that exhibit unacceptable adhesion force, friction, and wear even in dry operating environments.[8-10] Continual surface passivation and lubrication is essential to prevent wear, minimize friction and adhesion forces and enable long-term operation of silicon devices over a wide temperature range.

Various studies have shown alcohol vapors to be effective lubricants between silicon contacts.[11-13] In these experiments, the equilibrium adsorption of primary alcohol molecules was observed to reduce adhesion, friction, and wear of silicon oxide surfaces. Especially, as the alkyl chain length of alcohol increases (from ethanol to 1-pentanol), the

larger adhesion force decrease is observed at the same relative partial pressure of the alcohol vapor (with respect to the saturation vapor pressure).[12] However, these effects were investigated primarily with AFM in which asperity contacts, contact speeds, and thus shear stresses are much different from the MEMS case. Therefore, the lubrication effects of alcohol vapor in MEMS may vary from the AFM results and must be tested at the MEMS operation conditions.

In this chapter, alcohol lubrication of sidewall MEMS devices with 1-pentanol vapor is demonstrated. Adhesion, static friction, dynamic friction and lifetime of a diagnostic MEMS sidewall device are investigated as a function of the relative partial pressure of the alcohol vapors. The results from these measurements indicate that in-situ vapor-phase lubrication is a viable and effective means of delivering lubricating molecules to the working device surfaces enabling device longevity without deteriorating device functions.

9.3 Experimental Details

High purity 1-pentanol (Fisher Scientific) was used in the as-received condition. The partial pressure of the alcohol was regulated by passing dry nitrogen through a liquid 1-pentanol bubbler. The exiting gas from the bubbler was saturated with alcohol vapor molecules. The partial pressure of 1-pentanol relative to the saturation pressure (P^{sat}) was maintained by mixing the saturated vapor stream with dry nitrogen at a constant ratio.[13] The saturation vapor pressure of 1-pentanol at room temperature was below the lower

explosive limit for 1-pentanol (1.3 volume percent), making this alcohol safe for experiments at room temperatures, even in the case of an oxygen leak or ignition source in the test environment.

9.3.1 Specimen Preparation

The adhesion and friction forces, as well as operation lifetime of a diagnostic MEMS device was evaluated using a sidewall tribometer built using Sandia National Laboratories' SUMMiT^{TM} process.[14] This particular sidewall tribometer was adapted from an earlier device[15] and enabled characterization of static and dynamic friction, as well as adhesive pull-off forces, in a compact structure resistant to the effects of residual stress. Made up of a movable post and shuttle, the contact geometry was essentially a cylinder-on-flat with a cylindrical height of 2.26 μm and a radius of curvature of 50 μm. The typical root-mean-square surface roughness of these contacts was measured by contact mode atomic force microscopy and found to be on the order of 20 nm. Device surfaces were passivated during the release process with an amine-functionalized chemisorbed monolayer [tridecafluorotris(dimethylamino)silane, $CF_3(CF_2)_5(CH_2)_2Si(N(CH_3)_2)_3$, called FOTAS hereafter] rendering the silicon surfaces hydrophobic. Its reaction with silicon surfaces is similar to that of hexamethyldisilazane (HMDS), a well known hydrophobic-treatment agent. The amine end groups react with surface -OH groups forming a covalent bond to the silicon surface.[16] This SAM

treatment facilitated initial operation and prevented in-process adhesion due to water capillary formation between touching surfaces.

The MEMS devices were operated in a custom ultrahigh vacuum chamber (volume ~0.5 liters) with gas inlets and outlets allowing for control of the atmosphere around the test device. These devices were packaged in 24-pin ceramic packages for testing in the environmental chamber. The devices were attached to the packages using a low out-gassing adhesive (JM7000, Ablestik Co.) and wire bonded to the package pads using aluminum wire for signal delivery to the device. Nitrogen gas containing alcohol vapor with a known partial pressure was supplied to the chamber at a total flow rate of ~ 0.5 liters per minute, and allowed to purge the chamber for 30 minutes prior to testing. All tests were performed at room temperature.

Specimens for macroscopic pin-on-flat friction measurements consisted of silicon (100) wafers and quartz (SiO_2) spheres. The SiO_2 spheres were cleaned for 15 minutes in a UV/ozone chamber. FOTAS was deposited on the flat silicon surfaces in the same manner as that used for MEMS devices.

9.4 MEMS Tribological Measurements

A scanning electron microscopy (SEM) image of the MEMS sidewall tribology device is presented in Figure 1. This device was used to investigate tribological phenomena between sidewall contacts (encircled in Figure 1) with a cylinder-on-flat type contact geometry. Sliding motion was generated by applying bias voltages to different

sets of comb drives. The electrostatic force generated by the comb drives was calculated from:[17]

$$F_E = \frac{N\varepsilon h V^2}{g} \qquad \textbf{9-1}$$

where N is the number of comb fingers, ε is the permittivity (= 8.854 x 10^{-12} F/m), h the thickness of the comb fingers (= 6.91 μm), V the applied voltage, and g the gap between the fingers (= 2.2 μm). The electrostatic force acting on the system was therefore proportional to the voltage squared. One set of electrostatic comb actuators, referred to as the *load/unload* actuators (marked with A in Figure **9.1**), was used to apply forces normal to the nominal contact interface by bringing the post in and out of contact; a separate set of electrostatic comb actuators, referred to as the *push/pull* actuators (marked with B in Figure **9.1**), was used to laterally displace the shuttle perpendicular to the loading direction.

A charge coupled device (CCD) camera was used to capture the motion of the shuttle and post. In addition to the images, voltages applied to each of the comb actuators were recorded simultaneously. The captured images were then processed to determine the positions as well as drive voltages (hence force) of the shuttle and post as a function of time. Image processing used a pattern matching algorithm that determines the distance between a unique feature on the shuttle or post and one attached to the substrate, thereby capturing the motion of the shuttle or post relative to a fixed position. The standard deviation in position measurement using this technique for a non-actuated shuttle was ~40 nm.

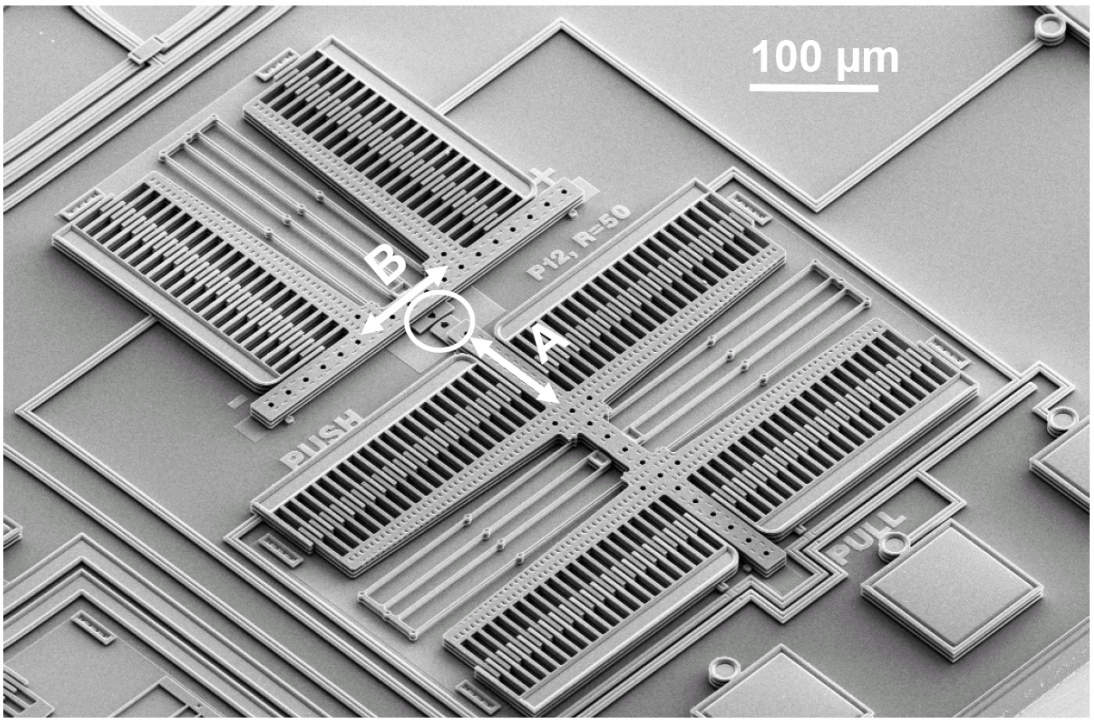

Figure **9.1**: SEM image of MEMS sidewall diagnostic tribometer. Sidewall contact area encircled. Loading/Unloading actuators cause the post (Labeled "A") to move and come into and out of contact. Push/Pull actuators cause the shuttle (Labeled "B") to move laterally and shear the contact.

Adhesion forces were measured by initially applying a 500 nN normal load to the contact with the load/unload actuators. The normal force was then ramped down, and the post position versus net normal force was determined. The adhesive force was determined as the net applied force when the post initially separated from the shuttle. The specifics for this measurement have been described elsewhere.[15] All adhesion measurements were repeated 10 times.

Static friction measurements were performed by applying 500 nN with the load/unload actuator while the shuttle was at the center of its range, at rest. After this load was applied by the post "A", a lateral force on the shuttle "B" was ramped linearly at 125 nN/sec to a peak force of 500 nN. The position of the shuttle was measured repeatedly every 20 msec. The static friction force was defined as the lateral force applied to the shuttle at the point when the shuttle first moved laterally. The post was then taken out of contact with the shuttle (unloaded). This procedure was repeated 10 times for each static lateral force measurement.

Dynamic friction and lifetime testing was performed with a 500 nN normal load applied with the load/unload actuator "A". Assuming smooth contact between cylindrical and flat surfaces, this load would produce a Hertzian contact area of 0.028 μm^2 and an average contact pressure of 18 MPa. The maximum force applied by the push/pull actuator was 500 nN, displacing the shuttle ~9 μm from the rest position in both directions. Using these operating conditions, friction coefficients of ~1.0 and less could be measured. An alternating linear force ramp was applied to the reciprocating shuttle at 100 Hz and provided a contact speed of ~2 mm/sec and maximum displacement amplitude of ~18 μm. During friction measurements at 100 Hz, the CCD camera was not

capable of tracking motion during the entire range of motion. For this reason, only images at the outermost displaced position were captured every few seconds. Friction in these MEMS devices was then determined by monitoring the difference in motion amplitude between the loaded contact and that when no load was applied. This difference in range of motion (a length) was multiplied by the spring constant of the push/pull actuator (~0.028 N/m) to yield a force. The friction coefficient was then calculated from the ratio of this product over the applied normal load.

Lifetime for the MEMS devices was defined as the length of time that the device continued to oscillate under the applied load (500 nN) with only the available electrostatic force (500 nN). Failure occurred when the oscillating motion stopped, indicating a friction coefficient larger than ~1. Since the force exerted by the comb-drive was not calibrated but estimated from Equation 1, the friction coefficient at failure varied from 0.9 to 1 in our experiments.

9.5 Pin-on-Flat (or Macroscopic) Friction Measurements

Linear wear tests (LWT) were performed inside a glovebox. The LWT contact consisted of a 3.2 mm diameter quartz ball and a silicon (100) wafer treated with FOTAS. A 98 mN load was used, providing an estimated Hertzian contact diameter of 33 μm, and a contact pressure of 115 MPa. The sliding speed was maintained at ~1.5 mm/sec (comparable with MEMS testing) and each cycle represents 1 pass across the sample. Within the glovebox, the nitrogen/alcohol gas mixture (~0.5 L/min) was directed at the contact from a tube ~3 cm away, providing a local environment whose partial pressure of

the 1-pentanol was ~95% that of the saturation pressure (P^{sat}). All tests were performed at room temperature.

9.6 Results and Discussion

9.6.1 DRY Environment

Dynamic friction testing of MEMS devices was performed in a dry N_2 environment (~7 ppm O_2 and <100 ppm H_2O) to investigate the frictional response and lifetime with the monolayer surface treatment alone. Figure **9.2** illustrates typical frictional behavior in dry nitrogen. In less than 10,000 cycles (<2 min at 100 Hz), the push/pull actuator no longer generates force sufficient to shear the contact and the device fails. The frictional response varies greatly from device to device and during each run. This is due to differences in real contact area from device to device, depending on the local surface roughness. The rapid failure of the MEMS tribometer is attributed to wear of the FOTAS layer, allowing unpassivated silicon dangling bonds to adhere across the interface.[18]

The force required to separate the contacts after they have seized during the dynamic friction test significantly increased, indicating wear of the FOTAS film and adhesion of silicon. The average force required to separate the surfaces immediately following failure (called pull-out force hereafter) was 586 ± 211 nN. Prior to operation, with the FOTAS film intact, the average adhesion force was 86 ± 30 nN. This ~7 fold increase in adhesion is due to the difference in surface energy between the FOTAS-

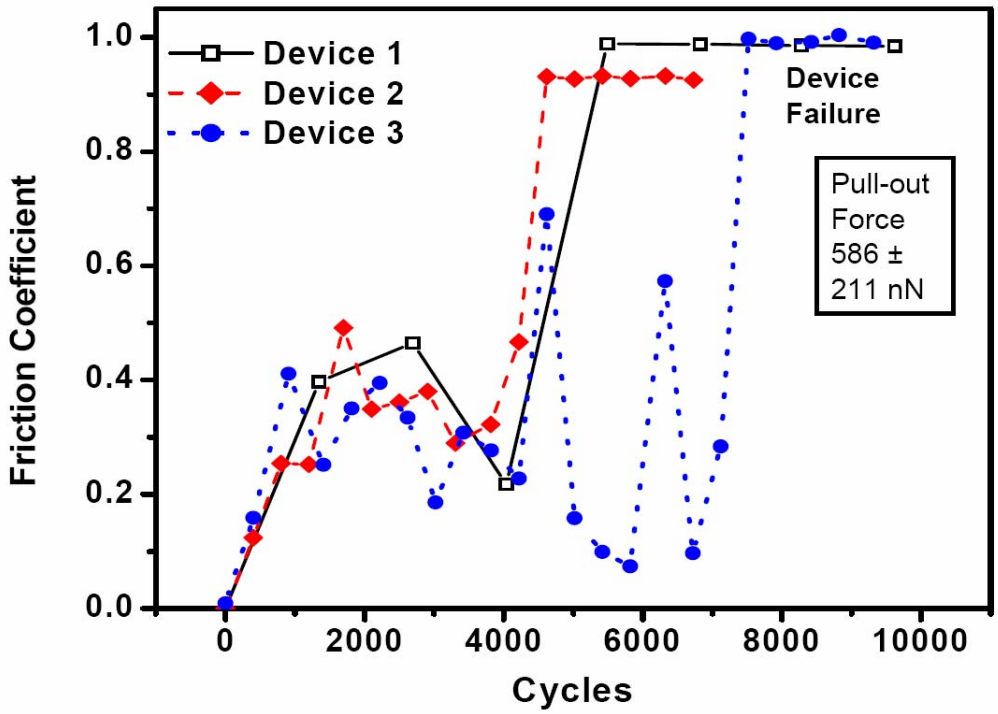

Figure **9.2**: Frictional response of three separate MEMS sidewall tribometer devices oscillating at 100 Hz under a 500 nN load, in dry N_2 at room temperature. Devices fail between 4000 and 8000 cycles.

covered surface and the worn surface. This increase is due to the stochastic removal (wear) of FOTAS and/or subsequent wear of underlying SiO_x and/or Si.

Once separated, repeated adhesion measurements on these devices revealed an average adhesion force of 260 ± 150 nN, only a factor of 3 increase from the initial adhesion force. While the adhesion force is smaller than the pull-out force at failure, it is much larger than the initial adhesion force prior to lateral motion. The reason for the large differences between the pull-off and adhesion forces after failure is due to the difference in the positions at which these forces were measured. Failure never occurred with the shuttle at the rest position (0 lateral displacement). Therefore, the position of the pull-out force measurement (the first separation immediately after failure) was always different from that of the adhesion force measurement (done always at the rest position). This indicates that the wear process was nonuniform, as the device stopped in the location of greatest adhesion. After failure, the static friction also increased ~3.3 times compared with the initial static frictional force prior to operation indicating a change in the surface topography and/or chemistry. As both static friction and adhesion forces were measured at the same shuttle position (the "at rest" position), the increases in these forces after failure seem to correlate well with each other as shown in Table **9.1**.

Table **9.1**: Adhesion and static friction forces measured before operation and after failure in dry nitrogen.

	Dry Nitrogen	
	Initial (nN)	After Failure (nN)
Adhesion	86 ± 30	260 ± 150
Static Friction	122 ± 24	396 ±73
Pull-out*	N/A	586 ± 211

* Pull-out is the force required to separate the post from the shuttle immediately

9.6.2 Vapor-Phase Lubricating Environment

One of the concerns related to vapor phase lubrication is capillary adhesion. The condensation of vapor at asperity contacts can generate capillary forces which will increase the total normal load at the contact. If capillary forces are excessive, contacting surfaces can adhere so strongly that lateral forces will be insufficient to generate device motion. If $(F_{adh+cap}+L)\mu > F_E$, the push/pull actuator will not produce force sufficient to shear the contact; where (μ) is the coefficient of friction, ($F_{adh+cap}$) the total adhesive forces (which includes capillary forces), (L) the applied load, and (F_E) the actuator force as expressed in Equation **9-1** . Assuming μ ~0.2 with a 500 nN load, if the total adhesive forces are greater than 400 nN, the device will not move.

Figure **9.3** shows the adhesion force of two MEMS devices as a function of the relative partial pressure of 1-pentanol. The increase in adhesion force with alcohol vapor is attributed to capillary forces at the real areas of contact at the post-shuttle interface. While capillary adhesion is typically a problem with water films,[18, 19] the magnitude of capillary forces with alcohol molecules is much smaller. This is due to the low surface tension of alcohol, 24.9 erg/cm^2 (1/3 the water surface tension) and large liquid molar volume, 108.7 cm^3/mol (6 times the water molar volume) in the case of 1-pentanol.[12, 20] According to the Kelvin equation, the capillary pressure is inversely proportional to the molar volume.[21]

$$P_{Capillary} = \frac{RT}{V}\ln\left(\frac{P}{P^{sat}}\right) \qquad \textbf{9-2}$$

At the same relative partial pressure (P/P^{sat}) as the molar volume increases, the capillary pressure "pulling" the surfaces into contact decreases. Additionally, unlike water which forms thick multilayers on silicon oxide under typical humidity conditions (10 ~ 90%), 1-pentanol closely follows the Langmuir adsorption isotherm, saturating at approximately one monolayer, minimizing the number of capillary bridges between rough surfaces. These characteristics mitigate the formation of excessively large capillary forces with 1-pentanol.

While adsorption of alcohol molecules slightly increases the observed adhesion between contacts, its effect on static friction is not observed. Figure **9.4** illustrates that there appears to be no change in the static friction force with increasing partial pressure of 1-pentanol in the environment. The difference in static friction exhibited by the two devices can be attributed to differences in roughness and real area of contact.

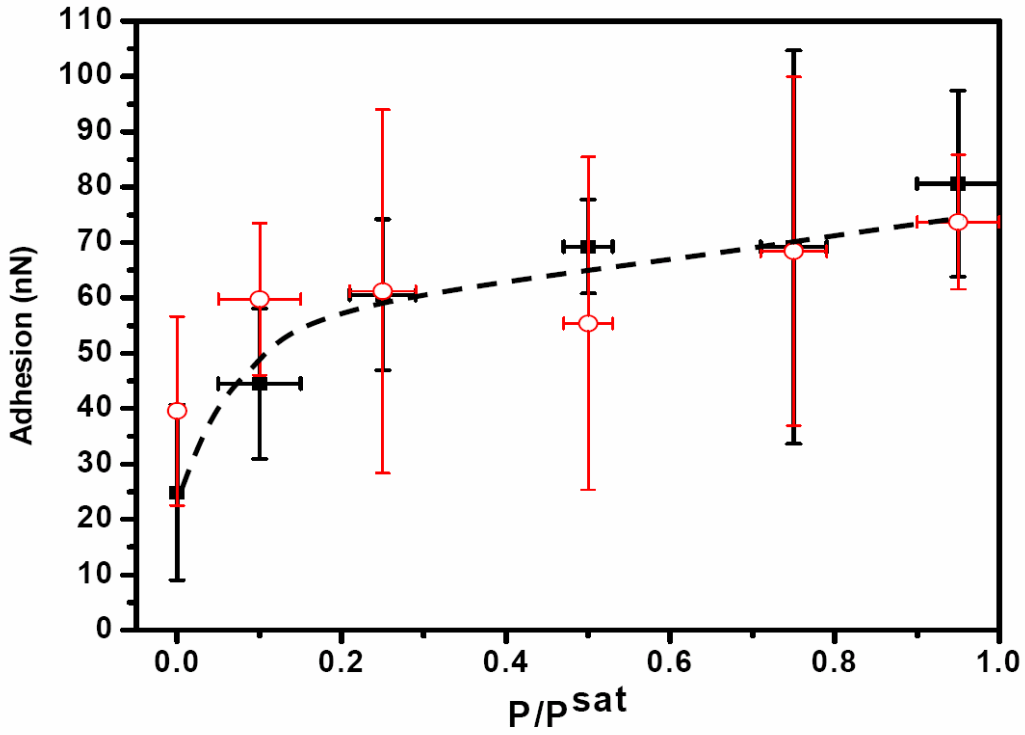

Figure **9.3**: Adhesion force of two different MEMS sidewall devices as a function of the relative partial pressure of 1-pentanol (P/P^{sat} where P^{sat} is the saturation pressure of the alcohol).

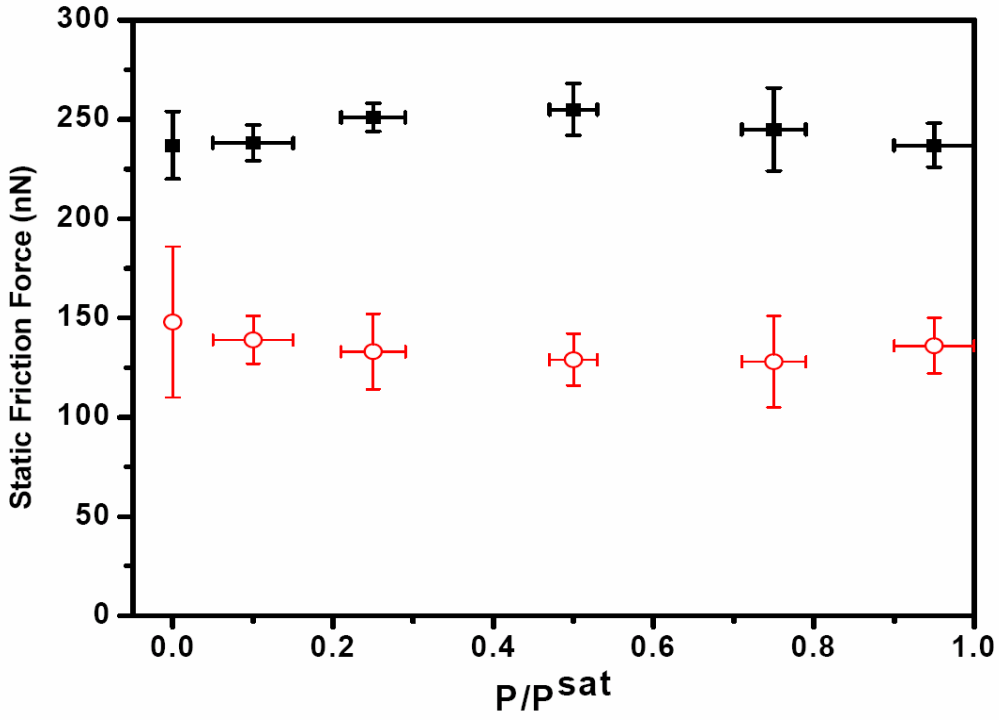

Figure **9.4**: Static frictional force of the same two MEMS sidewall devices (Figure 3a) as a function of the relative partial pressure of 1-pentanol.

Dynamic friction and lifetime measurements were also taken at various partial pressures of 1-pentanol with MEMS sidewall tribometers. Figure **9.5** compares the tribological performance of three devices operated in 1-pentanol vapors to those operated in dry N2 discussed previously. In each case, when 1-pentanol vapor was present, the device continued to operate, and failure was *never* observed. Eventually, the device was stopped manually for adhesion and static friction measurements. Additionally, the coefficient of friction was relatively constant below ~0.3 when alcohol vapors were present. In one long term test a device was allowed to run for over 10^8 cycles (11 days) at 15 ±5% of P^{sat}. This device was then stopped and examined with SEM for evidence of wear or debris. Even after such a long duration, no wear particles were observed in SEM imaging. Instead, there appeared to be a fluid-like deposit created near the tall asperities (Figure **9.6**). These deposits were not removed even with immersion in hot 1-pentanol solution (80°C for 2 hours). The growth and chemical makeup of this film is not fully understood yet and the subject of on-going investigation.

Linear wear testing was performed to produce sliding contact areas large enough for surface analysis as well as to investigate the effects of alcohol adsorption on friction and wear at a larger length scale. Figure **9.7** illustrates the importance of maintaining the alcohol vapor to maintain low friction. This experiment began with 95% of the saturation pressure (P^{sat}) of 1-pentanol present in the gas flow directed at the contact interface. When the concentration of 1-pentanol vapor in the gas flow was reduced to zero (after 500 cycles), the lubricating species in the contact region seemed to be removed gradually and friction increased correspondingly. Before substrate wear became significant, gas flow was reintroduced with 1-pentanol vapor at 95% of P^{sat} (after 900 cycles), and the

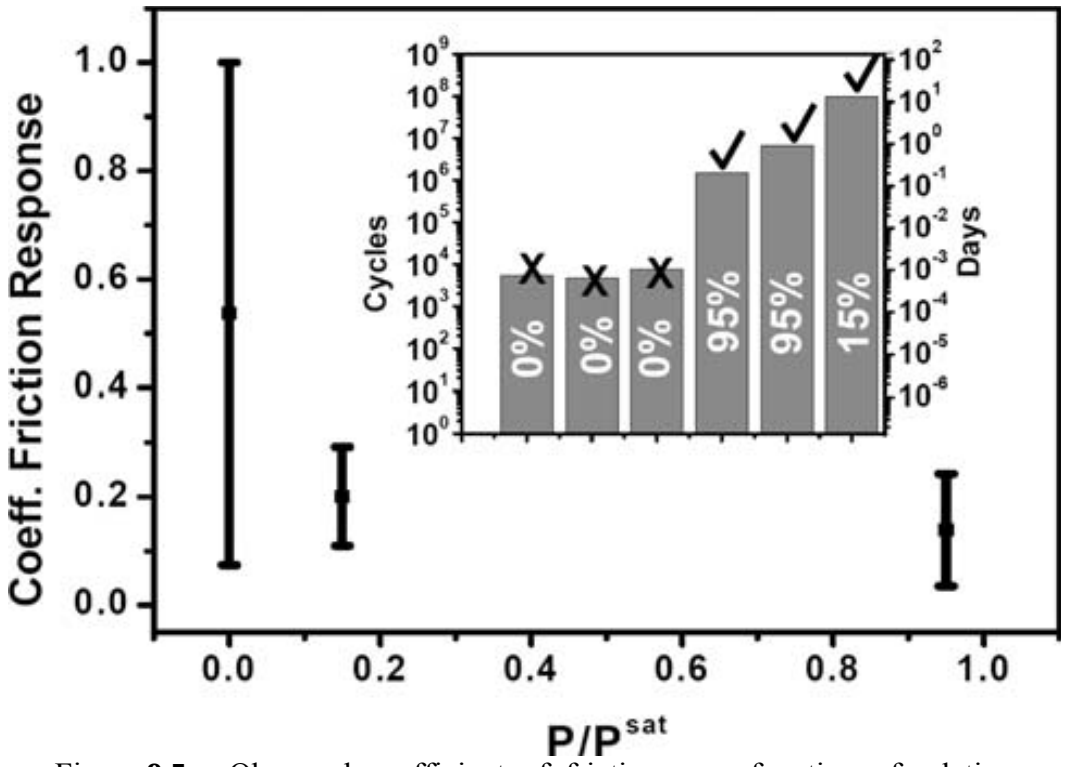

Figure **9.5**: Observed coefficient of friction as a function of relative partial pressure of 1-pentanol (reported as a range). Of six MEMS sidewall tribometer devices oscillating at 100 Hz under a 500 nN load, three were tested in dry N_2 and others at various relative partial pressures of 1-pentanol vapor. Devices DID NOT fail when 1-pentanol vapors were present. INSERT: cycles until failure or cycles until stopped by user. Note: (**X**) indicates failure, while (✓) indicates that the device was stopped by the user.

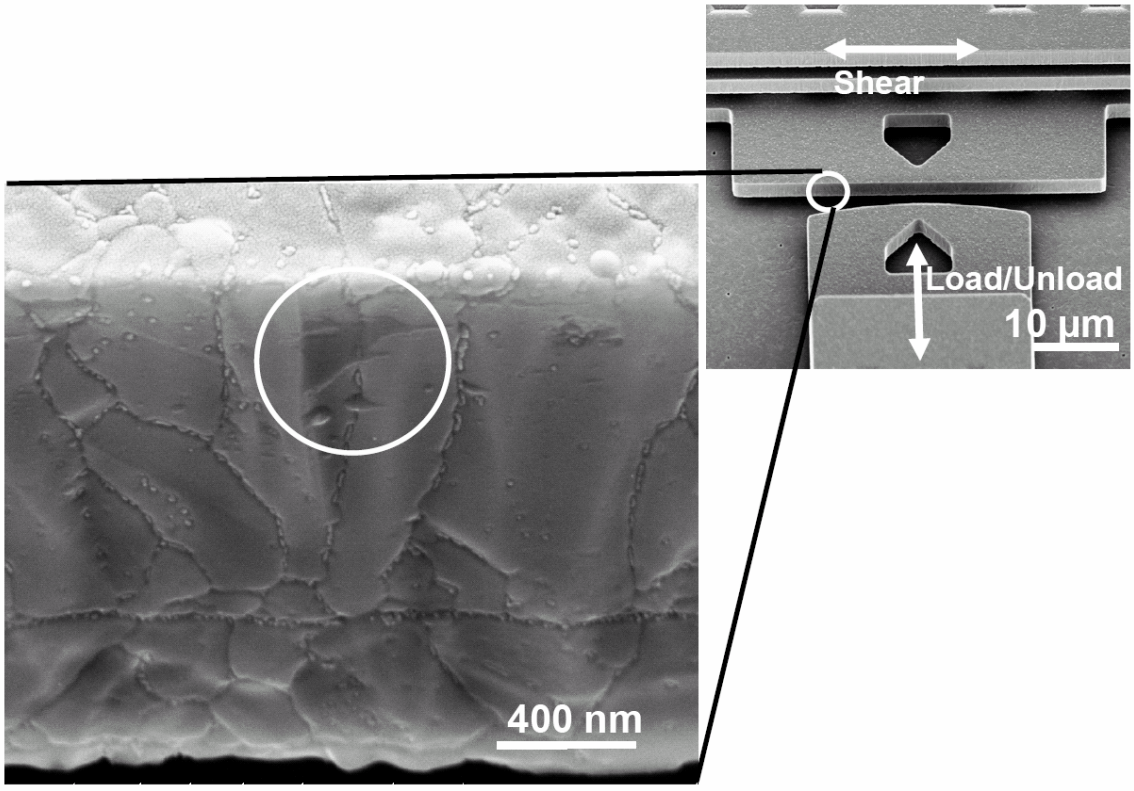

Figure **9.6**: SEM image of the MEMS sidewall surface following 1.02×10^8 cycles at 100 Hz in a 15 ±5% P/P^{sat} 1-pentanol environment.

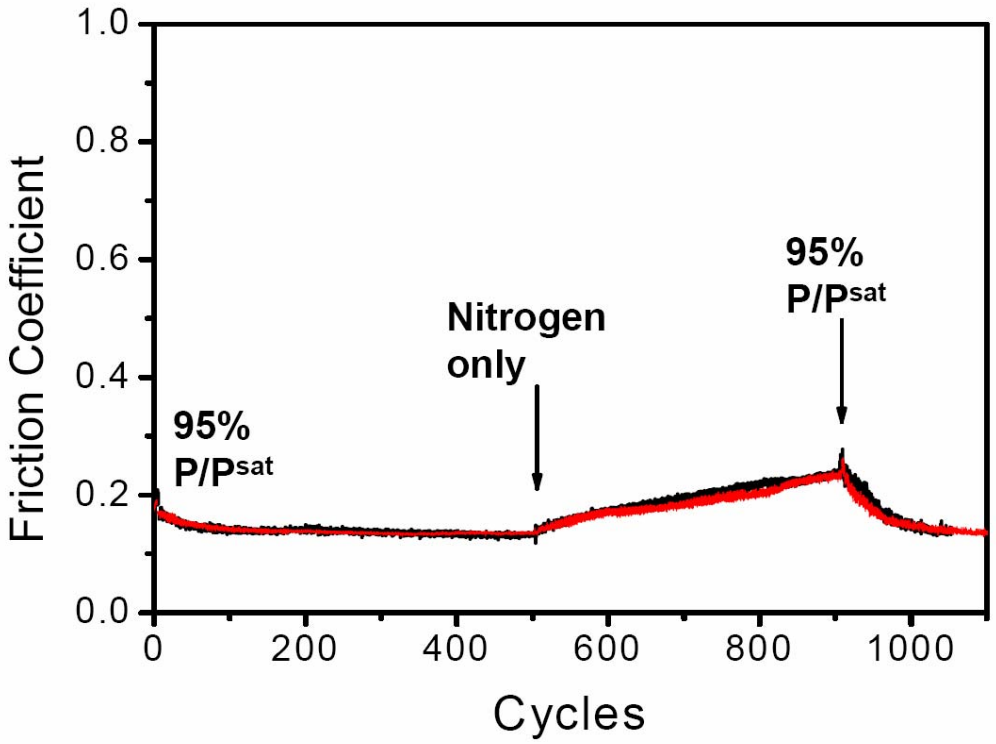

Figure **9.7**: Friction coefficient of FOTAS coated silicon as measured by LWT. Initially the environment contains 95% P/P^{sat} 1-pentanol. The environment was cycled from this condition to a dry N2 condition then back to a 95% P/P^{sat} environment as indicated at 500 and 900 cycles. Two lines (red and black) represent two separate experiments.

frictional behavior returned to the original steady state value near 0.15. This behavior was reproducible, as long as the sliding duration in dry N_2 was short enough to prevent damage to the substrate and produce large wear debris.

Separate spectroscopic investigations of the silicon wafers retrieved from LWT runs in 1-pentanol vapor indicate the formation of a high molecular weight oligomeric species inside the contact region.[11] This polymer-like film is a reaction product generated inside the contact and seems to play a significant role in preventing wear between silicon-silicon contacts. Similar polymer-like films have been perceived in other systems.[22] The fluid-like deposits observed in Figure **9.6** may have the same or similar chemical nature observed in the LWT experiments, helping to protect the MEMS surfaces from wear.

Recovering low friction upon re-introduction of alcohol vapor in LWT was also observed in MEMS devices as we tested the ability to re-start failed MEMS devices in alcohol vapor environments. Figure **9.8** illustrates the friction behavior of a MEMS device under different 1-pentanol P/P^{sat} conditions. After operating in a 95% P/P^{sat} environment for over 6.65 million cycles (18 hours), the device motion was stopped by the user momentarily and the chamber was purged with dry N_2. Once all the alcohol vapors were removed, the device was restarted again and the device failed after 10,000 cycles in the dry nitrogen environment. As in linear wear testing (Figure **9.7**), when the alcohol environment was exchanged with dry nitrogen, the friction coefficient began to increase until the friction force could not be overcome by the push/pull actuator, and the device stopped. Following this failure, the contact was separated and the 95% P/P^{sat} 1-pentanol environment was reintroduced. The device was restarted, and ran for another

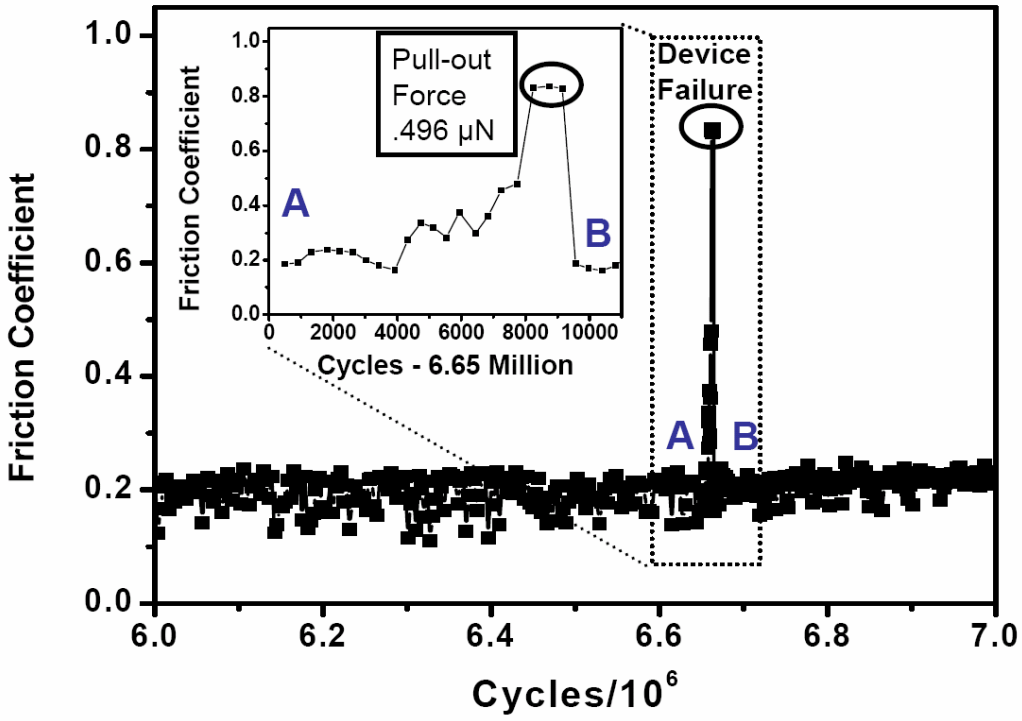

Figure **9.8**: Friction coefficient of MEMS device vs. cumulative cycles. Initially the environment contains 95% P/P^{sat} 1-pentanol. After 6.65 million cycles the environment was cycled from this condition to a dry N2 condition then back to a 95% P/P^{sat} environment labeled as "A" and "B" respectively. The insert is a magnification between points "A" and "B".

16.4 million cycles (over 45 hours) until it was stopped by the user. This test proved that the alcohol vapor was able to repassivate and lubricate the failed contacts, recovering device function after failure due to high friction. The ability to restart devices in alcohol vapor that failed to operate in dry nitrogen has been demonstrated several times.

In order to investigate changes in surface forces, during the 11 day test at 15 ±5% of P^{sat}, the device was stopped several times during operation to measure the adhesion force. As shown in Figure **9.9**, the adhesive force between the contacts increased slightly during testing over 11 days. This might be attributed to the buildup of the deposit seen in Figure **9.6**. As more polymer-like reaction product is produced through repetitive sliding, the gaps between tall asperities may fill. If the accumulated material is polymer-like and compliant, it may increase the contact area between the surfaces in regions where contact would not have occurred had the product not been present. This additional contact area would therefore increase the force required for separation. Alternatively, slight polishing of the real contact spots might occur at levels too small to be visualized in SEM imaging. This would also result in an increase in the contact area, leading to increase in the adhesion force. The growth mechanisms and kinetics of this film and accumulation are not yet fully understood.

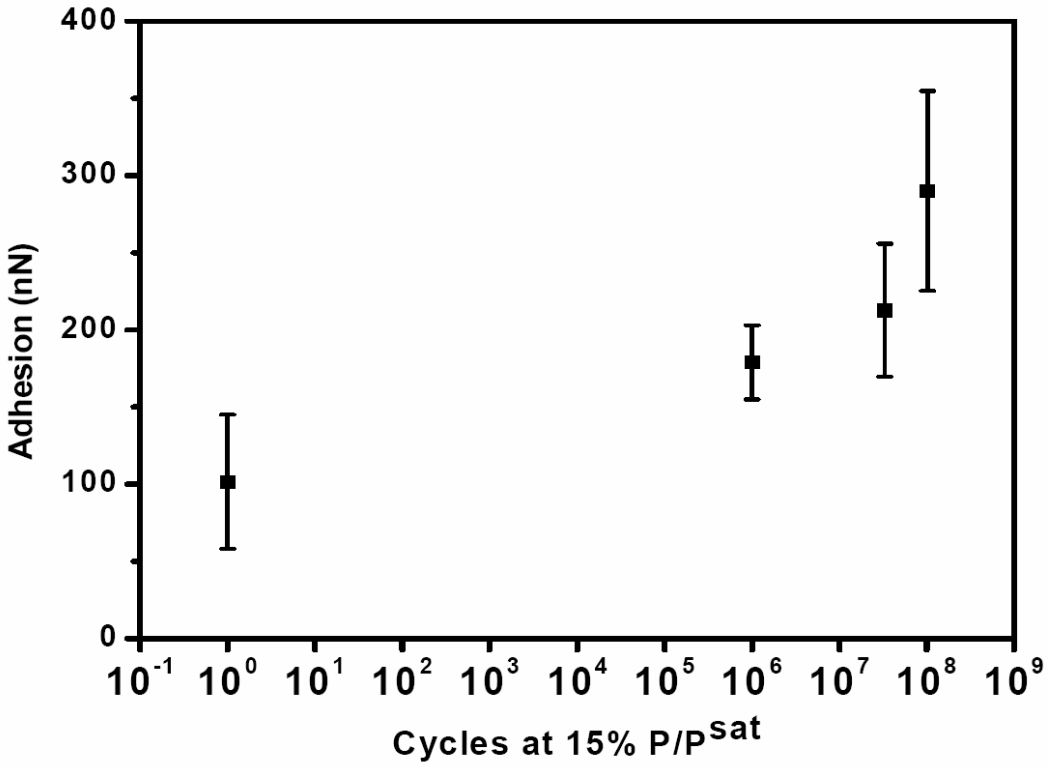

Figure **9.9**: Adhesion force of the MEMS sidewall device as a function of the number of cycles operating in a 1-pentanol P/P^{sat} environment of 15 ±5%.

9.7 Conclusions

In-situ vapor phase lubrication of MEMS devices with sliding contacts has been successfully demonstrated. Vapor phase lubrication for MEMS contacts with 1-pentanol vapor results in a replenishable lubricating film, providing extremely long operational lifetimes compared to chemisorbed monolayers alone. When alcohol vapor is removed from the environment, friction coefficient increases and eventually leads to device failure. Devices that have failed due to operation in dry N2 can be restarted in 1-pentanol vapor and operate as long as the alcohol concentration is maintained. With vapor phase lubrication, unprecedented operation lifetimes can be achieved with silicon MEMS devices.

9.8 References

1. K. H. L. Chau; S. R. Lewis; Y. Zhao; R. T. Howe; S. F. Bart; R. G. Marcheselli, *Sensors and Actuators a-Physical* **1996,** 54, (1-3), 472-476.
2. W. P. Eaton; J. H. Smith, *Smart Materials & Structures* **1997,** 6, (5), 530-539.
3. S. Verdonckt-Vandeboek in: *Proc. SPIE - The International Society for Optical Engineering*, SPIE-International Society for Optical Engineering, Bellingham, WA, 1997; K. Chau; F. P. J., (Eds.) SPIE-International Society for Optical Engineering: Bellingham, WA, 1997; p 180.
4. L. S. Fan; Y. C. Tai; R. S. Muller, *Sensors and Actuators* **1989,** 20, (1-2), 41-47.
5. S. A. Henck, *Tribology Letters* **1997,** 3, (3), 239-247.
6. R. Maboudian, *Surface Science Reports* **1998,** 30, (6-8), 209-270.
7. R. Maboudian; W. R. Ashurst; C. Carraro, *Tribology Letters* **2002,** 12, (2), 95-100.
8. M. A. Baker; J. Li, *Surface and Interface Analysis* **2006,** 38, (4), 863-867.
9. H. Liu; B. Bhushan, *Ultramicroscopy* **2002,** 91, (1-4), 185-202.
10. X. D. Xiao; J. Hu; D. H. Charych; M. Salmeron, *Langmuir* **1996,** 12, (2), 235-237.
11. D. B. Asay; M. T. Dugger; J. A. Ohlhausen; S. H. Kim, *Langmuir* **2008,** 24, (1), 155-159.
12. D. B. Asay; S. H. Kim, *Langmuir* **2007,** 23, (24), 12174-12178.

13. K. Strawhecker; D. B. Asay; J. McKinney; S. H. Kim, *Tribology Letters* **2005,** 19, (1), 17-21.

14. R. Nasby; J. J. Sniegowski; J. C. Smith; M. S.; B. C.; W. P. Eaton; P. J. McWhorter in: *Application of chemical-mechanical polishing to planarization of surface-micromachined devices, Tech. Digest, Solid State Sensors and Actuators Workshop*, Hilton Head, CA 1996; Hilton Head, CA 1996; pp 48-53.

15. S. J. Timpe; K. Komvopoulos, *Journal of Microelectromechanical Systems* **2005,** 14, (6), 1356-1363.

16. T. M. Mayer; M. P. de Boer; N. D. Shinn; P. J. Clews; T. A. Michalske, *Journal of Vacuum Science & Technology B* **2000,** 18, (5), 2433-2440.

17. W. C. Tang. Electrostatic Comb Drive for Resonant Sensor and Actuator Applications. University of California, Berkley, 1990.

18. S. T. Patton; J. S. Zabinski, *Tribology International* **2002,** 35, (6), 373-379.

19. K. Komvopoulos; W. Yan, *Journal of Tribology-Transactions of the Asme* **1997,** 119, (3), 391-400.

20. L. Segade; J. J. de Llano; M. Dominguez-Perez; O. Cabeza; M. Cabanas; E. Jimenez, *Journal of Chemical and Engineering Data* **2003,** 48, (5), 1251-1255.

21. A. W. Adamson; A. P. Gast, *Physical Chemistry of Surfaces, 6th Edition*. John Wiley & Sons: New York, 1997.

22. E. E. Graham; E. E. Klaus, *Asle Transactions* **1986,** 29, (2), 229-234.

Chapter 10

Competitive Adsorption of Water and 1-Pentanol on Silicon under Tribological Conditions

10.1 Summary

This chapter describes the effect of water vapor on the wear prevention capabilities of 1-pentanol vapor phase lubrication of silicon oxide surfaces. When water is present (as an adsorbed film), chemical wear of many oxides is accelerated. This is also true of silicon and its oxide. In contrast, when alcohol i.e. 1-pentanol vapors adsorb onto silicon oxide surfaces, wear rates greatly decrease and in many conditions nonexistent. When both water and alcohol vapors are present these two compete for adsorption onto the surface. While one molecule helps prevent wear, the other does the opposite. In the packaging of MEMS, it is typical to observe water levels on the order of 1000 ppmv without any desiccant and ~500 ppmv with a desiccant. This chapter studies the influence of water at these moisture concentrations pertinent to MEMS technologies and vapor phase lubrication. With sufficient alcohol vapor concentrations, 1-pentanol mitigates wear when little water is also present.

10.2 Introduction

Many macroscale observations of physical properties and their performance depend on the bulk properties of the materials comprising the physical system. For example, the weight of a system depends in the density of the bulk. Similarly, the viscosity of a fluid will determine, in large part, the energy required to pump the material within a system, assuming there is no significant change in the potential energy of the system. Various other macroscale phenomena depend greatly on bulk properties. There are however, a number of macroscale observations that depend not on the bulk properties of the system, but the chemical and structural properties at an interface. Examples include contact resistances, wettability, adhesion, corrosion, friction, and wear. In these systems, the behaviors of a miniscule number of molecules dominate observed behavior of the system.

The adsorption of volatile species onto surfaces has a dramatic effect on interfacial phenomena. Water, a common adsorbate present in the atmosphere, is essential to life and important in many geological and atmospheric events.[1] For these reasons, the influence of water at interfaces has been the subject of much research.[1-32]

Tribological phenomena like adhesion, friction, and wear all depend on the properties of interfaces in contact.[1, 4, 7-9, 14, 16-18, 23-26, 29, 32-55] Nanoscale thin films can help lubricate, change the adhesion between contacts, and/or cause wear.[4, 7-9, 14, 17, 18, 23-25, 29, 32, 38-40, 42-55] These tribological behaviors become increasingly more important as devices

shrink in size. Microelectromechanical systems (MEMS) are typically made of silicon and are so small that surface forces dominate their behavior.[56] In order to operate microscale devices, the actuation forces must be able to overcome these surface forces. Additionally, due to the extremely small size of these systems, wear must be prevented.

Recently, vapor phase lubrication (VPL) of MEMS devices has been shown to be very successful in minimizing friction and preventing wear.[55, 57, 58] In the study, 1-pentanol vapors were used as the VPL. The basic premise behind VPL is the ability of volatile lubricant molecules to readily adsorb onto the silicon (or silicon oxide) surface and provide a protective lubricant layer. If during contact, an asperity displaces the lubricant or it desorbes, a new lubricant molecule adsorbes from the gas phase replacing the missing lubricant, "healing" the surface. Wear of the underlying surface is then prevented. In one example of successful VPL, a device that had failed due to wearing of a protective hydrocarbon surface was able to operate following failure when the device ran in the presence of these vapor phase lubricants. The surface was then "healed".

While this study has generated much interest,[59] water was precluded from the system. While water can help lubricate many surfaces, it can cause the chemical wear of silicon.[37, 43, 50, 58] In a real packaged MEMS device, some water will be present. Therefore, while potential VPL hydrocarbons may prevent wear and minimize friction, if water is present, the effectiveness of the VPL hydrocarbons will be limited. In other systems, the adsorption of water and competing hydrocarbons are also of interest. In this study, we report the effect of water on 1-pentanol VPL of silicon.

Both experimental data from linear wear tests (LWT)/pin-on-disc tribometers, and MEMS are used to investigate the influence of water on friction and wear.

10.3 Experimental Setup

High purity 1-pentanol was used as-received from Fisher Scientific. Controlling the chemical constituents in the environmental was accomplished by one of two techniques. Concentrations of 1-pentanol and water vapors in the gas below the equilibrium saturation pressure (P^{sat}) condition were achieved by mixing one stream of dry nitrogen or argon with a stream saturated with 1-pentanol and a stream with water vapor. The saturated 1-pentanol stream was made by bubbling the carrier gas in a custom made bubbler that was kept just above room temperature. This provided a slightly supersaturated stream. The supersaturated stream was then sent into another bubbler kept at room temperature. The second bubbler was packed with glass beads to provide ample time for the exiting vapor to reach equilibrium, yielding a saturated stream. The humid stream was made by passing the carrier gas in a bubbler kept near the freezing point of water, providing a low humidity source. The water vapor content in the humid stream was then measured with a chilled mirror hygrometer prior to mixing. The second technique was used to achieve only saturated conditions. The pin-on-disc tribometer is enclosed in a chamber, which allowed for the control of the environment in the chamber. A reservoir of the desired condition, either liquid 1-pentanol or a mixture of liquid 1-pentanol and liquid water, was placed inside the chamber. In addition, a piece of kimwipe was immersed in the reservoir and placed near the rotating disc in order to provide a saturated VPL source at the substrate efficiently.

Wear testing was done with flat silicon (100) wafers with native oxides sliding against a quartz (SiO_2) sphere 3 mm in diameter. Prior to these experiments the wafers

were placed in an UV/Ozone chamber for ~15min followed by an RCA-1 cleaning and washing with copious amounts of MilliQ water. Quartz spheres were cleaned in the UV/Ozone chamber prior to use. Testing was done in a dry glovebox. The environment immediately surrounding the contact was controlled by flowing the Nitrogen/water/pentanol stream directly at the point of contact ~ 3 cm away with a total flowrate ~0.5L/min. For the pin-on-disc, a flow of nitrogen to the chamber was used to purged the atmospheric moisture from the system and ensure a dry condition. Following purging, a saturated liquid reservoir and kimmwipe were allowed to out-gas the VPL until the system equilibrated prior to beginning each test.

Friction measurements of MEMS devices were evaluated using a sidewall MEMS diagnostic tribometer built using Sandia National Laboratories' SUMMiT^{TM} process. Use and characterization of these devices has been described elsewhere.[57, 58, 60] In principle, friction is measured by comparing the range of motion of the shuttle with no load applied with the range of motion when a load is applied. This difference in range of motion, a length, is then multiplied by the spring constant of the shuttle yielding the frictional force. The effective coefficient of friction is then the ratio of the friction force to the applied load. Failure occurs when the actuation forces are insufficient to overcome the frictional forces, and motion stops. MEMS devices were operated in a custom chamber with a gas inlet and outlet allowing for controlling the environment of the device.

10.4 Results and Discussions

Macroscale friction measurements were taken between the silicon surface and a quartz sphere. Since the silicon surface was exposed to air and cleaned via UV/Ozone, a silicon oxide (SiO_x) exists on the surface. Under a 100 gram load, the measured frictional response as a function of contact cycles is illustrated in Figure **10.1**. In this experiment, the contact speed was kept constant at ~2 mm/sec. Each cycle represents the number of times the contact moves over the surface. In this case, water was not present (<70ppmv). Additionally, this load is one order of magnitude larger than previously reported VPL of silicon.[57, 58] At these conditions, the average Hertzian contact pressure is estimated to be 260 MPa. At these contact pressures, VLP successfully lubricates and minimizes friction once there is a sufficient concentration of pentanol in the vapor phase. At room temperature, the saturation pressure of pentanol is approximately 2200 ppmv (parts per million by volume). As the concentration of the alcohol increased from 0% to 22.7% P/P^{sat} (500 ppmv), there is a large difference in the frictional response. However, even at this relatively high partial pressure, there is insufficient film thickness/uniformity to prevent wear of the silicon surface. An indication of wear occurring is the observation of a very noisy frictional response. Increasing the relative partial pressure of the VPL pentanol vapors to 45.6% of P^{sat} improves the frictional response even more and greatly aids wear prevention. Increasing the partial pressure above this has little to no effect on the frictional response.

When comparable concentrations of water (in terms of ppmv) are present the observed frictional response changes. In Figure **10.2**, the same experiment was

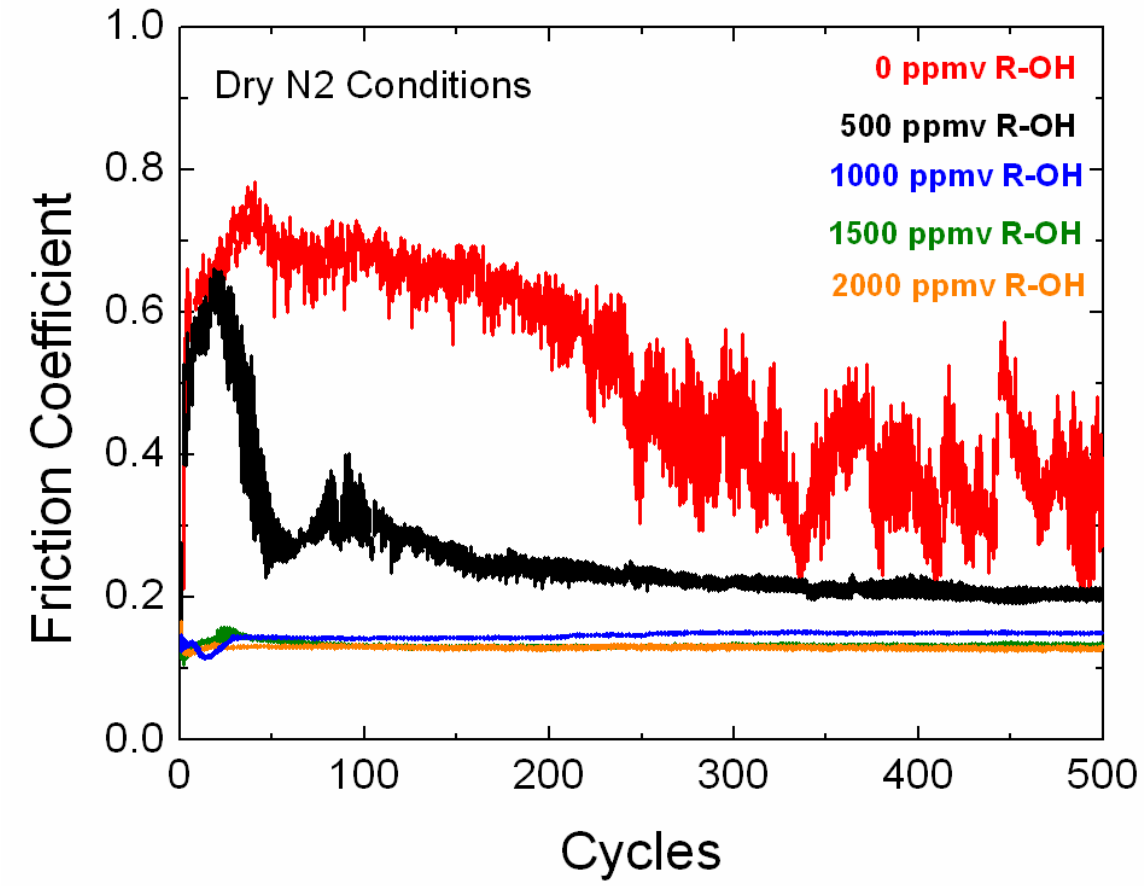

Figure **10.1**: Coefficient of friction observed over time as a 3 mm diameter quartz ball slides against a silicon (100) surface under a 100 gram load. In this case, the environment gradually changes from a dry N_2 to an environment rich with 1-pentanol vapors (R-OH where R = C5H11).

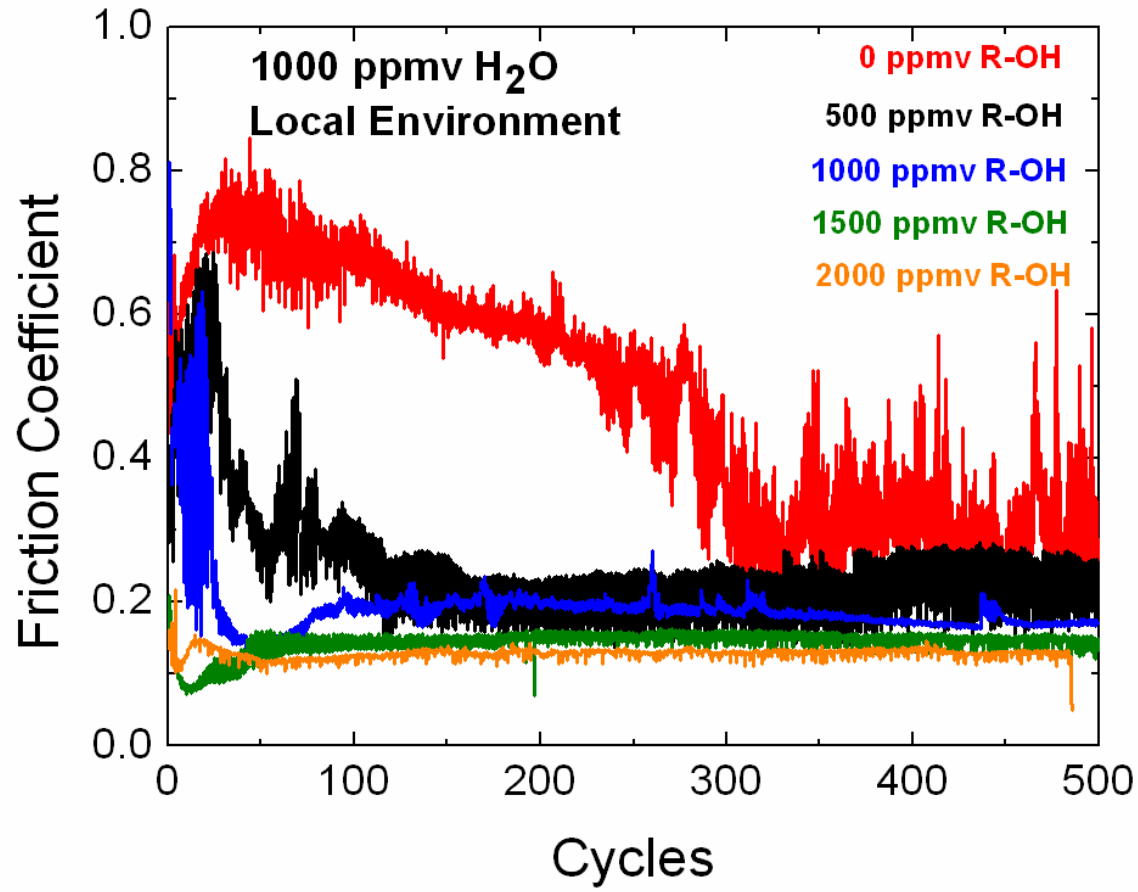

Figure **10.2**: Coefficient of friction observed over time as a 3 mm diameter quartz ball slides against a silicon (100) surface under a 100 gram load. In this case, the N_2 environment maintains a environment with 1000 ppmv of water vapor and each trace represents a different amount of 1-pentanol vapors (R-OH where R = C5H11).

performed, only 1000 ppmv of water was also present in the system. This ppmv of water is effectively ~3.5% relative humidity at room temperature. Comparison between Figures 1 and 2 yields the following observations. While the addition of pentanol does help lower the frictional response, the concentration of pentanol necessary to reduce the noise observed in the frictional response is much higher than that of the dry N_2 case. At a ratio of 1:1 (1000 ppmv alcohol: 1000 ppmv water) there is an equal probability of water colliding with the surface as there is with pentanol colliding with the surface. Once the ratio favors pentanol, the frictional response is more stable. However, even near saturation, friction is slightly more variable than in the dry case.

Wear of the silicon substrate was measured with a Veeco Wyko optical profilometer. Four separate sets of wear tests were performed and the observed wear at each condition was measured. In these experiments a fresh silicon sample and quartz sphere were brought into contact under a 100 gram load and allowed to slide for ~ 2mm a total of 500 times. Following these cycles, the total amount of material displaced on the flat surface was measured. Figure **10.3** plots the total displaced volume divided by the contact sliding distance and number of cycles. The error bars represent a 90% confidence interval. When no alcohol vapors are present, there is a large amount of wear. With the addition of water vapor, wear increases as expected. In the case of no water present, wear was sometimes observed for 750 ppmv and 1000 ppmv. Since wear is stochastic and was not always present at these conditions the error bars appear abnormally large. Above this concentration, wear is almost always completely prevented. When water is present, wear is almost always observed and on average larger than that observed when

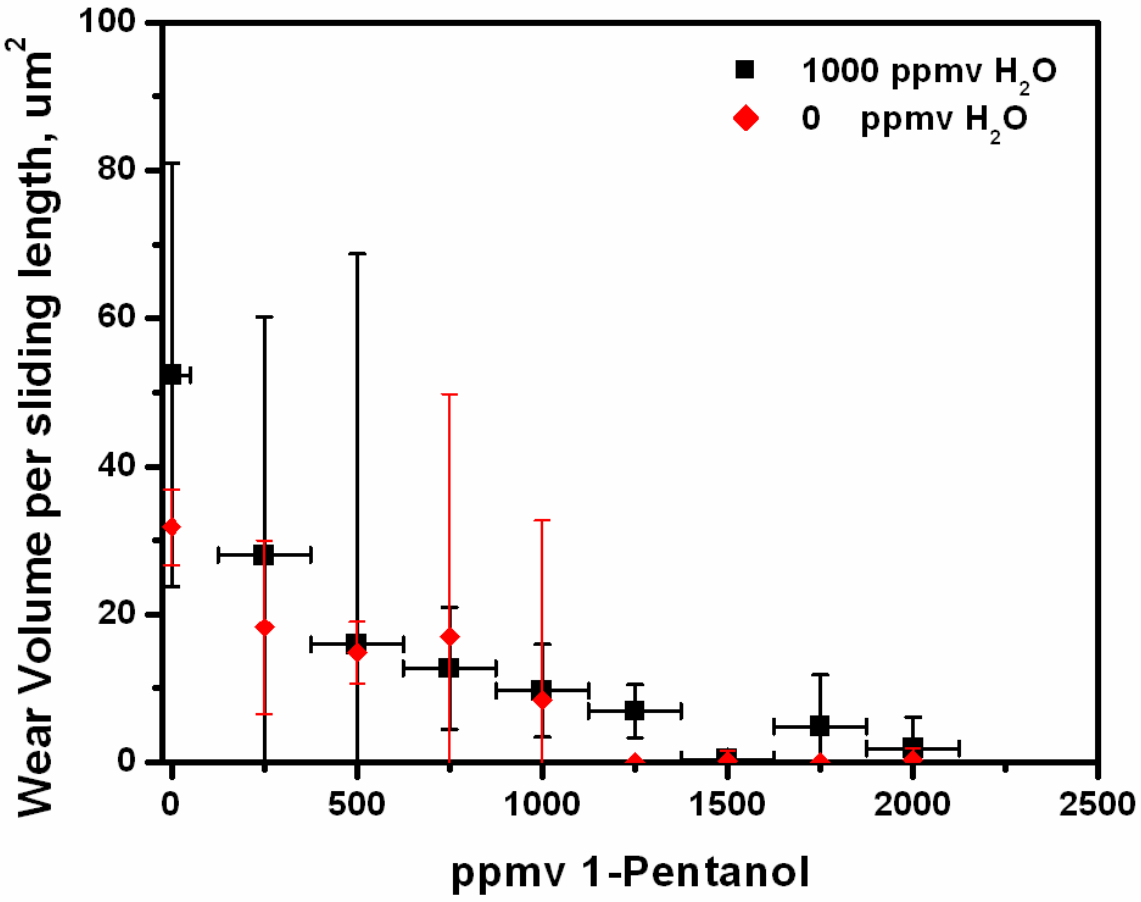

Figure **10.3**: Wear volume observed on the silicon (100) surface at different environmental conditions.

no water is present. Once the concentration of 1-pentanol vapors was 1500 ppmv or larger, wear of the silicon surface was greatly mitigated and in some tests nonexistent.

With the pin-on-disc tribometer, the effect of speed and load was investigated for the quartz balls rubbing against the flat silicon (100) wafers under saturated VPL conditions. Three saturated conditions were investigated, saturated 1-pentanol vapors, a liquid molar ratio pentanol:water that yielded a molar vapor ratio 2:1, and lastly a liquid molar ratio pentanol:water that yielded a molar vapor ratio of 1:1. In these tests, the speed varied from 2mm/s to 9mm/s while the load varied from 0.5N to 2.0N. Figure **10.4** shows the speed and load dependence at each saturated condition. In this case wear was measured from the volume of the wear scar on the spheres and normalized by dividing it by the total distance traveled and the applied load. Wear was observed to greatly increase once a critical load was reached (above ~ 1N). Wear also appeared to have no speed dependence within the range of 1mm/s to 10mm/s. These speeds were investigated because of their relevance to the contact speeds observed in some MEMS devices. While there was no speed dependence in these tests, the data suggests that adsorbed 1-pentanol molecules can effectively prevent wear up to a critical condition.

MEMS diagnostic tribometers as seen in Figure **10.5** were used to investigate the tribological response in these environments. Actuation is accomplished with electrostatic comb fingers and is described elsewhere.[57, 58, 60] One set of comb fingers are used to apply a load at the point of contact. The other set of comb fingers move the shuttle back and forth. In these experiments a 500 nN load was applied to the point of contact. The shuttle oscillated at a rate of 500 Hz. Each device was treated with a fluorinated self-assembled monolayer (SAM) FOTAS.

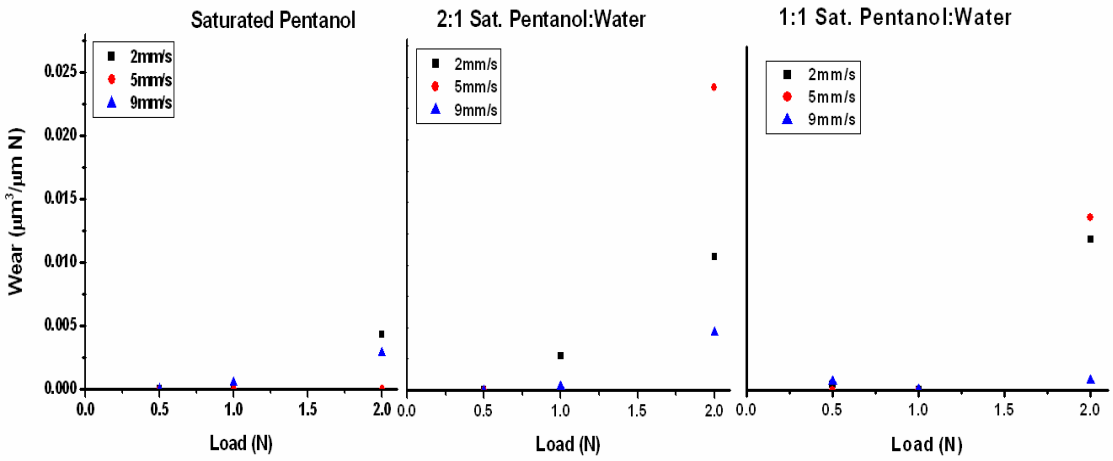

Figure **10.4**: Normalized wear volume of the quartz sphere at different loads, contact speeds, and environmental conditions. Data courtesy of Erik Hsiao.

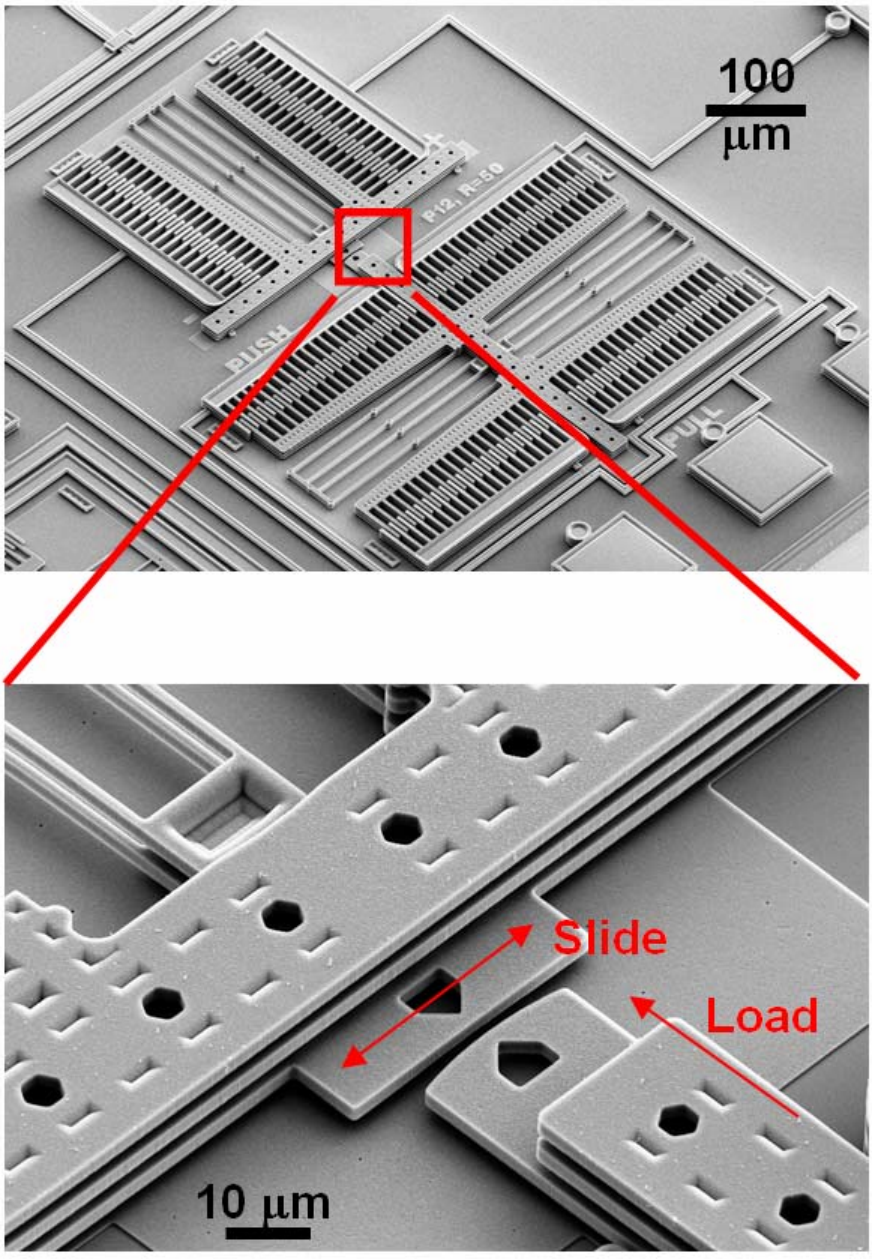

Figure **10.5**: Diagnostic MEMS sidewall tribometer.

Figure **10.6** illustrates the shuttle amplitude relative to the amplitude of the shuttle under no load for various environmental conditions. As in the macroscale case, when water alone is present, the device fails very quickly. When no water or alcohol is present the device also fails within the same relative timeframe. As observed before at a 100 Hz operation, the fluorinated SAM wears off after a few 10,000 cycles in dry operation, and the devices fail.[57] With the addition of alcohol vapors, the lifetime of the device increases. Table **10.1** contains the observed lifetime of these devices under various ppmv of water and alcohol. If the device lasted for 10^6 cycles, the device was stopped by the user. However, if the device failed within the 10^6 cycle test, the test ended and the number of cycles was recorded. Each test is a fresh separate device. From the table it is apparent that there is an operating window for longevity of MEMS encapsulated with water and pentanol vapors.

Table **10.1**: Maximum recorded cycles in MEMS devices at different operating partial pressures of water and 1-pentanol vapors.

1-Pentanol \ WATER ppmv	0	250	500	750	1000
0	$5x10^3$				$4x10^3$
500	$1x10^6$				
1000			$1x10^6$		
1500					
2000	$1x10^6$		$1x10^6$		$5x10^5$

devices run for 10^6 cycles or until failure

Red= early failure, Orange = moderate improvement, Green = No failure during testing

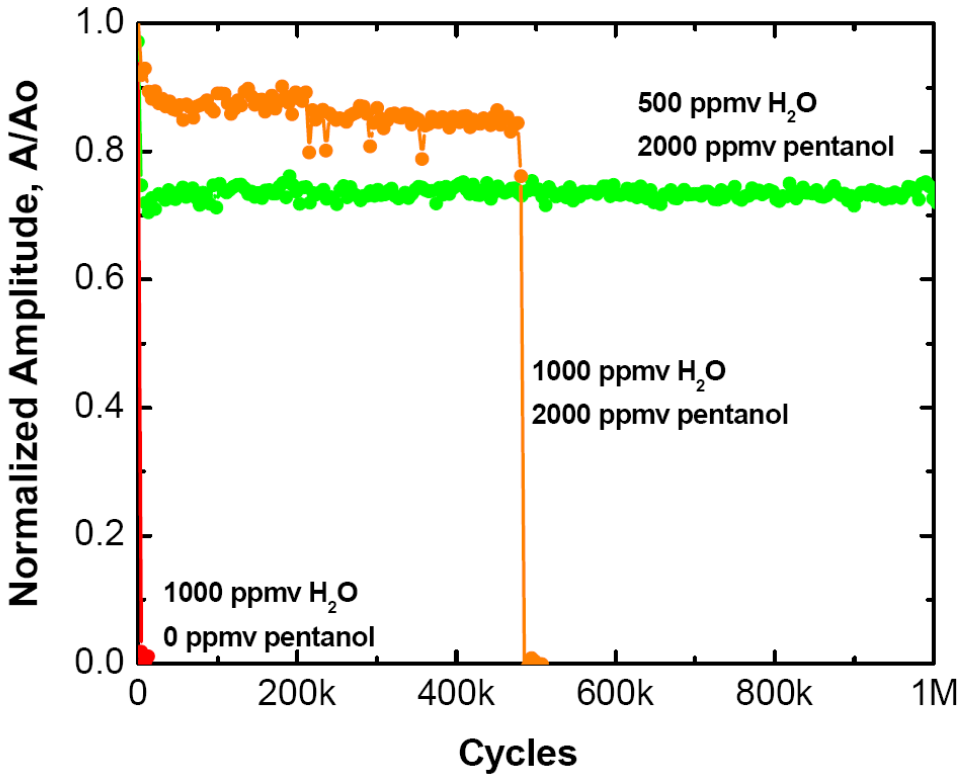

Figure **10.6**: MEMS Diagnostic device operating cycle lifetime vs. environmental conditions. Figure Courtesy of Mike Dugger.

This table and figure illustrate the effect of small amounts of water on the performance of a real MEMS device. Given this data, it appears the vapor phase lubrication of MEMS in slightly humid environments is possible with 1-pentanol vapors. Therefore, the incorporation of water vapor inside a MEMS package, something that is not completely avoidable, is not a potential "show stopper" with this technology.

10.5 Conclusions

In humid environments, the effectiveness of 1-pentanol vapors to lubricate and prevent wear of silicon and silicon oxide is hindered. In the case of MEMS contacts, the amount of water present is very critical to the lifetime of the device. However, given sufficient alcohol pressure and appropriate mitigation techniques to remove water from the device surroundings, vapor phase lubrication appears to keep the contacting surface of our MEMS protected against wear and eventual failure.

10.6 References

1. M. A. Henderson, *Surface Science Reports* **2002,** 46, (1-8), 5-308.
2. H. A. Al-Abadleh; V. H. Grassian, *Langmuir* **2003,** 19, (2), 341-347.
3. D. B. Asay; S. H. Kim, *Journal of Physical Chemistry B* **2005,** 109, (35), 16760-16763.
4. D. B. Asay; S. H. Kim, *Journal of Chemical Physics* **2006,** 124, (17), 5.
5. M. C. Bellissent-Funel, *European Physical Journal E* **2003,** 12, (1), 83-92.
6. A. J. Benesi; M. W. Grutzeck; B. O'Hare; J. W. Phair, *Journal of Physical Chemistry B* **2004,** 108, (46), 17783-17790.
7. M. Binggeli; C. M. Mate, *Applied Physics Letters* **1994,** 65, (4), 415-417.
8. M. P. de Boer; P. C. T. de Boer, *Journal of Colloid and Interface Science* **2007,** 311, (1), 171-185.
9. P. C. T. de Boer; M. P. de Boer, *Langmuir* **2008,** 24, (1), 160-169.
10. A. Dhinojwala; S. Granick, *Journal of the American Chemical Society* **1997,** 119, (1), 241-242.
11. D. H. Dolan; Y. M. Gupta, *Journal of Chemical Physics* **2004,** 121, (18), 9050-9057.
12. F. Dorazio; S. Bhattacharja; W. P. Halperin; K. Eguchi; T. Mizusaki, *Physical Review B* **1990,** 42, (16), 9810-9818.
13. G. E. Ewing, *Journal of Physical Chemistry B* **2004,** 108, (41), 15953-15961.
14. A. A. Feiler; P. Jenkins; M. W. Rutland, *Journal of Adhesion Science and Technology* **2005,** 19, (3-5), 165-179.

15. M. P. Goertz; J. E. Houston; X. Y. Zhu, *Langmuir* **2007,** 23, (10), 5491-5497.

16. T. Hasegawa; J. Nishijo; T. Imae; Q. Huo; R. M. Leblanc, *Journal of Physical Chemistry B* **2001,** 105, (48), 12056-12060.

17. M. Y. He; A. S. Blum; D. E. Aston; C. Buenviaje; R. M. Overney; R. Luginbuhl, *Journal of Chemical Physics* **2001,** 114, (3), 1355-1360.

18. J. Hu; X. D. Xiao; D. F. Ogletree; M. Salmeron, *Science* **1995,** 268, (5208), 267-269.

19. J. N. Israelachvili; P. M. McGuiggan, *Science* **1988,** 241, (4867), 795-800.

20. R. C. Major; J. E. Houston; M. J. McGrath; J. I. Siepmann; X. Y. Zhu, *Physical Review Letters* **2006,** 96, (17), 4.

21. P. B. Miranda; L. Xu; Y. R. Shen; M. Salmeron, *Physical Review Letters* **1998,** 81, (26), 5876-5879.

22. M. Nosonovsky; B. Bhushan, *Physical Chemistry Chemical Physics* **2008,** 10, (16), 2137-2144.

23. L. M. Qian; F. Tian; X. D. Xiao, *Tribology Letters* **2003,** 15, (3), 169-176.

24. L. F. Scatena; M. G. Brown; G. L. Richmond, *Science* **2001,** 292, (5518), 908-912.

25. L. Sirghi, *Applied Physics Letters* **2003,** 82, (21), 3755-3757.

26. W. Stumm; L. Sigg; B. Sulzberger, *Chemistry of the Solid-Water interface: Processes at the Mineral-Water and Particle-Water Interface in Natural Systems* Wiley: New York, 1992.

27. A. Verdaguer; G. M. Sacha; H. Bluhm; M. Salmeron, *Chemical Reviews* **2006,** 106, (4), 1478-1510.

28. E. A. Vogler, *Advances in Colloid and Interface Science* **1998,** 74, 69-117.

29. L. Xu; A. Lio; J. Hu; D. F. Ogletree; M. Salmeron, *Journal of Physical Chemistry B* **1998,** 102, (3), 540-548.

30. J. J. Yang; S. Meng; L. F. Xu; E. G. Wang, *Physical Review B* **2005,** 71, (3).

31. J. J. Yang; E. G. Wang, *Current Opinion in Solid State & Materials Science* **2006,** 10, (1), 33-39.

32. R. R. M. Zamora; C. M. Sanchez; F. L. Freire; R. Prioli, *Physica Status Solidi a-Applications and Materials Science* **2004,** 201, (5), 850-856.

33. B. Cappella; G. Dietler, *Surface Science Reports* **1999,** 34, (1-3), 1-+.

34. R. W. Carpick; N. Agrait; D. F. Ogletree; M. Salmeron, *Langmuir* **1996,** 12, (13), 3334-3340.

35. R. W. Carpick; N. Agrait; D. F. Ogletree; M. Salmeron, *Journal of Vacuum Science & Technology B* **1996,** 14, (2), 1289-1295.

36. R. W. Carpick; M. Salmeron, *Chemical Reviews* **1997,** 97, (4), 1163-1194.

37. T. E. Fischer; W. M. Mullins, *Journal of Physical Chemistry* **1992,** 96, (14), 5690-5701.

38. J. M. Helt; J. D. Batteas, *Langmuir* **2005,** 21, (2), 633-639.

39. J. Hu; X. D. Xiao; D. F. Ogletree; M. Salmeron, *Surface Science* **1995,** 327, (3), 358-370.

40. J. K. Jang; G. C. Schatz; M. A. Ratner, *Journal of Chemical Physics* **2004,** 120, (3), 1157-1160.

41. J. Y. Jang; G. C. Schatz; M. A. Ratner, *Physical Review Letters* **2004,** 92, (8).

42. R. Jones; H. M. Pollock; J. A. S. Cleaver; C. S. Hodges, *Langmuir* **2002,** 18, (21), 8045-8055.

43. F. Katsuki; K. Kamei; A. Saguchi; W. Takahashi; J. Watanabe, *Journal of the Electrochemical Society* **2000,** 147, (6), 2328-2331.

44. A. G. Khurshudov; K. Kato; H. Koide, *Wear* **1997,** 203, 22-27.

45. S. Kopta; M. Salmeron, *Journal of Chemical Physics* **2000,** 113, (18), 8249-8252.

46. M. A. Lantz; S. J. Oshea; M. E. Welland; K. L. Johnson, *Physical Review B* **1997,** 55, (16), 10776-10785.

47. S. Lee; Y. S. Shon; R. Colorado; R. L. Guenard; T. R. Lee; S. S. Perry, *Langmuir* **2000,** 16, (5), 2220-2224.

48. H. Liu; B. Bhushan, *Ultramicroscopy* **2002,** 91, (1-4), 185-202.

49. R. Maboudian; C. Carraro, *Annual Review of Physical Chemistry* **2004,** 55, 35-54.

50. W. Maw; F. Stevens; S. C. Langford; J. T. Dickinson, *Journal of Applied Physics* **2002,** 92, (9), 5103-5109.

51. T. M. Mayer; M. P. de Boer; N. D. Shinn; P. J. Clews; T. A. Michalske, *Journal of Vacuum Science & Technology B* **2000,** 18, (5), 2433-2440.

52. T. M. Mayer; J. W. Elam; S. M. George; P. G. Kotula; R. S. Goeke, *Applied Physics Letters* **2003,** 82, (17), 2883-2885.

53. U. Raviv; P. Laurat; J. Klein, *Nature* **2001,** 413, (6851), 51-54.

54. D. L. Sedin; K. L. Rowlen, *Analytical Chemistry* **2000,** 72, (10), 2183-2189.

55. K. Strawhecker; D. B. Asay; J. McKinney; S. H. Kim, *Tribology Letters* **2005,** 19, (1), 17-21.

56. S. H. Kim; D. B. Asay; M. T. Dugger, *Nano Today* **2007,** 2, (5), 22-29.

57. D. B. Asay; M. T. Dugger; S. H. Kim, *Tribology Letters* **2008,** 29, (1), 67-74.

58. D. B. Asay; M. T. Dugger; J. A. Ohlhausen; S. H. Kim, *Langmuir* **2008,** 24, (1), 155-159.

59. R. Courtland, in: *Nature*, 2008; p doi:10.1038/news.2008.740

60. S. J. Timpe; K. Komvopoulos, *Journal of Microelectromechanical Systems* **2005,** 14, (6), 1356-1363.

SYNOPSIS

The central objective of this thesis was to investigate the efficacy of vapor phase lubrication as a technology suitable for micro-scale devices i.e. silicon based MEMS devices. Vapor phase lubrication requires lubricants to have sufficient vapor pressure and strong binding to the lubricating substrate surfaces. In this study, simple linear alcohol molecules were used as potential lubricant vapors due to their high vapor pressure and capability for chemisorption onto the silicon surface. Given this premise, we have attempted to answer the following principal tasks: (1) Determine the surface coverage and adsorption phenomena of various vapor phase lubricants as a function of their partial pressure. (2) Investigate the influence of water as well as alcohol vapors on the tribological properties of silicon. (3) Test the effectiveness of this technology with real MEMS devices and structures.

Chapter 1 introduces the current state of the art in terms of tribology related to MEMS. While MEMS devices have been manufactured for many decades, there are no devices with rubbing contacts in the consumer market today. This is due to wear issues with silicon, hence, the need to develop a robust solution to this problem.

Water is prevalent everywhere. This thesis includes various studies investigating the effect of water on the tribological properties of silicon. In chapters 2 and 3, the structure of water is investigated. Because of this structure, adhesion of nano-asperity

contacts (chapter 4) is larger than the force expected from capillary forces. Additionally, water enhances the wear of silicon due to chemical wear (chapter 8).

The adsorption of alcohol vapors and their effect on adhesion, friction, and wear is a central theme in this thesis. As the chain length of the alcohol increases, the adsorption thickness tends to follow a true Langmuir isotherm, saturating at ~ 1 monolayer around 15% of the alcohol's relative saturation vapor pressure (chapter 5).

The adsorption of alcohol molecules onto the silicon surface has a dramatic effect on adhesion. In contrast to water, alcohol vapors greatly reduce the measured adhesion between nano-asperity contacts (chapter 5). This is due to their limited isotherm thickness, their larger molar volume, and low surface energy. Additionally, as alcohol molecules adsorb, friction is reduced at all length scales (chapters 7 – 10). This is due to the reduction in adhesive forces when alcohol vapors are present as well as the reduction in shear strength at the point of contact.

Chapter 6 is dedicated to AFM calibration. In order to have meaningful measurements of friction a simple calibration technique was developed. While there exists a number of different techniques for lateral force calibration, none of the current techniques are appropriate with our AFM system.

The effectiveness of alcohol vapor phase lubrication to prevent wear from a nano-asperity contact to macro-scale contacts is very exciting (Chapter 8). To our surprise, in the case of alcohol films on silicon surfaces, tribochemical reactions take place producing high molecular weight oligomeric films that help maintain low friction and prevent wear. One of the benefits of this new oligomeric material is that this material is produced only where intimate contacts are formed. Therefore, it is produced where it is needed most.

Additionally, the film prevents direct contact between silicon asperities. By preventing intimate contact, wear of the underlying silicon material is prevented. The ability to prevent wear is perhaps the most critical characteristic required for longevity in MEMS.

Lastly, *in-situ* gas-phase lubrication of MEMS devices was investigated with 1-pentanol vapor (chapters 9 and 10). The 1-pentanol vapor successfully maintained lubricating properties between silicon contacts of MEMS devices. In the presence of these vapors, MEMS devices with sliding contacts operated *without failure* for up to a factor of 1.7×10^4 longer than in dry N_2 gas alone, representing a dramatic improvement in operating life. In the case of SAM treated MEMS, the devices failed in less than 2 minutes. When alcohol vapors were present, neither failure nor wear was observed. What was observed were very small fluid like buildups in the contact regions. Even more interestingly, we were able to take failed devices and restart the devices under the gas-phase lubrication process, something also never before accomplished.

FUTURE DIRECTIONS

Although we have addressed several questions and problems related to vapor phase tribology and MEMS lubrication with this technology, there are yet a number of key questions that remain in order to develop this technology for use in MEMS.

Water causes wear of silicon as these surfaces touch and slide past each other and alcohol vapors can be used to prevent wear from occurring. However, it is not clear yet if wear is completely prevented, if oligomeric formation is hindered, and what dominates wear and friction when both water and alcohol vapors are present. Additionally, what is the structure of water and alcohol in this system and how are they arranged relative to one another? Is it layered, homogeneous, heterogeneous, and does the surface follow miscibility limits observed in bulk mixtures of these compounds? Answering these questions will help determine the effect of water on friction and wear when both water and alcohol is present as well as the conditions necessary to prevent wear when water is present.

Much of the work in this thesis is restricted to room temperature conditions. Real MEMS devices will be in operation across a wide temperature range. While 1-pentanol has been demonstrated as an effective lubricant at room temperature for MEMS, its effectiveness over a wide temperature range has yet to be quantified. Since the vapor pressure of a substance is only a function of temperature, lower molecular weight alcohols might be more suited for lower temperature operation and visa versa. In a real

device, a mixture of these molecules may be needed. Therefore, the tribological properties of mixed systems need also be studied.

In order to take advantage of vapor phase lubrication, MEMS devices must be encapsulated or sealed. Sealed environments present a number of engineering challenges. To begin with, the delivery mechanism of vapor phase lubricants to the working device surfaces need to be developed. Delivery mechanisms could include for example: the out gassing of a polymer saturated with lubricant molecules or small capillary reservoirs that can be heated to evaporate lubricant molecules. In addition, in a sealed environment, temperature gradients or rapid changes in temperature might cause bulk condensation of the lubricant vapors and must be avoided.

Lastly, in order to enable and optimize vapor phase lubrication for use in meso-scale and MEMS devices, *in situ* kinetic and mechanistic investigations into the formation of lubricant (oligomer/polymer) films formed by mechanically stimulated chemical reactions in controlled environmental chemistry must be understood. The formation of chemical species due to the dissipation of energy during shear is known as tribochemistry. Future research should focus on (1) the fundamental kinetics of *in situ* oligomer lubricant production via tribochemical reactions and (2) the role substrate chemistry and vapor-phase chemical constituents have on the formation of these oligomers. It is hypothesized that the reaction layer is formed by conversion of the alcohol to an olefin in the presence of an acid catalist surface. The olefin species then polymerize to form higher order alkanes. Once the chemical reaction pathway is determined, other potential molecules can be identified as potentially suitable for vapor phase lubrication of silicon surfaces.

While this thesis is centered on silicon as the structural material needing lubrication, the effectiveness of this technology in other devices made of other materials must be examined. Other structural materials that may work with vapor phase lubrication include ceramics like silicon nitride or sapphire and metal surfaces like steel and aluminum.

Appendix

Supporting Data

A.1 ATR-IR simulations were done with the following algorithm written in Mathcad.

$$\begin{pmatrix} \lambda_{water} \\ n_{water} \\ k_{water} \end{pmatrix} :=$$

nu	n	k
1562.5	1.347	0.018865
1652.893	1.324	0.04873
1666.667	1.313	0.044383
1724.138	1.266	0.014026
1818.182	1.303	0.005252
1901.141	1.318	0.00417
2000	1.331	0.005326
2083.333	1.336	0.007161
2145.923	1.338	0.000752
2222.222	1.3411	0.0064
2500	1.349	0.002091
2610.966	1.358	0.00147
2666.667	1.372	0.001543
2777.778	1.402	0.002465
2857.143	1.423	0.004043
2941.176	1.449	0.008209
3030.303	1.47	0.018826
3125	1.509	0.040965
3225.806	1.426	0.079478
3333.333	1.351	0.112435
3389.831	1.325	0.11913
3448.276	1.31	0.10587
3571.429	1.232	0.0407
3636.364	1.133	0.010439
3703.704	1.134	0.002195
3773.585	1.16	0.00099
3809.524	1.16	0.00099
3846.154	1.18	0.00089
3921.569	1.213	0.000856
4000	1.246	0.000718
4081.633	1.27	0.000517
4166.667	1.276	0.003487
4255.319	1.282	0.002439
4347.826	1.286	0.000183
4444.444	1.29	0.000132
4524.887	1.292	0.000118
4545.455	1.293	0.000122
4651.163	1.296	0.000141

$$\begin{pmatrix} \lambda_{ice} \\ n_{ice} \\ k_{ice} \end{pmatrix} :=$$

1515.152	1.223	0.024304
1538.462	1.225	0.023957
1562.5	1.226	0.02413
1587.302	1.228	0.025391
1612.903	1.232	0.026783
1639.344	1.234	0.027957
1652.893	1.235	0.028087
1666.667	1.235	0.026826
1694.915	1.232	0.02287
1724.138	1.227	0.018435
1754.386	1.226	0.013609
1785.714	1.226	0.010609
1818.182	1.226	0.00913
1851.852	1.227	0.007609
1886.792	1.231	0.006609
1923.077	1.236	0.005783
1960.784	1.241	0.005652
2000	1.247	0.005783
2040.816	1.252	0.006391
2083.333	1.258	0.007522
2127.66	1.266	0.009348
2173.913	1.273	0.012478
2222.222	1.28	0.014348
2272.727	1.288	0.012261
2325.581	1.299	0.009478
2380.952	1.307	0.007609
2439.024	1.316	0.006522
2500	1.327	0.005391
2564.103	1.34	0.004522
2631.579	1.356	0.003565
2777.778	1.395	0.004565
2816.901	1.408	0.005609
2857.143	1.422	0.007087
2898.551	1.445	0.009826
2941.176	1.49	0.013348
2985.075	1.515	0.01913
3030.303	1.53	0.027174
3076.923	1.55	0.03913
3125	1.557	0.067913

$\lambda_{water} := \lambda_{water} \cdot cm^{-1}$ $\lambda_{ice} := \lambda_{ice} \cdot cm^{-1}$

$S_{water\_n} := cspline(\lambda_{water}, n_{water})$ $S_{ice\_n} := cspline(\lambda_{ice}, n_{ice})$

$N_{water}(\lambda) := interp(S_{water\_n}, \lambda_{water}, n_{water}, \lambda)$ $N_{ice}(\lambda) := interp(S_{ice\_n}, \lambda_{ice}, n_{ice}, \lambda)$

$S_{water\_k} := cspline(\lambda_{water}, k_{water})$ $S_{ice\_k} := cspline(\lambda_{ice}, k_{ice})$

$K_{water}(\lambda) := interp(S_{water\_k}, \lambda_{water}, k_{water}, \lambda)$ $K_{ice}(\lambda) := interp(S_{ice\_k}, \lambda_{ice}, k_{ice}, \lambda)$

Now to account for the index of refraction of Si as a function of wavenumber at temp T

$$n_{Si}(T, \lambda) := 1.6 \cdot 10^{-4} \cdot \frac{T}{K} + 3.431 - 0.02643 \cdot \lambda \cdot \mu m + 0.004324 \cdot (\lambda \cdot \mu m)^2 - .0003194 \cdot (\lambda \cdot \mu m)^3 + 8.835 \cdot 10^{-6} \cdot (\lambda \cdot \mu m)^4$$

This relationship is taken from: The temperature-dependent spectral properties of filter substrate materials in the far-infrared (6–40 μm) By Gary Hawkins *, Roger Hunneman Infrared Physics & Technology 45 (2004) 69–'9679

Now for 4 layers:

$\Theta := 45 \cdot deg$

As follows:

Silicon (1), Ice (2), Water (3), Air (4)

The substrate is Silicon (1):

$$n_1(T, \lambda) := n_{Si}(T, \lambda) + 0. \cdot (-1)^{\frac{1}{2}}$$

On TOP of Silicon (ignoring oxide) is ICE (2):

$n_2(\lambda) := N_{ice}(\lambda) + K_{ice}(\lambda) \cdot \sqrt{-1}$

The thickness of the ice like layer:

$d_2 := 0nm$

On top of ICE is water (3)

$n_3(\lambda) := N_{water}(\lambda) + K_{water}(\lambda) \cdot \sqrt{-1}$

The thickness of the Water like layer:

$d_3 := 2nm$

The 4th layer is air (4):

$$n_4(\lambda) := 1 + 0.0 \cdot (-1)^{\frac{1}{2}}$$

The Fresnel Amplitude coefficients for each layer interface is:

$$r_{23P}(T,\lambda) := \frac{n_3(\lambda)^2 \cdot \sqrt{n_2(\lambda)^2 - n_1(T,\lambda)^2 \cdot \sin(\Theta)^2} - n_2(\lambda)^2 \cdot \sqrt{n_3(\lambda)^2 - n_1(T,\lambda)^2 \cdot \sin(\Theta)^2}}{n_3(\lambda)^2 \cdot \sqrt{n_2(\lambda)^2 - n_1(T,\lambda)^2 \cdot \sin(\Theta)^2} + n_2(\lambda)^2 \cdot \sqrt{n_3(\lambda)^2 - n_1(T,\lambda)^2 \cdot \sin(\Theta)^2}}$$

$$r_{23S}(T,\lambda) := \frac{\sqrt{n_2(\lambda)^2 - n_1(T,\lambda)^2 \cdot \sin(\Theta)^2} - \sqrt{n_3(\lambda)^2 - n_1(T,\lambda)^2 \cdot \sin(\Theta)^2}}{\sqrt{n_2(\lambda)^2 - n_1(T,\lambda)^2 \cdot \sin(\Theta)^2} + \sqrt{n_3(\lambda)^2 - n_1(T,\lambda)^2 \cdot \sin(\Theta)^2}}$$

$$r_{12P}(T,\lambda) := \frac{n_2(\lambda)^2 \cos(\Theta) - n_1(T,\lambda) \cdot \sqrt{n_2(\lambda)^2 - n_1(T,\lambda)^2 \cdot \sin(\Theta)^2}}{n_2(\lambda)^2 \cos(\Theta) + n_1(T,\lambda) \cdot \sqrt{n_2(\lambda)^2 - n_1(T,\lambda)^2 \cdot \sin(\Theta)^2}}$$

$$r_{12S}(T,\lambda) := \frac{n_1(T,\lambda) \cos(\Theta) - \sqrt{n_2(\lambda)^2 - n_1(T,\lambda)^2 \cdot \sin(\Theta)^2}}{n_1(T,\lambda) \cos(\Theta) + \sqrt{n_2(\lambda)^2 - n_1(T,\lambda)^2 \cdot \sin(\Theta)^2}}$$

$$r_{34S}(T,\lambda) := \frac{\sqrt{n_3(\lambda)^2 - n_1(T,\lambda)^2 \cdot \sin(\Theta)^2} - \sqrt{n_4(\lambda)^2 - n_1(T,\lambda)^2 \cdot \sin(\Theta)^2}}{\sqrt{n_3(\lambda)^2 - n_1(T,\lambda)^2 \cdot \sin(\Theta)^2} + \sqrt{n_4(\lambda)^2 - n_1(T,\lambda)^2 \cdot \sin(\Theta)^2}}$$

$$r_{34P}(T,\lambda) := \frac{n_4(\lambda)^2 \cdot \sqrt{n_3(\lambda)^2 - n_1(T,\lambda)^2 \cdot \sin(\Theta)^2} - n_3(\lambda)^2 \cdot \sqrt{n_4(\lambda)^2 - n_1(T,\lambda)^2 \cdot \sin(\Theta)^2}}{n_4(\lambda)^2 \cdot \sqrt{n_3(\lambda)^2 - n_1(T,\lambda)^2 \cdot \sin(\Theta)^2} + n_3(\lambda)^2 \cdot \sqrt{n_4(\lambda)^2 - n_1(T,\lambda)^2 \cdot \sin(\Theta)^2}}$$

$$t_{23S}(T,\lambda) := \frac{2 \cdot \sqrt{n_2(\lambda)^2 - n_1(T,\lambda)^2 \cdot \sin(\Theta)^2}}{\sqrt{n_2(\lambda)^2 - n_1(T,\lambda)^2 \cdot \sin(\Theta)^2} + \sqrt{n_3(\lambda)^2 - n_1(T,\lambda)^2 \cdot \sin(\Theta)^2}}$$

$$t_{23P}(T,\lambda) := \frac{2 \cdot n_2(\lambda) \cdot n_3(\lambda) \cdot \sqrt{n_2(\lambda)^2 - n_1(T,\lambda)^2 \cdot \sin(\Theta)^2}}{n_3(\lambda)^2 \cdot \sqrt{n_2(\lambda)^2 - n_1(T,\lambda)^2 \cdot \sin(\Theta)^2} + n_2(\lambda)^2 \cdot \sqrt{n_3(\lambda)^2 - n_1(T,\lambda)^2 \cdot \sin(\Theta)^2}}$$

$$X_2(T,\lambda) := 2\cdot\pi\cdot\lambda\cdot d_2\sqrt{-1}\cdot\sqrt{n_2(\lambda)^2 - n_1(T,\lambda)^2\cdot\sin(\Theta)^2}$$

$$X_3(T,\lambda) := 2\cdot\pi\cdot\lambda\cdot d_3\sqrt{-1}\cdot\sqrt{n_3(\lambda)^2 - n_1(T,\lambda)^2\cdot\sin(\Theta)^2}$$

$$M_s(T,\lambda) := \begin{pmatrix} 1 & t_{12S}(T,\lambda) \\ t_{12S}(T,\lambda) & 1 \end{pmatrix}\cdot\left[\frac{1}{t_{23S}(T,\lambda)}\cdot\begin{pmatrix} \exp(-X_2(T,\lambda)) & t_{23S}(T,\lambda)\cdot\exp(-X_2(T,\lambda)) \\ t_{23S}(T,\lambda)\cdot\exp(X_2(T,\lambda)) & \exp(X_2(T,\lambda)) \end{pmatrix}\right]\cdot\begin{pmatrix} \exp(-X_3(T,\lambda)) & t_{34S}(T,\lambda)\cdot\exp(-X_3(T,\lambda)) \\ t_{34S}(T,\lambda)\cdot\exp(X_3(T,\lambda)) & \exp(X_3(T,\lambda)) \end{pmatrix}$$

$$M_p(T,\lambda) := \begin{pmatrix} 1 & t_{12P}(T,\lambda) \\ t_{12P}(T,\lambda) & 1 \end{pmatrix}\cdot\left[\frac{1}{t_{23P}(T,\lambda)}\cdot\begin{pmatrix} \exp(-X_2(T,\lambda)) & t_{23P}(T,\lambda)\cdot\exp(-X_2(T,\lambda)) \\ t_{23P}(T,\lambda)\cdot\exp(X_2(T,\lambda)) & \exp(X_2(T,\lambda)) \end{pmatrix}\right]\cdot\begin{pmatrix} \exp(-X_3(T,\lambda)) & t_{34P}(T,\lambda)\cdot\exp(-X_3(T,\lambda)) \\ t_{34P}(T,\lambda)\cdot\exp(X_3(T,\lambda)) & \exp(X_3(T,\lambda)) \end{pmatrix}$$

$$R_S(T,\lambda) := \left(\left| \frac{M_s(T,\lambda)_{1,0}}{M_s(T,\lambda)_{0,0}} \right| \right)^2$$

$$R_P(T,\lambda) := \left(\left| \frac{M_P(T,\lambda)_{1,0}}{M_P(T,\lambda)_{0,0}} \right| \right)^2$$

$$\log\left(\frac{1}{R_S(300K, \lambda \cdot cm^{-1})^{11}} \right)$$

$$\log\left(\frac{1}{R_P(300K, \lambda \cdot cm^{-1})^{11}} \right)$$

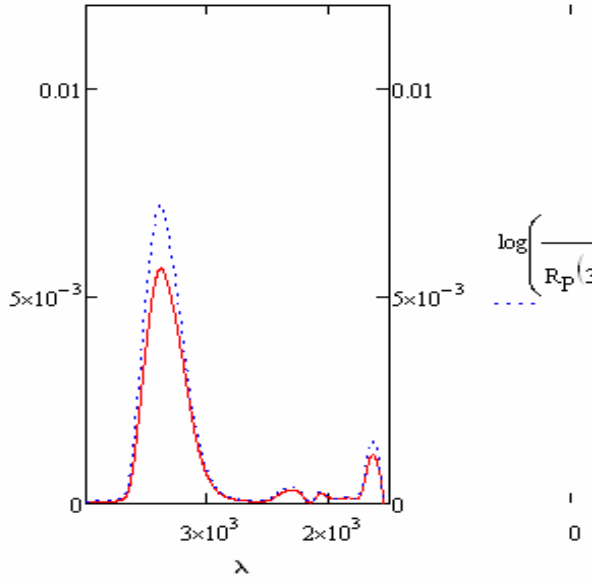

$$\log\left[\frac{1}{\left(R_S(300K, \lambda \cdot cm^{-1}) \cdot \sin(\Theta)^2 + R_P(300K, \lambda \cdot cm^{-1}) \cdot \cos(\Theta)^2 \right)^{11}} \right]$$

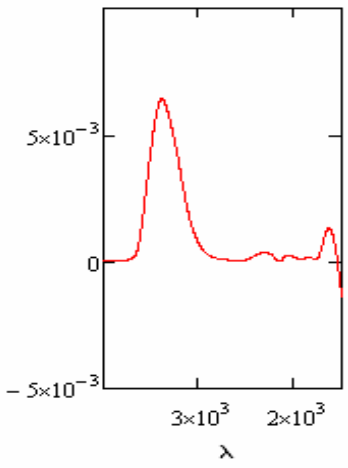

Calibration Factor for Integrated area use in determining Thickness:

$$\int_{2800}^{3680} \log\left[\frac{1}{\left(R_S\left(300K, \lambda \cdot cm^{-1}\right) \cdot \sin(\Theta)^2 + R_P\left(300K, \lambda \cdot cm^{-1}\right) \cdot \cos(\Theta)^2\right)^{11}}\right] d\lambda = 2.438$$

$$\frac{d_3}{\int_{2800}^{3680} \log\left[\frac{1}{\left(R_S\left(300K, \lambda \cdot cm^{-1}\right) \cdot \sin(\Theta)^2 + R_P\left(300K, \lambda \cdot cm^{-1}\right) \cdot \cos(\Theta)^2\right)^{11}}\right] d\lambda} = 0.82\,nm$$

A.2 Capillary Force Calculations (MathCAD program)

The following is an example of the toroidal approximation to the capillary force due to the meniscus that forms between a sphere and a plate.

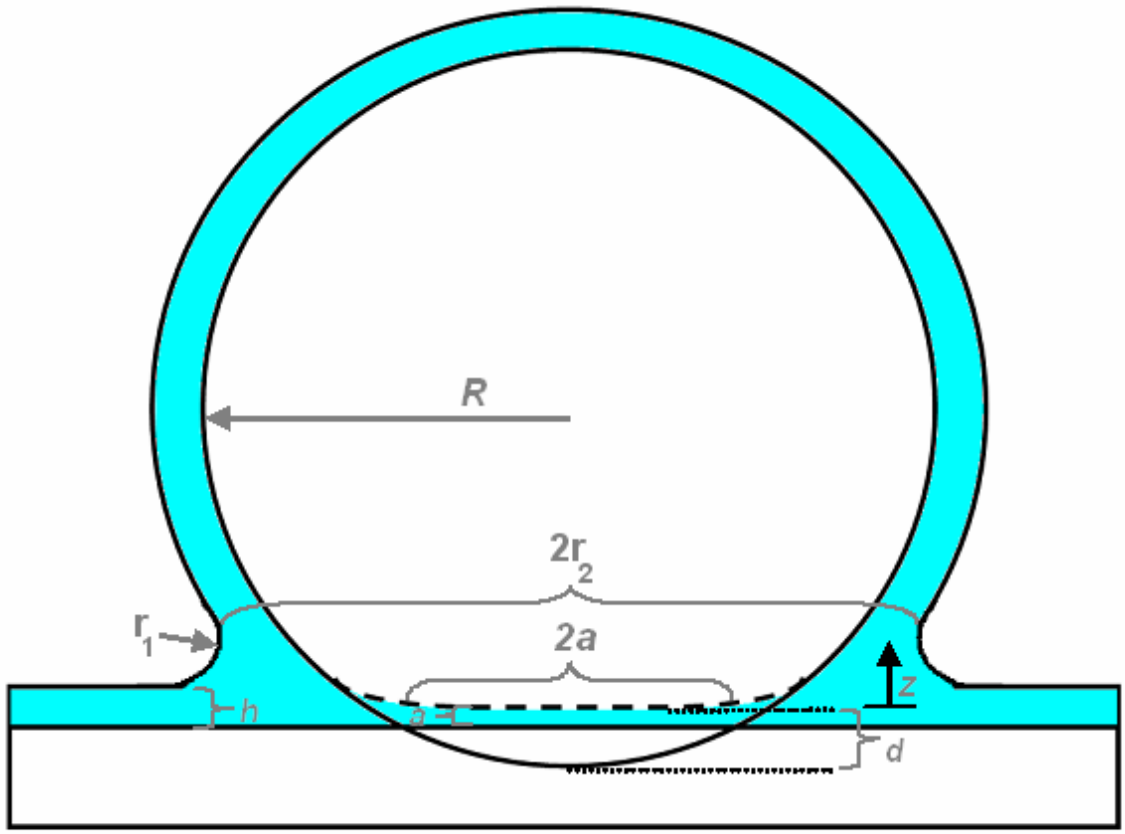

Hypotenuse: $\text{Hypot} = R_{tip} + h + r_1$

Height: $\text{Height} = R_{tip} - h - r_1 - d + \alpha$

Base: $\text{Base} = r_1 + r_2$

$\text{gram} \equiv \frac{\text{kg}}{1000}$

$\text{nN} \equiv 10^{-9}\text{N}$

Solving for r2 with trigonometry:

$$(r_1 + r_2)^2 + (R_{tip} - h - r_1 - d + \alpha)^2 = (R_{tip} + h + r_1)^2$$

$$r_2 = \begin{bmatrix} \sqrt{(2 \cdot R_{tip} + \alpha - d) \cdot (d - \alpha + 2 \cdot h + 2 \cdot r_1)} - r_1 \\ -r_1 - \sqrt{(2 \cdot R_{tip} + \alpha - d) \cdot (d - \alpha + 2 \cdot h + 2 \cdot r_1)} \end{bmatrix}$$

This is based strictly by lengths so, we need the positive root yielding:

$$r_2 = \sqrt{(2 \cdot R_{tip} + \alpha - d) \cdot (d - \alpha + 2 \cdot h + 2 \cdot r_1)} - r_1$$

We can use thermodynamics to relate r1 to r2 with the kelvin equation and.

$$\frac{1}{r_2} - \frac{1}{r_1} = \frac{R_g \cdot Temp}{Vol \cdot \gamma} \cdot \ln\left(\frac{P}{Psat}\right)$$

With our geometric boundary conditions we can now solve for r1 and r2 given any condition

$$\frac{1}{\sqrt{(2 \cdot R_{tip} + \alpha - d) \cdot (d - \alpha + 2 \cdot h + 2 \cdot r_1)} - r_1} - \frac{1}{r_1} = \frac{R_g \cdot Temp}{Vol \cdot \gamma} \cdot \ln\left(\frac{P}{Psat}\right)$$

One Equation, One Unknown

$R_g := 8.314 \frac{J}{mole \cdot K}$ $Temp := 298K$ $\gamma := 22.4 \frac{erg}{cm^2}$ $Mw := 46.07 \frac{gram}{mole}$ $\rho := .789 \frac{gram}{cm^3}$

$Psat := 1$ $Vol := \frac{Mw}{\rho}$

guess value: $r_1 := 3nm$

Given

$$\left[\frac{1}{\sqrt{(2 \cdot R_{tip} + \alpha - d) \cdot (d - \alpha + 2 \cdot h + 2 \cdot r_1)} - r_1} - \frac{1}{r_1}\right] \cdot nm = \frac{R_g \cdot Temp}{Vol \cdot gamma} \cdot \ln\left(\frac{P}{Psat}\right) \cdot nm$$

$R_{one}(R_{tip}, d, h, P, \alpha, gamma, Vol) := Find(r_1)$

$R_{one}(50nm, 0nm, 1nm, .1, 0nm, \gamma, Vol) = 0.226 \cdot nm$

$$R_{two}(R_{tip}, d, h, P, \alpha, \gamma, Vol) := \sqrt{(2 \cdot R_{tip} + \alpha - d) \cdot (d - \alpha + 2 \cdot h + 2 \cdot R_{one}(R_{tip}, d, h, P, \alpha, \gamma, Vol))} \ldots + -R_{one}(R_{tip}, d, h, P, \alpha, \gamma, Vol)$$

$$F_{CAP}(R_{tip}, d, h, P, \alpha, \gamma, Vol) := \frac{-R_g \cdot Temp}{Vol} \cdot \ln\left(\frac{P}{Psat}\right) \cdot \pi \cdot R_{two}(R_{tip}, d, h, P, \alpha, \gamma, Vol)^2$$

$$\frac{F_{CAP}(R_{tip} \cdot nm, 0nm, 1nm, .5, 0nm, \gamma, Vol)}{(4 \cdot \pi \cdot R_{tip} \cdot nm \cdot \gamma)}$$

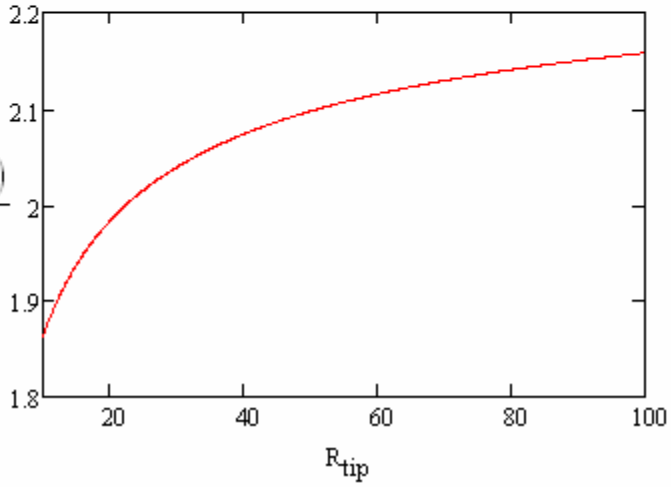

Now to include the real thickness as a function of partial pressure for Ethanol:

$$P := \begin{pmatrix} 0 \\ 6.8 \\ 10.2 \\ 14.8 \\ 24.8 \\ 45.1 \\ 64.9 \\ 74.4 \\ 88.7 \\ 99.8 \end{pmatrix} \% \qquad \text{Thickness} := \begin{pmatrix} 0 \\ 5.2 \\ 5.7 \\ 6.5 \\ 8.0 \\ 9.3 \\ 10.9 \\ 12.1 \\ 14.8 \\ 19.6 \end{pmatrix} \cdot 10^{-10}\,\text{m}$$

$$n := 4$$

$$\text{Fit}(x) := \text{interp}\left(\text{regress}\left(P, \frac{\text{Thickness}}{\text{nm}}, n\right), P, \frac{\text{Thickness}}{\text{nm}}, x\right) \cdot \text{nm}$$

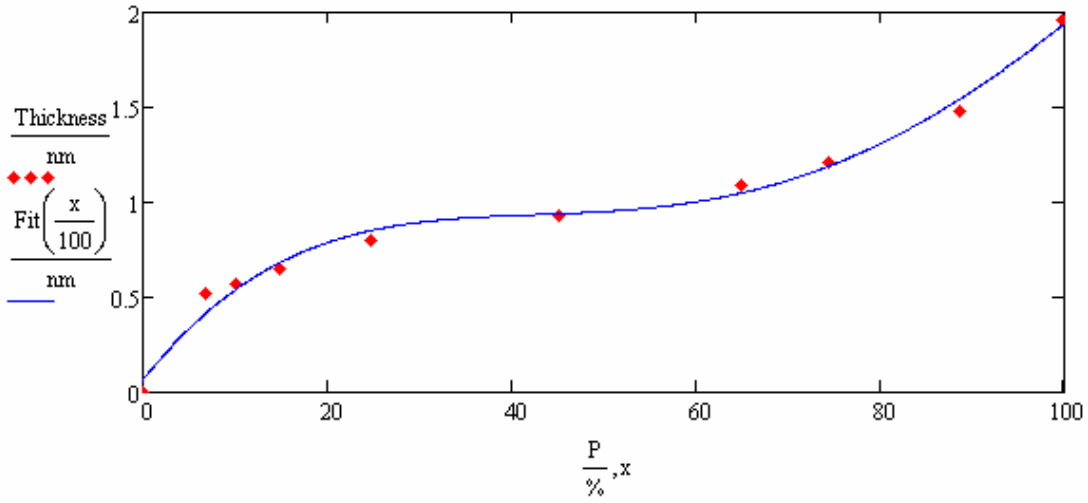

Fitting for butanol:

$$P_{C4} := \begin{pmatrix} 0 \\ 7.1 \\ 9.5 \\ 14.7 \\ 24.6 \\ 44.7 \\ 63.6 \\ 73.8 \\ 80.7 \\ 88.1 \\ 95 \end{pmatrix} \% \qquad Th_{C4} := \begin{pmatrix} 0 \\ 5.3 \\ 6.4 \\ 7 \\ 7.9 \\ 9.1 \\ 10.4 \\ 11.9 \\ 12.1 \\ 13.5 \\ 13.9 \end{pmatrix} \cdot 10^{-10}\,m \qquad n := 3$$

$$Fit_{C4}(x) := interp\left(regress\left(P_{C4}, \frac{Th_{C4}}{nm}, n\right), P_{C4}, \frac{Th_{C4}}{nm}, x\right) \cdot nm$$

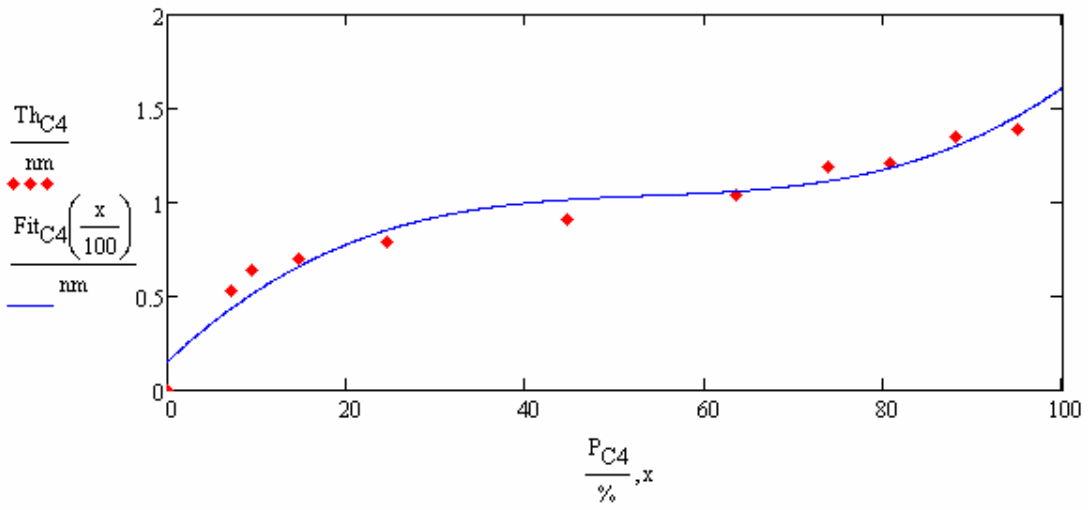

Fitting for Pentanol:

$$P_{C5} := \begin{pmatrix} 0 \\ 6.8 \\ 9.9 \\ 14.9 \\ 24.8 \\ 44.8 \\ 65.2 \\ 75.9 \\ 84.5 \\ 94.7 \end{pmatrix} \% \qquad Th_{C5} := \begin{pmatrix} 0 \\ 4.6 \\ 8.6 \\ 9.6 \\ 10.3 \\ 11.1 \\ 11.6 \\ 12.1 \\ 12.4 \\ 13 \end{pmatrix} \cdot 10^{-10} \cdot .8m \qquad nn := 6$$

$$Fit_{C5}(x) := interp\left(regress\left(P_{C5}, \frac{Th_{C5}}{nm}, nn\right), P_{C5}, \frac{Th_{C5}}{nm}, x\right) \cdot nm$$

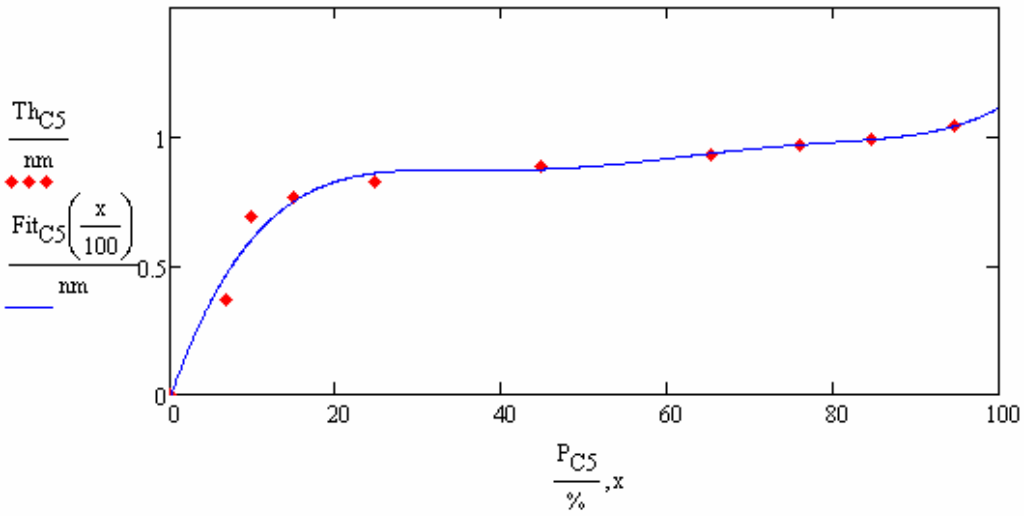

$$Fit_{avg}(P) := \frac{Fit(P) + Fit_{C4}(P) + Fit_{C5}(P)}{3}$$

$$F_{ETHANOL_{j,k}} := \frac{F_{TOTAL}\left(Tip_j, Fit_{avg}\left(Pres_k\right), Pres_k, 0nm, .1nm, \gamma_{R\_OH_0}, Volume_0\right)}{\left(4 \cdot \pi \cdot Tip_j \cdot \gamma\right)}$$

$$F_{PROPANOL_{j,k}} := \frac{F_{TOTAL}\left(Tip_j, Fit_{avg}\left(Pres_k\right), Pres_k, 0nm, .1nm, \gamma_{R\_OH_1}, Volume_1\right)}{\left(4 \cdot \pi \cdot Tip_j \cdot \gamma\right)}$$

$$F_{BUTANOL_{j,k}} := \frac{F_{TOTAL}\left(Tip_j, Fit_{avg}\left(Pres_k\right), Pres_k, 0nm, .1nm, \gamma_{R\_OH_2}, Volume_2\right)}{\left(4 \cdot \pi \cdot Tip_j \cdot \gamma\right)}$$

$$F_{PENTANOL_{j,k}} := \frac{F_{TOTAL}\left(Tip_j, Fit_{avg}\left(Pres_k\right), Pres_k, 0nm, .1nm, \gamma_{R\_OH_3}, Volume_3\right)}{\left(4 \cdot \pi \cdot Tip_j \cdot \gamma\right)}$$

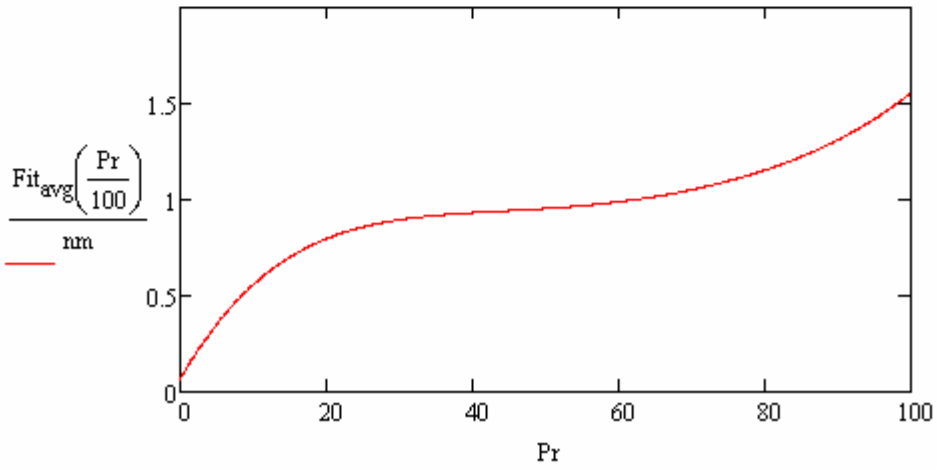

$$F_{ADH\_ETHANOL} := \begin{pmatrix} 280 \\ 172 \\ 162 \\ 158 \\ 124 \\ 73 \\ 53 \\ 43 \end{pmatrix} nN \qquad Relative_P := \begin{pmatrix} 0.001 \\ 5 \\ 10 \\ 15 \\ 30 \\ 60 \\ 85 \\ 98 \end{pmatrix} \%$$

$$F_{ADH\_PENTANOL} := \begin{pmatrix} 413 \\ 228 \\ 184 \\ 181 \\ 143 \\ 95 \\ 100 \\ 94 \end{pmatrix} nN \qquad F_{ADH\_BUTANOL} := \begin{pmatrix} 348 \\ 215 \\ 186 \\ 189 \\ 145 \\ 91 \\ 65 \\ 73 \end{pmatrix} nN$$

$$\frac{F_{CAP}\left(100nm, 0nm, Fit_{avg}\left(Pres_k\right), Pres_k, 0nm, \gamma_{R\_OH_0}, Volume_0\right)}{\left(4 \cdot \pi \cdot \gamma_{R\_OH_0} \cdot 100nm\right)}$$

$$\frac{F_{CAP}\left(100nm, 0nm, Fit_{avg}\left(Pres_k\right), Pres_k, 0nm, \gamma_{R\_OH_2}, Volume_2\right)}{\left(4 \cdot \pi \cdot \gamma_{R\_OH_2} \cdot 100nm\right)}$$

$$\frac{F_{CAP}\left(100nm, 0nm, Fit_{avg}\left(Pres_k\right), Pres_k, 0nm, \gamma_{R\_OH_3}, Volume_3\right)}{\left(4 \cdot \pi \cdot \gamma_{R\_OH_3} \cdot 100nm\right)}$$

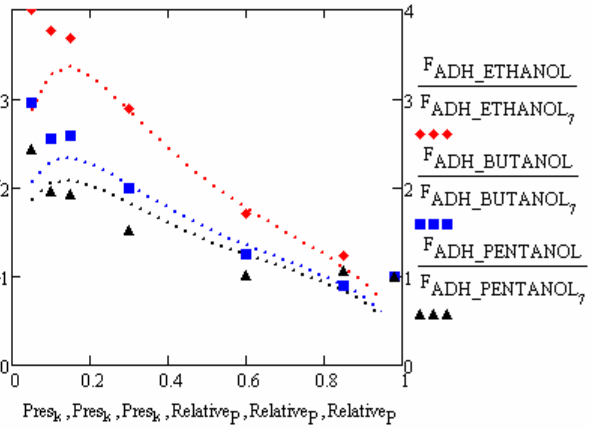

A.3 Silicon Cleaved in Air or Liquid Alcohol. (ToF-SIMS Data) Evidence of alkoxide formation from base linear alcohols.

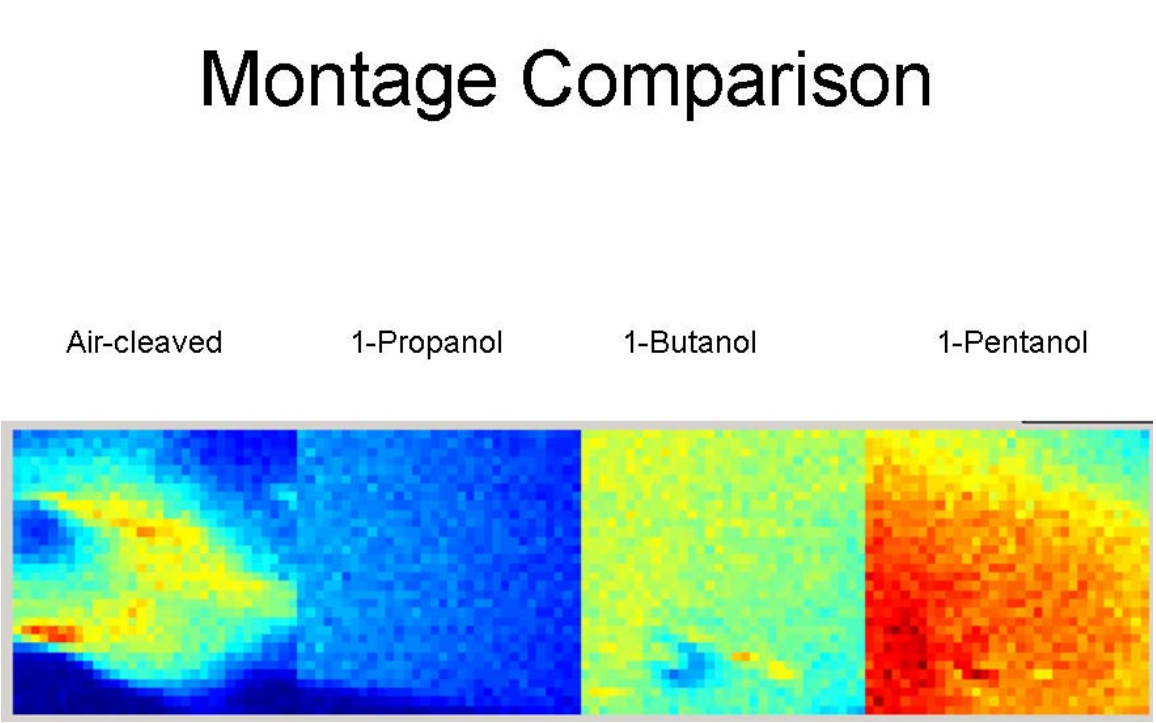

Figure **A.1**: Time-of-flight SIMS images (total intensity) of various silicon surfaces cleaved in different environments (alcohol cleavage experiments were done in bulk liquid). Montage of images for processing

Neg – 85 m/z ($C_5H_9O^-$)

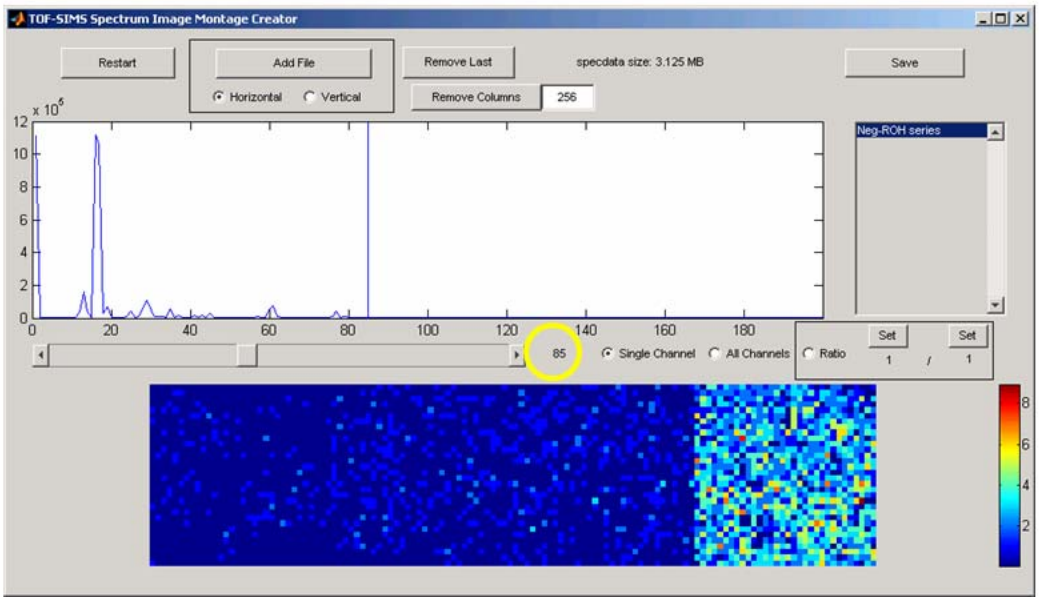

Figure **A.2**: M/Z 85 from the montage of images (primary alcohol fragment).

Neg – 71 m/z ($C_4H_7O^-$)

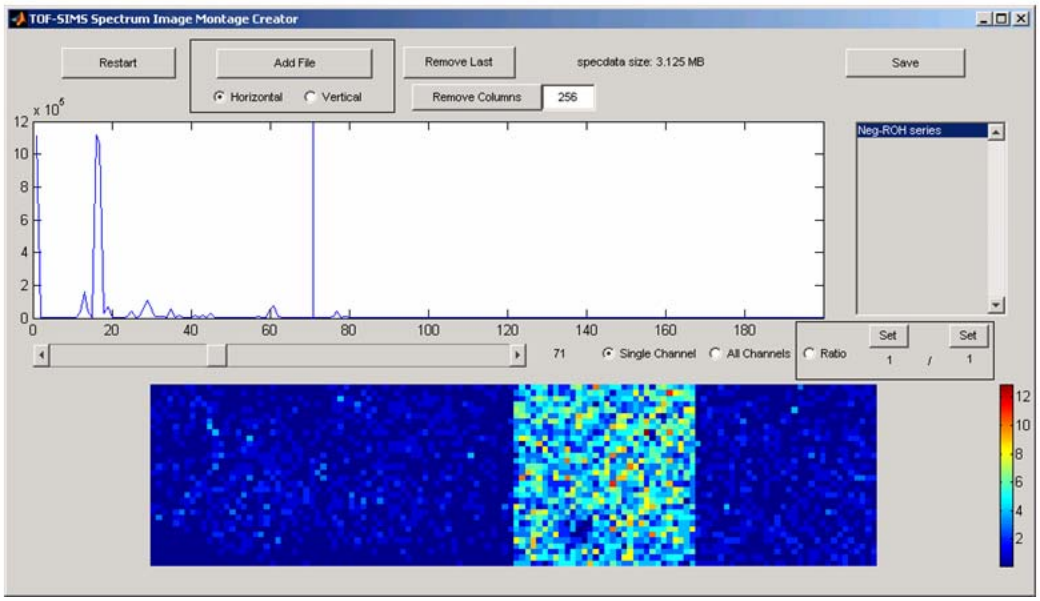

Figure **A.3**: M/Z 71 from the montage of images (primary alcohol fragment).

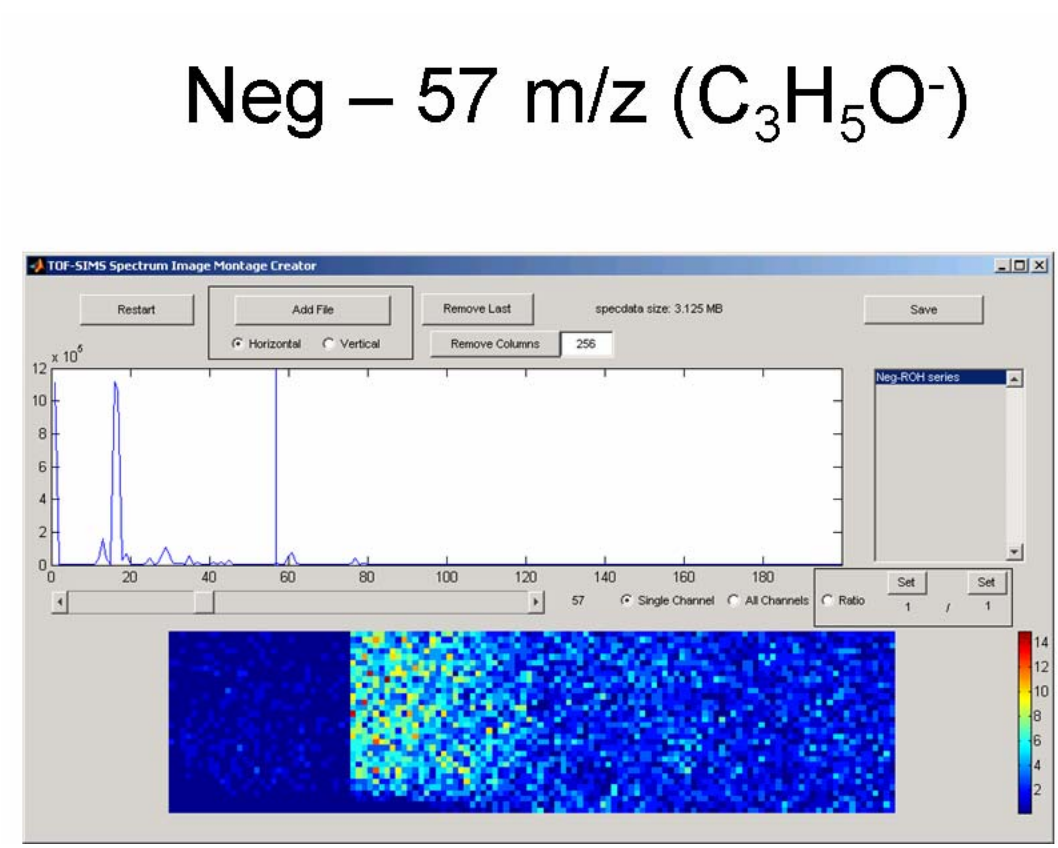

Figure **A.4**: M/Z 57 from the montage of images (primary alcohol fragment).

Neg – 103 m/z ($C_3H_7O_2Si^-$)

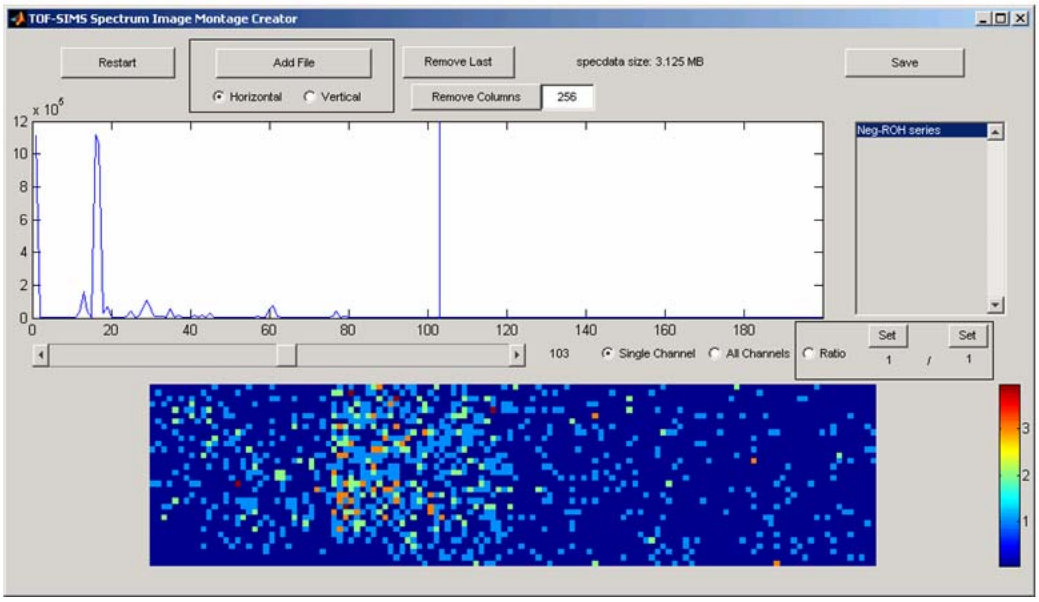

Figure **A.5**: M/Z 103 from the montage of images (primary alkoxide fragment).

Neg – 117 m/z ($C_4H_9O_2Si^-$)

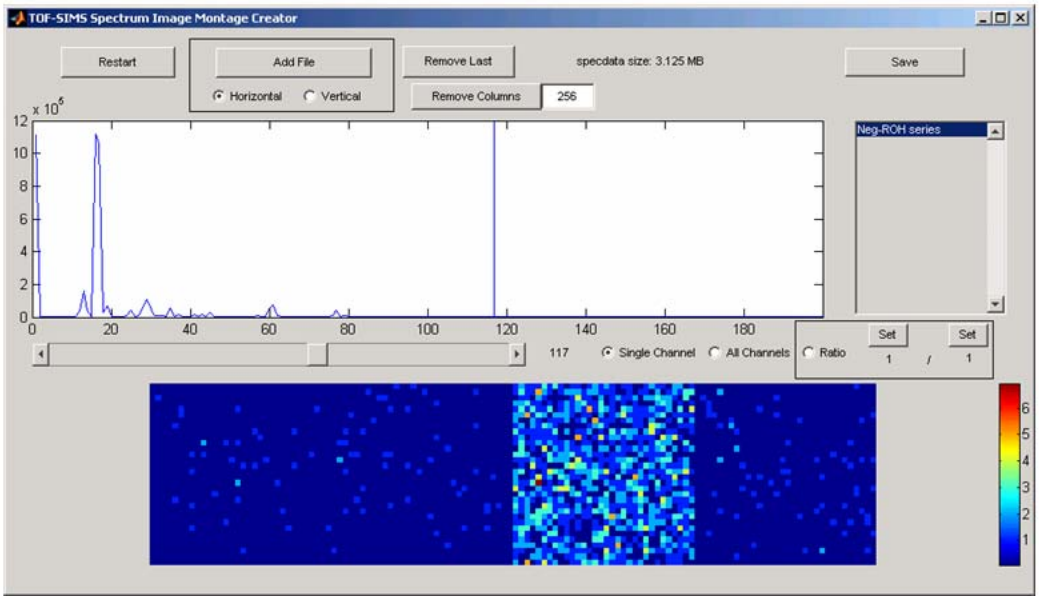

Figure **A.6**: M/Z 117 from the montage of images (primary alkoxide fragment).

Neg – 131 m/z ($C_5H_{11}O_2Si^-$)

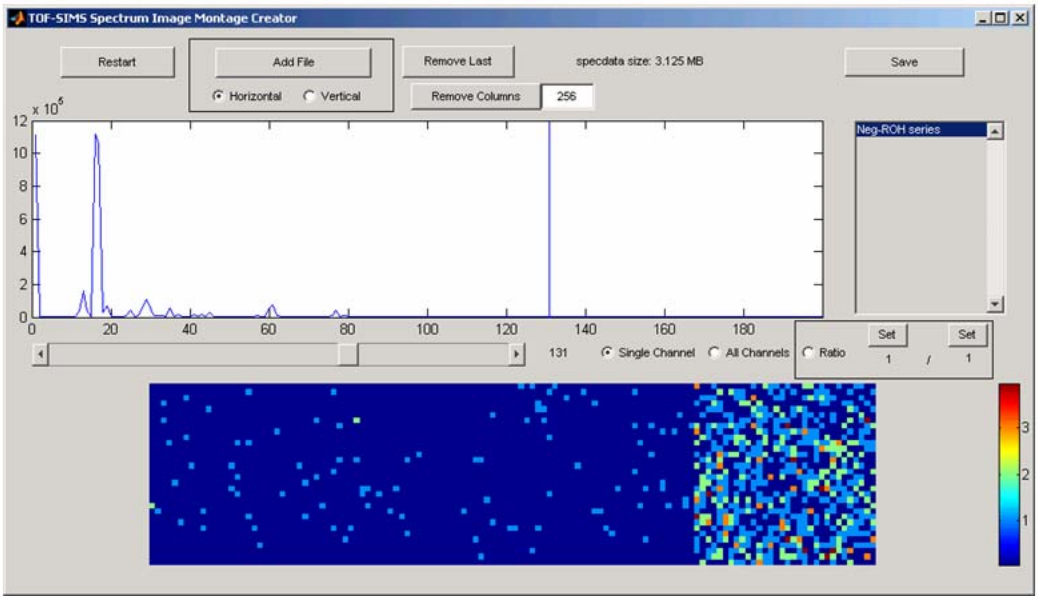

Figure **A.7**: M/Z 131 from the montage of images (primary alkoxide fragment).

A.4 Isotherm Data for Chapter 3

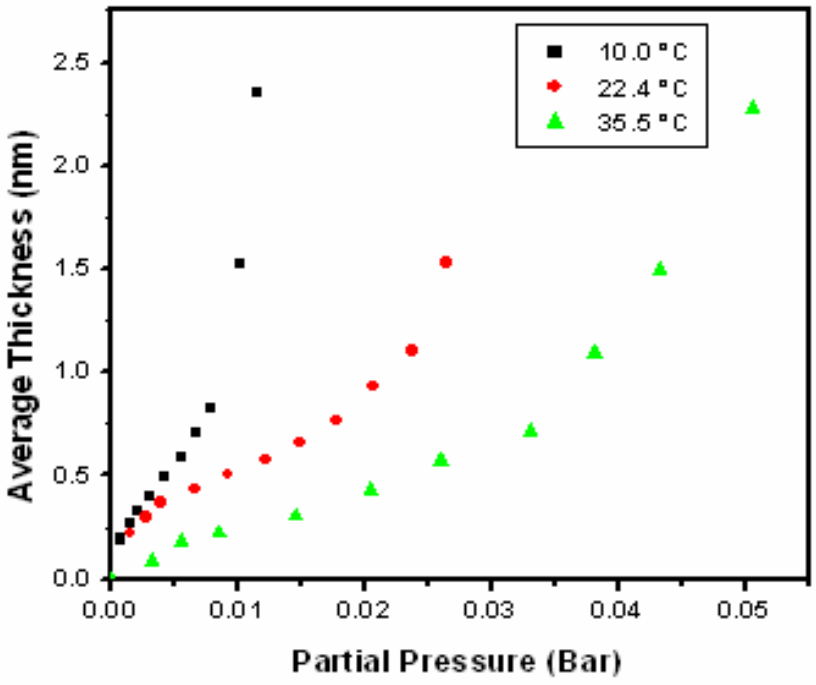

Figure **A.8**: Adsorption Isotherm of water on clean silicon oxide surface at various temperatures.

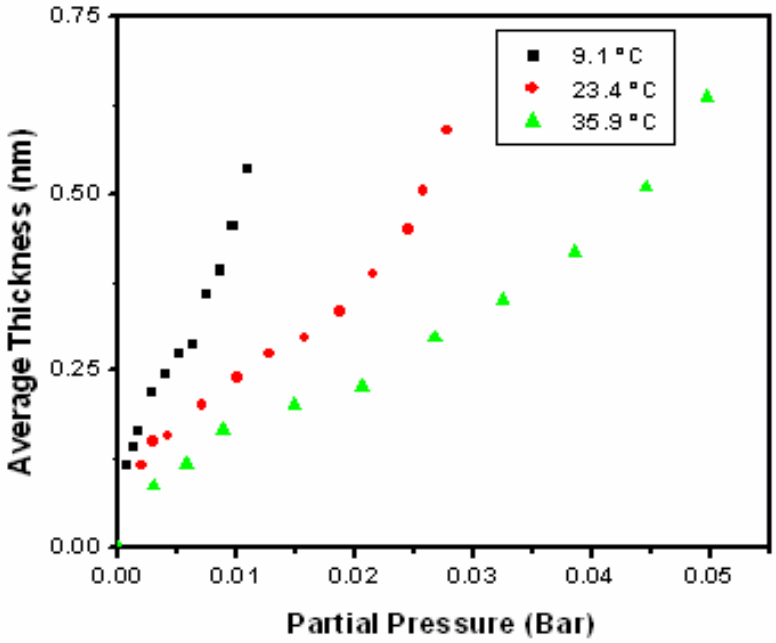

Figure **A.9**: Adsorption Isotherm of water on the partially methylated silicon oxide surface at various temperatures.

VITA

David B. Asay was born in 1975 in Provo, Utah. He received his bachelor's degree from Texas Tech University in Lubbock, Texas in 2003. During his undergraduate studies, he spent time at Elk Corp as a summer co-op engineer as well as ChevronPhillips Chemical working as a process engineer and a research engineer in their R&D facilities. Following these experiences and graduation from Texas Tech he attended Pennsylvania State University in 2003 and joined Professor Seong H. Kim's research group in pursuit of a doctorate degree in chemical engineering. In the summers of 2006 and 2007, David visited Sandia National Laboratories as a summer intern working with Mike Dugger studying MEMS and silicon tribology. David's research interests include, surface science, structure-property relationships of materials, nanotechnology, and interfacial phenomena in general. As of August 2008, his work has currently led to the following publications:

1. Barnette AL, Asay DB, Kim SH, Phys. Chem. Chem. Phys. (in press)
2. Asay DB, Dugger MT, Kim SH, Tribo. Lett. 29 (1): 67-74 **2008**.
3. Asay DB, Dugger MT, Ohlhausen JA, & Kim SH, Langmuir 24 (1): 155-159 **2008**.
4. Asay DB & Kim SH, Langmuir 23 (24): 12174-12178 **2007**.
5. Kim SH, Asay DB, & Dugger MT, Nanotoday 2 (5): 22-29 **2007**.
6. Asay DB & Kim SH, J. Chem. Phys. 124 (17): 174712 **2006.**
7. Asay DB & Kim SH, R. Sci. Inst. 77 (4): 043903 **2006.**
8. Strawhecker K, Asay DB, & Kim SH, Dekker Encyclopedia of Chemical Processing, 1143 **2006**.
9. Asay DB & Kim SH, J. Phys. Chem. B 109 (35): 16760-16763 **2005.**
10. Strawhecker K, Asay DB, McKinney J, *et al*., Tribo. Lett. 19 (1): 17-21 **2005.**